
**A NEW PERSPECTIVE
OF THE SOLAR WIND MICRO-STRUCTURE
DUE TO MULTI-POINT OBSERVATIONS
OF DISCONTINUITIES**

INAUGURAL – DISSERTATION
ZUR
ERLANGUNG DES DOKTORGRADES
DER MATHEMATISCH–NATURWISSENSCHAFTLICHEN FAKULTÄT
DER UNIVERSITÄT ZU KÖLN

VORGELEGT VON
THORSTEN KNETTER
AUS TROISDORF

KÖLN 2005

Berichterstatter: Prof. Dr. F. M. Neubauer

Prof. Dr. M. Kerschgens

Tag der mündlichen Prüfung: 7. Juli 2005

Abstract

We present a statistical analysis of directional discontinuities in the solar wind at 1 astronomical unit. It is the first study of this kind based on simultaneous observations at four nearby spacecraft. We use recent magnetic field and plasma data from the coordinated Cluster spacecraft flying in formation a few hundred to a few thousand kilometres apart. With four measuring platforms the ability to observe is considerably improved. For example, the simultaneous four-point measurements allow for determining the discontinuity normals by analysing the time differences between the occurrence of the discontinuity at each of the four spacecraft. The events used in our analysis are grouped in three sets according to the period of their observation, i.e., January - May of 2001, 2002 and 2003, respectively. The main distinction between these three data sets is the different spacecraft separation, from 100 km in 2002 to 5000 km in 2003, which enables us to investigate interplanetary discontinuities at different scales. Another difference between the three data sets are the different prevailing solar wind conditions. These include both slow solar winds and fast streams that map back to coronal holes on the Sun.

Our analysis demonstrates that the Minimum Variance Analysis (MVA), an established and widely used single-spacecraft technique to compute normals of discontinuities, is much less reliable than previously assumed. We determine new criteria to decide whether or not MVA yields reliable normal estimates. An important parameter is the ratio of intermediate to minimum eigenvalue λ_2/λ_3 of the magnetic covariant matrix. Instead of using 2 as the lower limit for λ_2/λ_3 for applicability of MVA, as is common practice, we strongly suggest applying MVA only if $\lambda_2/\lambda_3 > 10$. Furthermore, the accuracy of MVA increases with increasing spreading angle ω , the angle between the magnetic field vectors on the two sides of the discontinuity. We recommend MVA should not be used for $\omega < 60^\circ$.

Inaccurate MVA normal estimates have resulted in a dramatic overestimation of the number of rotational discontinuities in earlier studies. Using the relative timing technique, we do not find a single clear rotational discontinuity. A detailed error analysis of the multi-spacecraft tool puts this new result on a firm footing. Analysis of plasma data shows that many discontinuities do not satisfy the polarisation relation, a necessary condition for rotational discontinuities. Our results allow for the interpretation that the solar wind is dominated by tangential rather than rotational discontinuities which is in apparent contradiction to earlier single-spacecraft studies. This finding is particularly true for fast coronal hole streams where earlier observations claim a high abundance of rotational discontinuities.

Our new results entail significant implications for the dynamics of the solar wind microstructure and generation mechanisms for discontinuities. We also discuss possible consequences for the understanding of the source region on the Sun and for the propagation of cosmic rays through the heliosphere.

We study further properties of directional discontinuities, such as their thickness, their orientation in space and their large-scale curvature. We conclude that interplanetary discontinuities are 1-D structures superposed by non-isotropic fluctuations.

Zusammenfassung

In der vorliegenden Arbeit stellen wir eine statistische Untersuchung von Richtungsdiskontinuitäten im Sonnenwind in der Nähe der Erde vor. Es ist die erste Analyse dieser Art, die auf der gleichzeitigen Beobachtung an den Orten von vier anstelle von nur einem Satellit basiert. Dies ermöglicht die Anwendung überlegener Auswertungstechniken, wodurch ein Jahrzehnte währender Trugschluss bezüglich der Mikrostruktur des Sonnenwindes ausgeräumt wird und neuen Überlegungen die Tore geöffnet werden.

Bereits frühe Messungen mittels Magnetometern und Plasmainstrumenten an Bord von Satelliten offenbarten eine starke Variabilität des Sonnenwindes. Ein großer Teil dieser Variationen ist nicht kontinuierlich, sondern erfolgt in sehr sprunghaften Änderungen der Sonnenwindparameter, insbesondere in der Richtung des Magnetfeldes [Ness *et al.*, 1966]. Diese Richtungsdiskontinuitäten (DDs: directional discontinuities), typischerweise eingebettet in ein ansonsten relativ ruhiges Magnetfeld, waren theoretisch nicht vorhergesagt. Die Kenntnis ihrer Existenz verdanken wir alleinig der in-situ Beobachtung. Zahlreiche Untersuchungen mittels späterer Satellitenmissionen ermöglichten große Fortschritte im Verständnis dieser Strukturen. So wissen wir heute, dass es sich bei diesen häufig vorkommenden DDs wahrscheinlich um magnetohydrodynamische Tangential- (TDs) bzw. Rotationsdiskontinuitäten (RDs) handelt, und dass sie vermutlich in der Nähe der Sonne entstehen. Die entscheidende Frage jedoch, wie es überhaupt zu der Entstehung dieser Strukturen kommt, konnte bis zum heutigen Tage nicht geklärt werden. Ein wichtiger Schritt zur Klärung dieser Frage, aber auch zur Verbesserung unseres Verständnisses der Struktur des Sonnenwindes an sich, ist es, eine genaue Vorstellung der DDs zu entwickeln. Dieser Problematik stellen wir uns in dieser Arbeit.

TDs und RDs sind zwei sich deutlich voneinander unterscheidende Strukturen innerhalb der Magnetohydrodynamik (MHD). MHD-Diskontinuitäten werden generell als lokal ebene Flächen verstanden, die zwei Plasmen mit unterschiedlichen Eigenschaften voneinander trennen. Ein wesentlicher Unterschied zwischen TDs und RDs ist, dass bei RDs diese beiden Plasmen über das Magnetfeld miteinander verbunden sind, bei TDs ist dies nicht der Fall. Anders ausgedrückt, ist das Magnetfeld bei TDs parallel zur Trennfläche, und die Normalkomponente B_n ist somit Null. RDs hingegen besitzen ein von Null verschiedenes B_n . Da davon auszugehen ist, dass die Entstehung und die dynamische Entwicklung im Sonnenwind der beiden Diskontinuitätstypen unterschiedlichen Prinzipien unterliegen, ist zunächst zu klären, ob es sich bei den DDs im Sonnenwind um den einen oder den anderen Typ handelt. Neuere Ergebnisse aus statistischen Beobachtungsanalysen schlagen generell eine Dominanz der RDs vor (z.B. Neugebauer *et al.* [1984]). Diese tritt besonders deutlich im schnellen Sonnenwind, der den koronalen Löchern auf der Sonne entspringt, auf [Neugebauer and Alexander, 1991]. Im langsamen Sonnenwind hingegen ist das Verhältnis von RDs zu TDs eher ausgeglichen. Zur Unterscheidung der Diskontinuitätstypen wird häufig die Normalkomponente des Magnetfeldes benutzt. Ist diese groß, und zwar größer als Null innerhalb des angenommenen Fehlers, so handelt es sich um eine RD.

Ein generelles Problem bei dieser Methode ist es, die Genauigkeit, mit der B_n bestimmt wird, abzuschätzen. Diese wiederum ist unmittelbar mit der Güte der Normalenrichtung der Grenzfläche verknüpft. Genau an dieser Stelle setzt die vorliegende Arbeit an. Nahezu sämtliche

vorangegangenen statistischen Untersuchungen basieren auf den Daten eines einzelnen Satelliten. Das hat zur Folge, dass auch die zur Verfügung stehenden Analysewerkzeuge zur Bestimmung der Grenzflächennormalen begrenzt sind. Üblicherweise wird dazu, wie auch in vielen anderen Bereichen der Weltraumplasmaphysik, die *Minimum-Varianz-Analyse* (MVA) benutzt. Ein schwerwiegender Nachteil dieser Technik ist die Schwierigkeit, einen vernünftigen Fehler zu bestimmen.

Dank der Clustermission, die aus vier koordinierten Satelliten besteht, die in enger Formation die Erde umkreisen, können diese Probleme überwunden werden. Obwohl das Hauptziel von Cluster die Erkundung der Magnetosphäre ist, befinden sich die vier Raumfahrzeuge auch für beträchtliche Zeitspannen im Sonnenwind. Da es keine vergleichbare Multisatellitenmission im interplanetaren Raum gibt, nutzen wir die Gelegenheit, Cluster für unsere Zwecke einzuspannen.

Nach sorgfältiger Auswahl von DDs gemäß etablierter Kriterien, bleiben uns immerhin 366 Ereignisse im *ungestörten Sonnenwind*, d.h. außerhalb der *Vorschockregion*, in der Störungen aufgrund von an der *Bugstoßwelle* reflektierten Teilchen auftreten können. Diese 366 DDs unterteilen sich in drei Gruppen, entsprechend der Untersuchungszeiträume, in denen die Clusterbahn Sonnenwindanteile aufweist. Diese sind Januar - Mai im Jahr 2001, 2002, bzw. 2003, und unterscheiden sich zum einen durch unterschiedliche Satellitenabstände und zum anderen durch die vorherrschenden Sonnenwindbedingungen. Die verschiedenen Abstände erlauben eine Untersuchung der Diskontinuitäten auf unterschiedlichen Längenskalen (100 - 5000 km).

Die Benutzung von vier anstelle von nur einem Satelliten bietet nun diverse Vorteile. Einerseits können die MVA-Ergebnisse an nahe beieinander liegenden Orten miteinander verglichen werden, und es kann somit ein Maß für die Genauigkeit dieser Methode gefunden werden. Andererseits kann eine „echte“ Multisatellitenmethode (Triangulation) zur Bestimmung der Diskontinuitätennormalen angewendet werden. Diese basiert auf einfachen geometrischen Überlegungen und macht sich die Zeitdifferenzen zwischen dem Erscheinen einer Diskontinuität an den einzelnen Satelliten zunutze. Ein großer Vorteil dieser Methode gegenüber der MVA ist die einfache Fehlerbehandlung. Es stellt sich heraus, dass die Genauigkeit der Triangulation stark mit der Größe des aus den vier Raumfahrzeugen gebildeten Tetraeders korreliert. Ein weiterer wichtiger Faktor ist die geometrische Güte des Tetraeders, d.h. der Grad, zu dem die Figur, deren Eckpunkte die Positionen der vier Satelliten sind, einem regulären (gleiche Kantenlängen) Tetraeder ähnelt. Abgesehen von den eher wenigen Ereignissen, die mit kleinen Satellitenabständen (100 km) untersucht werden, erzielen wir eine sehr große Genauigkeit bei der Normalenbestimmung. Zum Beispiel sind die Normalen im Mittel bis auf 5° genau bestimmt, wenn die Abstände 5000 km (im Jahr 2003) betragen. In Einzelfällen, insbesondere bei hoher vorliegender geometrischer Güte des Tetraeders, sind die Normalen sogar noch besser bestimmt.

Der Vergleich der vier MVA-Normalen sowohl untereinander als auch mit der Triangulationsnormalen zeigt, dass die MVA sehr viel ungenauer ist als zuvor angenommen wurde. Wir können sogar zeigen, dass unter bestimmten Voraussetzungen eine Richtung bestimmt wird, die einer zufälligen Wahl gleichkommt. In anderen Fällen erweist sich diese etablierte Methode jedoch als recht zuverlässig. Ungünstigerweise überwiegt der erste Fall. Wir sind in

der Lage, die Voraussetzungen zu spezifizieren, bei denen MVA möglicherweise sinnvolle Ergebnisse liefert. Ein wichtiger Parameter dabei ist das Verhältnis des mittleren zum kleinsten Eigenwert λ_2/λ_3 . Die Eigenwerte geben die Varianzen der Magnetfeldkomponenten in Richtung der stärksten, mittleren und schwächsten Varianz an. Theoretisch sollte für eine 1-D-Struktur die minimale Varianz verschwinden, und die Richtung, in der dies der Fall ist, ist dann die Normale der Struktur. Sind mittlerer und kleinster Eigenwert nun aber ungefähr gleich groß, etwa aufgrund von überlagerten Fluktuationen, so kann die Richtung der minimalen Varianz nicht eindeutig bestimmt werden. Aus diesem Grund sollte λ_2/λ_3 groß sein. In früheren Arbeiten wurde häufig ein Minimalwert von $(\lambda_2/\lambda_3)^L = 2$ benutzt, um sinnvolle MVA-Ergebnisse zu gewährleisten [Neugebauer *et al.*, 1984; Horbury *et al.*, 2001b]. Unsere Multisatellitenanalyse zeigt jedoch, dass dies viel zu optimistisch ist. Wir empfehlen, $(\lambda_2/\lambda_3)^L = 10$ als untere Grenze zu wählen.

Wie bereits in Lepping and Behannon [1980] betont wird, spielt auch der Spreizwinkel ω , der Winkel zwischen dem Magnetfeld auf der einen und der anderen Seite der Diskontinuität, eine wichtige Rolle für die Genauigkeit. Große Winkel haben in der Regel aussagekräftigere Minimum-Varianz-Richtungen zur Folge. Diesem Ergebnis wurde bisher eher wenig Beachtung geschenkt - zu Unrecht, wie die vorliegende Arbeit zeigt. Wir empfehlen, MVA nicht zu benutzen, wenn ω kleiner als ungefähr 60° ist. Da MVA ein breites Anwendungsspektrum in der Weltraumplasmaphysik besitzt, sind diese neuen Erkenntnisse von höchstem allgemeinen Interesse.

Für die Analyse von interplanetaren Diskontinuitäten hat die deutliche Überschätzung der MVA-Genauigkeit dramatische Folgen. Die große Population der „eindeutig identifizierten“ RDs ist ausschließlich eine Folge der ungenauen MVA-Normalen. Beschränkt man sich bei der Anwendung der MVA nur auf die Fälle, bei denen von sinnvollen Ergebnissen auszugehen ist (großes λ_2/λ_3 und/oder ω), so schrumpft die Anzahl der aufgrund der Normalkomponente B_n des Magnetfeldes identifizierten RDs dramatisch. Anwendung der Triangulation liefert ausschließlich kleine Normalkomponenten. Tatsächlich zeigt die Fehleranalyse, dass die Werte von B_n für alle untersuchten Fälle konsistent mit Null sind. Anders ausgedrückt, sind alle unsere Ereignisse konsistent mit TDs, was im deutlichen Widerspruch zu sämtlichen früheren Arbeiten steht. Insbesondere trifft dies auf den schnellen Sonnenwind koronalen Ursprungs zu, der ja nach früherer Erkenntnis die meisten RDs beherbergen soll.

Neben der Normalkomponente des Magnetfeldes gibt es noch eine Reihe weiterer Kriterien, anhand derer man Diskontinuitäten klassifizieren kann. Beispielsweise ist die Erfüllung der *Polarisationsrelation* eine notwendige Bedingung für RDs. Diese wird von den meisten unserer Ereignisse nicht erfüllt. Somit sind nicht nur alle DDs unserer Stichprobe konsistent mit TDs, sondern die meisten sind auch inkonsistent mit RDs. Dies lässt erstmals die Schlussfolgerung zu, dass es im Sonnenwind keine RDs gibt.

Diese neuen Ergebnisse werfen eine Reihe von Fragen auf. Geht man tatsächlich davon aus, dass der Sonnenwind keine RDs enthält, so muss geklärt werden, ob RDs erst gar nicht entstehen oder ob sie zwar entstehen, aber kurzlebig sind. Zur Untersuchung der Stabilität sind beispielsweise Computersimulationen hilfreich. Wir können andererseits auch nicht ausschließen, dass einige der Diskontinuitäten RDs sind. In dem Fall stellt sich aber direkt die Frage, warum alle RDs so ein kleines B_n haben. Dies könnte Aufschlüsse über mögliche Entste-

hungsmechanismen liefern. Nach bisheriger Vorstellung entstehen RDs aufgrund von nicht linearen dynamischen Prozessen im Sonnenwind. Da wir keine RDs (mit großem B_n) finden, sollte diese Theorie ernsthaft überprüft werden. Eine weitere Möglichkeit wäre, dass die Stabilität von RDs an B_n geknüpft ist, so dass bis zur Ankunft bei der Erde nur solche mit kleinem B_n „überleben“.

Da die meisten interplanetaren Diskontinuitäten wahrscheinlich in der Nähe der Sonne entstehen, enthalten deren Eigenschaften eventuell Informationen über die Sonne. Die Häufigkeit, mit der RDs und TDs in den unterschiedlichen Arten des Sonnenwindes auftreten, hat eine Vorstellung geprägt, wie mögliche Prozesse auf der Sonne die Entstehung von DDs erklären (siehe z.B. *Neugebauer and Alexander* [1991] und Referenzen darin). Die vorgeschlagenen Mechanismen stehen in engem Zusammenhang mit der Heizung der Korona [*Parker*, 1991b]. Unsere neuen Beobachtungsergebnisse könnten auch hier neue Impulse setzen.

Die Möglichkeit, dass alle oder die meisten DDs im Sonnenwind TDs sind, ist auch von großer Bedeutung für die Charakterisierung der Topologie des interplanetaren Magnetfeldes. Im Gegensatz zu RDs, trennen TDs Plasmaregionen voneinander, die magnetisch nicht miteinander verbunden sind. Eine große Anzahl von TDs würde also bedeuten, dass der Sonnenwind aus vielen solcher Regionen besteht, zwischen denen kein Plasmafluss existiert. Dies könnte Auswirkungen auf die Ausbreitung kosmischer Strahlung in der Heliosphäre haben.

Neben der Klassifizierung von DDs beschäftigen wir uns mit weiteren statistischen Eigenschaften dieser Strukturen. Beispielsweise finden wir, dass aufgrund der allgemein schlechten Übereinstimmung der Minimum-Varianz-Richtung mit der lokalen Diskontinuitätsnormalen frühere Arbeiten über die großskalige Krümmung von DDs vorsichtig zu interpretieren sind. Es erscheint uns nicht möglich, eine Aussage anhand von MVA-Ergebnissen zu treffen.

Die Multisatellitenanalyse erlaubt ferner eine verbesserte Bestimmung der Diskontinuitätsdicken. Unsere Ergebnisse stimmen aber im Wesentlichen mit früheren Einzelsatellitenergebnissen überein. Insbesondere zeigt sich, dass die minimal auftretende Dicke tatsächlich einige Protonengyroradien beträgt.

Aufgrund der genaueren Normalenbestimmung kann außerdem eine aussagekräftigere Statistik über die Orientierung der DDs im Raum erstellt werden. Ein Großteil der Grenzflächennormalen liegt in der Ebene der Ekliptik.

Die gleichzeitige Beobachtung der DDs an vier verschiedenen Orten und die Anwendung verschiedener Auswertetechniken führt schließlich zu einer Modellvorstellung dieser Strukturen: Interplanetare Diskontinuitäten setzen sich zusammen aus „idealen“ 1-D-Strukturen, die zumindest auf der Clusterskala (5000 km) planar sind, und überlagerten anisotropen Fluktuationen.

Die sich aus der vorliegenden Arbeit ergebenden möglichen Konsequenzen, etwa für die Ausbreitung kosmischer Strahlung in der Heliosphäre oder der koronalen Heizung, können hier nur am Rande diskutiert werden. Es erscheint jedoch erstrebenswert, sich dieser Problematiken im Lichte der neuen Erkenntnisse anzunehmen.

Contents

1	Introduction	1
2	The solar wind	5
3	Discontinuities	9
3.1	Classification of MHD discontinuities	9
3.1.1	Theory	10
3.1.2	Criteria used in observations	16
3.2	Observations of solar wind discontinuities	18
3.3	Origin and stability of solar wind discontinuities	20
3.4	The importance of solar wind discontinuities	24
4	The Cluster mission	27
4.1	Mission overview and historical background	28
4.2	Orbit and separation strategy	29
4.3	The satellites and their payload	31
4.3.1	Fluxgate magnetometer (FGM)	31
4.3.2	Cluster ion spectrometry (CIS)	32
5	Geometrical considerations of the Cluster array	33
5.1	1-D geometric factors	34

5.2	2-D geometric factors and the volumetric tensor	35
5.3	A simple performance study	39
5.4	Evolution of the tetrahedron along one orbit	41
5.5	Constellations used in our analysis	44
6	The set of discontinuities used in this work	53
6.1	Solar wind periods	54
6.2	Search criteria	55
6.3	Application of the search criteria	59
6.4	Avoiding foreshock activity - Final set of DDs	63
6.5	Prevailing solar wind conditions - Coronal holes	70
6.5.1	Solar activity cycle	71
6.5.2	Using ACE as a solar wind monitor	72
6.5.3	Wang-Sheeley model	78
6.5.4	Extreme ultra violet imaging	82
6.5.5	The helium I 1083 nm absorption line	84
6.5.6	DDs in coronal hole flow	85
7	Determination of discontinuity normals	87
7.1	Overview of normal determination techniques	88
7.2	Sonnerup-Cahill minimum variance analysis	90
7.2.1	Description of the method	91
7.2.2	Summary of past error analysis approaches	95
7.3	Cross product method for TDs	99
7.4	Triangulation	99
7.4.1	Description of the method	100
7.4.2	Barycentric formalism - error analysis	103
8	Statistical analysis of discontinuities at 1AU	109
8.1	Single spacecraft analysis	110
8.2	Classification result from triangulation compared to MVA	114
8.3	Reexamination of MVA - consequences	118

8.3.1	Parameters affecting the precision of MVA	120
8.3.2	Dependence on the eigenvalue ratio λ_2/λ_3	122
8.3.3	Dependence on the spreading angle ω	130
8.3.4	Variability of λ_2/λ_3 and ω	134
8.3.5	Superposed wave fields - one example	138
8.3.6	New classification criteria for single-spacecraft studies	142
8.4	Consistency tests for triangulation	144
8.5	Surface curvature on the Cluster scale and beyond	147
8.6	Distribution of the discontinuity normals in space	151
8.7	Discontinuity thickness	156
8.8	Using plasma data to identify possible RDs	161
8.8.1	Necessary conditions for RDs to be tested	162
8.8.2	Data coverage and selection of intervals	163
8.8.3	Thermal anisotropy	164
8.8.4	Continuity of ρA	166
8.8.5	Polarisation relation	168
8.8.6	Propagation relative to the ambient plasma	175
8.8.7	Properties of possible RDs	179
9	Triangulation error analysis	185
9.1	Method and symmetry considerations	186
9.2	Parameters affecting the error	191
9.3	Histograms and average values of the errors of \mathbf{n} and U	196
9.4	Consistency with the assumption of tangential discontinuities	198
10	Discussion and summary	205
A	Mathematics of a tetrahedron	215
A.1	Area of the sides	215
A.2	Volume of the tetrahedron	216
A.3	Circumscribing sphere	216
A.4	The regular tetrahedron	216

A.5	Calculating the quality factors Q_{GM} , Q_{RR} and Q_{R8}	217
B	Tables	219
C	MVA error analysis	221
D	Generalised formalism of the relative timing technique	223

List of Figures

3.1	Illustration of a TD and an RD	14
3.2	Example of an interplanetary discontinuity	15
3.3	Classification scheme used in this work.	17
3.4	Interwoven field lines of a bipolar magnetic region	21
3.5	Illustration of the magnetostatic theorem	21
4.1	GSE coordinate system	29
4.2	Cluster orbit	30
4.3	Spacecraft separations during the Cluster mission	30
5.1	The shape of the polyhedron as a function of E and P	39
5.2	Systematic deformation of a regular tetrahedron	39
5.3	Characteristics of the tetrahedra illustrated in Figure 5.2	40
5.4	Cluster 2 orbit from doy 52 2001 05:30 UT until doy 54 2001 14:40 UT	42
5.5	Tetrahedron characteristics for the orbit shown in Figure 5.4	43
5.6	Extreme cases of the tetrahedra used in our analysis	46
5.7	Spacecraft positions relative to Cl 4 for all DDs	48
5.8	Shape, orientation and location of the tetrahedra used in our analysis	49
5.9	Histograms of E and P for 2003, and of R_{ϕ}^c and R_{θ}^c for 2003 and 2001	51
6.1	Overview of days suitable for solar wind analysis with Cluster	55

6.2	Illustration of the Burlaga-method	57
6.3	Problem of simultaneous identification of a DD at different spacecraft	58
6.4	Number of DDs identified by the TS- and the B-method	60
6.5	Relative number of DDs found simultaneously at all four spacecraft as a function of the spacecraft separation	61
6.6	Foreshock geometry in the ecliptic plane and illustration of the parameter D	65
6.7	Six cases describing the evolution of D across a DD	66
6.8	D versus time for two typical days with Cluster in the solar wind	67
6.9	Correlation between D and foreshock waves	69
6.10	Monthly averaged sunspot numbers for cycle 23 through December 2004	72
6.11	Overview of the DDs found and the prevailing solar wind conditions in 2001	74
6.12	Same as Figure 6.11 for 2002	75
6.13	Same as Figure 6.12 for 2003.	76
6.14	FS I from Figure 6.13	79
6.15	Comparison of the Wang-Sheeley model predictions with the mapped polarity and velocity of FS I measured at ACE	81
6.16	SOHO images and Coronal hole map from the HeI 1083nm absorption line	83
6.17	Distributions of the magnetic field and plasma parameters observed with Cluster in the vicinity of the selected DDs in 2003	86
7.1	Variance ellipsoid	93
7.2	Illustration of the triangulation technique	101
7.3	Determination of the relative timings	102
7.4	Illustration of the barycentric coordinates and the reciprocal vectors	104
7.5	Cone of uncertainty.	107
8.1	Histogram of ω obtained from Cl 1	111
8.2	Classification results	115
8.3	Variance ellipsoids obtained from the magnetic field data of a DD	119
8.4	Distribution of λ_2/λ_3 and λ_1/λ_2	120
8.5	Relationship between λ_2/λ_3 and ω	121
8.6	Distributions of λ_2/λ_3 and ω	122
8.7	Dependence on $(\lambda_2/\lambda_3)^L$	123

8.8	Dependence of the classification result on $(\lambda_2/\lambda_3)^L$	127
8.9	Probability distribution of $\theta_{Bn} = \angle(\langle \mathbf{B} \rangle, \mathbf{n})$ and distributions of $ B_n /B_{max}$. .	129
8.10	Same as Figure 8.7 for ω^L	131
8.11	Dependence of the classification result on ω^L	133
8.12	Distributions of $\Delta(\lambda_2/\lambda_3)/(\lambda_2/\lambda_3)_{max}$ and $\Delta\omega/\omega_{max}$	135
8.13	Average values of $\Delta X/X_{max}$ ($X = \lambda_2/\lambda_3, \omega$) versus average separation	137
8.14	1-D discontinuity and superposed fluctuations	139
8.15	Distributions of $\Delta(B_n /B_{max})$	143
8.16	Consistency tests for the triangulation method	145
8.17	Average angle between normals from single-spacecraft analysis methods . . .	149
8.18	Angles and differences between $ B_n /B_{max}$ as a function of separation	150
8.19	Distributions of the normals in space	153
8.20	Spatial distribution of normal estimates	155
8.21	Histograms of the discontinuity thickness in s	158
8.22	Histograms of the discontinuity thickness in km	159
8.23	Same as Figure 8.22, but only in the range $d = 0 - 1000$ km	160
8.24	Intervals to average plasma and field data over.	164
8.25	Distributions of T_{\parallel}/T_{\perp}	165
8.26	Distributions of $\{n\}$	167
8.27	Distributions of $\{\rho A\}$	167
8.28	Polar scatter diagram of the change in velocity versus Θ_{VB}	169
8.29	Distribution of the angle Θ_{VB}	169
8.30	Distributions of R_{VB}^{iso}	171
8.31	Distributions of R_{VB}	173
8.32	Firehose factor	174
8.33	Histograms of the normal component of the Alfvén velocity $ \mathbf{V}_A \cdot \mathbf{n} $	176
8.34	$\mathbf{V} \cdot \mathbf{n}$ versus U and probability distributions of $(\mathbf{V} - \mathbf{U}) \cdot \mathbf{n}$	177
8.35	Consistency test for propagating RDs	178
8.36	$ (\mathbf{V} - \mathbf{U}) \cdot \mathbf{n} $ versus the magnitude of the Alfvén speed $ \mathbf{V}_A \cdot \mathbf{n} $	179
9.1	Error cone of the triangulation normal for two examples	187

9.2	Distribution of the angle between the measured normal \mathbf{n} and the 1330 normals $\hat{\mathbf{n}}_i$, and of the 1331 velocities \hat{U}_i	188
9.3	Illustration of the “error fan” when \mathbf{R}^a , \mathbf{R}^c and \mathbf{n} are perpendicular to each other.	189
9.4	Histograms of $\langle S_x \rangle$	190
9.5	Histograms of $\angle(\mathbf{n}, \mathbf{R}^c)$ and $\angle(\mathbf{n}, \mathbf{R}^a)$	190
9.6	Histograms of the time differences between the spacecraft	192
9.7	Dependence of the error on U	193
9.8	Dependence of the error on the planarity P	194
9.9	Illustration of the influence of the orientation on the error	195
9.10	Dependence of the error on the orientation of the tetrahedron relative to \mathbf{n} . . .	196
9.11	Histograms of dn and dU for δt^{min} and δt^{max}	197
9.12	$ B_n /B_{max}$ and θ_{Bn} with error bars for all DDs	200
9.13	Velocity U in with error bars for δt^{max}	201
9.14	Histograms of $ B_n /B_{max}$, $(90^\circ - \theta_{Bn})$ and $ \mathbf{V} \cdot \mathbf{n} - U $ compared to the associated error values for δt^{max} and a smaller value of δt	203

INTRODUCTION

The space between the planets in our solar system is not empty. It is filled with charged particles emanating from the Sun. This streaming plasma is called the solar wind. The existence of this continuous flow of charged particles was inferred only about half a century ago from the observation that the plasma tails of comets always point almost radially away from the Sun [*Biermann*, 1951]. With the beginning of the space age in the late 1950s and early 1960s, *in situ* observations of the interplanetary medium by means of spacecraft measurements confirmed the existence of the solar wind. These early observations revealed that the solar wind is highly variable in nature. The strong fluctuations are particularly distinct for the direction of the magnetic field which is “frozen” in the plasma and thus carried out from the Sun into interplanetary space. A fundamental feature is that variations of the field direction, and to some extent also of the plasma parameters, are not continuous. Typically, rapid changes of the magnetic field are embedded in a comparatively quiet background. These fundamental solar wind features were identified to be *magnetohydrodynamic discontinuities* and are the subject of the present work.

The recognition that discontinuities are ubiquitous features of the solar wind is solely based on observations and was not predicted by theory. Although much progress has been made in the past decades since the first report on solar wind discontinuities [*Ness et al.*, 1966], the most basic question is still waiting for a conclusive answer: why is the solar wind discontinuous? There have, to date, been many attempts to answer this question. We now know that the discontinuities are most likely generated on or near the Sun. Solar wind research and in particular the study of discontinuities (which constitute a major part of the solar wind *micro-scale* fluctuations) therefore also concerns processes that take place on the Sun. A deeper understanding of solar wind discontinuities is perhaps one of the “pieces of the puzzle” necessary to reveal the Sun’s greatest secrets, namely the heating of the corona and the acceleration of the solar wind.

Understanding the true nature of the discontinuities is also imperative for characterising the basic topology of the interplanetary magnetic field (IMF). This, in turn, may be relevant for the analysis of the deflection of cosmic rays on their way through the solar system. These energetic charged particles only “see” the IMF when entering the heliosphere. Since low-energy cosmic ray particles are guided along the field lines, “kinks” in the magnetic field are probably important scatterers of these particles. Hence, an important question is, whether or not interplanetary discontinuities basically resemble “kinks” in the magnetic field. While the so-called *rotational discontinuities* do resemble kinks, the *tangential discontinuities* separate plasma regions that are not magnetically connected.

Another important aspect of solar wind research is that interplanetary space provides an excellent laboratory for plasma physics. Kinetic or magnetohydrodynamical effects that are unachievable in limited terrestrial laboratories can be investigated. For instance, non-linear dynamic processes and their possible importance for the generation of discontinuities can be studied.

Progress in understanding solar wind discontinuities has been highly dependent upon the available technology. The general approach is empirical in nature. Many statistical studies based on *in situ* measurements were performed from the beginning of the space age until the 1980s. At that time it was generally believed that the structures characterised by the sharp rotations of the magnetic field can be divided into rotational and tangential magnetohydrodynamic discontinuities. Whereas earlier observations suggested a predominance of tangential discontinuities, more recent investigations claim a more equal occurrence rate of both types of discontinuities with a tendency towards more rotational discontinuities. After the initial boom in *in situ* studies, the development of computers and software then favoured the investigation of discontinuities by computer simulation. In the 1990s, new observational data was delivered by the Ulysses mission. This was the first spacecraft to leave the ecliptic plane, so that measurements at high heliographic latitudes became possible. This was an important step since the solar wind over the Sun’s poles generally (at least at *solar activity minimum*) maps back to different source regions on the Sun, and has therefore different characteristics than the solar wind near the ecliptic.

Almost all of the observational results have in common that they are based on single-spacecraft data sets. In this work we present the first extensive statistical investigation of interplanetary discontinuities using four-point measurements.

The experimental setup that we use is called Cluster. It is a space mission designed to explore the interaction between the solar wind and the Earth by visiting the key regions of Earth’s magnetosphere. One of the key issues of the Cluster mission is to better understand the polar lights, which are the longest known (and perhaps most beautiful) manifestation of the solar-terrestrial interaction. The main feature of Cluster is that it consists of four identical coordinated spacecraft flying in close formation. This makes it possible for the first time to separate between spatial and temporal variations in three dimensions. Although Cluster is primarily designed to study the magnetosphere, parts of the orbit also traverse the undisturbed solar wind. Since there is no other multi-spacecraft mission like Cluster in the interplanetary medium, we avail ourselves of the opportunity to study solar wind discontinuities on the basis of multi-point observations.

The varying separations between the Cluster spacecraft, ranging from 100 to 5000 km allow the study of discontinuities (which typically have a transition layer width of about 4000 km) on various length scales. This allows us to reexamine earlier hypotheses regarding thickness or large scale surface curvature of interplanetary discontinuities. Most importantly, the simultaneous use of four spacecraft enables us to overcome tremendous drawbacks associated with single-spacecraft analysis tools in estimating the discontinuity orientation in space. We will be able to show that the established single-spacecraft technique, the *Minimum Variance Analysis* (MVA), is much less reliable than previously assumed. Moreover, we can define circumstances in which MVA may yield reliable results and those where this technique should not be applied. Since MVA is a widely used analysis tool in many fields of space plasma physics, this result is important and should be of general interest.

The orientation of a discontinuity, i.e. its normal, also plays a key role in determining the type of these structures. We will demonstrate that the occurrence rate ratio of rotational to tangential discontinuities observed in earlier studies is strongly biased by the misinterpretation of MVA results. This has given a false picture of the solar wind micro-structure, on which proposals for discontinuity generation mechanisms, in connection with the solar wind dynamics and processes on the Sun, are based. Using the relative timings between discontinuity occurrence at the four spacecraft, we apply a method to determine the discontinuity normals that is completely independent from MVA. One striking advantage of this technique, as opposed to MVA, is that its error can be easily assessed. It turns out that the accuracy of the relative timing method strongly depends on the separations between the spacecraft and particularly on the geometrical shape formed by the four satellites. When the separations are large (5000 km) and the four spacecraft constitute the vertices of a *regular tetrahedron*, the multi-point technique is remarkably accurate. As a result, a completely new understanding of the solar wind micro-structure develops, with all its consequences, for instance regarding possible discontinuity generation processes.

This dissertation is organised as follows: In order to understand the medium in which interplanetary discontinuities live and what role they play in that medium, it is necessary to present some basics of the solar wind. We do this in chapter 2. Chapter 3 presents the necessary theoretical background on magnetohydrodynamical discontinuities, summarises the knowledge about interplanetary discontinuities prior to this work and further illuminates the relevance of these structures in a global context. The Cluster mission is briefly introduced in chapter 4. The most striking attribute of this mission is that it consists of four coordinated spacecraft allowing for a wide range of new analysis techniques. The configuration, i.e., the relative positions of the four satellites, is of essential importance for any kind of multi-spacecraft analysis. Therefore, a detailed review of existing parameters to determine the geometrical quality of the Cluster array and a subsequent thorough description of the prevailing configurations at the times when we observe discontinuities is given in chapter 5. In chapter 6 we present the identification criteria that we apply to select the events used in our statistical analysis. The resulting sample is characterised and subdivided according to the prevailing solar wind conditions. One of the most important prerequisites for analysing discontinuities is the precise knowledge of the surface normal. Indeed, the new results presented in this work predominantly deal with this issue. For that reason, a comprehensive review of techniques to determine discontinuity normals used in this work (particularly MVA, and the

multi-spacecraft method) is presented in chapter 7. Thereafter we present our main results (chapter 8) followed by a detailed error analysis of the multi-spacecraft technique (chapter 9). Finally, we discuss and summarise our results in chapter 10.

THE SOLAR WIND

The solar wind is a continuous but highly variable stream of charged particles emanating from the Sun's hot atmosphere (corona). It consists mainly of protons, electrons and alpha particles ($\approx 5\%$). This flow is caused by the enormous temperature of the ionised corona ($\approx 10^6$ K) and the gradient to the interstellar medium which encloses the heliosphere. The pressure gradient is larger than the gravitational force of the Sun. The solar wind plasma is collisionless beyond a few solar radii, and because of its high conductivity the solar magnetic field is "frozen" in the plasma. The radially expanding solar wind transports the field into interplanetary space while its footpoints remain anchored in the solar atmosphere. As a result of the combined motion of outflow and the 27-day solar rotation period, the *interplanetary magnetic field* (IMF) becomes bent into an Archimedian spiral form. After *Parker* [1958], who postulated this characteristic field configuration, it is usually referred to as the *Parker spiral*. At 1 AU¹ this spiral makes an angle of approximately 45° to the Earth-Sun line and the field magnitude is approximately 5 nT on average.

The existence of a hot expanded solar atmosphere has been known for a long time from observations during solar eclipses. It aroused scientific interest at the latest in the 19th century. A spectacular observation took place on 1 September 1859: While sketching sunspot groups, R. C. Carrington and R. Hodgson independently witnessed one of the most intense solar flares. Only 18 hours later one of the strongest magnetic storms was registered [*Carrington*, 1859; *Hodgson*, 1859]. Hence, to reach Earth in that time, the disruption must have travelled at a velocity of 2300 km/s, which is a remarkably fast propagation speed even according to current knowledge. More important, a connection between eruptions on the Sun and disturbances of the Earth's magnetic field was established. However, until 1951 the general belief was that interplanetary space is basically a vacuum which is disrupted by eruptions on the Sun. Eventually the observation that the plasma tails of active comets always point almost

¹1 astronomical unit (AU) is the mean distance between the Earth and the Sun.

radially away from the Sun led Ludwig Biermann to postulate that the solar corpuscular radiation is continuous rather than intermittent [Biermann, 1951]. Shortly before the beginning of the space age Parker [1958] developed a dynamic model and predicted that interplanetary space was filled with a plasma flowing rapidly outward from the Sun. Parker [1958] also coined the phrase “solar wind” to describe the outward flowing solar corona which supplies the pressure required to stand off the local interstellar medium, to exert the necessary force on cometary plasma tails and to transmit solar disturbances to the geomagnetic field. The first *in situ* observation of the solar wind was realised by four Soviet space probes in 1959. Their measurements were consistent with Parker’s theory. The first conclusive measurement were then performed by the Mariner 2 spacecraft in 1962. This satellite obtained a spectrum of the solar wind every 3.7 minutes almost continuously for 113 days. There was no longer any doubt that Parker had been correct. The solar wind exists. The measurements revealed that the solar wind is organised into low- and high-speed streams (velocities ≈ 350 and 700 km/s, respectively). In all streams, the density was found to be anti-correlated with speed [Neugebauer and Snyder, 1966]. These basic features of the solar wind were confirmed by all subsequent spacecraft measurements in interplanetary space.

The fundamental issue in all solar wind research certainly deals with the solar wind’s origin: What accelerates the solar wind? To date no conclusive answer has been found to this question that is also closely related to the fundamental issue in coronal physics in general: How is the corona being heated? We know that the solar wind is accelerated because the corona is hot, and the corona exists because there is something heating it. However, we do not know what heats the corona. Since *in situ* measurements in the vicinity of the solar surface are impossible, *in situ* solar wind measurements shall help finding underlying mechanisms.

Our understanding of the solar wind has improved substantially in the last decades. The organisation of the solar wind in two different types is firmly established by now. As already found by Neugebauer and Snyder [1966] the most apparent difference between the two types is the flow velocity. Furthermore, the proton density is known to be smaller in fast streams ($n_p \approx 3 \text{ cm}^{-3}$ at 1 AU) than in the slow streams ($n_p \approx 10 \text{ cm}^{-3}$ at 1 AU). The fast solar wind is characterised by its relatively low variability. In contrast, the slow solar wind is highly variable. There is now increasing evidence that the acceleration of fast and slow solar wind might be the result of different mechanisms. High-speed solar wind can usually be traced back to *coronal holes*, regions in the corona where the density and the temperature are lower than at other places in the corona. The weak, diverging and open magnetic field lines in coronal holes extend radially outward and do not immediately return back to the Sun. The open field lines allow the plasma to flow outward into interplanetary space. The larger the coronal hole, the faster is the flow speed. The slow solar wind traces back to the active regions in the solar atmosphere where the magnetic field lines close back down to the solar surface. It is still unclear how the slow solar wind escapes from these regions.

The distribution of the coronal holes and the active regions in the Sun’s atmosphere vary with the 11-year *solar activity cycle*. At *solar maximum* (large number of sunspots) the active regions predominate. At *solar minimum* (small number of sunspots) the coronal holes expand and cover both poles of the Sun. Around solar minimum sporadically tongues of the polar coronal holes cross the solar equator. Hence an observer in the ecliptic (for instance near

Earth) observes alternating fast and slow streams with a period of 27 days (the synodic solar rotation period).² We also find such recurring fast streams in the data to be analysed in this work. Their existence enables us to relate the observed characteristics of the discontinuities to the respective solar wind types and thus to the different source regions on the Sun.

The simple pattern of fast and slow wind is occasionally disrupted by the third type of solar wind flow which is sometimes referred to as the *transient solar wind*. This type consists of streams caused by isolated eruptions of material from the Sun's atmosphere known as *coronal mass ejections* (CMEs). They can happen at any time during the solar cycle but are more common during solar maximum.

One of the most striking features of the solar wind is its variability. It is well known that the observable solar wind parameters, such as velocity, density, temperature and magnetic field, are variable on time scales ranging from seconds to more than a decade. For instance, the subject of the present work, the discontinuities, have a time scale of the order of 10 seconds when observed from a spacecraft. An observer that rotates with the Earth around the Sun finds a recurrence of solar wind structures with a period of 27 days. The latter is particularly apparent during solar minimum and during decreasing solar activity although due to the permanent evolution of the solar wind structures in time, a strict repetition is neither expected nor observed. The reorganisation of the Sun's magnetic field during the 11-year activity cycle causes a variation of the solar wind on a time scale of a decade.³

Many of these variations are caused by the permanently changing conditions on the Sun. Therefore, solar wind research is closely connected to the processes that take place on or near the Sun. On the other hand, the solar wind itself is a highly dynamic system providing a diversity of magnetohydrodynamical and kinetic effects.

Because of the variety of scales on which the fluctuations take place it is useful to define certain ranges. Four different scales are introduced: macro-scale (> 100 h), meso-scale ($1 - 100$ h), micro-scale (30 s - 1 h) and kinetic-scale (< 30 s) (see *Burlaga [1969a]* and references therein). An important component of the macro-structure (and partially of the meso-structure) are the corotating structures as for instance stream-stream interaction regions, i.e. regions where a fast stream interacts with a slow stream. Sector boundaries, i.e. regions where the polarity of the magnetic field changes, also belong to this category, as well as the Archimedian spiral structure of the magnetic field is certainly a macro-scale phenomenon. An early suggestion for the solar wind structure on the meso-scale is that it consists of a collection of intertwined and twisted filaments, regions with different plasma and field properties, that are separated by tangential discontinuities [*McCracken and Ness, 1966*]. This model is sometimes referred to as the “spaghetti-model”. Further observations revealed that the existence of an ensemble of such filamentary tubes with distinct boundaries enclosing well-ordered magnetic field lines are difficult to identify. Therefore *Burlaga [1969a]* suggests to think of the interplanetary medium as discontinuous rather than filamentary. In this model the solar wind is structured by an ensemble of discontinuities rather than by pairs of discontinuities as in the “spaghetti-model”.

²More details on the solar cycle are discussed in section 6.5.1.

³Note that from one period to the next the magnetic polarity changes. Thus, a full cycle is completed after 22 years.

A considerable part of the micro- (and kinetic) structure consists of discontinuities, the subject of this dissertation. Other phenomena at this scale include Alfvén waves and non-linear magnetohydrodynamic (MHD) waves. However, we point out that our understanding of the solar wind at this scale is far from being complete. *Belcher and Davis Jr.* [1971] propose that large-amplitude Alfvén waves propagating outward from the Sun with a broad wavelength range dominate the micro-scale structure at least 50% of the time. The largest amplitude Alfvénic fluctuations are found in stream-stream interaction regions. To identify Alfvén waves *Belcher and Davis Jr.* [1971] use the polarisation relation that requires the fluctuations in velocity to be strictly correlated to the field fluctuations (see next chapter). Furthermore, *Belcher and Davis Jr.* [1971] find nearly constant density and field magnitude, as required for Alfvén waves. However, these conditions are necessary, but not sufficient. Using only one satellite *Belcher and Davis Jr.* [1971] are unable to confirm propagation of the identified structures. In a more recent study *Denskat and Burlaga* [1977] utilise the relative timings between the Explorer 33 and 35 spacecraft to show that Alfvénic fluctuations are probably not solely Alfvén waves. Indeed, they present evidence which indicates that tangential discontinuities and possibly other types of static structures are found among Alfvénic fluctuations.

Much of the so far accumulated insight into the solar wind is gained from *in situ* observations (mostly single-spacecraft). More recently, computer simulations have contributed to the understanding of dynamic processes in the interplanetary medium. For many applications the MHD approximation is sufficient (see e.g. *Burlaga* [1971a]). Therefore, many simulations are based on MHD theory. However, kinetic theory should be used for the smallest scale (of seconds or less) because the characteristic length scales then become comparable to the proton gyro-radius. Hence, to resolve the structure of discontinuities, hybrid simulations⁴ are common in more recent studies (see the following chapter).

Although much progress has been made regarding the micro- and the kinetic-structure lately, particularly due to high resolution data and hybrid simulations, the most fundamental question is still waiting for a conclusive answer: Why is the solar wind discontinuous? The rapid changes in the magnetic field direction (and the plasma parameters) in the form of MHD discontinuities have not been predicted, but are purely empirical. In order to tackle this problem a reliable observational basis on the true nature of interplanetary discontinuities is essential. In this work we considerably contribute to that issue by means of multi-point observations with Cluster. We also discuss in how far our ground-breaking new results may be related to the fundamental questions of coronal heating and the acceleration of the solar wind.

⁴In hybrid simulations the protons are treated as particles and the electrons as a fluid.

DISCONTINUITIES

In the previous chapter we have shown that rapid changes in the magnetic field and plasma parameters are a fundamental, and not yet fully understood, feature of the solar wind. Discontinuities also occur when the solar wind hits an obstacle such as for instance the Earth's (or another planet's) magnetic field. The interaction forces the supersonic flow to slow down to subsonic speed, i.e., a bow shock is generated. Another example is the magnetopause which separates the shocked solar wind plasma from the planetary plasma (magnetosphere). The general belief is that the magnetopause is in parts a tangential and in parts a rotational discontinuity. Hence, discontinuities are important structures in space plasma physics in general.

In this chapter we introduce discontinuities in the framework of MHD theory and show how they are classified into shocks, rotational, tangential and contact discontinuities (section 3.1). Then we present the present observational status on solar wind discontinuities (section 3.2). Since these observations are seemingly in good accordance with theoretical considerations regarding possible generation mechanisms (section 3.3), a picture on the origin of interplanetary discontinuities and their connection to the solar atmosphere has developed. Section 3.3 also presents some results of hybrid simulations regarding the stability of discontinuities. These are important for our own conclusions based on multi-point observations which are by no means consistent with the earlier conclusions. Moreover, we detail the motivation of studying solar wind discontinuities (section 3.4).

3.1 Classification of MHD discontinuities

In the first part of this section we present a theoretical treatment of MHD discontinuities. The aim is to introduce the subject of the present work and to show that the properties of the

possible discontinuities are derived from first principles. In the second part we give a brief overview of the criteria used in earlier works on interplanetary discontinuities and present the criteria that we use.

3.1.1 Theory

A discontinuity spatially separates two plasma regions with different properties. An observer crossing the discontinuity experiences rapid changes in the magneto-plasma parameters.

MHD theory permits such discontinuities. However, only certain well-defined changes from one side to the other are allowed (jump conditions). In fact, it turns out that five distinct types of discontinuities are possible. Their derivation in a thermally *isotropic* plasma is presented in several textbooks (e.g. *Landau and Lifschitz* [1967]). The theory for an *anisotropic* plasma has been developed in response to the first solar wind measurements [*Hudson*, 1970; *Neubauer*, 1970]. The treatment for the general case of an anisotropic plasma presented below resembles that of *Hudson* [1970]. The special case of an isotropic plasma will be discussed subsequently. We limit the discussion to the basic physical considerations from which the jump conditions used in this dissertation are derived.

We do not concern ourselves with the detailed structure of the discontinuities. We assume that the bulk properties of the plasma on both sides of the discontinuity can be observed. The two sides are denoted by the subscripts 1 and 2. This means, we presume that the plasma densities ρ_1 and ρ_2 , the bulk velocities \mathbf{V}_1 and \mathbf{V}_2 (relative to the spacecraft), the magnetic fields \mathbf{B}_1 and \mathbf{B}_2 and the plasma pressures p_{\parallel} and p_{\perp} (in the rest frame of the plasma) are known. The subscripts \parallel and \perp denote the components parallel and perpendicular to the magnetic field, respectively.

Let the discontinuity be a plane surface, with normal \mathbf{n} , which moves at speed \mathbf{U} relative to the spacecraft frame. Assuming that the discontinuity surface is an infinite plane, $U = \mathbf{U} \cdot \mathbf{n}$ is the only component of \mathbf{U} having physical significance. Further assumptions are time stationarity in the discontinuity rest frame and that the only spatial variation is in the direction of \mathbf{n} . We point out that the latter assumption, i.e., that spatial variations only occur in one direction, defines a one-dimensional (1-D) structure. We stress this here because the concept of one-dimensionality will play an important role in parts of this work.

The following notation for the difference of a quantity X between the two sides of the discontinuity is used here and in the rest of this work:

$$[X] = X_2 - X_1 \tag{3.1}$$

Moreover, the subscripts t and n denote the component of a vector tangential and normal to the surface, respectively. The absolute value of a vector quantity \mathbf{X} is denoted as X .

Conservation of mass, momentum, energy, the tangential component of the electric field and the normal component of the magnetic field yield the following jump conditions at the

discontinuity (see *Hudson* [1970]):

$$[B_n] = 0 \quad (3.2)$$

$$[\rho(\mathbf{V} - \mathbf{U}) \cdot \mathbf{n}] = 0 \quad (3.3)$$

$$B_n[\mathbf{V}] = G[\mathbf{B}/\rho] \quad (3.4)$$

$$\left[p_{\perp} + \frac{B^2}{2\mu_0} + \frac{G^2}{\rho} - \frac{B_n^2}{\mu_0} \left(1 - \frac{(p_{\parallel} - p_{\perp})\mu_0}{B^2} \right) \right] = 0 \quad (3.5)$$

$$\left[G\mathbf{V}_t - \frac{B_n\mathbf{B}_t}{\mu_0} \left(1 - \frac{(p_{\parallel} - p_{\perp})\mu_0}{B^2} \right) \right] = 0 \quad (3.6)$$

where $G \equiv \rho_1(\mathbf{V}_1 - \mathbf{U}) \cdot \mathbf{n} = \rho_2(\mathbf{V}_2 - \mathbf{U}) \cdot \mathbf{n}$ is the mass flux normal to the surface. Equation 3.2 results from $\nabla \cdot \mathbf{B} = 0$, equation 3.3 describes the conservation of mass, equation 3.4 results from $[\mathbf{E}_t] = 0$ and equations 3.5 and 3.6 result from the conservation of the flux of normal and transversal momentum, respectively. Another equation can be derived from the conservation of energy. These equations define the basic jump conditions. They are necessary conditions for any type of discontinuity.

The distinct types of discontinuities are then obtained by distinguishing between those that are stationary, i.e., that do not propagate with respect to the ambient plasma ($G = 0$) and those that are propagating ($G \neq 0$). Non-propagating discontinuities are the contact discontinuity (CD) and the tangential discontinuity (TD), and propagating discontinuities are the fast shock, the slow shock and the rotational discontinuity (RD).

CDs have a non-zero component of the magnetic field through the surface, but no plasma crosses the surface ($G = 0$, $B_n \neq 0$). From equation 3.4 it follows that $\mathbf{V}_1 = \mathbf{V}_2$, i.e., plasmas on the two sides of a CD are in rest relative to each other. The density and internal energy density can change across the CD. Due to the rapid diffusion along the field lines it is expected that a CD would rapidly broaden into a smooth transition. In fact, CDs have not been observed in the solar wind.

Most of the micro-scale fluctuations observed in the solar wind are characterised by small density and field magnitude changes. Instead, the fluctuations are mostly in the direction of the magnetic field. Changes in the field direction are expected predominantly for RDs and TDs. Therefore, the relatively rare fast and slow shocks are not considered in this work. In the following we present the properties of RDs and TDs.

TDs are non-propagating. In contrast to CDs, however, the magnetic field is tangential to the surface ($G = 0$, $B_n = 0$). This considerably simplifies the jump conditions, and most equations are identically satisfied. Equation 3.5 yields:

$$\left[p_{\perp} + \frac{B^2}{2\mu_0} \right] = 0 \quad (3.7)$$

Hence, the total pressure (kinetic plus magnetic) is the same on both sides of a TD. All other changes from one side to the other are arbitrary. Since $B_n = 0$, the two sides are not magnetically connected: a TD separates two completely distinct plasmas which for instance may be of different chemical composition. Another possibility to distinguish a TD from any other pressure-balance structure is to show that it does not propagate with respect to the

ambient plasma:

$$U = \mathbf{U} \cdot \mathbf{n} = \mathbf{V} \cdot \mathbf{n} \quad (3.8)$$

i.e., the discontinuity velocity relative to the spacecraft must be the same as the normal component of the solar wind velocity measured in the spacecraft frame. To test whether or not propagation takes place, U must be known from observation, which is only possible when at least four spacecraft are available. Note that for TDs, the conditions are the same for isotropic and anisotropic plasmas.

RDs are propagating structures. Moreover, there exists a non-zero magnetic field normal component ($G \neq 0$, $B_n \neq 0$). The bulk velocity equals the Alfvén velocity \mathbf{V}_A on both sides of the RD in the discontinuity rest frame:

$$\mathbf{V}_{Ai} = \mathbf{V}_i - \mathbf{U} = \pm \frac{\mathbf{B}_i}{\sqrt{\mu_0 \rho_i}} \sqrt{A_i} \quad i = 1, 2 \quad (3.9)$$

where

$$A = 1 - \frac{(p_{\parallel} - p_{\perp})\mu_0}{B^2} \quad (3.10)$$

is the *firehose factor*, a measure for the anisotropy of the plasma. Note that $A = 1$ in the isotropic case.

The propagation with Alfvén velocity implies that \mathbf{B}_{1t} and \mathbf{B}_{2t} need not be parallel (this can be shown by evaluating equations 3.4 and 3.6 [Hudson, 1970]). Since B_n is continuous, this means that the field vector \mathbf{B} rotates in the RD plane, see also Figure 3.1.

The Alfvén velocities on the two sides of an RD are related by equation 3.3:

$$G = \rho_1 \mathbf{V}_{A1} \cdot \mathbf{n} = \rho_2 \mathbf{V}_{A2} \cdot \mathbf{n} \quad (3.11)$$

Together with equation 3.2 it follows:

$$[\rho A] = 0 \quad (3.12)$$

Substituting equation 3.11 into equation 3.5 it follows that (as TDs) also RDs are pressure-balance structures:

$$\left[p_{\perp} + \frac{B^2}{2\mu_0} \right] = 0 \quad (3.13)$$

Substituting equation 3.11 into equation 3.4 yields the polarisation relation:

$$[\mathbf{V}] = \pm \sqrt{\frac{\rho A}{\mu_0}} \left[\frac{\mathbf{B}}{\rho} \right] \quad (3.14)$$

This directly implies another necessary condition for RDs:

$$\rho_1 A_1 = \rho_2 A_2 = \frac{\mu_0 (\mathbf{V}_1 - \mathbf{V}_2)^2}{(\mathbf{B}_1/\rho_1 - \mathbf{B}_2/\rho_2)^2} > 0 \quad (3.15)$$

Since ρ_1 and ρ_2 are positive, it follows:

$$A_1 > 0 \text{ and } A_2 > 0 \quad (3.16)$$

Note that equation 3.16 is equivalent to the condition that the plasma does not suffer from the firehose instability.¹

Apparently, several necessary conditions need to be fulfilled to identify a discontinuity as an RD. These conditions are somewhat different in the isotropic case ($A = 1$): Then equation 3.12 implies that the density is continuous. Further it can be shown that for $A = 1$ also the kinetic pressure and the field magnitude are conserved. Also the polarisation relation simplifies. Hence, in the case of an isotropic plasma the conditions for an RD are:

$$[B] = 0, [\rho] = 0, [p] = 0, [\mathbf{V}] = \pm [\mathbf{B}] / \sqrt{\mu_0 \rho} \quad (3.17)$$

Figure 3.1 presents a schematic of a TD (left) and an RD (right), and below the most important characteristics of these two MHD discontinuities are summarised.

Tangential discontinuity (TD):

- \mathbf{V} is tangential to the TD surface in the discontinuity rest frame ($U = \mathbf{V} \cdot \mathbf{n} \Rightarrow$ TDs are convected structures
- \mathbf{B} is tangential to the TD surface ($B_n = 0 \Rightarrow$ two sides are not magnetically connected \Rightarrow different chemical compositions are possible
- total pressure is conserved
- all other parameters may change arbitrarily, particularly B and ρ
- conditions are the same for an isotropic plasma

Rotational discontinuity (RD):

- propagation with Alfvén velocity \mathbf{V}_A in the plasma frame
- $B_n \neq 0 \Rightarrow$ the two sides are magnetically connected
- total pressure is conserved
- $[\mathbf{V}]$ and $[\mathbf{B}/\rho]$ are related by a definite polarisation relation
- $[pA] = 0$, and $A > 0$ on both sides
- conditions are different for an isotropic plasma, e.g. $[B] = 0$ and $[\rho] = 0$

The derived theoretical properties of RDs and TDs offer a variety of possibilities to distinguish between these two types of discontinuities in the solar wind. Under the assumption that the solar wind is isotropic, the conservation of B and ρ is often used to identify RDs. Strictly speaking this is not correct, since the solar wind plasma is most likely not strictly isotropic. Also note that although TDs may have large jumps in field magnitude and density, they do

¹The condition for the firehose instability is usually written as $p_{\parallel} > p_{\perp} + B^2/\mu_0$ (see e.g. *Treumann and Baumjohann* [1997]).

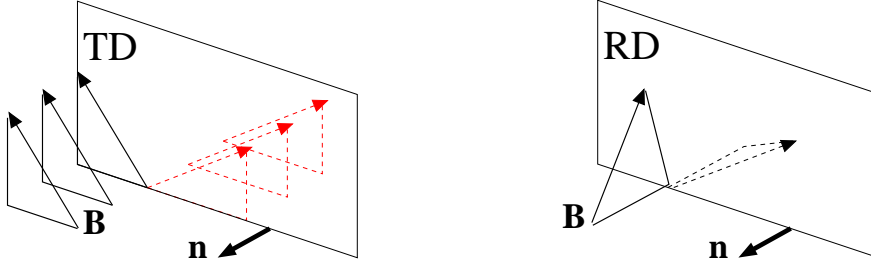


Figure 3.1: Illustration of a TD (left) and an RD (right). The discontinuities are approximated by planar sheets with normal \mathbf{n} . The magnetic field vectors on both sides are shown. The different colours on the two sides of the TD indicate that the chemical compositions may be different.

not have to. Another possibility is to use the polarisation relation. However, since TDs may also satisfy this condition although not required by theory, it is not a sufficient condition for RDs. Because of this it is easy to mistake a TD for an RD. The best way to definitely identify an RD is to prove a large magnetic field normal component, i.e., B_n must be larger than its error. Then the discontinuity is inconsistent with being a TD. Indeed, this issue is an important, perhaps the most important, subject of this work, since using four instead of only one spacecraft considerably increases the accuracy in the determination of B_n .

To conclude this section we present a discontinuity as it appears in solar wind data measured by one of the four Cluster spacecraft. Figure 3.2 shows one of the discontinuities we use in our statistical analysis. Plotted are from top to bottom: the magnetic field (three components in a coordinate system to be specified later and magnitude), the proton velocity in the same representation, the proton temperature and the proton density. The discontinuity is clearly visible in the middle of the shown four minute interval where most quantities rapidly change. Before and after the discontinuity the shown parameters are rather constant. Note that this is a relatively ideal situation. In general, the background fluctuations which are also visible in Figure 3.2 are somewhat stronger and complicate the analysis. The discontinuity is characterised by a strong rotation of the magnetic field vector. As is rather typical for solar wind discontinuities, the magnitude is almost the same on both sides. Only a slight decrease is observed. Note that there is a strong “dip” in the magnitude during the transition. Such so-called *magnetic holes* (or *magnetic decreases*) are often observed in connection with discontinuities [Turner *et al.*, 1977]. Also the velocity vector rotates during the transition and the velocity magnitude increases by about 10 km/s. Due to its variability it is difficult to see whether the temperature differs on the two sides. It appears to be slightly lower after the discontinuity. The density increases. As an additional information, not visible in Figure 3.2, we may add that the magnetic field normal component B_n is very small for this particular event. In fact, it is consistent with being zero within uncertainty.

What can we conclude from these information? A remarkable feature is that the vectorial changes in velocity $[\mathbf{V}]$ and in magnetic field $[\mathbf{B}]$ are apparently correlated. For both vector quantities the z -component strongly increases, whereas the changes in the x - and the y -component are more moderate (V_x and B_x decrease and V_y and B_y increase). This kind of behaviour corresponds to the requirement for RDs to satisfy the polarisation relation 3.14.

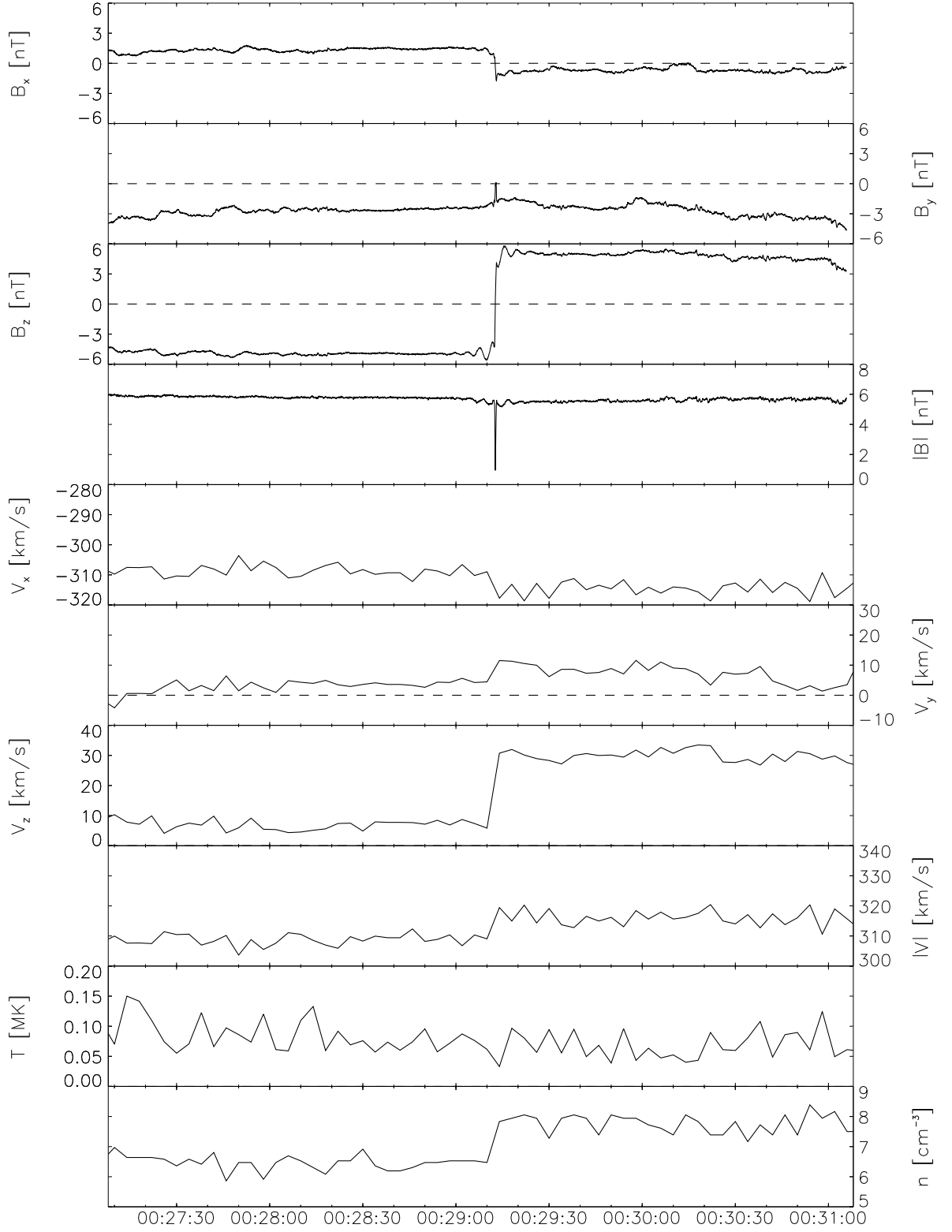


Figure 3.2: Example of an interplanetary discontinuity. High-resolution magnetic field data (22 vectors/s) and 4 s proton data from one of the Cluster spacecraft are shown.

Can we conclude that the shown discontinuity is an RD? Since B_n is consistent with being zero, it could as well be a TD. Also the jumps in density, field magnitude and temperature (although rather moderate) would rather suggest a TD. Hence, we could as well conclude that the discontinuity shown in Figure 3.2 is a TD that coincidentally fulfils the polarisation relation. Provided that good-quality information on the thermal anisotropy are available, one could test whether the density jump is consistent with equation 3.12.

We do not go any further. Our intention here is only to give a preview of the kind of problems we are willing to tackle in this work.

3.1.2 Criteria used in observations

Different authors have suggested several criteria to categorise solar wind discontinuities into RDs and TDs. Some of them use the requirement that the polarisation relation 3.14 must be fulfilled by RDs [Burlaga, 1971b; Martin *et al.*, 1973; Belcher and Solodyna, 1975; Solodyna *et al.*, 1977]. However, this technique can only yield an upper bound for the number of RDs since TDs may coincidentally also fulfil equation 3.14. Indeed, in many cases TDs also appear to have an Alfvénic character although MHD theory does not postulate this for TDs [Denskat and Burlaga, 1977; Neugebauer *et al.*, 1984]. Hence, a definite assignment to RDs only by means of the polarisation relation is not possible.

Burlaga [1968] uses simultaneously plasma and magnetic field data to identify TDs on the basis of a constancy of the total pressure. If additionally the magnetic field intensity and the density vary across the transition, then these pressure-balance structures are assumed to be not RDs (equations 3.17). Turner and Siscoe [1971] use a similar technique. TD candidates are found by scanning for substantial changes in density between the two sides of the discontinuity. However, any TD with $[\rho] = [B] = 0$ would be identified as RD within this criterion.

These criteria have in common that plasma data are needed. An inherent problem thereby is the partial unavailability and the lower time resolution and quality of plasma data compared to magnetic field data. Moreover, the applied necessary conditions for RDs do not exclude TDs. To unambiguously identify an RD, a non-zero magnetic field normal component B_n needs to be verified. In fact, this is the most frequently used criterion. Smith [1973a] is the first author to present a method that is based on magnetic field data alone. Besides the field component $|B_n|$ normal to the discontinuity surface also the change of field magnitude $||B|$ across the transition is considered. Both parameters are normalised by the maximum magnitude B_{max} upstream and downstream of the discontinuity, such that they range from zero to unity. Note that the second criterion relies on the assumption of an isotropic solar wind. This is often justified by the estimate $A = 0.9 \pm 0.1$ presented in Burlaga [1971b]. Provided that the firehose factor is indeed close to unity, the field magnitude should be conserved across an RD, but can be arbitrary for TDs (see previous section). A serious challenge to this method is the ability to give a satisfactory quantitative estimate for the error in $|B_n|/B_{max}$ which is closely related to the determination of the discontinuity normal. A value of 0.4 is arbitrarily chosen as a likely value when estimates based on the single-spacecraft *Minimum*

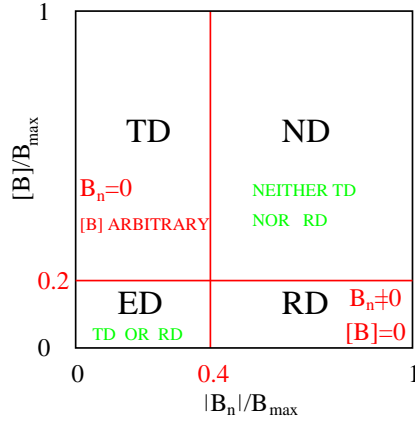


Figure 3.3: Classification scheme used in this work.

Variance Analysis (MVA) technique are used [Smith, 1973a]. Consequently, Smith classifies discontinuities as rotational when $|B_n|/B_{max} > 0.4$ and $|[B]|/B_{max} < 0.22$. The threshold 0.22 is also reasoned by error estimate arguments and the assumption of an isotropic solar wind. These classification principles have been adopted by several authors [Mariani *et al.*, 1973; Lepping and Behannon, 1980; 1986; Neugebauer *et al.*, 1984; Tsurutani *et al.*, 1996a; Horbury *et al.*, 2001b; Söding, 1999].

As other authors [Horbury *et al.*, 2001b; Söding, 1999], we follow Neugebauer *et al.* [1984] who define the following classification criteria:

Rotational	(RD):	$ B_n /B_{max} \geq 0.4;$	$ [B] /B_{max} < 0.2$
Tangential	(TD):	$ B_n /B_{max} < 0.4;$	$ [B] /B_{max} \geq 0.2$
Either	(ED):	$ B_n /B_{max} < 0.4;$	$ [B] /B_{max} < 0.2$
Neither	(ND):	$ B_n /B_{max} \geq 0.4;$	$ [B] /B_{max} \geq 0.2$

A discontinuity with a small normal field component and small change in magnitude could be either rotational or tangential. This is why Neugebauer calls them *Either Discontinuities* (EDs). Without additional information (e.g. plasma data) it is not possible to determine whether an ED is an RD or a TD. NDs are inconsistent with MHD RDs or TDs. Figure 3.3 illustrates this classification scheme.

The success of this method inherently depends on the ability to determine the true normal of the discontinuity surface. In this regard Cluster provides a great opportunity to overcome tremendous drawbacks associated with single-spacecraft tools. The important issue of discontinuity normal determination is comprehensively discussed in chapter 7.

Besides the above classification scheme we also utilise the polarisation relation, equation 3.12 and the fact that TDs are convected structures whereas RDs propagate with Alfvén velocity to identify possible RDs among the EDs. The according results are presented in chapter 8.

3.2 Observations of solar wind discontinuities

In this section we provide a brief overview of the observational results on interplanetary discontinuities. We do not aim for completeness. Mostly results relevant to this dissertation are reviewed. In particular we emphasise the various classification results different authors have presented.

Since the surprising observation that most variations in the *interplanetary magnetic field* (IMF) are discontinuous [Ness *et al.*, 1966], discontinuities are known to be a fundamental feature of the solar wind. Realizing that most of these sharp changes are predominantly in the field direction, Burlaga [1969a] introduces the term *directional discontinuity* (DD): The change in field direction $\omega = \angle(\mathbf{B}_1, \mathbf{B}_2)$ must be larger than 30° in less than 30 s. Besides the relatively rare interplanetary shocks, these events are considered to be either RDs or TDs.

With an average occurrence rate of one to two per hour [Burlaga, 1969a; Tsurutani and Smith, 1979] (depending on details such as the used identification criteria, the prevailing solar wind conditions and the radial distance from the Sun) DDs are abundant structures in the solar wind. The distribution of the time intervals between successive DDs in a given ω range follows an exponential decrease [Burlaga, 1969a]. This means that DDs tend to occur in clusters rather than being equally spaced in time.

An important question is whether DDs are produced near the Sun and then convected to larger heliocentric distances, or whether they are produced at all distances, for instance in colliding solar wind stream regions. In order to answer this question, the occurrence rate of DDs as a function of radial distance from the Sun has been determined [Burlaga, 1971b; Mariani *et al.*, 1973; Tsurutani and Smith, 1979; Barnstorf, 1980; Neubauer and Barnstorf, 1981; Lepping and Behannon, 1986; Tsurutani *et al.*, 1996a; Söding, 1999]. All of these studies reveal a decrease of DD occurrence rate with increasing heliospheric distance. We do not concern ourselves with details as precise decrease rates. We only note that heliospheric distances ranging from approximately 0.3 AU to approximately 10 AU are considered. Assuming that the observed correlation is real² then it may imply that DDs are generated closer to the Sun than 0.3 AU and disintegrate at larger distances. However, it can as well imply that the ratio of generation rate to disappearance rate becomes smaller as heliocentric distance increases, or that the discontinuities change size in some manner such that the used identification criteria bias the result [Lepping and Behannon, 1986].

Another important observation in this regard is that most Alfvénic fluctuations in the solar wind propagate outward, away from the Sun [Belcher and Davis Jr., 1971]. The interpretation of this asymmetry of the propagation directions is that most of the disturbances are created close to the Sun, below the critical point where the solar wind becomes super-Alfvénic, since then inward propagating fluctuations could not be convected outward with the solar wind. Several observations have confirmed that also nearly all RDs propagate outward from the Sun (see e.g. Neugebauer and Buti [1990]), which suggests that it is rare for RDs to be created beyond the critical radius. Therefore, it is the general belief that most of the DDs observed in

²Note that the occurrence rate also depends on the prevailing solar wind conditions. For instance, more DDs are observed in fast streams.

the solar wind have their origin in the solar corona, below the critical distance at which the wind becomes super-Alfvénic [Neugebauer and Alexander, 1991].

The relative abundance of RDs and TDs in the solar wind has been controversially discussed. The following summary provides an overview. *Siscoe et al.* [1968] find that for the majority of the discontinuities they study the rotation of the magnetic field vector takes place in a plane. This is equivalent to the condition $B_n = 0$. Since $\mathbf{B}_1 \neq \mathbf{B}_2$, *Siscoe et al.* [1968] conclude that these structures (80% of the total number of their events) are TDs. However, the method they use is not appropriate to study RDs (this will be explained in chapter 7), and they cannot rule out a substantial contribution of RDs. Utilising the polarisation relation for RDs for an anisotropic plasma, *Burlaga* [1971b] comes to a similar conclusion as *Siscoe et al.* [1968]: less than 25% of the DDs are RDs, and the majority of DDs are thus TDs. On the other hand, *Belcher and Solodyna* [1975] find that DDs are predominantly RDs using a similar technique. Using the absolute value of the magnetic field normal component *Burlaga et al.* [1977] find some indication for a predominance of TDs. *Neubauer and Barnstorf* [1981] come essentially to the same conclusion. Studies that use both, the normal magnetic field component and the change in field magnitude across the transition usually find a predominance of RDs: *Smith* [1973a]; *Lepping and Behannon* [1980]; *Mariani et al.* [1983] find around twice as many RDs than TDs. *Lepping and Behannon* [1986] come to the same conclusion. However, in a second estimate *Lepping and Behannon* [1986] consider the total number of RDs to be the sum of those DDs with substantial normal components plus an estimated number of those DDs with small normal components. The latter estimate is based on the assumption that there is a uniform distribution of RDs per degree of discontinuity cone angle $\beta = \cos^{-1}(|B_n|/B)$. In that case the number of RDs and TDs is almost balanced. *Neugebauer et al.* [1984] estimate that the number of RDs is by a factor 5-9 higher than the number of TDs. In addition, *Neugebauer et al.* [1984] suggest that most of the ambiguous cases (EDs) are also predominantly RDs. Hence, a clear dominance of RDs is concluded. *Horbury et al.* [2001b] finds a similar ratio when estimating the surface normals by MVA. Also *Tsurutani et al.* [1996a] find a predominance of RDs.

All of these studies, particularly those that use the magnetic field normal component to separate RDs from TDs, have in common that a certain amount of “clear RDs” can be identified by means of a large value of B_n . The exact percentages of RDs and TDs vary. In general, however, one can say that particularly the more recent investigations predominantly claim a dominance of RDs. Certainly, much of the discussed discrepancies are due to the different classification criteria used. Another reason, however, are the prevailing solar wind conditions. For instance, the DDs considered in *Burlaga* [1971b] were all in slow solar wind, and *Belcher and Solodyna* [1975] consider high-speed regions, which may indicate that RDs are more likely to be found in the fast solar wind. Indeed, several investigations confirm that the frequency of occurrence of RDs and the ratio of the number of RDs to the number of TDs both increase with increasing solar wind speed [*Martin et al.*, 1973; *Turner*, 1973; *Burlaga et al.*, 1977; *Solodyna et al.*, 1977; *Neubauer and Barnstorf*, 1981; *Barnstorf*, 1980]. A detailed study on the dependence of occurrence of RDs and TDs on solar wind type is presented in *Neugebauer and Alexander* [1991]. There it is found that not all types of fast solar wind promote a high RD abundance. The occurrence rate of RDs does not increase with solar wind speed for flows associated with coronal mass ejections. The highest frequency of occurrence

of RDs is found in fast streams originating from coronal holes on the Sun. Moreover, the occurrence rate of RDs in all flows from magnetically open field regions is approximately linearly related to the solar wind speed. In contrast, a high rate of TDs is found in solar wind streams originating in the active regions of the Sun where the field lines are closed. The observed dependence on solar wind type is of considerable importance, since it is consistent with ideas on how RDs and TDs are generated, as we shall discuss in the following section.

We point out that the results presented above are solely based on DD normals estimated from single-spacecraft techniques. There have also been a few studies utilising the relative timings between three spacecraft to determine the normals [Burlaga and Ness, 1969; Horbury *et al.*, 2001b]. Naturally, the demand of having three adequate spacecraft (from different missions) simultaneously operating in the solar wind leads to only a very few events that can be analysed this way. Also, the relative positions of the spacecraft may not be optimal. Nevertheless, results of considerable interest could be found. The six events investigated in Burlaga [1969a] are all consistent with TDs. Horbury *et al.* [2001b] finds that in contrast to their single-spacecraft analysis (see above), the relative timing method yields many more DDs with small values of B_n , indicating an abundance of TDs. Certainly, one may argue that the problems associated with their specific investigation possibly do not allow for a definitive conclusion, but we are convinced now that these findings are worthwhile to be pursued. Indeed, the results presented in Horbury *et al.* [2001b] motivate major parts of the present work.

Note that we could only give a brief overview of earlier results in this section. Some more results shall be presented in later chapters when we need them. Of interest are for instance the large scale surface curvature of the DD surfaces, the distribution of the spreading angle ω , the discontinuity thickness and the orientation of the DDs in space.

3.3 Origin and stability of solar wind discontinuities

The observational results presented in the previous section suggest that possible generation processes of RDs and TDs depend on the solar wind type. The ratio RD:TD is larger in solar wind that maps back to coronal holes on the Sun (open field lines), whereas relatively more TDs are observed in solar wind streams that map back to active regions (closed field lines). As a matter of fact, these observations are consistent with a theory presented in Parker [1987; 1990; 1991a;b]. Parker suggests that the heating of the active regions of the solar corona is due to explosive dissipation of magnetic energy at many tangential discontinuities. The creation of these TDs is explained as follows (see Parker [1991a] for a review): The convection-driven continuing displacement of the photospheric foot-points of the bipolar magnetic field winds and interweaves the field lines into a complicated topology (see Figure 3.4). The basic *magnetostatic theorem* states that nearly all strongly deformed magnetostatic field topologies (embedded in an infinitely conduction fluid) spontaneously develop internal surfaces of tangential discontinuities as the field relaxes to equilibrium. The surfaces of the TDs lie along the topological separatrices, and are a consequence of the balance between magnetic pressure and tension in any field in which the field lines are significantly wound

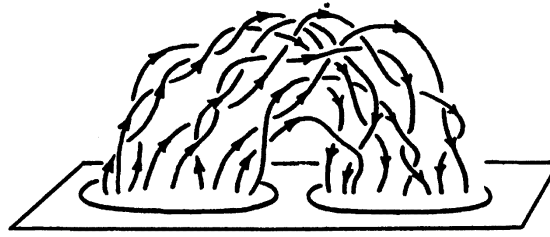


Figure 3.4: A schematic drawing of the interwoven field of a bipolar magnetic region, arising from the random shuffling of the foot-points of the field by the photospheric convection. Taken from Parker [1991a].

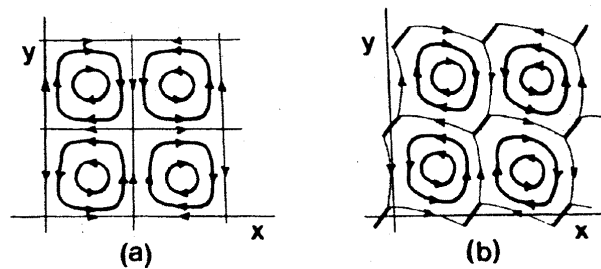


Figure 3.5: Illustration of the magnetostatic theorem. Cross section through a continuous equilibrium magnetic field (a), and deformation by application of external forces (b). Taken from Parker [1991b].

and interwoven [Parker, 1991b].

The essential point in the magnetostatic theorem is the fragile nature of continuous field configurations. The slightest deviation from the ideal form, that is necessary for a continuous field, introduces TDs [Parker, 1991b]. Consider, for instance, a continuous equilibrium field, e.g. a close-packed rectangular array of alternately twisted flux tubes extending uniformly in the z -direction, as is sketched in Figure 3.5 (a). Almost all deformations of this continuous field cause flux bundles with the same helicity to come into contact (Figure 3.5 (b)). The separatrices are then surfaces of TDs [Parker, 1991b].

The situation is different on coronal holes, because there only one end of the field is attached to the Sun. Therefore, any transverse field produced by the motion of the foot-points simply propagates to infinity along the field, and the field remains continuous. Hence, TDs do not develop in the mean field as a consequence of the random motion of the foot-points of the field in the photospheric convection. Part of the energy and momentum of the waves may contribute to the acceleration of the solar wind above coronal holes [Parker, 1991b].

Indeed, a fundamental feature of the solar wind that maps back to coronal holes is the ubiquitous presence of large amplitude Alfvén waves [Tsurutani *et al.*, 1994; Goldstein *et al.*, 1995; Smith *et al.*, 1995]. With $|\Delta \mathbf{B}|/|\mathbf{B}|$ being typically ≈ 1 to 2, these waves are highly non-linear [Tsurutani *et al.*, 1994; 1996a]. Tsurutani *et al.* [1994; 1996a] find that the occurrence of RDs is strongly related to the occurrence of such wave trains. They even suggest that RDs are an integral part of the Alfvén waves in the sense that RDs are the steepened edge of a phase-steepened non-linear Alfvén waves.

A few years before *Tsurutani et al.* [1994] suggested that RDs observed in the solar wind are dynamically generated by the phase-steepening of non-linear Alfvén waves, *Neugebauer and Buti* [1990] addressed the same question. Whereas Tsurutani’s conclusions are essentially based on the characteristic appearance of Alfvén waves in solar wind magnetic field data, *Neugebauer and Buti* [1990] search for some evidence that steepening indeed takes place. They refer to theoretical studies of non-linear Alfvén waves [*Sakai and Sonnerup*, 1983; *Buti*, 1988; *Kennel et al.*, 1988]. The theory presented by these authors predicts that the evolution of non-linear waves into solitons is possible only for left- (right-) hand-polarised waves for $\beta' = c_s^2/(V_A^2 \cos^2 \theta_{Bn}) < 1$ ($\beta' > 1$), where c_s is the sound speed, V_A the Alfvén speed and θ_{Bn} the angle between the propagation vector and the magnetic field. The solitons can degenerate into RDs in the limiting case that their speed approaches the sound speed [*Neugebauer and Buti*, 1990].

Neugebauer and Buti [1990] search for the predicted correlations between β' , the sense of polarisation of the discontinuity and changes of magnetic field strength and plasma density across the discontinuity (the fluctuations in the magnitude of the magnetic field and the density fluctuations are in (out of) phase for $\beta' < 1$ ($\beta' > 1$) [*Neugebauer and Buti*, 1990]), but they cannot find significant evidence for the evolution of RDs from steepened Alfvén waves.

Neugebauer and Buti [1990] suggest that this negative result may be due to the fact that the observations were made far from the regions in which the discontinuities were formed. Hence, the properties of the RDs created close to the Sun may be changed to such an extent that any original correlations are no longer detectable at 1 AU.

Despite the lack of evidence, the concept that RDs evolve from waves that are generated in open field line regions as described above is widely accepted, because the observations presented in the previous section are consistent with the discussed ideas of RD and TD generation. It is a major issue of the present work to revise the observational results, and thus indirectly the suggested generation mechanisms, particularly the idea of phase steepening.

Also note that *Parker* [1991b] does not explain the existence of TDs in fast solar wind from coronal holes. *Ho et al.* [1995] and *Tsurutani et al.* [1996b] study solar wind emanating from the large polar coronal holes. They find that the TDs they observe may be divided into two types. One of them is associated with mirror-mode structures, and usually occurs in pairs, at the edges of these structures. These mirror-mode associated TDs have small directional changes of the field vector ($< 40^\circ$) across them and comprise $\approx 19\%$ of all TDs in the high heliographic latitude regions [*Ho et al.*, 1995].

Although the coronal hole flow is known to be comparatively constant, *Neugebauer et al.* [1995] and *McComas et al.* [1995] find many small stream-stream interactions in solar wind coming from high latitude coronal holes. *Neugebauer et al.* [1995] calls these structures “microstreams”. *Ho et al.* [1995] and *Tsurutani et al.* [1996b] conclude that the interaction of these “microstreams” may be responsible for the other type of TD that they find ($\approx 50\%$ of all TDs they observe). These TDs are usually associated with velocity gradients and clearly separate two different plasma regions (in contrast to the mirror-mode associated TDs). Furthermore, this second type of TDs has large directional field changes across the discontinuity ($> 60^\circ$).

Generally TDs can also be generated when a shock interacts with another discontinuity. However, shocks are rare (at least beyond 0.3 AU). Therefore, this possible mechanism probably only contributes a small part to the total population of TDs in the solar wind.

Stability of RDs

In the following we briefly summarise results on the stability of RDs. We do not discuss any details. We only aim to answer whether RDs are long-lived structure, or whether they are short-lived, i.e., we want to know whether it is likely to observe RDs at 1 AU when they are generated near the Sun.

In the previous discussion we were mostly interested in the field and plasma properties on the two sides of a discontinuity. Looking at DDs in high resolution magnetic field data reveals an inner structure, i.e., the field generally rotates smoothly within the transition layer over a time scale of seconds. Details of this inner structure are of interest in particular in the kinetic theory. It is for instance *a priori* unclear whether the rotation of the tangential magnetic field can be larger than 180° . A right-handed rotation of, say, 200° may have different properties (for instance regarding stability) than a left-handed rotation of 160° although the “end-product” on the two sides of the discontinuity may be the same.

To investigate the structure and stability of RDs in the kinetic limit, a number of hybrid simulation (kinetic ions, massless fluid electrons) studies have been performed in the past [Swift and Lee, 1983; Lee *et al.*, 1989; Richter and Scholer, 1989; Goodrich and Cargill, 1991; Omid, 1992; Krauss-Varban, 1993; Krauss-Varban *et al.*, 1995; Karimabadi *et al.*, 1995]. Apart from Karimabadi *et al.* [1995] who conduct both 1-D and 2-D simulations, generally 1-D codes are used, i.e., all variables are functions of time and one spatial variable which is along the normal of the discontinuity. Note that the results may strongly depend on the chosen parameters such as the plasma beta (the ratio of thermal to magnetic pressure), or on the method used to form the RD.

Many of the simulations suggest that RDs with rotations of the tangential field larger than $|\alpha| = 180^\circ$ tend to be unstable (e.g. Swift and Lee [1983]; Omid [1992]; Karimabadi *et al.* [1995]). This finding is in agreement with observations of solar wind RDs [Neugebauer and Buti, 1990]. Swift and Lee [1983] present the first simulation results using a hybrid code. They find that when the rotation angle of the tangential magnetic field is 180° or less, *symmetric* RDs, i.e. RDs with $[B] = 0$, are stable for both senses of rotation. Lee *et al.* [1989] investigate the stability of RDs with $\alpha = 180^\circ$. In agreement with Swift and Lee [1983], Lee *et al.* [1989] also find that RDs are relatively stable. However, Swift and Lee [1983] and Lee *et al.* [1989] investigate the temporal evolution only of RDs with relatively large angles between the upstream magnetic field and the RD normal ($\theta_{Bn} > 45^\circ$).

In the study by Richter and Scholer [1989], the stability of symmetric RDs in which the magnetic field rotates by 180° are investigated both, in the quasi-parallel ($\theta_{Bn} < 45^\circ$) and the quasi-perpendicular ($\theta_{Bn} > 45^\circ$) regimes. For $\theta_{Bn} = 60^\circ$ and left-hand sense of rotation, they obtain nearly the same results as Swift and Lee [1983] and Lee *et al.* [1989]. At the end of the simulation runs there is almost no thickening of the transition region. Also the

right-hand rotation appears stable for $\theta_{Bn} = 60^\circ$. However, RDs with $\theta_{Bn} < 45^\circ$ are found to be unstable and to disintegrate into waves for both senses of rotation. This result is in apparent contradiction to solar wind observations carried out so far, where a large number of RDs with small angles θ_{Bn} could be found. Note, however, that *Neugebauer* [1989] shows that the complexity of the structure of RDs indeed increases as θ_{Bn} decreases. Since the RDs observed at 1 AU are presumed to be created in the solar corona and are (according to the observations so far) stable over the two to six days required for them to travel from the Sun to 1 AU, the minimum lifetime of RDs is much longer than Richter and Scholer's simulation times of ≈ 40 s [*Neugebauer*, 1989]. Therefore, *Neugebauer* [1989] suggests that the observed complexity of the structures at small θ_{Bn} should not be interpreted as evidence for the instability of quasi-parallel RDs, as *Richter and Scholer* [1989] do.

The disagreement between simulation and observation appeared to be resolved by the results presented in *Goodrich and Cargill* [1991]. Using a larger simulation box and longer runs, they obtain stable solutions even at $\theta_{Bn} = 30^\circ$. *Goodrich and Cargill* [1991] show that the break-up of quasi-parallel RDs observed by *Richter and Scholer* [1989] is transitory in nature, and that a more stable structure evolves later in the simulations. Certainly, the observational results presented in this dissertation will again provide a new slant on the whole subject.

More recent hybrid simulations also indicate that RDs are stable structures, at least in the quasi-perpendicular case [*Omidi*, 1992; *Krauss-Varban*, 1993; *Krauss-Varban et al.*, 1995; *Karimabadi et al.*, 1995].

As a final note we may add that there is a general problem with applying a 1-D hybrid code to RDs, which could make the results of such studies of limited interest. The 1-D simulation allows only wave vectors in the RD normal direction. If in reality decay of the RD were to occur by generation of waves with k vectors parallel to \mathbf{B} , this would be less and less possible in the simulation for increasing angles θ_{Bn} [*Richter and Scholer*, 1989].

3.4 The importance of solar wind discontinuities

Many aspects that motivate the investigation of solar wind discontinuities are already included in the previous sections and chapters. DDs are a fundamental feature of the interplanetary medium and contribute a major part to the micro-scale fluctuations of the solar wind. However, they are not fully understood yet. In particular there are ambiguities regarding their true nature and origin. In the following we summarise the relevance of research on interplanetary discontinuities, and demonstrate the importance of identifying the true MHD type of these discontinuities.

First of all the knowledge of the ratio RD:TD is of considerable interest to characterise the topology of the IMF. By definition, the magnetic signature of a TD reveals the crossing of two regions not magnetically connected. In other words, when a TD is observed, the local medium is split into two distinct plasma regions, in contrast to an RD. A high occurrence of TDs implies that the solar wind is formed of many such regions, with no plasma flow between them. This might have consequences for the diffusion coefficients of energetic particles. If

the majority of DDs are TDs, then low-energy cosmic rays with gyro-radii less than the average discontinuity separation would tend not to be scattered by the DDs. Thus, the mean free path would in fact be much greater than the distance between the DDs [Sari and Ness, 1969]. In contrast, if DDs are predominantly RDs, then cosmic rays travelling along field lines are likely to encounter and be scattered by them.

Secondly, interplanetary space provides an excellent laboratory to observe plasma effects which are unachievable in the limited terrestrial laboratories. For instance, questions regarding non-linear dynamics can be tackled. Do processes such as phase-steepening of Alfvén waves as discussed in the previous section indeed take place? Apparently, earlier observations suggest that such processes may be possible. This issue is closely connected to the fundamental problem of finding applicable generation processes of interplanetary discontinuities. The essential question still waiting for a conclusive answer is: why is the solar wind discontinuous? Certainly, an indispensable first step in finding an answer is to provide a reliable observational statement on which types of discontinuity exist in the solar wind at all.

Using space as a laboratory of plasma physics also allows to study the structure of the boundary layers which is important for instance for investigating the stability of discontinuities. As discussed in the previous section, comparison with simulation may be a promising approach in this regard. Also the width of the boundary layers is an important parameter in the theory of discontinuities. Discontinuities occurring in nature provide an excellent opportunity to contribute to this issue.

Thirdly, the identification of MHD discontinuities (RDs versus TDs) in connection with finding possible generation mechanisms may play an important role for processes that take place in the solar corona. Two of the long-standing goals of solar wind research have been to identify and to understand the mechanisms for heating the solar corona and accelerating the solar wind. Among the obstacles to realising these goals are the limitations of coronal observations to remote sensing at a variety of electromagnetic wavelengths and the limitation of direct, in situ measurements to distances outside the regions where the heating and acceleration occur. If we accept the premise that most of the DDs observed in the solar wind originate close to the Sun, their properties may help to understand their role in the physics of the corona. Recent observations of the base of the solar corona [Solanki *et al.*, 2003] support Parker's idea that the active regions of the solar corona are heated by dissipation of magnetic energy at reconnecting TDs. Theorists will want to know on a quantitative level whether such TDs are common, i.e., whether the heating associated with the dissipation of magnetic energy can account for the observed coronal heating. Since observations of the lower corona are difficult, a quantitative evaluation of TDs in the solar wind might help.

Finally, also the interaction of interplanetary discontinuities with the (Earth's) magnetosphere should be mentioned. For instance, Burlaga [1969a] finds a relation between the occurrence rate of DDs and geomagnetic activity. There tend to be more DDs during geomagnetic disturbed times [Burlaga, 1969a]. Also note that the orientation of the IMF immediately upstream of the Earth's bow shock and magnetopause is known to be an important parameter in the rate of reconnection and hence energy input into the Earth's magnetosphere (see e.g. Scholer [1991]). In particular, sharp changes in the polarity of the north-south component of

the magnetic field, from northward to southward, can trigger dayside reconnection.³ A key objective of space weather forecasts is the prediction of arrival times of such southward turnings. Typically, magnetic field and plasma data from an upstream monitor spacecraft in halo orbit around the libration point L1, around 1.5×10^6 km sunward of the Earth, are used for such predictions, measuring the solar wind around an hour before it arrives at the bow shock. Certainly, to predict the Earth arrival time of southward magnetic field turnings a precise knowledge of the discontinuity normal is essential. Hence, the general field of space weather delivers a reason to carefully test existing techniques to evaluate discontinuity normals, a key objective of the present study.

An important parameter for the interaction of interplanetary discontinuities with the magnetosphere is the transversal extension of the discontinuities. There have been some attempts to estimate large scale surface curvature of DDs [Burlaga and Ness, 1969; Lepping *et al.*, 2003]. These will be revised in the present work also.

We have addressed several fundamental problems above which are related to the research on interplanetary discontinuities. Certainly, it is far beyond the scope of this work to provide conclusive solutions to these problems. Our claim is to deliver observational input that may be relevant for some of the discussed topics. The aim of this section was to give an overview that helps to understand the relevance of interplanetary discontinuities and the research on them in a more global context and to demonstrate that this kind of research is not solely of academic interest. It contributes to answering fundamental questions.

³Note that the DD shown in Figure 3.2 is a good example for a *northward* turning of the IMF (z points northwards).

THE CLUSTER MISSION

In the previous chapters we have introduced the physical subject of this work. Before presenting our own results, it is necessary to describe the “experimental setup” that we use. The unique tool utilised in this work is the Cluster mission. The outstanding feature of this space mission is that it consists of four coordinated spacecraft flying in close formation. This motivates to split the experimental description in two parts. In the first part we give a brief overview of the mission and the instruments that we use (this chapter). The second part (next chapter) is solely devoted to describe the configuration built by the four spacecraft. The geometry of the shape defined by the four points in space (the spacecraft positions) is of considerable importance for any kind of multi-spacecraft analysis. Since the multi-spacecraft idea is the essential point of the Cluster mission and also of the present work, the second part will be discussed in some detail. It will be necessary to introduce a theoretical framework that allows for a convenient description of the spacecraft formation. It is definitely worthwhile to go through this formalism, as it enables us to describe the shape and orientation of the formation by means of intuitive parameters. This will be of particular relevance for assessing the accuracy of our multi-point analysis method to determine the discontinuity normals \mathbf{n} and velocity U relative to the spacecraft array.

For a comprehensive overview of the Cluster mission see *Escoubet et al.* [1997]; *Credland et al.* [1997]; *Escoubet et al.* [2001]. Various techniques to analyse multi-spacecraft data are compiled in *Paschmann and Daly* [1998].

4.1 Mission overview and historical background

The four-spacecraft Cluster mission, together with the SOLar and Heliospheric Observatory (SOHO) mission¹, constitute the first cornerstone project of the ESA Horizon 2000 programme, which was designed to make major progress in the investigation of the nature of Sun-Earth interactions. These two missions are also known as the “Solar-Terrestrial Science Programme” and have the American space agency NASA as a partner. The idea is that SOHO monitors the Sun and the solar wind, whereas Cluster studies the magnetosphere and near Earth space in the meantime.

The Cluster mission was first proposed in November 1982, and was ready for launch in 1996, only seven months after the successful launch of SOHO. Unfortunately, the four Cluster spacecraft were destroyed when the Ariane 5 rocket exploded during its maiden launch on 4 June 1996. The Cluster team suggested to revive the unique project by using spare parts to build another spacecraft. It was named Phoenix after the mythical bird that rose from the ashes. On 3 April 1997, the ESA science programme committee agreed that three new Cluster spacecraft should be built alongside Phoenix, and Cluster II was born. Finally, the four Cluster II (in the following named Cluster) spacecraft were successfully launched in pairs on two Soyuz rockets from Baikonur Cosmodrome, Kazakhstan on 16 July and 9 August 2000. The commissioning phase was completed on 31 January 2001. Since then Cluster has been operating successfully. Originally funded to operate for 27 months, and now in an extended mission phase until December 2005, the spacecraft and payload continue to perform well and are expected to do so for several years to come. Recently another extension of four years (until December 2009) has been granted to the Cluster team.

The key objective of the Cluster mission is to study physical processes involved in the interaction between the solar wind and the magnetosphere by visiting the key magnetospheric regions like the polar cusps, the auroral zone and the magnetotail. Also the magnetopause and the bow shock are key objectives of Cluster. The continuing variations of the solar wind lead to continuing motions of these boundary layers. Four-point measurements are extremely helpful to study this motion and also the geometry of these boundaries. In general, the four coordinated Cluster spacecraft allow for the first time to separate between spatial and temporal variations in three dimensions. With only one satellite this is not possible, as one cannot distinguish between variations that are temporal in nature and variations that occur because the satellite has moved from one place to another. At least two spacecraft are necessary to separate spatial and temporal variations. However, two points in space define a straight line. Hence, with two spacecraft only one dimension can be explored. At least four non-coplanar spacecraft are necessary to obtain three-dimensional information. In addition, the simultaneous four-point measurements permit to derive differential plasma quantities. For instance, the current density near the four spacecraft can be derived from the magnetic field measurements using Ampère’s law.

¹SOHO operates permanently in the solar wind between Sun and Earth. We shall also benefit from this mission in this work (section 6.5).

4.2 Orbit and separation strategy

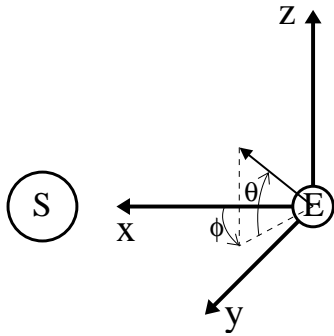


Figure 4.1: GSE coordinate system.

Unless otherwise noted we always use the *Geocentric Solar Ecliptic* (GSE) coordinate system which is illustrated in Figure 4.1. Earth is in the origin, the x -axis points towards the Sun, the z -axis is perpendicular to the ecliptic plane (positive North) and the y -axis completes the right-handed system (see e.g. *Hapgood* [1992]). This system is fixed with respect to the Earth-Sun line. The angles ϕ and θ are used as indicated in Figure 4.1: θ is the angle between the vector to be represented and its projection in the ecliptic plane (positive angles point northwards), and ϕ is the angle between the projection and the Earth-Sun line. ϕ is measured in a positive sense, i.e., counterclockwise as viewed from the positive z -axis. Unless otherwise noted ϕ ranges from 0° to 360° and θ from -90° to 90° .

In order to meet the scientific objectives of the mission, the orbit was chosen with a perigee at 4 Earth radii (R_E), an apogee at $19.6 R_E$, an inclination of 90° and a line of apsides around the ecliptic plane. The orbital period is 57 h. Figure 4.2 shows four orbits of one Cluster spacecraft at one month intervals in the GSE equatorial plane. The first shown orbit (starting on 1 December 2000) has its apogee at dusk. Then, as the Earth is rotating around the Sun, the apogee rotates towards local noon. This way the Cluster orbit will cross all regions of scientific interest during the course of the mission. Figure 4.2 also shows the position of the magnetopause and the bow shock (dashed red lines) and the IMF (green lines) for nominal conditions. The region marked by the fat dark green magnetic field lines indicates the *foreshock region*, the region of the solar wind that is magnetically connected to the Earth's bow shock and thus subject to disturbances due to reflected particles. The thin light green lines indicate the undisturbed solar wind. Only those segments of the orbit traversing this latter region are of interest in this work. Apparently, Cluster is not primarily designed for extensive studies of the undisturbed solar wind. However, there are still considerably long intervals with all four spacecraft in this region of space.² The careful selection of these intervals is one important issue of the present work (chapter 6).

Since each of the four spacecraft has its own orbit, the spacecraft configuration continuously varies along the orbit. Therefore, the spacecraft do not constitute the vertices of a regular tetrahedron (all pairs of spacecraft are equally spaced) most of the time. This leads to the necessity to establish a separation strategy, to be discussed in the next chapter (section 5.4). Here we only briefly discuss the size of the Cluster array, i.e., the separations between the four satellites. Using the thrusters on board each spacecraft, the inter-spacecraft separation distance has been changed several times already, ranging from 100 to 5000 km, depending on the spatial scales of the structures to be studied. Figure 4.3 gives an overview. Note that the shown distances correspond to the separations at that parts of the orbit where a regular

²Note that the spacecraft are slowest near apogee. Therefore the hourly positions are closest to each other at this part of the orbit.

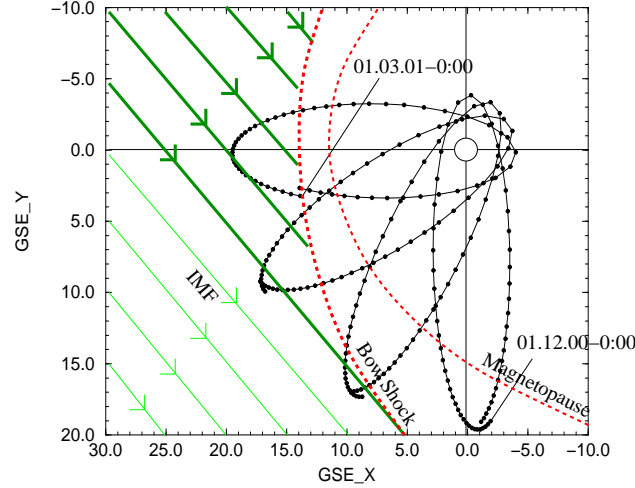


Figure 4.2: Cluster orbit. The orbital plane rotates with respect to the GSE z -axis. The complete rotation takes one year. Hourly positions are marked by the black circles.

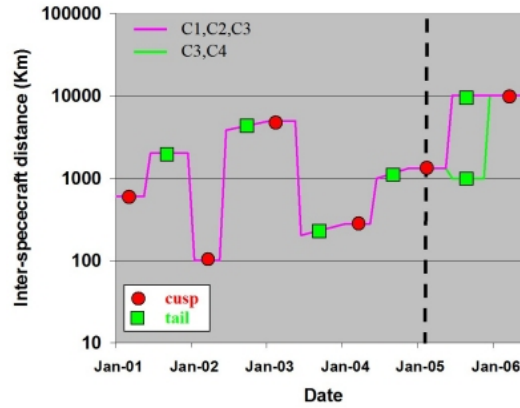


Figure 4.3: Distance between the spacecraft during the Cluster mission. The first three cusp-intervals (red circles) are used in this work. Taken from <http://clusterlaunch.esa.int/>.

tetrahedron is constituted. The separation manoeuvres are performed at approximately six-month intervals. The red circles indicate the intervals when apogee is on the sunward side of Earth (solar wind), and the green squares indicate intervals with apogee in the magnetotail. The intervals marked by the first three red circles (2001, 2002 and 2003) are used in this work. The respective nominal separations are 600, 100 and 5000 km, which enables us to study interplanetary discontinuities on various scales. Note that in the second half of this year (2005) the separations will be adjusted to 10000 km. This large separation will be maintained in the solar wind period in the first half of next year. In the course of this work we will realize that it would be of great interest to continue our study using the tetrahedron of 10000 km side length.

4.3 The satellites and their payload

The four Cluster spacecraft are named after Latin-American dances: Rumba (formerly Phoenix), Salsa, Samba and Tango. We choose a more prosaic nomenclature: Cl 1, Cl 2, Cl 3 and Cl 4, respectively. The four spacecraft are identical. They are spin-stabilised, with a nominal spin rate of 15 rpm. The spin axis points toward the North ecliptic plane. Each satellite carries the same set of eleven experiments to measure the electric and magnetic fields from DC to high frequencies, and electron and ion distribution functions at spin resolution. In the following we only briefly introduce the instruments that we use in this work. These are the fluxgate magnetometer (FGM) and the Cluster ion spectrometry (CIS) experiment.

4.3.1 Fluxgate magnetometer (FGM)

After about four and a half years in operation, the FGM instruments on board the four spacecraft are still in an excellent condition. For a detailed description of the instrument see *Balogh et al.* [1997; 2001]. The principal investigator of this instrument used to be A. Balogh. Now E. Lucek (both are from Imperial College in London, UK) fills the position. With the supervisor of this dissertation, F.M. Neubauer, being co-investigator of the FGM instrument, the Institute of Geophysics and Meteorology in Cologne is also involved in this experiment.

The FGM instrument on each spacecraft consists of two triaxial fluxgate magnetometers and an on-board Data-Processing Unit (DPU). In order to minimise the magnetic background of the spacecraft, one of the magnetometer sensors (OB sensor) is located at the end of a 5.2 m radial boom, and the other (IB) sensor at 1.5 m inboard from the end of the boom. In the default configuration, the OB sensor is used as the primary sensor. Data are also acquired simultaneously from the IB sensor at a lower rate.

The magnetometers have several operation ranges to provide good resolution in the solar wind (expected field magnitudes between 3 and 30 nT), and up to the highest field values expected in the magnetosphere along the Cluster orbit (up to 1000 nT). The digital resolution in the solar wind range is 7.8×10^{-3} nT [Balogh et al., 1997]. All components of the magnetic field are measured with an accuracy approaching 0.1 nT Balogh et al. [2001]. The time resolution of the FGM data is 22 vectors/s in normal mode. The highest available time resolution is 67 vectors/s (burst mode). All of the data that we use are in normal mode.

Unfortunately, these data comprise a spin signal at ≈ 0.25 Hz according to the 4 s spin period of the satellites. To eliminate this signal we routinely apply a recursive notch filter (see *Hanstein et al.* [1986] for details). In order to test whether the filtering significantly impacts our results we have performed parts of the analysis also with the unfiltered data. We find that whereas the results can be considerably different for the unfiltered data as compared to the filtered data in individual cases, statistically the main results are the same.

Whenever we refer to high resolution FGM data in this work we mean the notch-filtered data in normal mode resolution.

4.3.2 Cluster ion spectrometry (CIS)

For a detailed description of the instrument see *Rème et al.* [2001]. The principal investigator of this instrument is H. Rème from CESR in Toulouse, France.

The CIS instrument measures the full, three-dimensional ion distribution of the major magnetospheric ions (H^+ , He^+ , He^{++} and O^+) from thermal energies up to about 40 keV/e with a time resolution of one spacecraft spin period. The CIS package consists of two different instruments: a Hot Ion Analyser (HIA) and an ion COmposition and DIstribution Function analyser (CODIF) plus a Data Processing System (DPS) which permits extensive on-board data processing. Using a time-of-flight technology, CODIF gives the mass per charge composition with an angular resolution of 22.5° . HIA does not offer mass resolution but has an angular resolution capability ($5.6^\circ \times 5.6^\circ$) adequate for ion-beam and solar wind measurements. Each analyser has two different sensitivities in order to increase the dynamic range.

Unfortunately the CIS package is not functioning on all four spacecraft. CIS does not operate at all on Cl 2, and additionally the HIA instrument is switched off on Cl 4.

We use the HIA instrument for our analysis of solar wind discontinuities. The HIA selects the incoming ions according to the ion energy per charge by electrostatic deflection. The electrostatic analyser consists of three concentric spherical elements. These three elements are an inner hemisphere, an outer hemisphere, which contains a circular opening, and a small circular top cap which defines the entrance aperture. The incoming particles are deflected through 90° . In the analyser a potential is applied between the inner and the outer plate, and only charged particles with a limited range of energy and an initial azimuth angle (angle about the spin axis) are transmitted. The particle exit position is a measure of the incident polar angle (angle out of the spin plane) which can be resolved by a suitable position-sensitive detector system. The HIA instrument has $2 \times 180^\circ$ field of view sections parallel to the spin axis with two different sensitivities (“high G ” and “low g ”). The 180° “low g ” section allows for the detection of the solar wind, and the required high angular resolution is achieved through the use of $8 \times 5.625^\circ$ central anodes, with the remaining 8 sectors having a 11.25° resolution. This configuration provides “instantaneous” 2-D distributions sampled once per 62.5 ms (1/64 of one spin, i.e., 5.625° in azimuth), which is the nominal sweep rate of the high voltage applied to the inner plate of the electrostatic analyser to select the energy of the transmitted particles. For each sensitivity section, a full 4π steradian scan is completed after every spin of the spacecraft, i.e. after 4 s, giving a full, 3-D distribution of the ions in the energy range of 5 eV/e to 32 keV/e. The moments of these 3-D distributions are used in this work.

GEOMETRICAL CONSIDERATIONS OF THE CLUSTER ARRAY

Four non-coplanar points in space define a tetrahedron. If the separations between each pair of points are equal, then it is a regular tetrahedron. The four Cluster spacecraft form a tetrahedron which in general is not regular. The shape of this polyhedron evolves continuously along the orbital trajectories of the spacecraft.

The tetrahedral geometry is a principal factor affecting the precision of physical parameters derived from four-point measurements. For many applications, including the determination of discontinuity normals by relative timings, a configuration close to a regular tetrahedron is highly desirable.

Because of the scientific importance of the spacecraft configuration, many *quality factors* to describe the geometric shape of the tetrahedron have been suggested. The early one-dimensional geometric factors provide a measure for the degree of regularity of the tetrahedron. In order to obtain more detailed information about the tetrahedral geometry, such as *elongation* E and *planarity* P and the orientation, 2-D parameters are necessary.

In this chapter we introduce some of the 1-D quality factors (section 5.1) and the more sophisticated 2-D parameters (section 5.2)¹. The latter are closely related to the important *volumetric tensor* which we also discuss in detail in section 5.2. We demonstrate the quality factors' performances by systematically deforming a regular tetrahedron (section 5.3). The evolution of the tetrahedral geometry along the orbital trajectory is presented in section 5.4. Important for our statistical study, and particularly for the error analysis in chapter 9, is the tetrahedral geometry at the actual time of discontinuity occurrences. These configurations are discussed in section 5.5.

¹The summary of the quality factors presented here resembles the treatment in *Robert et al.* [1998].

5.1 1-D geometric factors

The question of how to quantify the degree of tetrahedral regularity was first addressed in the context of the Cluster mission by *von Stein et al.* [1992]. They introduced the Q_{GM} parameter which is defined as

$$Q_{GM} = \frac{\text{True Volume}}{\text{Ideal Volume}} + \frac{\text{True Surface}}{\text{Ideal Surface}} + 1 \quad (5.1)$$

The *ideal* volume and surface are calculated for a regular tetrahedron with a side length equal to the average of the six distance between the four points. It can be shown that each term is less or equal to unity, thus $Q_{GM} \in [1, 3]$. This quality factor attempts to describe the “fractional dimension” of the tetrahedron: $Q_{GM} = 3$ can only be achieved when the configuration is a regular tetrahedron. A value of 1 indicates that the four spacecraft are in a line, since only then the first two terms are both zero. However, there is nevertheless some difficulty with this interpretation: $Q_{GM} = 2$ is not a sufficient condition for planarity. It is perfectly possible to deform a regular ($Q_{GM} = 3$) tetrahedron continuously until it resembles a straight line ($Q_{GM} = 1$) without it resembling a plane at any time.

In their paper on tetrahedron shape *Robert and Roux* [1993] present 17 different parameters as ratios of various volumes, sizes and areas. One of these is particularly useful in estimating the error in the determination of the spatial gradient of the magnetic field [*Robert et al.*, 1998]. It is defined as

$$Q_{RR} = \mathcal{N} \cdot \left(\frac{\text{True Volume}}{\text{Sphere Volume}} \right)^{\frac{1}{3}} \quad (5.2)$$

where the sphere is the circumscribing sphere of the tetrahedron (all four points on its surface) and \mathcal{N} is a normalisation factor to make $Q_{RR} = 1$ for a regular tetrahedron. In appendix A we show

$$\mathcal{N} = \left(\frac{9\pi}{2\sqrt{3}} \right)^{\frac{1}{3}}$$

Q_{RR} ranges from 0 to 1.

Twenty five geometric factors are defined and compared with respect to their ability to provide a reliable index for the accuracy of the determination of the current density by *Robert et al.* [1995b]. Two of them are Q_{SR} and Q_{R8} to be defined below:

$$Q_{SR} = \frac{1}{2} \left(\frac{a+b+c}{a} - 1 \right) \quad (5.3)$$

where a , b and c are the lengths of the major, middle and minor semi-axes of the ellipsoid representing the *volumetric tensor* defined in section 5.2. Since $a \geq b \geq c$, Q_{SR} takes values between 0 and 1, where $Q_{SR} = 1$ indicates a regular tetrahedron ($a = b = c$), and $Q_{SR} = 0$ indicates that the four spacecraft are in a line ($b = c = 0$).

The final 1-D quality factor we present is similar to Q_{GM} and is defined as

$$Q_{R8} = \frac{\text{True Volume}}{\text{Ideal Volume}} \quad (5.4)$$

Q_{R8} ranges from 0 to 1.

Appendix A contains more details of the mathematics of a tetrahedron and instructions on how to calculate the presented 1-D quality factors.

5.2 2-D geometric factors and the volumetric tensor

None of the 1-D parameters is capable of giving sufficient information about the shape and orientation of the tetrahedron. This can only be done in a 2-D parameter space. The two parameters we derive in this section were introduced by *Robert et al.* [1995a]. They are closely connected to the *volumetric tensor* which for N vertices (or spacecraft) is defined as²

$$\mathbf{R} = \frac{1}{N} \sum_{\alpha=1}^N (\mathbf{r}_{\alpha} - \mathbf{r}_b)(\mathbf{r}_{\alpha} - \mathbf{r}_b)^T \quad (5.5)$$

where \mathbf{r}_{α} is the position of spacecraft α in an arbitrary system of coordinates and

$$\mathbf{r}_b = \frac{1}{N} \sum_{\alpha=1}^N \mathbf{r}_{\alpha} \quad (5.6)$$

is the *mesocentre* [Harvey, 1998]. Note that the mesocentre coincides with the centre of mass if the spacecraft have identical mass. In component form the volumetric tensor reads³:

$$R_{jk} = \frac{1}{N} \sum_{\alpha=1}^N (r_{\alpha j} - r_{bj})(r_{\alpha k} - r_{bk}) \quad (5.7)$$

where $r_{\alpha j}$ is the j -component of vertex α and r_{bj} is the mean value, over all α , of $r_{\alpha j}$. If the origin of coordinates is chosen to be the mesocentre, then the tensor \mathbf{R} can be written as

$$R_{jk} = \frac{1}{N} \sum_{\alpha=1}^N r_{\alpha j} r_{\alpha k} \quad (5.8)$$

The volumetric tensor is determined uniquely from the known orbital positions of the N spacecraft. Its fundamental importance originates from the ubiquitous way in which it appears whenever a boundary normal or spatial gradient is determined from multi-point observations, for which purpose it must be inverted (see section 7.4 and e.g. *Harvey* [1998]; *Chanteur* [1998]; *Chanteur and Harvey* [1998]). Mathematically, \mathbf{R} cannot be inverted if it is singular, i.e., if one of its eigenvalues is zero and the spacecraft are coplanar. Physically, the equivalent condition is that one of its eigenvalues is less than the uncertainty in the spacecraft position: the spacecraft are too close to being coplanar for the spatial gradient or the boundary normal to be determined completely.

The volumetric tensor is symmetric. A symmetric tensor describes a quadratic form which can be represented by an ellipsoid in space. This ellipsoid has three principal axes, each lying in the direction of one of the eigenvectors of the tensor, with a semi-length determined by the corresponding eigenvalue. This provides a description of the geometry of the polyhedron

²The formalism presented here is valid for $N \geq 4$. Of course, for this work the special case $N = 4$ is relevant. Dyadic notation is used: \mathbf{a}^T denotes the transpose of the column vector \mathbf{a} , and the dyad $\mathbf{a}\mathbf{b}^T$ is a tensor of rank two.

³Note that we use the summation convention whenever this simplifies the mathematics, i.e., when in any expression a term contains a product of two subscribed array elements with the same Latin index, then that term is understood to be summed over the values 1, 2 and 3 of the index. Summations over Greek indices, used to indicate the spacecraft, are written explicitly.

which is intuitively simple and yet adequate to evaluate the geometric worth of the data for studying any particular scientific objective [Harvey, 1998; Robert *et al.*, 1998]. A derivation of this is presented in the following:

Consider a plane defined by its normal \mathbf{n} . Let \mathbf{r}_0 be any point in this plane and $a = \mathbf{n} \cdot \mathbf{r}_0$. The mean square distance $\sigma^2(\mathbf{n})$ of the N spacecraft from the plane is given by

$$\begin{aligned} \sigma^2(\mathbf{n}) &= \frac{1}{N} \sum_{\alpha=1}^N [\mathbf{n} \cdot (\mathbf{r}_\alpha - \mathbf{r}_0)]^2 = \frac{1}{N} \sum_{\alpha=1}^N (n_j r_{\alpha j} - a) (n_k r_{\alpha k} - a) \\ &= \frac{1}{N} \sum_{\alpha=1}^N r_{\alpha j} r_{\alpha k} n_j n_k - 2a \frac{1}{N} \sum_{\alpha=1}^N \mathbf{n} \cdot \mathbf{r}_\alpha + a^2 \end{aligned} \quad (5.9)$$

Differentiation with respect to a shows that for fixed but arbitrary \mathbf{r}_α and \mathbf{n} , the minimum value of σ^2 occurs when $a = \frac{1}{N} \sum_{\alpha=1}^N \mathbf{n} \cdot \mathbf{r}_\alpha$ (for any direction \mathbf{n}). Therefore

$$\mathbf{r}_0 = \frac{1}{N} \sum_{\alpha=1}^N \mathbf{r}_\alpha = \mathbf{r}_b \quad (5.10)$$

The plane of minimum mean squares contains the mesocentre \mathbf{r}_b of the polyhedron [Harvey, 1998].

Introducing equation 5.10 and the tensor R of equation 5.5 into equation 5.9, the root mean square “deviation” σ of the spacecraft from their mesocentre in the \mathbf{n} -direction may be expressed as

$$\sigma(\mathbf{n}) = \sqrt{R_{jk} n_j n_k} \quad (5.11)$$

The *dimension*, or *thickness*, of the polyhedron in that direction is defined as twice this value [Harvey, 1998].

As the direction of the unit vector \mathbf{n} varies over 4π , the value of $\sigma(\mathbf{n})$ describes the surface of an ellipsoid. A line in any direction \mathbf{n} intersects this surface at two points whose separation is equal to the thickness of the polyhedron in that direction. There are three directions in which $\sigma(\mathbf{n})$ is stationary. These are the principal axes of the ellipsoid defined by the eigenvectors \mathbf{R}^a , \mathbf{R}^b and \mathbf{R}^c of R . We denote the corresponding values of $\sigma(\mathbf{n})$ by a , b and c , with

$$a \geq b \geq c$$

a^2 , b^2 and c^2 are the eigenvalues of R corresponding to the eigenvectors \mathbf{R}^a , \mathbf{R}^b and \mathbf{R}^c , and a , b , and c represent respectively the major, middle and minor semi-axes of the ellipsoid [Harvey, 1998].

Thus, the volumetric tensor, and the associated ellipsoid, provide a simple way to visualise the features of the global shape of a polyhedron. For instance, an ellipsoid reduced to a sphere corresponds to a regular polyhedron, an ellipsoid reduced to a plane ellipse corresponds to the spacecraft being coplanar and an ellipsoid reduced to a line corresponds to the alignment of the spacecraft. At this point it may be noted that, even if the volumetric tensor was to be renormalised so that the spacecraft of a regular tetrahedron actually lie on the surface of the sphere, for an arbitrary configuration the spacecraft would generally not lie on the surface of the corresponding ellipsoid.

In order to describe the size and the shape of the polyhedron it is useful to have parameters that are intuitively descriptive. This can be realized by using the three eigenvalues. From these we can construct one parameter indicating the size and two parameters measuring elongation and planarity. Furthermore, in the general case of an anisotropic configuration two directions are required to define the orientation of the polyhedron in space.

When the polyhedron is isotropic, all three eigenvalues are equal ($a^2 = b^2 = c^2$).

If it is stretched in one direction, a^2 becomes greater than the other two eigenvalues ($a^2 > b^2, c^2$). If stretched further (or equivalently, if squeezed in the two orthogonal directions) until $b = c = 0$, the spacecraft would lie on a straight line. This motivates to define the *elongation*, or prolateness, as

$$E = 1 - \frac{b}{a} \quad (5.12)$$

It ranges from 0 to 1, where $E = 0$ ($a = b$) means no elongation, and $E = 1$ ($b = c = 0$) corresponds to the maximum possible elongation, i.e., all spacecraft are in a line. Furthermore, the eigenvector \mathbf{R}^a defines the direction of elongation.

If the isotropic polyhedron is squashed in one direction, c^2 becomes smaller than the other two eigenvalues ($c^2 < a^2, b^2$). If squashed further until $c = 0$ the spacecraft would lie in a plane. Accordingly, the *planarity*, or oblateness is defined as

$$P = 1 - \frac{c}{b} \quad (5.13)$$

It also ranges from 0 to 1, where $P = 0$ ($b = c$) means no planarity and $P = 1$ ($c = 0$) corresponds to the maximum possible planarity, i.e., all spacecraft are in a plane. Furthermore, the eigenvector \mathbf{R}^c defines the normal of planarity. Note that $b = 0$ can only occur when $c = 0$. In that case $E = 1$ and P is undefined.

In general the polyhedron is both stretched and squashed in mutually orthogonal directions. Together with the direction of elongation and the normal of planarity the dimensionless parameters E and P define the physically important characteristics of the shape of the polyhedron.

Finally, the parameter describing the characteristic size is defined as

$$L = 2a \quad (5.14)$$

Choosing the largest eigenvalue a^2 here is convenient, because it is always non-zero. The size can be measured in any convenient unit of length.

Table 5.1 summarises the derived parameters. They are sufficient to describe the physically important characteristics of a polyhedron. The direction of elongation and the normal of planarity are by definition orthogonal, and so only three angles (e.g. the three Euler angles) are needed to completely describe the orientation of the ellipsoid in three dimensions. These three angles plus the values of L , E and P provide a complete description of the volumetric tensor.

The shape of the polyhedron as E and P vary over their permitted ranges is indicated in Figure 5.1. Robert *et al.* [1998] define five general shapes to characterise the polyhedra according to the E and P parameters:

Table 5.1: Set of parameters sufficiently describing the physically important characteristics of a polyhedron. The set consists of three scalars and two vectors.

Shape	Orientation	Characteristic Size
elongation $E = 1 - \frac{b}{a}$	direction of elongation \mathbf{R}^a	$L = 2a$
planarity $P = 1 - \frac{c}{b}$	normal of planarity \mathbf{R}^c	

- *Pseudo-Sphere*: E and P are small (bottom left corner in the E - P diagram Figure 5.1) corresponding to pseudo-regular polyhedra.
- *Pancake*: E is small and P is large (top left corner in the E - P diagram) corresponding to an ellipsoid which is a nearly flat circle.
- *Cigar*: E is large and P is small (bottom right corner in the E - P diagram) corresponding to a long ellipsoid with a pseudo-circular section.
- *Knife-Blade*: E and P are large (top right corner in the E - P diagram) corresponding to polyhedra which are both elongated and flat.
- *Potato*: Polyhedra that do not belong to one of the above categories. They are located at the centre of the E - P diagram.

Note that the eccentricity of an ellipse is defined by $e = \sqrt{1 - (b/a)^2}$ also ranging from 0 to 1. The question arises whether elongation and planarity would have been better defined accordingly. Then E and P would be simply the eccentricities $e_c = \sqrt{1 - (b/a)^2}$ and $e_a = \sqrt{1 - (c/b)^2}$ of the ellipsoid respectively in the plane of planarity (containing the middle and major axes), and in the plane perpendicular to the elongation (containing its minor and middle axes). Both definitions are acceptable, but the elongation and planarity as defined above yield a more uniform distribution of points in the E - P plane. This point is, of course, entirely subjective because there is no *a priori* uniform distribution, but the statement is certainly true for typical Cluster orbits [Robert *et al.*, 1998].

Also note that the volumetric tensor does not describe a tetrahedron ($N = 4$) completely. A complete description would require the position of three of the apexes with respect to the fourth apex, i.e., nine independent quantities of which three describe orientation and six describe shape. The symmetric volumetric tensor has only six independent quantities, of which only three describe shape.

As a final remark we may add that in the special case of four spacecraft, \mathbf{R} yields the volume V of the tetrahedron. For this reason it is called the volumetric tensor. Harvey [1998] shows that the volume is one third of the product of the three characteristic dimensions:

$$\frac{V}{8abc} = \frac{1}{3} \Leftrightarrow V = \frac{8}{3} \sqrt{|\mathbf{R}|} \quad (5.15)$$

<div><div>P</div><div>E</div></div>	0	low	intermediate	large	1
1	Circle	Ellipsoid of increasing eccentricity			Straight Line
large	Ellipsoid of increasing oblateness	Pancake	Elliptical Pancake	Knife Blade	
intermediate		Thick Pancake	Potatoes	Flattened Cigar	
low		Pseudo-Sphere	Short Cigar	Cigar	
0	Sphere	Ellipsoid of increasing prolateness			

Figure 5.1: The shape of the polyhedron as a function of E and P . Taken from Robert et al. [1998].

5.3 A simple performance study

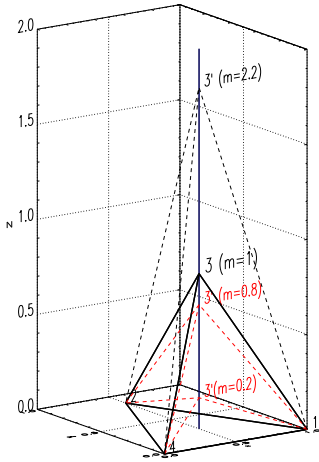


Figure 5.2: Systematic deformation of a regular tetrahedron of unit side by scaling the z -component of vertex 3 by the factor m .

The primary objective of this section is to demonstrate the performance of the quality factors by systematically deforming a regular tetrahedron. We start with a regular tetrahedron of unit side. We may take e.g. $\mathbf{r}_1 = (1, 0, 0)$, $\mathbf{r}_2 = (1/2, \sqrt{3}/2, 0)$, $\mathbf{r}_3 = (1/2, \sqrt{3}/6, \sqrt{6}/3)$ and $\mathbf{r}_4 = (0, 0, 0)$, where \mathbf{r}_α are the position vectors of the four vertices or spacecraft $\alpha = 1, 2, 3, 4$. This tetrahedron is plotted in Figure 5.2 (thick solid black lines). By multiplying the z -component of vertex 3 with a factor $m \geq 0$ (i.e., moving vertex 3 along the vertical blue line) we can artificially create irregular tetrahedra which are either elongated ($m > 1$) or squashed ($m < 1$) in one direction. For $m = 0$ all spacecraft are in a plane ($P = 1$), and $m \rightarrow \infty$ corresponds to $E = 1$. Note that by this construction either $E = 0$ or $P = 0$. We deliberately omit the general case here, where the tetrahedron is both stretched and squashed in mutually orthogonal directions, since we solely aim for a quantitative understanding of the various parameters, especially of

E and P . The described procedure corresponds to moving along the left, respectively the bottom side in the E - P diagram (Figure 5.1). The direction of elongation ($m > 1$) and the normal of planarity ($m < 1$) both coincide with the z -axis of Figure 5.2. Three irregular tetrahedra corresponding to $m = 2.2$, $m = 0.8$ and $m = 0.2$ (dashed lines) are plotted; those with $m < 1$ ($P > 0$) are plotted in red. Note that the vertices 1, 2 and 4 and the edges connecting them are the same for all tetrahedra in our “reservoir”, regardless of m . Figure 5.2 gives an idea of how m acts on the shape of the tetrahedron.

Figure 5.3 demonstrates how m is related to the quality factors defined in the previous sec-

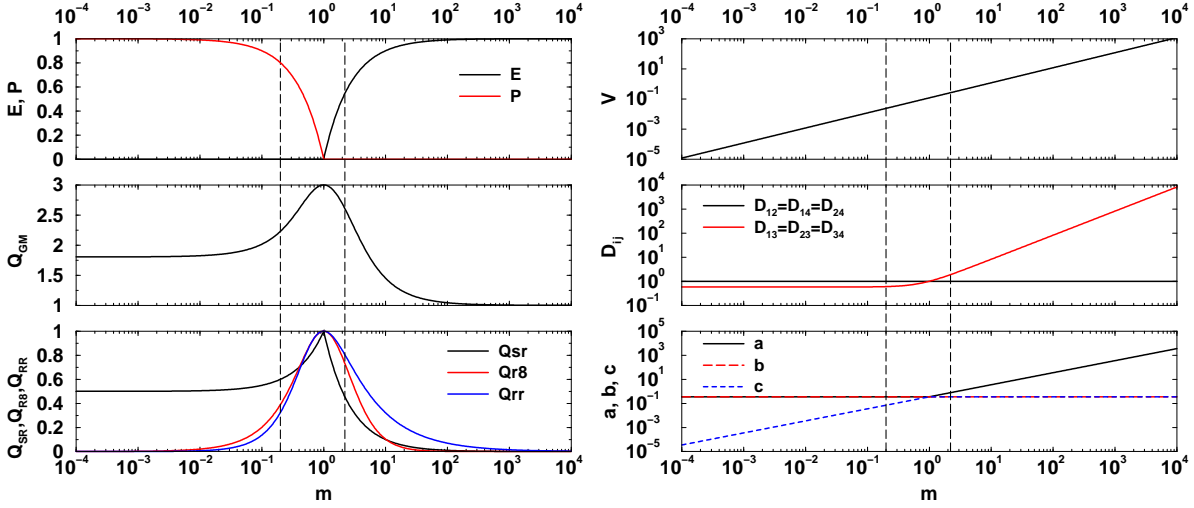


Figure 5.3: Quality factors (left) and tetrahedron volume, side lengths and semi-axes lengths in arbitrary units as a function of m (right).

tions. The left side shows these parameters as a function of m and the right side shows the tetrahedron volume, the side lengths D_{ij} and semi-axes lengths of the corresponding ellipsoid. To produce these plots we varied m in the range from 10^{-4} to 10^4 with $\Delta(\log m) = 0.01$, i.e., the shown geometrical quantities are calculated for 801 different values of m .

For $m \leq 1$, $E = 0$, and for $m > 1$, $E(m)$ strictly increases, approaching unity for $m \rightarrow \infty$. The behaviour of the planarity is reversed. As $m \rightarrow 0$, P approaches unity and strictly decreases until $m = 1$. Q_{GM} approaches the asymptotic value $Q_{GM} \approx 1.8$ for $m \rightarrow 0$. In the notation of “fractional dimension” it should be 2. On the other hand $Q_{GM} = 2$ for the elongated tetrahedron defined by $m = 4.3$. Nevertheless, this concept still remains interesting. A value close to 1 indeed indicates a highly elongated configuration, and Q_{GM} close to 3 ensures that the tetrahedron is close to being regular. Similar to Q_{GM} , the factor Q_{SR} yields information on the geometrical shape. $Q_{SR} \approx 0.5$ indicates a planar configuration with some confidence, whereas a value close to 0 can only result from a strongly elongated tetrahedron and $Q_{SR} \approx 1$ strongly indicates a regular tetrahedron. As can be seen from Figure 5.3 the two remaining factors, Q_{R8} and Q_{RR} are more or less symmetric around $m = 1$, especially Q_{R8} . Both asymptotic values are 0. Thus, they do not give real or direct information on the geometrical shape, but can be considered as the degree of degeneration of the tetrahedron. For a detailed study of the 1-D parameters and their interrelation to the 2-D parameters, making use of the five general ellipsoid shapes, see *Robert et al.* [1998].

Although the Cluster tetrahedra used in our analysis will be discussed in section 5.5 it may be instructive to briefly introduce the limiting cases already in this section. To avoid large errors caused by planar spacecraft configurations we introduce a cut-off value $P_c = 0.8$ (see also section 5.5 and chapter 9 where we demonstrate that this is a reasonable choice). Whenever applying relative timings, we either omit those cases with $P > P_c$ or we give a caveat. The most elongated tetrahedron occurring during DD observation is characterised by $E = 0.55$ (see section 5.5). The values $m = 0.2$ and $m = 2.2$ correspond to these upper boundaries in P and E . They are indicated by the vertical dashed lines in Figure 5.3. Note that since E and P are strictly monotonic functions in m for $m > 1$ and $m < 1$, respectively, $m = 0.2$ and

$m = 2.2$ are the minimum and maximum values representing the range of deformation that we are facing in our multi-spacecraft analysis. The corresponding tetrahedra shown in Figure 5.2 clearly illustrate this range. According to the above construction we can thus state that the flattest configuration that we use ($P = 0.8$) can be realized by reducing the “height” of a regular tetrahedron to 20% of its original value. To “generate” the most elongated configuration the height must be increased to 220%. The value $m = 0.8$ corresponds to $P = 0.21$, an intermediate value rather typical for the tetrahedra we use in 2003 (see section 5.5). Note, however, that the real configurations that we consider are both stretched and squashed in mutually orthogonal directions, e.g. the most elongated tetrahedron that we use in our analysis is also the most flattened one (see Figure 5.8).

According to our construction, the side lengths D_{ij} ($i, j = 1, 2, 4$) connecting the vertices 1, 2 and 4 are unity regardless of m , and the edges connecting vertex 3 to the other three vertices have the same length $D_{13}(m) = D_{23}(m) = D_{34}(m)$ (Figure 5.3). This symmetric deformation process causes the middle semi-axis b of the ellipsoid representing the volumetric tensor to be constant in m . The major semi-axis is constant for $0 \leq m \leq 1$ and increases linearly⁴ for $m \geq 1$. For the error analysis the minor semi-axis c is most relevant (see section 5.5). Its value is zero for $m = 0$ and linearly increases for $0 < m \leq 1$. For $m \geq 1$, c is constant. Note that $c(m = 0.2) = c(m = 1)/5$. Thus, assuming a characteristic size $L = 2a = 1000$ km of the regular tetrahedron ($m = 1$) the thickness of the ellipsoid in the direction normal to planarity would still be $2c = 200$ km for $m = 0.2$ ($P = P_c$), a significant value related to the accuracy of orbit determination (see section 5.5).

5.4 Evolution of the tetrahedron along one orbit

In this section we apply the quality factors in order to study the evolution of the tetrahedron shape along a typical Cluster orbit. We have chosen the orbit starting at 05:30 UT on day of year (doy) 52 in 2001 which is plotted in Figure 5.4. The bow shock and the magnetopause are also shown. The colour code indicates the region of geo-space traversed by the spacecraft. Note that from our set of DDs, 16 were found in the shown solar wind region (red). In Figure 5.5 the tetrahedron characteristics for this particular orbit are plotted both, versus time and in a E - P diagram. The origin of time coincides with doy 52, 05:30 UT, the perigee of the orbit. To allow for a better comparison with Figure 5.4, the apogee and the perigee are indicated in all plots of Figure 5.5, and in addition the northern cusp is marked in the E - P diagram.

Relative to the geocentric distance D_E , the spacecraft appear to be close to each other, and the four distances are superposed in the figure. One can see, however, that the inter-spacecraft distances D_{ij} vary in high proportions, and thus the shape of the tetrahedron has a strong variation along the orbit. In particular, the volume of the tetrahedron reaches a value close to zero twice (around hour 3 and hour 54 of the orbit). Accordingly the 1-D quality factors take their minimum values at these points. Since the minor semi-axis c is also almost zero here and the middle semi-axis b has a non-zero value, the tetrahedron is almost fully flat (the planarity has its maximum close to 1.) The ecliptic projection of the normal of planarity \mathbf{R}^c

⁴Note that the increase is in fact linear, the exponent in the double logarithmic plot is 1.

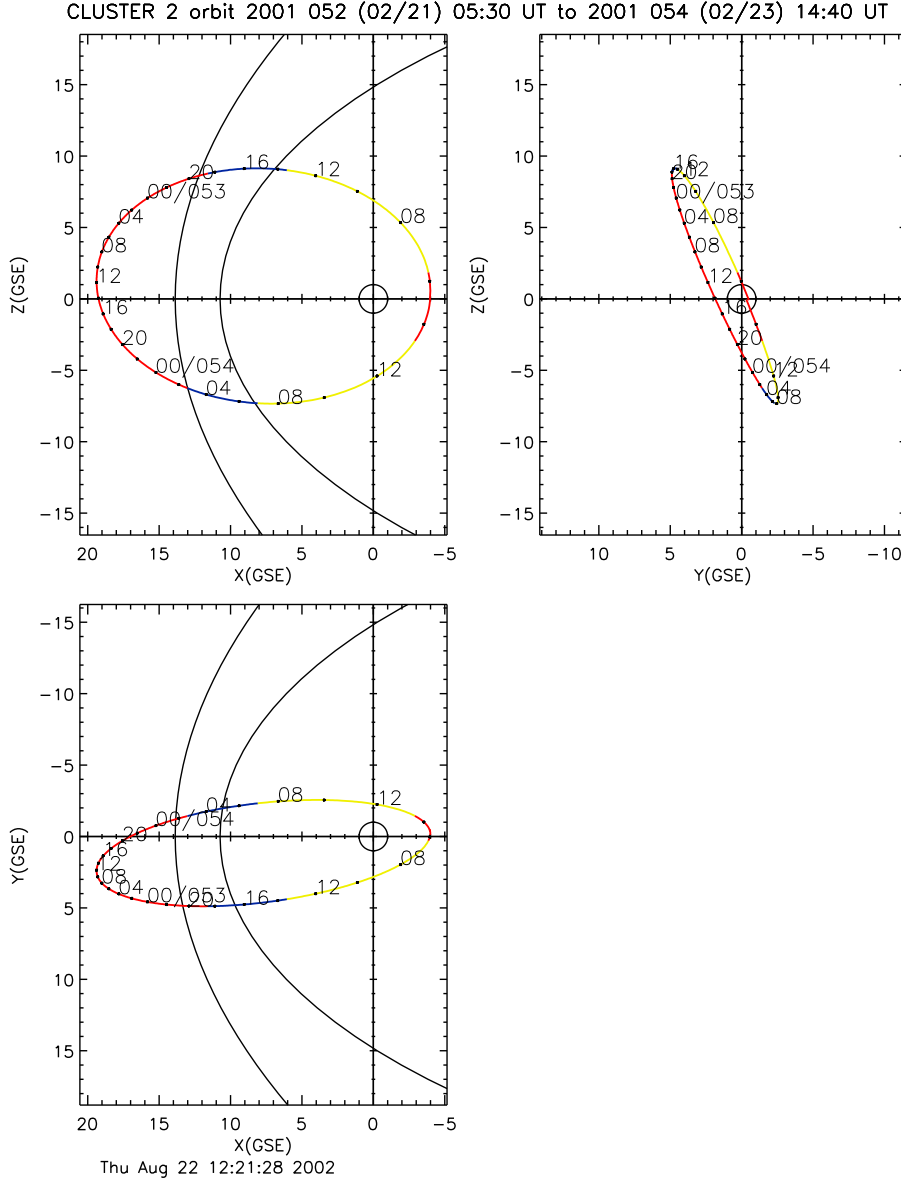


Figure 5.4: Cluster 2 orbit from day 52 2001 05:30 UT until day 54 2001 14:40 UT. The three panels located in the upper left, upper right and lower left show x-z, y-z and x-y projections of the orbit, respectively, in GSE coordinates. The orbit traces are colour coded according to the region of geo-space traversed by the spacecraft. Red: if in the solar wind or inside the magnetosphere and within $3 R_E$ of the model neutral sheet. Blue: if in the model magnetosheath; the magnetopause boundary is the Roelof-Sibeck model [Roelof and Sibeck, 1993] using nominal conditions. Yellow: magnetosphere, other than above. Taken from <http://www-spf.gsfc.nasa.gov>.

is aligned with the GSE y-axis ($\phi \approx 90^\circ$).

When apogee is around local noon (as for the orbit we presently discuss) special emphasis in terms of separation has been put on the northern cusp and the southern magnetopause/bow shock. In these two areas a perfect tetrahedron is constituted [Escoubet *et al.*, 1997]. Equipped with the necessary theoretical framework we are now able to adequately describe the evolution of the configuration along the orbit. The northern cusp is traversed at 14:30 UT on day 52, corresponding to hour 9 in Figure 5.5. Note that at this point and later

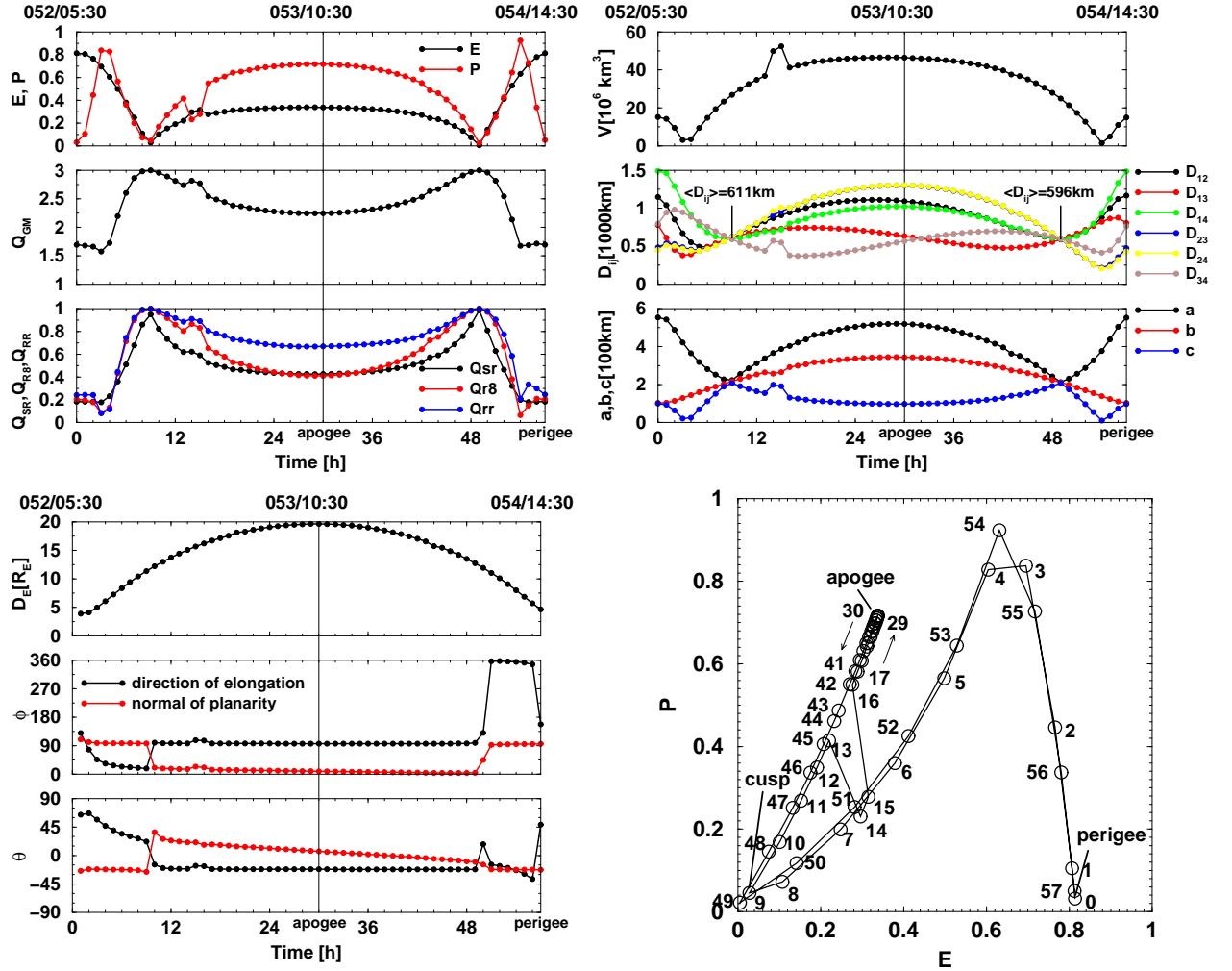


Figure 5.5: Tetrahedron characteristics for the orbit shown in Figure 5.4 plotted with time (upper left and right and lower left) and a hodogram of the successive positions of the tetrahedron in the E - P diagram (lower right). The two plots at the top show the same quantities as Figure 5.3. In addition the geocentric distance R_E and the orientation (ϕ and θ) of the tetrahedra are plotted (lower left). Hourly values are plotted, indicated by circles. In the E - P diagram the orbit hours are plotted next to the symbols.

at hour 49 the inter-spacecraft distances are all equal. The side length of the regular tetrahedron at the northern cusp is the nominal separation distance, for a specific interval of the Cluster mission. It is 600 km for the solar wind period (i.e., when apogee is on the day-side of the magnetosphere) in 2001, 100 km in 2002 and 5000 km in 2003. The semi-axes a , b and c also have equal values, and thus the elongation and the planarity are zero. Also the 1-D parameters indicate regularity ($Q_{GM} = 3$ and $Q_{SR} = Q_{R8} = Q_{RR} = 1$). The orientation of the tetrahedron changes rapidly at these two points. At the northern cusp \mathbf{R}^c rotates from ($\phi \approx 90^\circ$, $\theta \approx -25^\circ$) to ($\phi \approx 20^\circ$, $\theta \approx 25^\circ$).

An advantage of having a regular tetrahedron at the northern cusp is that the configuration stays quite close to a regular tetrahedron throughout the magnetosheath and solar wind. Approaching apogee the elongation and the planarity increase, have a local maximum at apogee and decrease again. In this part of the orbit the tetrahedron is more flattened than elongated ($P > E$). The normal of planarity rotates clockwise about the GSE z -axis, i.e., ϕ decreases

from 20° to 0° . At the same time θ also decreases to zero. Back in the magnetosphere the spacecraft approach perigee and thus gain speed. As a consequence the configuration gets more and more elongated. At perigee the elongation reaches its maximum value and the spacecraft constitute a “string-of-pearls”.

In order to quickly characterise the distortion of the tetrahedron and its evolution along one orbit another way is to plot a hodogram of the successive positions of the tetrahedron in an E - P diagram (lower right of Figure 5.5) rather than plotting the characteristics with time. The apogee corresponds to the portion of the figure where the different points are very close to each other, the velocity being low and the shape slowly varying. The elongation E takes moderate values here, whereas P is rather large. The perigee corresponds to the portion of the figure where the points are widely spaced, because the spacecraft velocity along the average trajectory is large. The tetrahedron is strongly elongated in this area. The transition of the cusp (around hour 9) is located clearly in the pseudo-sphere region as defined in section 5.2. During the rest of the curve the E - P parameters can take extreme values. In particular the tetrahedron is very flat around hours 3 and 4 and around hour 54.

Note that the rather continuous progression of the shown parameters has an irregularity around hours 14 and 15, which is caused by a spacecraft manoeuvre implemented at that time.

5.5 Constellations used in our analysis

Although the selection of the discontinuities to be used in our analysis is subject of the following chapter, it appears to be reasonable to characterise the corresponding spacecraft constellations during the discontinuity observations already in this section. In the following chapter we will show that overall 366 events are found that are suitable for further investigations. Of these, 129 events are observed in 2001, 33 in 2002 and 204 in 2003. Using the quality factors for all 366 events and studying in particular the extreme cases in terms of elongation and planarity, we are able to provide a clear insight into the prevailing geometrical characteristics.

A comprehensive knowledge of the present configurations is imperative for any multi-spacecraft analysis. This is especially true for the relative timing analysis used in this work. Since the tetrahedral geometry is one of the principal factors affecting the precision of this method we routinely monitor all five quality factors introduced in this chapter when analysing DDs. However, ultimately decisive for the question whether or not the geometrical quality is sufficient for our multi-spacecraft analysis are the 2-D parameters. Since the Cluster array is rather squeezed to a planar configuration than stretched in the solar wind, the most important indicator is the planarity P . To avoid large errors due to degenerated configuration we have introduced a cut-off value of $P_c = 0.8$. For $P > P_c$ the corresponding DD is not considered, or a caveat is given. Note that not only the degree of irregularity is relevant for the error analysis, but also the orientation of the tetrahedra. Since the error is largest in the direction normal to planarity (see section 7.4.2 and chapter 9) it is crucial to be aware of any preferences of that direction, since this might cause a bias in the results.

Looking at the extreme cases of tetrahedra shape in our data sets already yields a detailed overview of the geometrical characteristics we are facing. Figure 5.6 shows these configurations. From top to bottom they are sorted according to their size, maximum in 2003 (top) and minimum in 2002 (bottom). The left column shows the best configuration according to regularity in the particular year. The second column shows the worst, i.e. most anisotropic, configuration considered in our analysis. We also show the flattest configuration observed at DD occurrence in 2003 (rightmost tetrahedron in the top row) in order to demonstrate the wide range of shapes present in our tetrahedra reservoir. In Table 5.2 the most important parameters characterising the shown tetrahedra are summarised.

The vertices are the positions of the four spacecraft numbered accordingly. Note that we have translated the origin of the GSE system to the location of the southernmost spacecraft, i.e., the one with the smallest z -component. This is always Cl 4 in 2001 and Cl 3 in 2002 and 2003 (see also Figure 5.7). The thick lines connect the vertices. They are dashed when covered by one of the sides. The solid green line indicates the normal of planarity \mathbf{R}^c and the red line the direction of elongation \mathbf{R}^a . The dashed lines in the corresponding colour are the projections on the bounding walls. The axes have the same length in all three dimensions for each plot. Note, however, that the sizes of the seven boxes are all different, the side lengths are approximately 5000 km, 1000 km and 200 km for the top, middle and the bottom row, respectively. Also the perspective may change to allow for the best 3-D interpretation and comparison between the tetrahedra. However, it is the same among the three configurations from 2003 and among the two from 2001.

To get the correct 3-D picture of the shapes presented it is necessary to consider the projections of the vertices on the $x-y$, $x-z$ and the $y-z$ plane (guided by the thin dashed lines). Also helpful are the separation distances D_{ij} given in Table 5.2. Then it can be realized that all four vertices of the best configuration in 2003 (top left) are close to (or on) different walls of the bounding box, and thus the almost perfect regularity (see quality factors in Table 5.2) can be perceived. Note that the plane defined by the vertices 2, 3 and 4 (side 2-3-4) is almost parallel to the $y-z$ plane. For solar wind observations this means that signals coming from the Sun will be first observed at these three spacecraft and some time later at Cl 1. A DD, e.g. with a normal parallel to the x -direction would be observed almost simultaneously at Cl 2, Cl 3 and Cl 4. Next to this tetrahedron the worst configuration in 2003 used in our analysis is shown. It is elongated in the direction approximately given by the edge connecting vertex 1 and 4 (see also the red line and D_{14} from Table 5.2). Vertex 2 is behind side 1-3-4. This tetrahedron is flattened (see also the quality factors in Table 5.2, especially $P = 0.8$). However, the projections of the points 4, 2 and 1 on the $x-z$ and the $x-y$ plane are far from being aligned. Thus, vertex 2 is not in the same plane as the other three vertices. From Table 5.2 we see $2c = 470$ km, i.e., the tetrahedron significantly expands in the direction normal to planarity. This is different for the rightmost tetrahedron ($P = 0.99$, $2c = 26$ km). The two configurations are quite similar, apart from vertex 2 being much closer to side 1-3-4 here. The points 1, 2 and 4 are aligned now (all three projections of these points are aligned). Thus, all four spacecraft are almost in one plane. Note that the thickness $2c = 26$ km is close to the accuracy of orbit determination (see below).

Whereas we have a large variety of different tetrahedra shapes ranging from almost perfectly

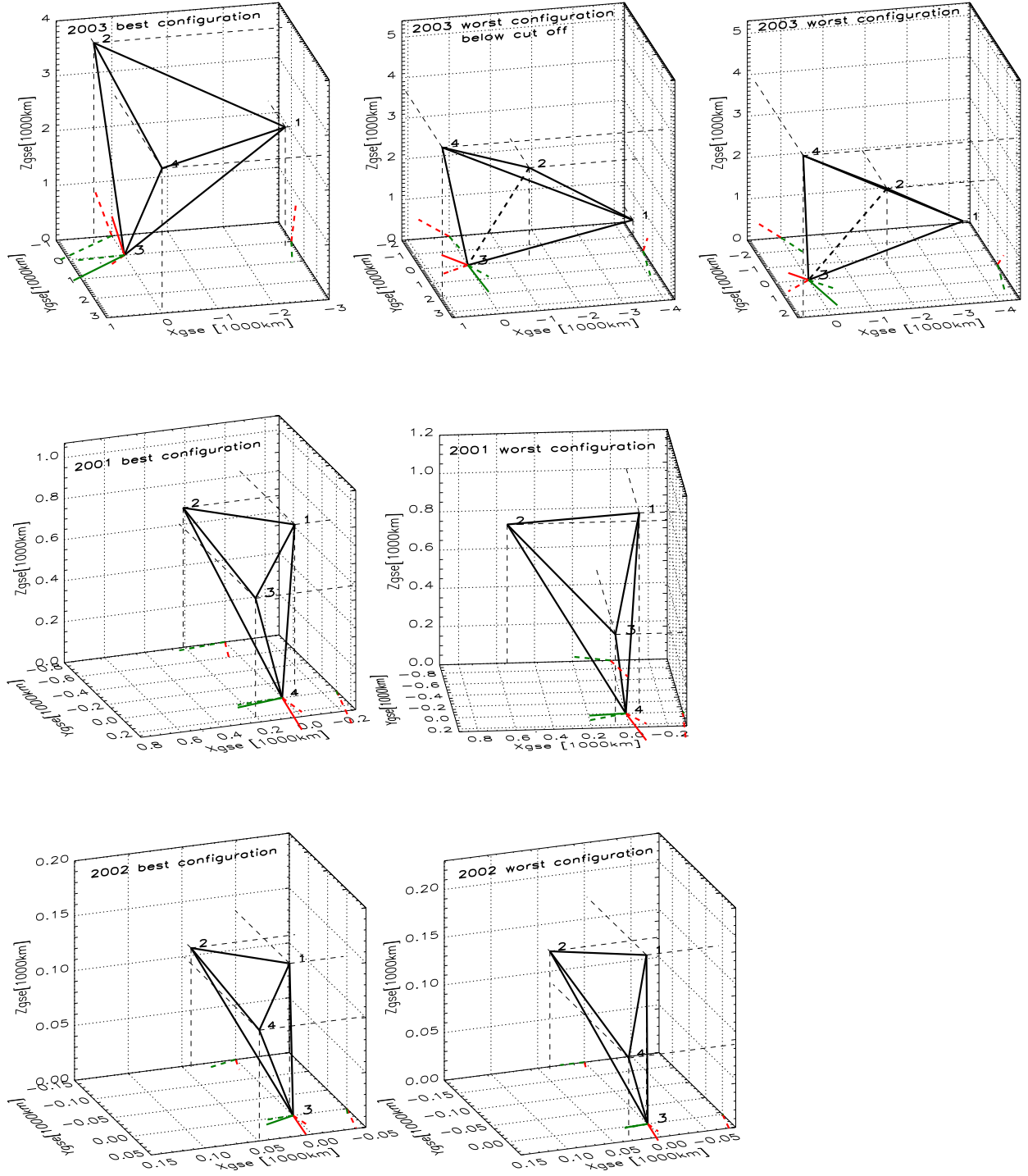


Figure 5.6: Extreme tetrahedra. From top to bottom: 2003, 2001, 2002 (descending order of size). The leftmost column shows the best configuration and the second column the worst configuration in terms of planarity P used for analysis in each year. The third tetrahedron in the top row is the flattest configuration observed at DD occurrence in 2003. Details of these tetrahedra are summarised in Table 5.2.

Table 5.2: Parameters characterising the seven tetrahedra shown in Figure 5.6. From top to bottom: day of year, side lengths D_{ij} , quality factors and semi-axes a , b and c of the ellipsoid describing the volumetric tensor. To identify the tetrahedra we use two letters defining their position in Figure 5.6, the first letter indicates the row (**T**op, **M**iddle, **B**ottom), and the second letter indicates the column (**R**ight, **M**iddle, **L**eft). The spacecraft separations and the lengths of the semi-axes are given in km.

	TL	TM	TR	ML	MR	BL	BR
doy	22	44	30	53	34	52	54
D_{12}	3659	3556	3982	827	1100	137	185
D_{13}	3604	4404	5180	479	649	136	173
D_{14}	3659	7192	8162	828	1028	81	106
D_{23}	3737	2724	2759	1066	1303	182	225
D_{24}	3674	3728	4181	1069	1309	182	224
D_{34}	3751	4542	4592	699	553	120	99
E	0.029	0.546	0.597	0.281	0.337	0.300	0.351
P	0.025	0.797	0.989	0.578	0.718	0.571	0.718
Q_{GM}	2.998	1.844	1.565	2.489	2.243	2.480	2.231
Q_{SR}	0.959	0.273	0.204	0.511	0.425	0.500	0.416
Q_{R8}	1.000	0.188	0.009	0.608	0.408	0.604	0.400
Q_{RR}	0.999	0.132	0.002	0.745	0.666	0.719	0.660
a	1338	2543	2892	412	521	70	89
b	1299	1155	1164	296	345	49	58
c	1267	235	13	125	97	21	16

isotropic to almost totally flat (P ranges from 0.03 to 0.99) in 2003, the solar wind configurations are all similar in 2001 and 2002. The extreme cases in terms of E and P are shown in the middle (2001) and in the bottom (2002) row of Figure 5.6. The “archetype” is a relatively flat “wedge” with the small side 1 – 3 – 4 extending approximately in the z -direction. Especially in 2002 the northernmost spacecraft (always Cl 1) is located almost directly above the southernmost spacecraft (always Cl 3 in 2002 and Cl 4 in 2001). Cl 2 is displaced far in the negative y -direction (see also D_{23} and D_{24} in Table 5.2). Again, the projections on the walls of the bounding box help visualising this.

Figure 5.7 demonstrates that the shown examples for the years 2001 and 2002 are in fact typical for the whole reservoir of tetrahedra we use in these two years. Shown are the spacecraft coordinates relative to Cl 4 at the time of DD occurrences. Note that the abscissa is not continuous in time. Discontinuous jumps in the coordinates are related to long gaps between DD occurrences, appearing e.g. when Cluster is in the magnetosphere. Over the course of the solar wind period⁵ the relative positions are fairly constant near apogee (i.e., in the solar wind) and the sequence of spacecraft is always the same in the y - and the z -direction. Cl 4 is furthest to the south followed by Cl 3, Cl 2 and Cl 1 in 2001. In the positive y -direction we find consecutively Cl 2, Cl 1, Cl 4 and Cl 3, where Cl 2 is largely separated from the others

⁵The apogee of the Cluster orbit is on the day-side of the magnetopause approximately from January until May (see chapter 4).

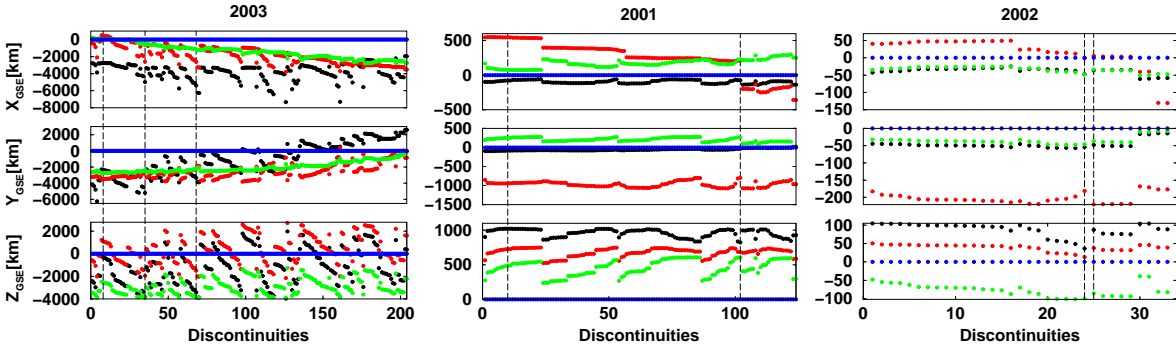


Figure 5.7: Spacecraft positions relative to Cl 4 for all DDs in the order of temporal occurrence. From top to bottom the x , y and z -components are shown. From left to right: 2003, 2001, 2002 (decreasing order of tetrahedron size). The typical colours for the individual spacecraft are used (Cl 1: black, Cl 2: red, Cl 3: green, Cl 4: blue). The dashed vertical lines indicate the tetrahedra shown in Figure 5.6. The specific tetrahedra can be identified using the doy given in Table 5.2.

(≈ 1000 km), yielding the direction of elongation. Note that Cl 1 and 4 are very close to each other in the $x - y$ plane and largely separated in the z -direction (as in Figure 5.6). A constant ordered sequence is also observed in the x -component, apart from Cl 2. Over the course of the solar wind period the relative position of this spacecraft changes from being closest to the Sun (largest x -component) to being closest to Earth. This corresponds to a clockwise rotation of the tetrahedron about the z -axis in the GSE system, i.e., approximately about the edge 1 – 4. This can also be seen in Figure 5.6. Whereas Cl 2 is clearly the furthest to the Sun on doy 34 (right tetrahedron), its x -component is close to that of Cl 3 on doy 53 (left tetrahedron). Apart from the exchange of Cl 3 and Cl 4 the geometry of the spacecraft constellation is qualitatively the same in 2002 (see Figure 5.7 (right)). Thus, the general shape of the tetrahedra present in our analysis in 2001 and 2002 is well represented by the extreme configurations shown in Figure 5.6.

Because of the large separation distances the variability of the tetrahedron shape is much greater in 2003. However, some regularities can be found also. For instance, Cl 1 is generally located closest to Earth (see Figure 5.7 (left)). Over the course of the year this spacecraft rotates clockwise about the GSE z -axis (increasing y -component and decreasing x -component), similar to Cl 2 in 2001 and 2002.

The parameters characterising shape, orientation and location of all tetrahedra associated with the 366 DDs are shown in Figure 5.8. The format is the same as in Figure 5.5. As noted above, the shape and the orientation of all tetrahedra are similar to each other in 2001 and 2002, whereas large fluctuations between the various events are observed in 2003. Hence, the above definition of a flattened “archetype” of all tetrahedra in 2001 and 2002 is indeed justified. Note that the order of side lengths is generally the same for all events, e.g. D_{24} (D_{23}) is always largest in 2001 (2002). The only exception is the smallest side length. It is alternately D_{34} and D_{13} in 2001 and D_{34} and D_{14} in 2002, i.e., the position of Cl 3 (Cl 4) moves “up and down” relative to Cl 1 and Cl 4 (Cl 3) (cf. Figure 5.6). The spacecraft separations differ strongly from DD to DD in 2003, especially D_{14} . This side basically determines the degree of regularity of the specific tetrahedra (see also Figure 5.6); the spread of the semi-axes lengths correlates to the fluctuations of D_{14} . The minor semi-axis c is particularly small, the major semi-axis a large, and the volume is small, whenever D_{14} is large. Consequently, all quality

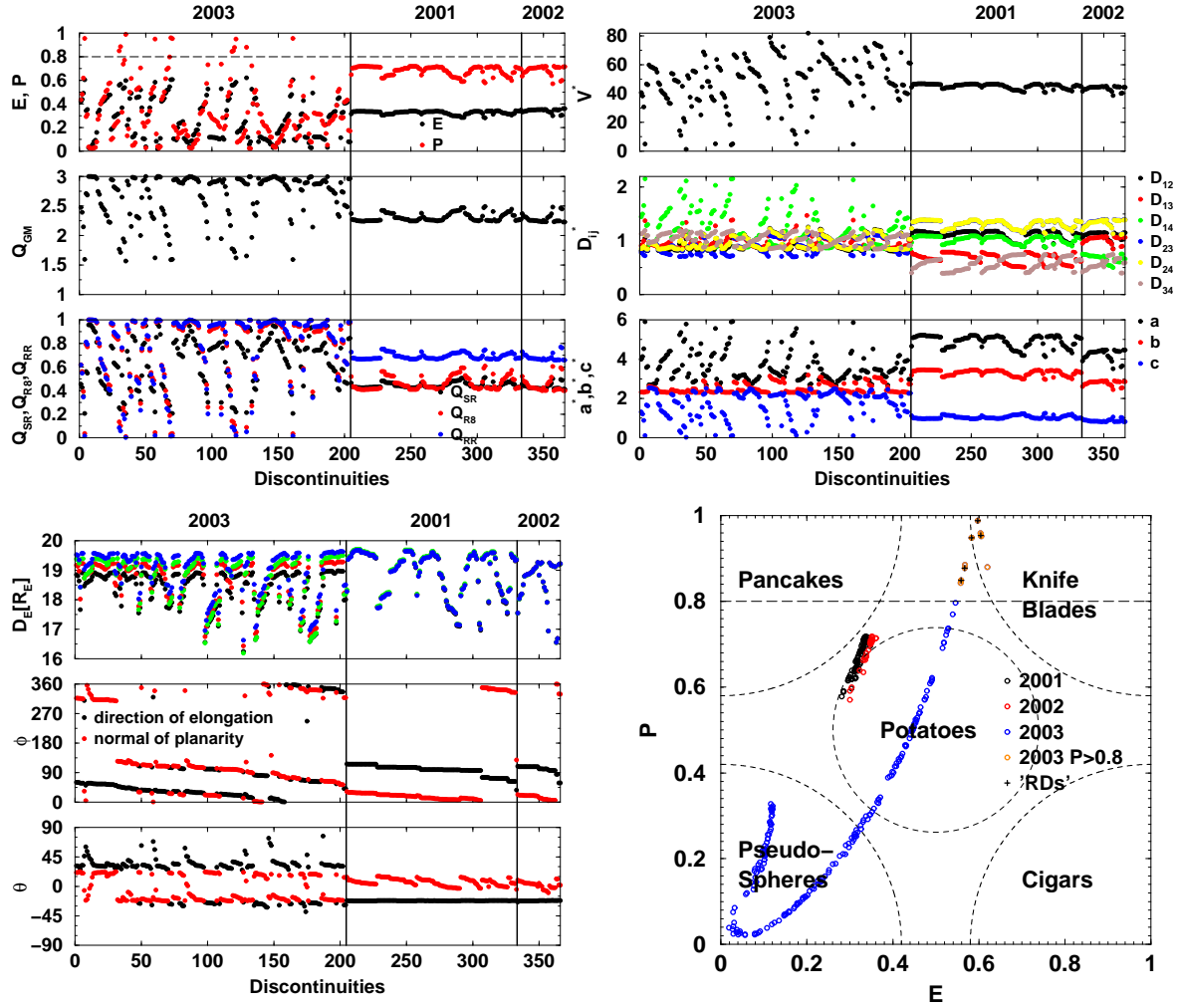


Figure 5.8: Parameters characterising shape, orientation and location of the tetrahedra used in our analysis. The format is the same as in Figure 5.5. The three sets of DDs found in the different years are separated by the vertical lines. From left to right, the sets from 2003, 2001 and 2002 are shown, i.e., sorted according to the tetrahedra sizes. The DDs of each set are plotted in their order of occurrence. The parameters shown in the upper right plot are scaled for better comparison. The unit of V^* is 10^8 km^3 for the events in 2003, 10^6 km^3 for 2001 and 5000 km^3 for 2002. The spacecraft separations D_{ij}^* are scaled by the average distance, i.e. $D_{ij}^* = D_{ij} / \langle D_{ij} \rangle$, where the average is over all six pairs and all events in the respective set. The three values of $\langle D_{ij} \rangle$ are given in Table B.1. The unit of the semi-axes lengths a^* , b^* and c^* is 500 km for the events in 2003, 100 km for 2001 and 20 km for 2002. In the upper left and in the lower right plot the value of $P_c = 0.8$ is indicated by the horizontal line.

factors indicate degenerated tetrahedra for these events. For most events, however, the value of D_{14} is similar to the other side lengths, and thus a , b and c have similar values, indicating regular tetrahedra. The absolute value of c is of some importance for the error analysis (see below). Whereas it only barely fluctuates around 100 km in 2001 and around 20 km in 2002, c ranges between 13 and 1267 km in 2003.

The relatively constant semi-axes and tetrahedra volumes yield barely fluctuating quality factors for the events in 2001 and 2002. The planarity ($\langle P \rangle = 0.68$) is approximately twice as large as the elongation $\langle E \rangle = 0.33$ for most events in these two years. The average value

of Q_{GM} is 2.31 in 2001 and similar in 2002. The fluctuations of the quality factors are much larger in 2003. However, for most events E and P are small. The average values are $\langle P \rangle = 0.32$ and $\langle E \rangle = 0.27$. Also, $\langle Q_{GM} \rangle = 2.68$ and the abundance of values close to 3 indicates a predominance of rather regular tetrahedra during DD observation in 2003. Note that whereas Q_{R8} and Q_{RR} vary over the total range from 0 to 1, $Q_{SR} > 0.2$ for all DDs. This is because the elongation is never extreme.

The distance D_E of the Cluster spacecraft to Earth ranges roughly between 16 to 20 R_E for the events considered in our analysis. The spacecraft separations are large enough to resolve the individual satellite positions in 2003 on the scale in Figure 5.8. The sequence of spacecraft according to D_E is mostly the same, with Cl 1 being closest to Earth and Cl 4 furthest away from Earth.

The direction of elongation and of the normal of planarity vary both, within a single orbit (see also Figure 5.5) and over the course of the solar wind period. The general trend is indeed a decrease in ϕ , i.e., a clockwise rotation about the GSE z -axis within all three years. Note that in 2003 there are some large jumps in ϕ and θ from one DD to the next. These events are widely separated in time. More important, the tetrahedra with deviating orientation are all close to regularity, i.e., \mathbf{R}^a and \mathbf{R}^c are somewhat ambiguous in these cases. In any case, considering all 366 DDs, the normal of planarity covers all azimuthal directions. (Note that rotating the normal of planarity by 180° does not change the orientation.)

In order to quickly characterise the shape of the tetrahedra we are facing, a more concise representation is the E - P diagram (lower right of Figure 5.8). The locations of the five general ellipsoid shapes defined in section 5.2 are indicated. The tetrahedra associated with the DDs found in 2001 and 2002 are all confined to a small area ($P \in [0.58, 0.72]$, $E \in [0.28, 0.35]$ for the tetrahedra in 2001 and $P \in [0.57, 0.72]$, $E \in [0.30, 0.36]$ for the events in 2002). Note that although the scatter is much larger for the events in 2003, especially regarding planarity, the distribution is confined close to a single path in the E - P space with one end in the “pseudo-spheres” region and the other end in the “knife blades” region. The values of E and P are correlated, i.e., the tetrahedra with small P also have small values of E , and those being very flat are also the most elongated ones. There are no “pancake” or “cigar” like configurations in our data set. Thus, we are in the convenient situation not being forced to ban many events because of awkward spacecraft constellation. The dashed vertical line indicates P_c . The tetrahedra above this line are marked orange, denoting the events we treat with extra caution. The meaning of the black crosses will be explained in a later chapter. The majority of tetrahedra, however, is located in the opposite corner, in the “pseudo-spheres” region.

This means that the prevailing configurations in 2003 are much more regular than the “worst configuration below cut-off” presented in Figure 5.6. Figure 5.9 (left) shows a histogram of the values of E and P in 2003. There is a group of nine tetrahedra with $0.69 < P < 0.80$, 13 fail the constraint $P < P_c$ (see also the E - P diagram in Figure 5.8). The remaining 182 constellations have $P < 0.62$, and for 139 tetrahedra (68% of all events in 2003) the planarity is even $P < 0.34$. Thus, if we were to name a typical configuration prevailing during DD observations in 2003 this would be an almost regular tetrahedron comparable to the “best configuration” in Figure 5.6.

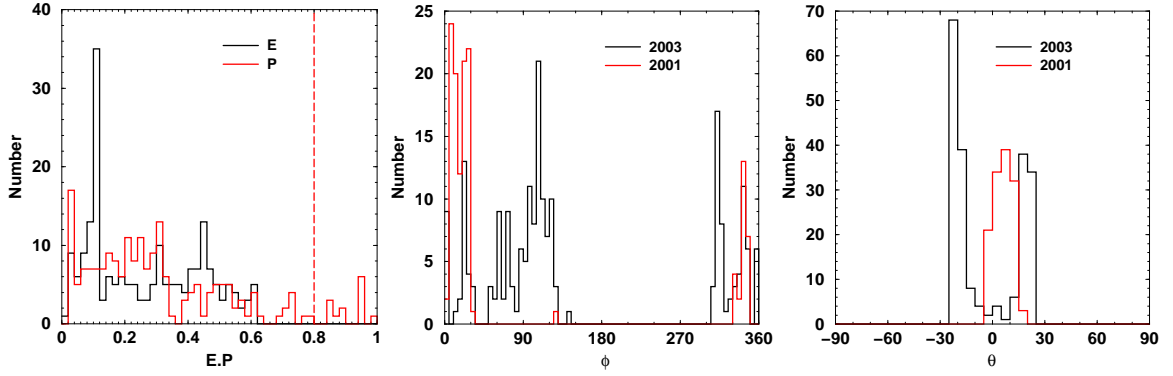


Figure 5.9: Histograms of the values of E (black) and P (red) for 2003 (left), and of R_ϕ^c (middle) and R_θ^c (right) for 2003 (black) and 2001 (red).

For the other rather flat configurations the normal of planarity is variable. Figure 5.9 (middle and right) shows histograms of R_ϕ^c and R_θ^c for the events in 2003 and in 2001⁶. This direction is always close to the ecliptic ($|\theta| \leq 25^\circ$ for all DDs). The normals of planarity are even more concentrated around zero with a tendency toward positive values in 2001 ($\theta \in [-5^\circ, 20^\circ]$). For the majority of events $-25^\circ \leq \theta \leq -15^\circ$ in 2003, another peak is between $\theta = 15^\circ$ and $\theta = 25^\circ$. For the total of the 366 DDs the whole range $-25^\circ \leq \theta \leq 25^\circ$ is quite well covered. For the vast majority of events $\phi = 0^\circ \pm 30^\circ$ in 2001, with a maximum in the interval $[5^\circ, 30^\circ]$. Thus, generally the normal of planarity is indeed roughly aligned with the GSE x -axis in 2001. The angle ϕ varies between 305° and 145° in 2003. Therefore, all possible orientations in the ecliptic projection are represented. The distribution is not uniform, however. For the majority of events $\phi \in [50^\circ, 140^\circ]$, i.e., the normal of planarity is roughly aligned with the GSE y -axis for these events and therefore approximately perpendicular to the prevailing direction in 2001.

It is important to be aware of the variability of \mathbf{R}^c since the error in DD normal determination from relative timings is largest in the direction normal to planarity (see section 7.4.2 and chapter 9). Thus, the error is generally not isotropic, i.e., it cannot be visualised as a cone with a circular base. Instead, the base is degenerated to an ellipse. For the discussion of our results it is also important to note that the orientation of the tetrahedra is not related to the direction of the IMF. The latter is described by the Parker spiral in long time averages, but is locally undetermined. Therefore, no systematic bias is introduced due to irregular tetrahedra when we relate the DD normals determined from relative timings to the local magnetic field.

So far we have mainly focused on the shape and the orientation of the configurations. Another important factor affecting the precision of multi-spacecraft analysis results is the size of the tetrahedra related to the scale of the physical structures studied. The average separations for the constellations used in our analysis are $\langle D_{ij} \rangle = 160$ km, 940 km and 3860 km in 2002, 2001 and 2003, respectively, where the average is taken over all six pairs of spacecraft and over all events in the particular year.⁷ The average separation is about 1/20 of the median DD thickness in 2002. In fact, the complete Cluster array is inside the transition layer simultane-

⁶From Figure 5.8 it can be seen that the range of values in 2002 is similar to the range in 2001. Therefore we do not show the 2002 events.

⁷In appendix B a listing of the minimum, maximum and average separation distance for each of the six pairs of spacecraft is given.

ously for a large fraction of the traversal time for all 33 events. The extension of the array exceeds the DD thickness for a significant number of events in 2001. However, the average separation is still below the median value of the DD thickness in this year. The largest separation ($D_{24} = 1309$ km) observed in 2001 approximately equals the median value. Finally, the largest side lengths are given in 2003. Here even the smallest observed spacecraft distance ($D_{23} = 2704$ km) is larger than the median DD thickness, i.e., in most cases individual spacecraft are inside the transition zone during disjoint time intervals. Note that the relative timing method gains precision with increasing absolute values of the time differences.⁸ Thus, in addition to the generally more regular shape of the tetrahedra, the large spacecraft separations favour good quality multi-spacecraft results for the events in 2003.

It is also important to compare the thickness $2c$ of the tetrahedron in the direction normal to planarity (\mathbf{R}^c) to the accuracy of orbit determination (see section 5.2). The tolerance of the satellite separation distances is 10 km for separation distances less than 1000 km and 1% for separation distances greater than 1000 km [DDID, 2000]. Comparison with the values in Table 5.2 shows that even the minimum values of $2c$ occurring in our analysis exceed the error in position.

We close this chapter with a final remark on the tetrahedra presented in this last section. The positions of the four spacecraft are taken for each of them at the time when it crosses the DD. Therefore, they form a tetrahedron which does not correspond to any instantaneous configuration of the array. However, typical time lags between occurrence at the four spacecraft range from tenths (2002) to tens (2003) of seconds. With the typical spacecraft velocity of approximately 1 km/s near apogee, the difference between the fictitious and the real configurations is small.

⁸This statement applies to the separation scales considered in this work. For larger separations e.g. the validity of the assumptions for the relative timing method to be applicable must be scrutinised more carefully.

THE SET OF DISCONTINUITIES USED IN THIS WORK

This chapter consists of two parts. The purpose of the first part (sections 6.1-6.4) is to present how the set of DDs used in our subsequent analysis is selected and to present the selection results. The second part (section 6.5) is motivated by the observational result that the frequency of occurrence of RDs and the ratio of the number of RDs to the number of TDs are both considerably larger in the fast solar wind originating from coronal holes on the Sun (see chapter 3). In order to test this hypothesis with the enhanced possibilities of the Cluster mission we divide the set of DDs identified in sections 6.1-6.4 according to their origin on the Sun. In particular we prove the existence of a considerable subset of DDs embedded in solar wind originating from coronal holes.

The selection of events consists of four successive steps: (1) The identification of periods when the apogee of the Cluster orbit is on the day-side of the magnetosphere. This is the case from December until June (see chapter 4), however, appreciable intervals with Cluster in the solar wind are observed only from January until May in each year. (2) The identification of intervals during which all four spacecraft simultaneously measure solar wind data within each orbit (section 6.1). (3) An automated search for DDs using established algorithms (section 6.2 and 6.3). (4) Ensure that the found DDs are free of foreshock activity (section 6.4).

In addition to these four steps we visually inspect each of the DDs in the resultant set after performing step (4). As a final step (not subject of this chapter) we discard events that are likely to be subject to large errors when the analysis methods described in the following chapter are applied to them.

6.1 Solar wind periods

Since Cluster is primarily a magnetospheric mission, only a small part of the orbit traverses the solar wind. We use Cluster data from 1 February 2001 (beginning of the scientific data recording on board the Cluster spacecraft) until the end of the solar wind part of the Cluster orbit in 2003. According to step (1) we thus identify three periods with the apogee of the Cluster orbit being on the sunward side of the magnetopause in this time interval, namely one at the beginning of 2001, one at the beginning of 2002 and one at the beginning of 2003. The last period also contains some days at the end of 2002. Table 6.1 shows the first and the last day, the number of days and the total time with all four Cluster satellites simultaneously providing solar wind magnetic field data in each of these three periods. The solar wind intervals are identified by “eye-balling” the magnetic field data, and are taken from one outbound bow shock crossing to the following inbound bow shock crossing. In these parts of the orbit we search for intervals with simultaneous measurements. Each day providing a considerable amount of time with simultaneous measurements contributes to the number of days in the fourth column in Table 6.1, and the total time shown in the fifth column is the sum of all intervals with simultaneous measurements. Note that the first two periods (2001 and 2002) suffer from extended data gaps for one or more satellites. At the end of the year 2002 the data coverage was extended from 50% to 100%. Therefore, the total time with all four spacecraft simultaneously measuring solar wind magnetic field data is almost by an order of magnitude larger in the third period (2003) as compared to the other two periods. Figure 6.1 gives a detailed overview of the times with all four spacecraft measuring solar wind magnetic field data on a daily basis. It clearly shows that particularly the second period (2002) suffers from bad data coverage. Useful intervals are usually short in duration, making the identification of suitable DDs for our analysis difficult in this period.

Note that the solar wind intervals discussed above are preliminary, since the only two requirements for identifying them are (1) all four satellites are sunward of the bow shock and (2) all four FGM instruments simultaneously deliver data. Foreshock activity has not been accounted for so far.

The next step, step 3, is to run automated search algorithms for DDs on the identified solar wind periods. This procedure is detailed in the following two sections.

Table 6.1: First and last day, number of days and total number of hours with all four spacecraft providing simultaneously solar wind magnetic field data for each of the three periods identified. “name” denotes the name of the set of DDs that we identify in the respective periods.

name	first day	last day	# days	time [h]
<i>DD</i> ₂₀₀₁	3 Feb 2001	23 Apr 2001	22	274
<i>DD</i> ₂₀₀₂	12 Jan 2002	23 Apr 2002	23	170
<i>DD</i> ₂₀₀₃	27 Dec 2002	30 Apr 2003	82	1120

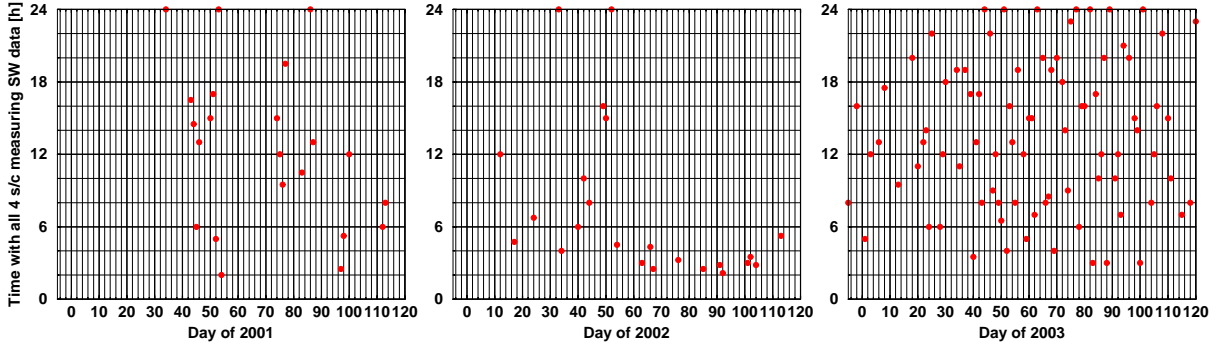


Figure 6.1: Overview of days suitable for solar wind analysis with Cluster. Shown is the time with all four spacecraft simultaneously measuring magnetic field solar wind data for each of these days. Note that the third period (right) also includes two days at the end of 2002. Days left of day “zero” denote the last days of 2002, e.g. day “-1” of 2003 corresponds to 31 December 2002.

6.2 Search criteria

Several similar criteria for detecting solar wind directional discontinuities (DDs) have been published in the past [Siscoe *et al.*, 1968; Burlaga, 1969a; Mariani *et al.*, 1973; Tsurutani and Smith, 1979; Lepping and Behannon, 1986]. They have in common that a sharp change in the magnetic field embedded in a comparatively quiet background is identified. The two most commonly used techniques in statistical studies, similar to ours, are those developed by Tsurutani and Smith [Tsurutani and Smith, 1979] (in the following referred to as TS) and Burlaga [Burlaga, 1969a] (referred to as B). Other authors use methods which are almost identical to either one of the two techniques. For instance, Belcher [1975]; Barnstorf [1980] use methods nearly the same as the B-method. More recent studies most often use the TS-method [Neugebauer *et al.*, 1984; Horbury *et al.*, 2001b]. In order to provide consistency with these earlier works we also use the B- and the TS-method. They will be described in the following.

Tsurutani and Smith [1979] introduce four principal requirements for a selection method:

- (1) The criteria should be as similar as is possible to those used in previous DD studies to allow for comparison.
- (2) The criteria should not bias against DDs occurring in regions characterised by weak magnetic fields. This constraint is necessary both because of the variability in field strength with radial distance from the Sun and because of the time variability of field strength at a given heliocentric distance.
- (3) The criteria should not bias against any type of DD, i.e., either RDs or TDs.
- (4) The criteria should be implementable on a computer to eliminate human error and to allow processing of large data sets.

The TS-method consists of three criteria [Tsurutani and Smith, 1979] which we denote by TS1-TS3. Tsurutani and Smith [1979] apply them to data averaged over 60 s.

$$\text{TS1: } |\Delta \mathbf{B}| \geq B_{\max}/2$$

$$\text{TS2: } |\Delta \mathbf{B}| \geq 2\delta, \quad \text{with } \delta^2 = \max\left(\frac{1}{5} \sum_{j=i-k-4}^{i-k} |\mathbf{B}_j - \mathbf{B}_{j-1}|^2, \frac{1}{5} \sum_{j=i}^{i+k} |\mathbf{B}_{j+1} - \mathbf{B}_j|^2\right)$$

TS3: Discontinuities are separated by at least 3 min.

The main criterion TS1 states that the magnitude of the vector change $|\Delta \mathbf{B}| = \mathbf{B}_i - \mathbf{B}_{i-k}$ across the DD exceeds one half the larger of the field magnitudes on either side of the DD. Based on an empirical evaluation of the effect of varying k , *Tsurutani and Smith* [1979] find $k = 3$ to be a nearly optimum choice. Choosing $k < 3$ would not allow for the identification of thick DDs, and choosing $k > 3$, field changes other than discontinuities, such as Alfvén waves, tend to be misinterpreted as discontinuities. TS2 ensures that the vector jump across the DD is large in comparison with the general level of vector fluctuations on either side of the DD. The fluctuation level is measured as the root mean square of the magnitude of the field changes adjacent to the DD. Vector field changes between five successive vectors following \mathbf{B}_i and preceding \mathbf{B}_{i-k} are used. TS3 is a consequence of a need to detect relatively thick DDs as well as thin DDs. To ensure that a thick DD is not detected more than once, it is required that adjacent DDs are separated by three minutes.

The main criterion of the B-method coincides with the definition of a DD (section 3.1), i.e., a rotation of the magnetic field vector by more than 30 degrees in less than 30 s [*Burlaga*, 1969a]. Three further criteria ensure among others that the fluctuations in the vicinity of the DD are small. We denote the B-criteria by B1-B4. *Burlaga* [1969a] applies them to 30 s average data.

- B1: The angle ω between two successive field vectors must satisfy $\omega > 30^\circ$.
- B2: If criterion B1 is satisfied between the field vectors \mathbf{B}_1 and \mathbf{B}_2 then an average is computed for the two points preceding \mathbf{B}_1 and for the two points following \mathbf{B}_2 (data points marked by ovals in the upper left part of Figure 6.2). The angle $\bar{\omega}$ between these two average values must also satisfy $\bar{\omega} > 30^\circ$. This procedure eliminates noise points and highly disturbed regions.
- B3: The DDs obtained by step B1 are classified in single, double, triple and higher multiples (see Figure 6.2). A single is simply a $> 30^\circ$ change in field direction which occurs in 30 s. These are most common. A large number of DDs obtained in step B1 occur in pairs, i.e., two DDs occur separated by a 30 s interval. Such doubles, illustrated in Figure 6.2, can be considered a single DD. A double would be seen if a true DD occurred during a 30 s average of the field quantities. Therefore, both singles and doubles are regarded as true DDs. The method of computing $\bar{\omega}$ gives two values of $\bar{\omega}$ for a double: one computed from the ovals in Figure 6.2 and one from the squares. A further requirement for doubles is that these two angles are equal within 15° . Triples and higher multiples are eliminated from the set obtained in step B1. They could be the result of several closely spaced DDs or a large gradient.
- B4: Discontinuities which are separated by less than four data points (i.e., 2 minutes when 30 s averages are used) are disregarded.

Following *Söding* [1999] we apply the B-method to 60 s average magnetic field data to provide better consistency among the two techniques. As a final check, the selected DDs are individually inspected, and ambiguous DDs are eliminated.

In order to compare the two methods, it is instructive to consider the case of a constant magnetic field magnitude ($B_1 = B_2 = B_{max}$). In that case TS1 can also be written as $\omega \gtrsim 28.96^\circ$,

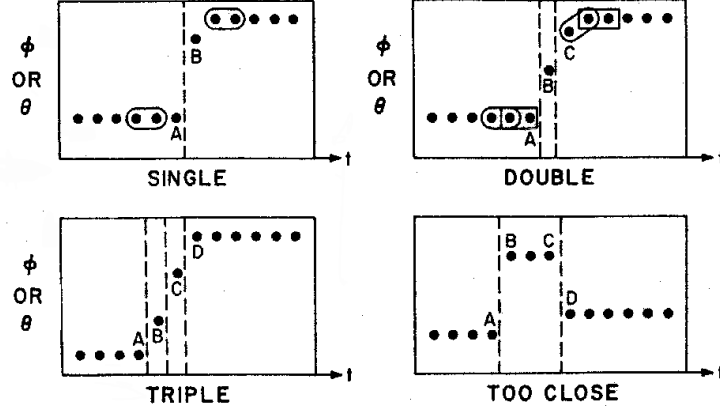


Figure 6.2: Illustration of the B-method. Each point represents an average value. $A \hat{=} B_1$, $B \hat{=} B_2$. Taken from Burlaga [1969a].

i.e. TS1 would select slightly more events as potential DDs than B1 ($\omega > 30^\circ$). Note that in most cases the change in magnitude across DDs is in fact rather small [Siscoe *et al.*, 1968; Burlaga, 1969a; Smith, 1973a]. However, in contrast to B1, TS1 also selects events with smaller angular change provided that the field magnitude changes. Hence, the criterion TS1 is more general than B1: all DDs that satisfy B1 also satisfy TS1, but not vice versa. The crucial difference is that B1 only accounts for directional changes, whereas TS1 also accounts for changes in the field magnitude. In addition, the B-method is incapable of detecting thick DDs, because ω is measured between two consecutive field vectors, whereas $|\Delta \mathbf{B}|$ is computed using vectors separated by 3 min in the TS-method.

However, due to the differences in the additional criteria, the B-method can identify DDs that are rejected by the TS-method. For example, the avoidance of DDs embedded in a strongly fluctuating background field is realised by different means. It appears that the restriction TS2 using five data points on each of the two sides of the potential DD is stronger than B2 where only two data points are used on either side. A structure that satisfies B2 but not TS2 certainly exists.

Note that the threshold values in both the TS- and the B-method are empirical and not based on physical discontinuity models. In particular the threshold spreading angle of 30° is arbitrary. The TS-method ostensibly avoids this arbitrary threshold angle. However, since significant changes in the field amplitude are rare, the TS1 effectively corresponds to $\omega \gtrsim 30^\circ$.

For multi-spacecraft observations, an additional complication is that a DD has to be simultaneously detected at all four spacecraft. Since the separation between the Cluster spacecraft is relatively small it is unlikely that a DD is only observed at some of the spacecraft but not at the others. Nevertheless, detection of a DD at one spacecraft but not at another does happen. However, the explanation is usually not the tempting conclusion of having found a genuine “edge” of a DD, but an artifact of the thresholding in the TS- or B-method. The measured values at one spacecraft may be marginally above the threshold values, but marginally below at another.

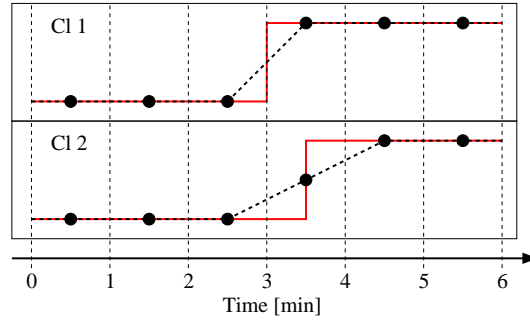


Figure 6.3: Problem of simultaneous identification of a DD at different spacecraft due to differing averaging intervals. Shown are hypothetical magnetic field data measured at two spacecraft (CI 1 top and CI 2 bottom). The red line indicates high resolution data, and the black circles are 60 s averages. These are connected by the black dashed line. Each of these average values is obtained by averaging the high resolution data bounded by the vertical dashed lines.

We define a DD to be observed simultaneously at two or more spacecraft if a DD is detected at these spacecraft within one minute (or within ± 1 data point). Hence, if at CI i a DD is identified at the k 's data point of the day and at CI j a DD is identified at data point $k - 1$, k or $k + 1$, then we say this DD is simultaneously found by spacecraft i and j . This definition is reasonable, because (1) we do not observe time lags > 1 min and (2) according to TS3 and B4 confusion between different DDs is not possible.

Because a DD sampled in high time resolution may have a different appearance when averaged over chronologically shifted 1 min intervals the time lag may be another reason for detecting a DD at one spacecraft but not at another. Figure 6.3 illustrates the problem. An infinitely thin DD which appears as a sharp jump in high resolution data (red line) is considered. We assume the time lag between CI 1 and CI 2 to be exactly 30 s. Finally, the time grid is such that at CI 1 the 60 s averaging interval of the last averaged data point before the DD lies completely on the “left” side of the DD, and the entire interval used to obtain the first 60 s average field vector after the DD lies on the “right” side. Let us assume the field rotates by an angle $\omega = 40^\circ$ across the DD. Then, the DD appears as a “single” DD at CI 1, i.e., the rotation takes place exactly between two data points. Due to the 30 s time lag one of the 60 s average data points is centred at the time where the true transition takes place at the position of CI 2. For that data point one half of the averaging interval is on one side and the other half on the other side of the DD. Therefore the DD appears thicker at CI 2 than it does at CI 1. The 40° rotation is split into two 20° rotations. Thus, the DD would fail the B1 criterion at the position of CI 2.

Since generally the time lags we observe are much smaller than 30 s (the average values in our analysis are 0.1 s in 2002, 1.3 s in 2001 and 5.11 s in 2003) we do not expect this effect to be crucial. Nevertheless, shifted averaging intervals may cause small differences in the individual time series which particularly for marginal cases can be decisive for whether or not a DD is identified.

Due to the additional constraint that a DD must be identified at all four spacecraft, our selection process is stricter than application of the TS- or the B-method to a single spacecraft.

6.3 Application of the search criteria

We independently apply both criteria, TS1-TS3 and B1-B4, to data from the intervals with simultaneous solar wind measurements at all four spacecraft. We find that in the majority of events a DD is detected consistently at all four spacecraft, at least by one of the two methods. This section provides a statistical analysis of the events where a DD is only identified by one of the two methods or only at some of the four spacecraft. Furthermore, we show that our data is consistent with previous reports if interpreted as single-point observations.

Figure 6.4 shows the total number of DDs identified in each of the three periods separately for the TS-method (left) and the B-method (right). On the right hand side of each plot the identification results for the individual satellites Cl i are shown. Note that the total number of DDs found is almost the same at each satellite, i.e., there is no bias as expected for equal spacecraft. However, the DDs identified at the individual spacecraft are not always identical. The left side of the plots in Figure 6.4 shows the number of DDs detected simultaneously at all four spacecraft (4sat), at exactly three spacecraft (3sat), at exactly two spacecraft (2sat) and at exactly one spacecraft (1sat). For the majority of events a DD is identified simultaneously at all four spacecraft. Otherwise a DD is most likely to be observed at exactly one spacecraft. Apart from the B-method in 2002 the least probable scenario is that two spacecraft identify a DD, whereas the other two do not. This means that for the vast majority of events the identification criteria yield the same result at three or at all four spacecraft.

For our further analysis we only use those DDs that are found by at least one of the two methods simultaneously at all four spacecraft. In other words, the preselection consists of the set union of TS_4 and B_4 , where TS_4 is defined as the set of DDs identified simultaneously at all four spacecraft using the TS-method, and B_4 is defined accordingly. For the reminder of this thesis we do not distinguish by which method a DD has been identified. Therefore we want to state which method provides the majority of DDs. Table 6.2 gives an overview. The classification of the DDs contained in the set union $B_4 \cup TS_4$ into those DDs found by both methods ($B_4 \cap TS_4$) and those DDs found solely by one of the two methods ($TS_4 \setminus B_4$ and $B_4 \setminus TS_4$) is remarkably constant regarding the three solar wind periods. In agreement with the discussion in the previous section the TS-method yields most events of our preselection. Only $\approx 10\%$ are solely identified by the B-method, $\approx 63\%$ solely by the TS-method and $\approx 27\%$ by both.

Table 6.2: Cardinal numbers of $B_4 \cup TS_4$, $B_4 \cap TS_4$, $TS_4 \setminus B_4$, $B_4 \setminus TS_4$, TS_4 and B_4 . For the intersection $B_4 \cap TS_4$ and the difference quantities $TS_4 \setminus B_4$ and $B_4 \setminus TS_4$ the percentages of the set union cardinal number are given in brackets.

name	$B_4 \cup TS_4$	$B_4 \cap TS_4$	$TS_4 \setminus B_4$	$B_4 \setminus TS_4$	TS_4	B_4
DD_{2002}	372	100 (27%)	240 (64%)	32 (9%)	340	132
DD_{2001}	489	137 (28%)	310 (63%)	42 (9%)	447	179
DD_{2003}	2673	715 (27%)	1700 (63%)	258 (10%)	2415	973

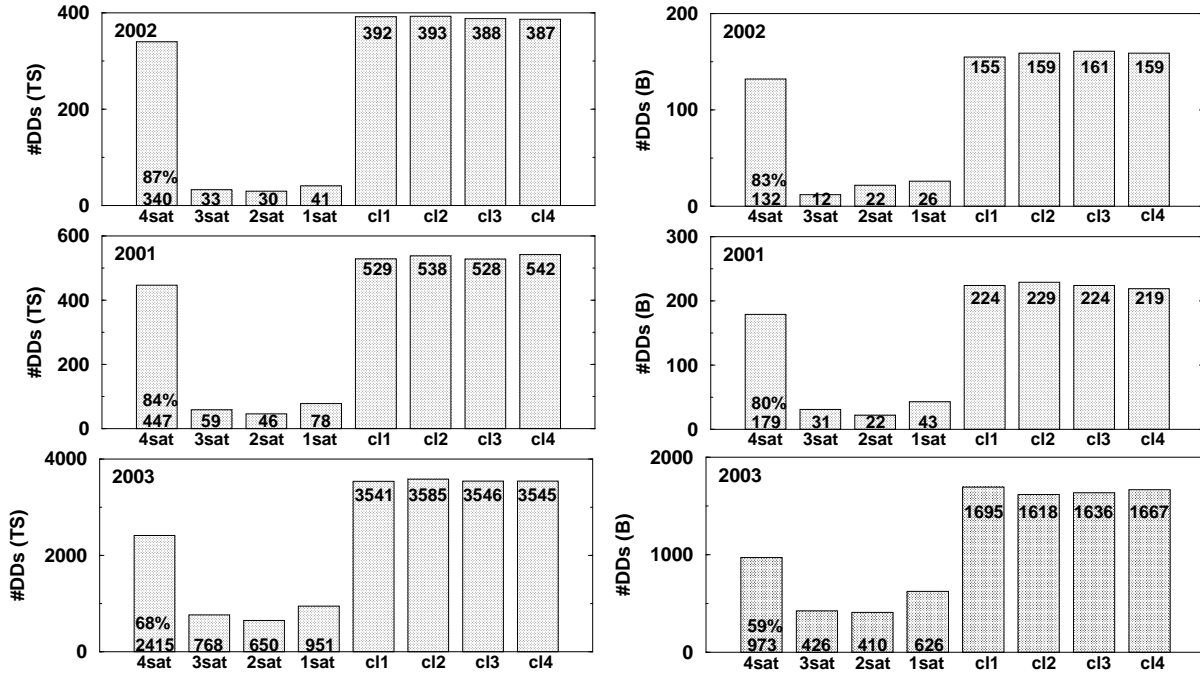


Figure 6.4: Number of DDs identified by the TS-method (left) and by the B-method (right) in each of the three solar wind periods of the Cluster orbit. The periods are sorted according to the spacecraft separation in the respective years, i.e., from top to bottom: 2002, 2001 and 2003.

Analysis of events identified by less than four spacecraft

In the previous section we have discussed possible reasons why a DD may not be identified by all four spacecraft. Consideration of the relative number of DDs simultaneously detected at all four spacecraft as a function of spacecraft separation offers some further insight: Figure 6.5 shows this relative number as a function of the nominal spacecraft separation for each of the three solar wind periods separately for the TS- and the B-method.

The figure shows, in agreement with the discussion in the previous section, that consistency among the four spacecraft is better for the TS-method than for the B-method. Due to the time lag a DD may appear differently at the various spacecraft when the field vectors are averaged over 60 s depending on the time of the true DD relative to the time grid. As a consequence B1 may be fulfilled at one spacecraft but not at another. Since $|\Delta \mathbf{B}|$ in TS1 is not computed from consecutive field vectors this effect is less relevant for the TS-method.

For both methods the consistency between spacecraft decreases with increasing separation as intuitively expected. The question is whether this dependence is a consequence of real spatial or temporal changes in the magnetic field structure or simply a result of increasing time lags with increasing separation. The effect of the time lags will undoubtedly be of some importance at 5000 km separation and noticeable at 600 km. However, at 100 km separation, the time lags are well below 1 s, and their effect cannot account for the increase from 0.83 (or 0.87) to 1.

Although we have not studied this quantitatively, it appears that many of the cases with different identification results at the different spacecraft are marginal, i.e the criteria are barely

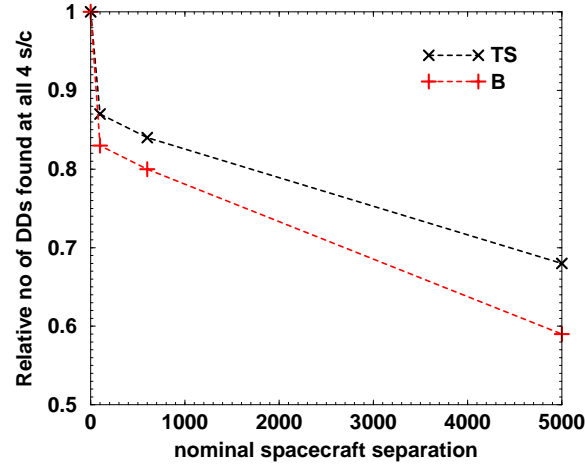


Figure 6.5: Relative number of DDs found simultaneously at all four spacecraft as a function of the spacecraft separation. Since measurement at the same point in space must yield identical search results we added the theoretical value $(0,1)$.

fulfilled at some spacecraft and barely not fulfilled at the others. In most cases, however, the main criterion (either TS1 or B1) is satisfied simultaneously at all four spacecraft, but the secondary constraints, in particular TS2 and B2, are fulfilled at some spacecraft and not fulfilled at the others. Hence, although it is tempting to draw conclusions regarding the true structure of the actual discontinuity from Figure 6.5, such as propositions on the lateral size, we abstain from doing so. A plausible conclusion is that the actual discontinuity is always observed at the location of all four spacecraft (apart from the artificially created discrimination in marginal cases), but due to differing appearances in the averaged data and due to differing levels of background fluctuations (to be accounted for by the criteria TS2 and B2) in marginal cases the detection is inconsistent. Both effects gain importance with increasing separations.

Note that we assume that the observed magnetic field structure is composed of an “actual discontinuity” and a certain level of background fluctuations. This type of model will be important in later chapters.

Also note that the DDs identified so far, though being sunward of the bow shock, could be subject to foreshock activity. Hence, background fluctuations not directly related to the actual discontinuities are likely to influence the results.

Consistency with previous single-point observations

Although the focus of this thesis is on four-point observations, it is useful to compare the acquired data to previous one-point observation studies to ensure consistency. The remainder of this section provides this comparison, treating each satellite as an independent mission.

According to previous studies [Burlaga, 1969a; Tsurutani and Smith, 1979] the TS-method identifies two events per hour on average whereas the B-method yields only about one DD per hour. Using each of the four Cluster satellites as a separate mission we find on average 1.95 DDs/h in 2001, 2.29 DDs/h in 2002 and 3.17 DDs/h in 2003 for the TS-method and

0.82 DDs/h in 2001, 0.93 DDs/h in 2002 and 1.48 DDs/h in 2003 using the B-method. These values are in good agreement with those found by *Burlaga* [1969a]; *Tsurutani and Smith* [1979]. Note that the occurrence rate fluctuates strongly from year to year. In particular relatively large values are found in 2003. In section 6.5 we will show that this is due to fast solar wind streams present in this year. This correlation between the solar wind speed and the occurrence rate is also consistent with earlier observations [*Burlaga et al.*, 1977; *Solodyna et al.*, 1977; *Barnstorf*, 1980; *Lepping and Behannon*, 1986]. Also in agreement with earlier studies [*Burlaga et al.*, 1977; *Tsurutani and Smith*, 1979; *Barnstorf*, 1980; *Lepping and Behannon*, 1986; *Tsurutani et al.*, 1994; 1995; 1996a; *Ho et al.*, 1996] we observe the occurrence rate to be highly variable from day to day (see section 6.5). Finally, the time difference between occurrence of two consecutive DDs is found not to be constant, even within one day. Instead, there is a tendency for DDs to occur in clusters [*Burlaga*, 1969a]. Although we have not quantified this, we consistently observe clustering.

Note, however, that Cluster is not suitable for that kind of analysis because the four spacecraft are not permanently in the solar wind, and the search results as presented in this section are still hampered by possible foreshock activity.

Also note that due to the additional constraint that a DD must be identified at all four spacecraft we only use a subset of the DDs identified at the individual spacecraft in our subsequent analysis.

To summarise, our single spacecraft results regarding DD occurrence are in good agreement with earlier studies: (1) The number density of identified DDs is not constant in time but fluctuates strongly from day to day. These fluctuations are correlated to the fluctuations of the solar wind speed. (2) The tendency of DDs to occur in clusters is also visible within one day and (3) a frequency of one (B-method) and two (TS-method) DDs per hour is observed on average. This consistency contributes to our argumentation that the ensemble of DDs used in our analysis does not differ statistically from those in earlier studies. We present further evidence in section 8.1.

We have shown that most DDs are simultaneously identified at all four spacecraft. The ratio of DDs simultaneously found at all four spacecraft to the average number of DDs identified at each single spacecraft decreases with increasing spacecraft separation. We suggest that this is partly due to the time lag between DD observations at the various satellites. A physical reason may be that the general level of vector fluctuations on either side of the DD differs considerably from spacecraft to spacecraft.

The total number of potential DDs identified for further analysis is 489 in 2001, 372 in 2002 and 2673 in 2003. Most of them ($\approx 90\%$) are identified by the TS-method. Although there were many more DDs visible at all four spacecraft than were identified by the TS- and the B-method, we use only these DDs to provide consistency with earlier work. The next step is to discard those DDs which are likely to be inside the Earth's foreshock region.

6.4 Avoiding foreshock activity - Final set of DDS

The DDS upstream (sunward) of the bow shock selected in the previous section cannot *a priori* be regarded as being free of any influence of the Earth. The region upstream of the bow shock and immediately downstream of the sheet of interplanetary magnetic field lines tangential to the bow shock is subject to disturbances. This region, magnetically connected to the bow shock, is referred to as the foreshock region.

As indicated in Figure 4.2 (section 4.2) Cluster only sporadically traverses the undisturbed solar wind. Large portions of the orbit upstream the bow shock are in the foreshock region. The careful selection of DDS in the undisturbed solar wind is the subject of this section.

Due to the interaction with the Earth's magnetic field the solar wind decelerates and flows around the magnetosphere. The bow shock is built where the transition from super-sonic to sub-sonic velocity takes place. The major part of the solar wind particles transmits through the bow shock into the magnetosheath. A small part ($\approx 1\%$), however, is reflected and moves along the field lines opposite to the solar wind flow direction with velocities two to three times the solar wind velocity [Tsurutani and Rodriguez, 1981]. For this reason interactions between the two populations and wave phenomena result. Since the interplanetary magnetic field is convected with the solar wind this region of disturbed solar wind (foreshock) can only be observed downstream of the sheet of interplanetary magnetic field lines tangential to the bow shock: While the particles move back towards the Sun the field lines they are attached to move downstream towards Earth [Scholer, 1991]. Therefore this curved surface is called foreshock border. It is guaranteed that on the upstream side of this border no foreshock activity takes places. Note that since the reflected particles are not infinitesimally fast, the true border is closer to Earth. The angle between the theoretical and the true foreshock border depends on the particular species being reflected. Since electrons are faster than ions, this angle is larger for the ion foreshock border than it is for electrons [Treumann and Baumjohann, 1997].

According to the Parker spiral the acute angle between the interplanetary magnetic field and the Earth-Sun line is 45° at 1 AU. However, the spiral form is only valid for long-term averages. Due to the high variability of the field direction on small time scales this angle can have any value. Consequently, the position of the foreshock border is constantly changing.

In order to decide whether Cluster is inside or outside the Earth's foreshock, the position of the bow shock must be known. In response to the variable solar wind the bow shock must also be regarded as a variable surface. The distance of the sub-solar point (point on the surface being closest to Sun) from Earth fluctuates around $15 R_E$ (Earth radii). The bow shock extends downstream of the sub-solar point and can be approximated by a hyperbolic surface. Existing models determine an average position of the bow shock by fitting a two or three dimensional function to the transition coordinates of several spacecraft that cross the bow shock [Fairfield, 1971; Peredo *et al.*, 1995]. The function describes a surface of second order which includes ellipsoids and hyperboloids.

We use the model proposed by Peredo *et al.* [1995] where besides the transition coordinates also the corresponding solar wind plasma data are utilised to give the shape and position of the bow shock according to the prevailing solar wind conditions. Peredo *et al.* [1995] bin the

bow shock crossings into four ranges of the observed Alfvénic Mach number $M_A = V_{sw}/V_A$, where V_{sw} is the solar wind and V_A the Alfvén velocity. Best-fitting bow shock surfaces are then derived for each subset and for the total of the crossings. Since their data set lacks any crossings with latitude below -50° , *Peredo et al.* [1995] need to assume a north-south symmetry.

Criterion to decide if Cluster is inside or outside the foreshock region

The technique we use to decide whether Cluster is inside or outside the foreshock region is based on the geometrical considerations above and is illustrated in Figure 6.6. We say a spacecraft is inside the foreshock region if the magnetic field line that goes through the spacecraft is connected to the bow shock. Otherwise the spacecraft is in the undisturbed solar wind. For the computation the position vector \mathbf{r}_0 of the spacecraft, the magnetic field vector \mathbf{B}_0 and the position of the bow shock must be known. Introducing the straight line $S: \mathbf{s}_0 = \mathbf{r}_0 + m\mathbf{B}_0$ into the bow shock model equation from *Peredo et al.* [1995] and solving this equation for m shows whether this line intersects the bow shock or not: If real solutions for the parameter m exist then the straight line intersects the bow shock and the spacecraft is inside the foreshock region. If no real solution exists then there are no intersections and the spacecraft is outside the foreshock region.

This method has been used in previous studies [*Sperveslage*, 1999]. Uncertainties are: (1) the variability of the magnetic field, (2) the magnetic field lines are not necessarily straight lines and (3) the bow shock is only on average approximated by the model equation. The true variability of the bow shock cannot be accounted for by the model. Also note that we do not distinguish between different Alfvénic Mach numbers. Instead we always use the bow shock model *Peredo et al.* [1995] derive using the total number of crossings.

Besides the “yes-no”-decision explained above it is instructive to know how far away from the foreshock border a spacecraft is located. Following *Sperveslage* [1999] we define D as the shortest distance between the magnetic field line which goes through the measuring spacecraft and the foreshock border (see Figure 6.6). In other words, D is the radius of the cylinder around S that is tangent to the bow shock. We calculate D in computing the band of straight lines which are parallel to S and which are tangential to the bow shock. For each of these straight lines we then compute the distance to S . The shortest of these distances is D . We denote the corresponding tangent by T . If the spacecraft is within the foreshock region we define D to be negative. Positive values of D indicate that the spacecraft is outside the foreshock region. For $D = 0$ the spacecraft is located in the foreshock border.

In order to decide which of the DDs in our preliminary set selected in the previous section can be used for further analysis we seek a criterion based on the considerations above. The first and most important requirement on this criterion is that all DDs that are likely to be influenced by foreshock activity are discarded. The second requirement, however, is not to be too generous in dropping DDs, so that enough events for a meaningful statistical study remain after this selection step. With the apogee of Cluster (19-20 R_E) being only a few R_E larger than the distance of the subsolar point of the bow shock to Earth this is a delicate task.

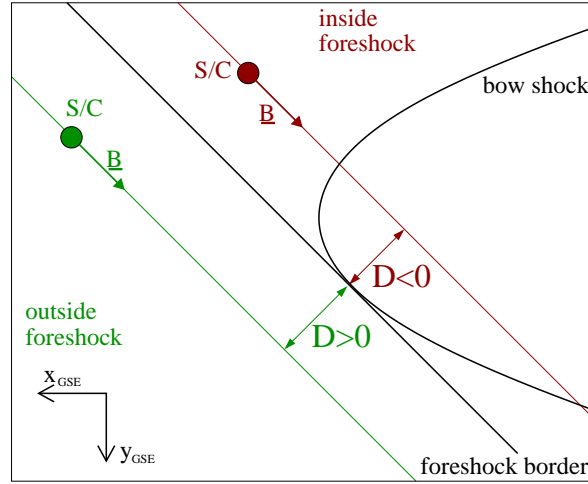


Figure 6.6: Foreshock geometry in the ecliptic plane and illustration of the parameter D . Shown is the bow shock, the foreshock border and two spacecraft measuring the (same) magnetic field which is used to determine the orientation of the foreshock border. A spacecraft left of the foreshock border (e.g. the green spacecraft) is outside the foreshock. The red spacecraft is inside the foreshock.

As a consequence of the field rotation across the DD the position of the foreshock border generally changes when the DD passes the spacecraft. Therefore, Cluster can be outside the foreshock region on one side of the DD, but inside the foreshock region on the other side. The criterion must be capable to detect DDs which could be subject to foreshock activity on either side. Also the time resolution of the magnetic field data used to determine the straight line S is important. On the one hand we aim to avoid decisions based on high frequency field fluctuations, i.e., the data should be averaged over sufficiently long time intervals. On the other hand the averaging intervals should not be too long, since then one might miss crossings of the foreshock border due to a changing field direction.

To find a criterion that accomplishes the formulated tasks we calculate the distance D for different time resolutions of the magnetic field and plot this parameter together with the magnetic field. In order to see how the value of D correlates with visible foreshock waves we visually inspect a considerable fraction of the data. In addition, we investigate how the parameter D evolves as a function of time across several DDs. Six different cases, examples of which are shown in Figure 6.7, are possible: (1) D is constantly greater 0 over long periods of time before, after and during the DD passes by, i.e., Cluster is outside the foreshock region for the whole time (upper left). (2) $D > 0$ a long time before and after the DD, but $D < 0$ for a short time interval during the transition, i.e., Cluster dips into the foreshock region for a moment (upper right). (3) and (4) are the complementary cases to (1) and (2), i.e Cluster is inside the foreshock region the whole time or most of the time (middle panel of Figure 6.7). Finally, cases (5) and (6) are those where D changes sign when the DD crosses Cluster. We observe all six types.

Which of these cases is observed depends on the details of the field rotation. Let us for example consider the green spacecraft in Figure 6.6 and assume the shown magnetic field vector represents the downstream side of the DD. Then a counter-clockwise field rotation around the GSE z -axis of, say, 90° yields a D -signature corresponding to case 2. If the

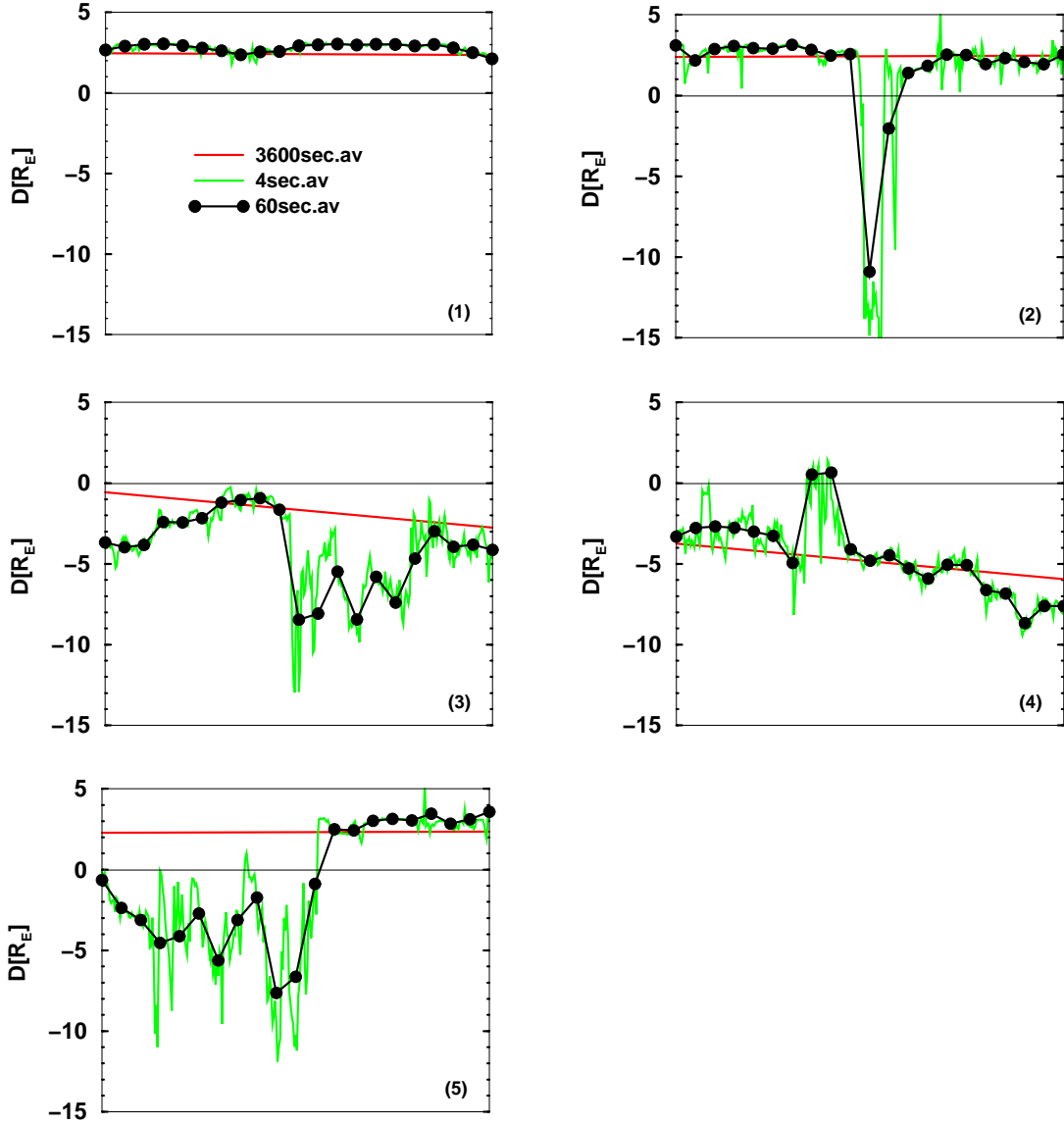


Figure 6.7: Six cases describing the evolution of D across a DD. Shown are 4 s, 60 s and hourly averages. The DD is in the centre of the 20 min intervals. The first group (top) corresponds to DDs considered as being outside the foreshock region, the second group (middle) to DDs inside the foreshock and the third group (bottom) contains DDs where Cluster is inside the foreshock on one side and in the undisturbed solar wind on the other side. The complementary case (6) is not shown.

rotation angle is only $\approx 30^\circ$ then the upstream magnetic field points towards the bow shock and case 6 is realised. Finally, if the rotation axis lies in the ecliptic and is perpendicular to the downstream \mathbf{B} then the straight line S does not intersect the bow shock for any rotation angle, i.e case 1 is realised.

These considerations demonstrate that a selection criterion eliminating events that are likely to be influenced by foreshock activity introduces some bias: Certain magnetic field evolutions will be discriminated against. Note, however, that this not necessarily implies a bias against a specific type of DD. A discrimination against either RDs or TDs can only appear when they have different statistical properties regarding orientation. Certainly, both RDs and TDs are possible.

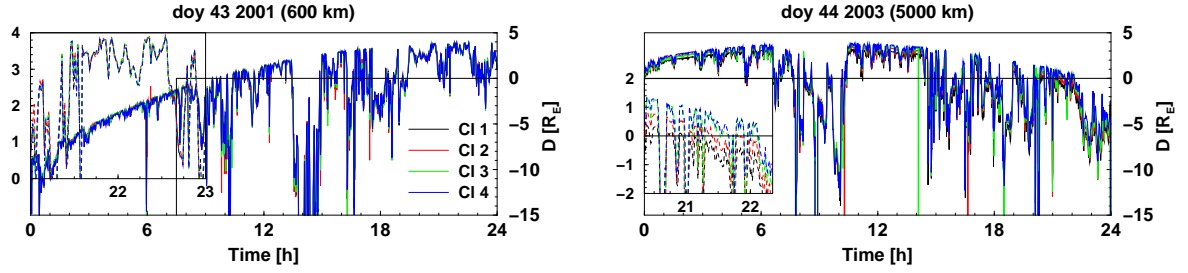


Figure 6.8: D versus time for two typical days with Cluster in the solar wind. Shown are day 43 of year 2001 (left) and day 44 of year 2003 (right). The bow shock crossing on the former day is indicated by the vertical line. The inserts show a 2 hour interval at the end of each day. D is plotted for each spacecraft separately. The standard Cluster colour coding (Cl 1: black, Cl 2: red, Cl 3: green and Cl 4: blue) is used.

In principle, cases 2-6 may be influenced by foreshock activity. However, for case 2, inspection of the data shows that the duration of negative D is generally small and that in these cases no foreshock waves are observed in the magnetic field data. Therefore, in order to keep as many events as possible and to minimise the bias introduced due to this selection process, we formulate the following criterion: We use 60 s magnetic field averages to determine D and consider a time interval ± 10 minutes on either side of each DD, i.e we have 21 consecutive values of D in the vicinity of the DD (as in Figure 6.7). We then classify the DDs into three groups according to the number k of positive D values: (I) outside foreshock ($k \geq 14$), (II) inside foreshock ($k \leq 7$) and (III) ambiguous ($7 < k < 14$). This classification combines cases 1 and 2 in group I, cases 2 and 3 in group II and cases 5 and 6 in group III.

A gradual change in field direction on one or both sides of the DD can cause further sign changes of D . However, the time interval, the time resolution and the classification are chosen such that the above assignment is valid in most cases according to our experience. Only the events in group I are considered in our further analysis. In other words, we select all DDs with more than 2/3 positive D values in the vicinity of the event. This way the spacecraft are most likely outside the foreshock region on both sides of the DD. Note, however, that during the field rotation Cluster may be inside the foreshock region for a short period of time.

Another requirement on the criterion follows from the necessity to account for the size of the Cluster array, as will be discussed below.

Figure 6.8 shows 60 s averages of D versus time for two typical days with the apogee of Cluster in the solar wind. On the left hand side day 43 of 2001 and on the right hand side day 44 of 2003 are shown. Both are on the evening side of Earth. Whereas Cluster is in the solar wind (upstream of the bow shock) the whole day 44 of 2003, on day 43 of 2001 the outbound crossing of the bow shock is at $\approx 07:30$ (indicated by the vertical line). The behaviour of D follows the trajectory of the spacecraft on average. Before the bow shock traversal, D is by definition negative and increases approximately until apogee is reached. The value of D turns from negative to positive values approximately 2.5 h after the bow shock crossing. The fluctuations superposed to the otherwise gradual “orbit-induced” behaviour are due to changes in the field direction. Rapid jumps of D correspond to DDs.

Table 6.3: Number and percentage of DDs (related to the total number of DDs in $B_4 \cup TS_4$) that are observed outside the foreshock, inside the foreshock, and the number of ambiguous DDs.

name	$B_4 \cup TS_4$	outside	inside	ambiguous
DD_{2002}	372	57 (15%)	255 (69%)	60 (16%)
DD_{2001}	489	146 (30%)	254 (52%)	89 (18%)
DD_{2003}	2673	257 (10%)	2067 (77%)	349 (13%)

Several insights can be gained from Figure 6.8. Firstly, intervals with Cluster being outside the foreshock region ($D > 0 R_E$) can be clearly identified. (Note, however, that generally $D < 4 R_E$). Within these intervals thin “dips” in D are observed, sometimes causing D to be negative for a short duration (DDs according to case 2). The DDs surviving our selection criterion are typically taken from such intervals.

Secondly, D is significantly different at the various positions of the four spacecraft in 2003. According to section 5.5, Cl 4 has the largest distance from the bow shock and Cl 1 is closest to Earth. The insert in Figure 6.8 shows a magnification of a 2 hour interval at the end of the day (20:21-22:21). In the beginning of this interval all four spacecraft are outside and at the end the whole array is inside the foreshock region. However, in between the foreshock border cuts through the tetrahedron.

Our criterion must ensure that the whole array of spacecraft is outside the foreshock region. Therefore, we generate a fifth time series where each entry $D_{min}(t_k)$ is defined as $D_{min}(t_k) = \min(D^1(t_k), D^2(t_k), D^3(t_k), D^4(t_k))$, where D^i is the value of D at spacecraft i . The 2/3-criterion defined above is then applied using $D = D_{min}$. Note that in 2001 and 2002 it is almost irrelevant whether D is taken at any of the four spacecraft or if D_{min} is used. Even in the insert in Figure 6.8 (left) the four lines representing D coincide. However, in 2003 when the tetrahedron is large, the difference is significant: Whereas using the position vector of Cl 4 yields 372 DDs that satisfy our foreshock criterion, using Cl 1 only 272 such DDs can be identified. Using D_{min} , 257 DDs are regarded as being outside the foreshock region.

Application of the criterion

The resulting number of DDs regarded as being inside or outside the foreshock region or regarded as ambiguous according to our criterion are summarised in Table 6.3. Also shown is the number of DDs in the preliminary set $B_4 \cup TS_4$ (from previous section).

Note that the number of ambiguous DDs is relatively small. As discussed above these are predominantly events with Cluster being inside the foreshock region on one side but outside the foreshock region on the other side (cases 5 and 6). Therefore, for the vast majority of events (86% of the total number of DDs) the status is identical on both sides. This means that for the majority of DDs discarded in this step the field direction on both sides is such that Cluster is in the foreshock region. The details of the field rotation are irrelevant for the selection process. Hence, for a bias against RDs or TDs to be introduced some mechanism

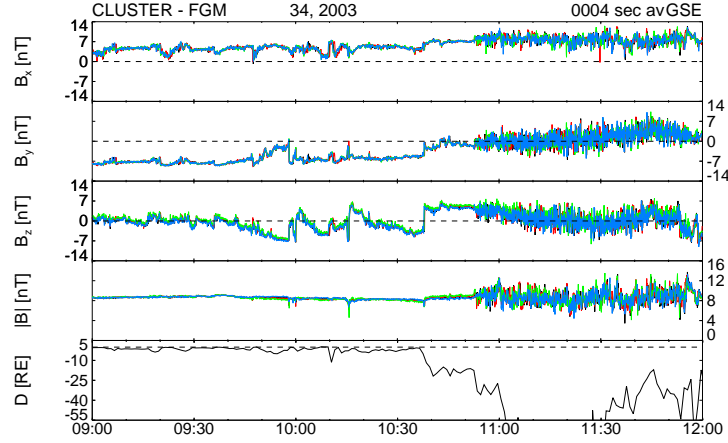


Figure 6.9: Correlation between D and foreshock waves. Shown are the components and the magnitude of 4 s Cluster magnetic field averages in GSE coordinates and the parameter $D = D_{min}$ (60 s averages) for a three hour solar wind period. The standard colour code is used to indicate the individual spacecraft.

would have to be presumed causing the field direction on both sides to be statistically different for RDs than for TDs, such that Cluster is more likely to be in the foreshock region in the vicinity of either type of DD. Since DDs are most likely produced on or near the Sun and undergo dynamic changes in the solar wind until they reach 1 AU, a mechanism of that type is hard to think of. Hence a bias against RDs or TDs is unlikely.

Unfortunately, but expected because of the orbit characteristics, most DDs are observed in the foreshock region. One might argue that our criterion is too strict. Comparing D_{min} with observable foreshock waves in the magnetic field for a considerable amount of data indeed indicates that our selection process is rather conservative. Figure 6.9 shows an example interval. Plotted are 4 s magnetic field averages and 60 s averages of $D = D_{min}$. Foreshock waves appear after 10:52. Note that between 9:00 and 10:37 D is negative almost the whole time and fluctuates around $\approx -1 R_E$. No foreshock waves are visible. Nevertheless the DDs visible in this interval are discarded from our set. A DD at 10:37 then causes D to rapidly decrease to $\approx -18 R_E$. Not until ≈ 15 min later when another decrease of D to $\approx -35 R_E$ is observed eventually foreshock waves set in. Probably we could use more DDs than we actually do. However, application of our rather strict criterion ensures that no foreshock disturbances tamper our results. The remaining DDs are definitively in the undisturbed interplanetary medium. Note that in addition to the above criterion we visually inspect the solar wind data ambient to the selected DDs, as is done in Figure 6.9.

In Table 6.3 it can be seen that the relative number of DDs regarded as being outside the foreshock region is variable. Whereas in 2001 30% of the total number of DDs are selected, only 15% and 10% are selected in 2002 and 2003, respectively. The reasons are simple. The large size of the Cluster array in 2003 may explain the relatively poor yield in 2003. However, although the spacecraft separations are smallest in 2002 the relative number of selected DDs is only half the number found in 2001. According to our criterion the minimum apogee of the four spacecraft is decisive for selection. Due to friction losses the apogee of each spacecraft decreases with time. Whereas the minimum apogee is $19.7 R_E$ in 2001, it is $19.2 R_E$ in 2002

Table 6.4: *Final number of events selected for analysis.*

DD_{2002}	DD_{2001}	DD_{2003}
33	129	204

and only $18.9 R_E$ in 2003. Maybe even more important than the orbit characteristics is the fact that the measurements started not until 1 February in 2001 in contrast to 2002 and 2003. Although sporadically traversing the solar wind in January, Cluster is always particularly close to the bow shock in that time and thus likely to be in the foreshock region.

Final set of DDs

As a final quality check the selected events are individually inspected in different time resolutions. Another 17 (24, 53) DDs are dropped from the sample in 2001 (2002, 2003) either because the field variations are very complex or because no significant discontinuity can be found in the high resolution data. Table 6.4 summarises the final number of events that we use in our analysis. The names DD_{yyyy} exactly denote these sets of DDs selected in the respective years. Because of both the different spacecraft separations and different solar wind conditions prevailing during observation of the three sets a strict separation is necessary and instructive. Note that not all of the events in Table 6.4 are suitable for the analysis methods to be applied later. This, however, we discuss in due time.

In summary, we have selected a total number of 366 DDs suitable for further analysis which can be regarded as true (i.e., without influence of Earth) interplanetary discontinuities. In the following section these DDs are characterised according to the prevailing solar wind conditions.

6.5 Prevailing solar wind conditions - Coronal holes

The aim of this section is to provide an overview of the prevailing solar wind conditions during the observation periods of the selected DDs. In particular we prove that a considerable amount of solar wind data used for DD analysis in this thesis originates from coronal holes on the Sun.

The correlation of DDs to solar wind type, and thus to the source region on the Sun, is of considerable interest for understanding their generation mechanisms. As is detailed in sections 3.2 and 3.3 many earlier observations, and theories for the generation of RDs based on these observations, claim that the solar wind originating from coronal holes is characterised by abundant RDs.

In section 6.5.1 we show in which phase of the solar activity cycle our measurements are made. In section 6.5.2 we use the ACE spacecraft as a solar wind monitor to demonstrate that different types of solar wind are present during our three periods of observations. In particular

strong indications for solar wind that maps to coronal holes on the Sun are presented for the 2003 observations. The subsequent three sections (6.5.3-6.5.5) solely provide further evidence for these coronal hole flows. Finally we give an overview of the identified DDs that are unambiguously identified to be in coronal hole flows (section 6.5.6). There we define a subset DD_{2003CH} of DD_{2003} which will be used in chapter 8 to test the hypothesis of abundant RDs in solar wind that emanates from coronal holes on the Sun.

6.5.1 Solar activity cycle

Asking for the present solar wind conditions, the first question must be in which phase of the solar cycle the measurements are made. The 11-year cycle of the Sun's magnetic activity is best described by the number of sunspots visible on the Sun. Since most forms of solar activity are magnetic in origin, they undergo the same cycle. The number of active regions, with their energetic radiation and bright magnetised loops, as well as the total number of solar eruptions or flares, also vary from a maximum to a minimum and back to a maximum in about 11 years [Lang, 2001]. However, solar activity does not completely disappear at the minimum in the sunspot cycle. In fact, recent major eruptions on the Sun (end of 2004/beginning of 2005) demonstrate that considerable activity can be observed also near solar minimum. The size and location of coronal holes in the Sun's atmosphere vary throughout the 11-year cycle. During the minimum phase of the solar cycle there are two large and relatively stable coronal holes on the Sun, one at each pole. Thus, an observer in the ecliptic plane (such as Cluster) predominantly detects slow solar wind originating from the active regions of the Sun near the equator. After solar minimum the polar coronal holes start to shrink. At the same time the coronal holes deform and occasionally cross the solar equator causing fast streams to be observed in the ecliptic. Near solar maximum the polar coronal holes disappear, and instead small variable coronal holes at mid-latitudes are observed. Since the solar wind velocity correlates with the size of the coronal hole [Wang and Sheeley Jr., 1990] the expected maximal solar wind speed is relatively slow. During the declining phase these isolated coronal holes combine, and finally they reform as the large connected polar coronal holes. Note that the polarity is reversed compared to the preceding solar minimum. Therefore the period of a complete cycle is actually 22 years. During the declining phase (particularly towards solar minimum) large coronal holes can be observed that cross the equator, sometimes from pole to pole. These coronal holes can be remarkably stable and can persist over several solar cycles. The observer in the ecliptic plane then detects the periodic recurrence of fast solar wind according to the rotation of the Sun.

Figure 6.10 shows monthly averages of the sunspot numbers of cycle 23. In order to better identify solar maximum and the subsequent solar minimum we also plot a prediction by Hathaway *et al.* [1999]. The shaded areas indicate the observation periods of the analysis of this thesis. All three periods are in the declining phase of this cycle. Whereas the first period (in 2001) almost coincides with solar maximum, the third period (in 2003) is almost in the middle of the declining phase. According to the discussion above we thus expect to observe different types of solar wind in the respective periods: Possible fast streams corresponding to coronal holes in 2001 are expected to be short in duration and to cause relatively slow maxi-

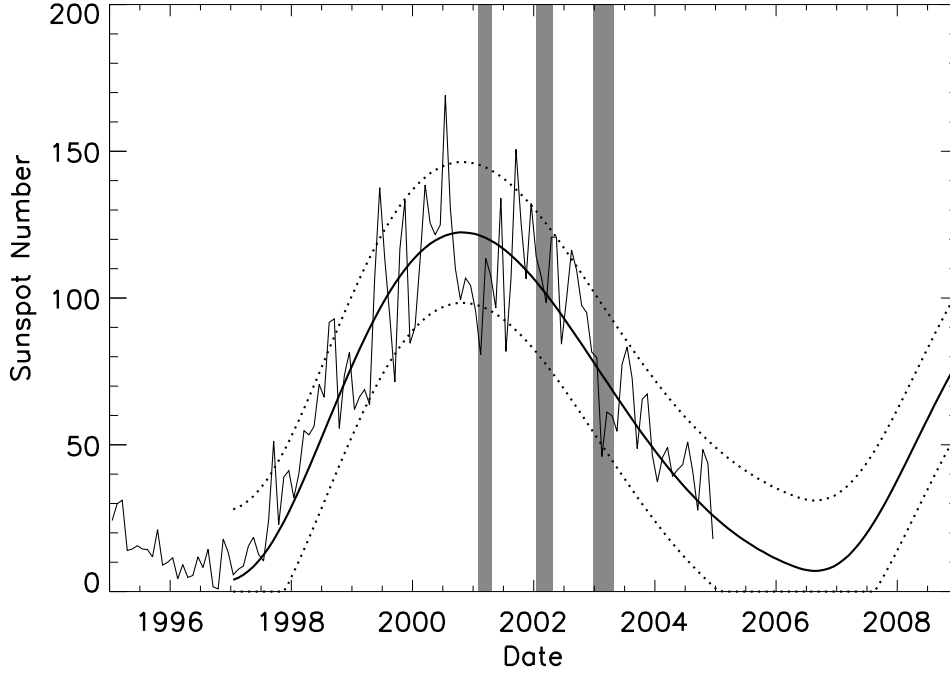


Figure 6.10: Monthly averaged sunspot numbers (thin solid line) for cycle 23 through December 2004 derived from the International Sunspot Numbers, compiled by the Sunspot Index Data Centre in Belgium. The data are taken from <http://science.msfc.nasa.gov>. The thick line shows the sunspot number predicted by Hathaway et al. [1999], and the dotted lines show the expected 5 and 95 percentile levels. The three periods with Cluster providing solar wind data (see Table 6.1) are indicated.

mal solar wind speeds. In contrast, large and stable coronal holes may provide considerable amounts of persisting fast solar wind data in 2003. This circumstance enables us to compare our results obtained in different solar wind conditions.

6.5.2 Using ACE as a solar wind monitor

In order to consistently monitor the prevailing solar wind conditions an observation platform is needed that, unlike Cluster, continuously measures solar wind data. We utilise data from the Advanced Composition Explorer (ACE) spacecraft [Stone et al., 1998]. Launched 25 August 1997, ACE orbits the L1 libration point which is a point of Earth-Sun gravitational equilibrium about 1.5 million km sunward of Earth.

Figures 6.11-6.13 give a comprehensive overview of the prevailing solar wind conditions during the periods used in our analysis. The first 120 days, i.e., 1 January until 30 April, of each year are shown (2001 in Figure 6.11, 2002 in Figure 6.12 and 2003 in Figure 6.13). Panels 1-4 show the search results of the TS- (panel 1 and 3) and the B-method (panel 2 and 4) for each day. The absolute number of DDs found per day is shown in the first two panels. Since the time with all four spacecraft simultaneously delivering solar wind data is different on each day (see Figure 6.1) we normalise these numbers by the relevant time

with Cluster in the solar wind. The resulting occurrence rates (number of DDs per hour) are shown in panels 3 and 4. The respective number of DDs simultaneously detected at all four spacecraft is indicated by the black bars and the search results at each individual spacecraft by the coloured horizontal lines (the standard colour code is used). In panel 6 four different colours are used to indicate the intervals with all four spacecraft simultaneously measuring solar wind data (grey) and the exact times of the identified DDs. DDs detected by either the TS- or the B-method are marked by black lines. The subset of these DDs which are outside the Earth's foreshock region are marked green and finally the DDs used in our analysis are marked red. Note that the above intervals and events are plotted on top of each other in the order as itemised above so that barely grey or green intervals are seen. Also note that the lines indicating individual events generally cannot be resolved. The red bars in panel 5 present the total number of DDs contained in connected solar wind intervals.

Panels 7-13 show 12 h averages of ACE plasma and magnetic field measurements. The proton velocity (panel 7), density (panel 8) and temperature (panel 9) and the α -particle to proton ratio (panel 10) are from the Solar Wind Electron, Proton, and Alpha Monitor (SWEPAM) instrument [McComas *et al.*, 1998]; the charge state ratio O^{7+}/O^{6+} (panel 11) is from the Solar Wind Ion Composition Spectrometer (SWICS) instrument [Gloeckler *et al.*, 1998]; and the magnetic field data (panel 12 and 13) is from the Magnetic Field Experiment (MAG) [Smith *et al.*, 1998]. The magnetic polarity P (panel 12) is the cosine of the angle Φ^* between the field direction in the R-T plane¹ and the expected direction of an outward directed Parker spiral. Hence, $P = 1$ for an outward directed nominal magnetic field vector, and $P = -1$ if the field points towards the Sun along the Parker spiral. Panel 13 of Figures 6.11-6.13 shows the field magnitude. Note that the ACE data are shifted by 50 minutes in order to account for the time lag between ACE and Cluster.

Several issues relating to Figures 6.11-6.13 are discussed in the following. First, the poor solar wind data coverage of Cluster in 2001 and 2002 as compared to 2003 is apparent. Second, although the DD occurrence rate is 1/h for the B-method and 2/h for the TS-method on average (see also section 6.3) it strongly fluctuates from day to day. In particular from Figure 6.13 it can be seen that these fluctuations are similar for both search methods (TS and B). More important, the fluctuations of the DD occurrence rate are correlated with the solar wind velocity (compare panels 3 and 4 to panel 7, in particular in Figure 6.13). This agrees with earlier studies, see also section 6.3. Söding [1999] finds that this correlation is linear and a purely geometric effect: If the solar wind velocity is high, a larger plasma volume is searched in a given time compared to periods of slow solar wind.

Different types of solar wind

Comparing the solar wind velocities shown in Figures 6.11-6.13, it becomes obvious that distinct types of solar wind are prevailing in the three different periods of observation. In 2001 (close to solar maximum) the velocity is generally rather low. Occasionally fast streams

¹The ACE magnetic field data is given in the so-called RTN coordinate system, which is a spacecraft centred coordinate system, R is the Sun to spacecraft unit vector, T is perpendicular to R and in the plane of the solar equator and N completes the right-handed triad.

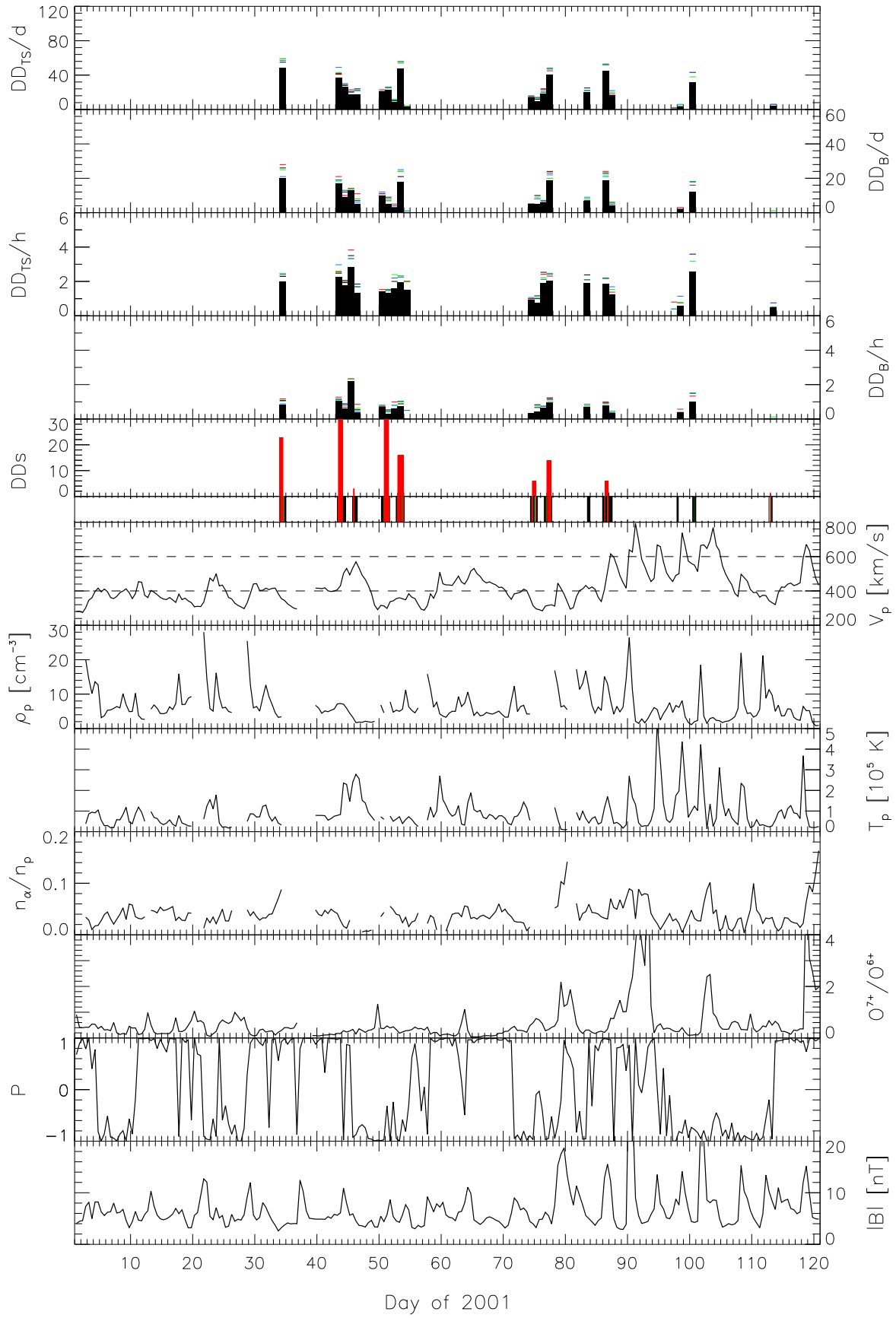


Figure 6.11: Overview of the DDs found and the prevailing solar wind conditions in 2001. 12 h averages of ACE data are shown.

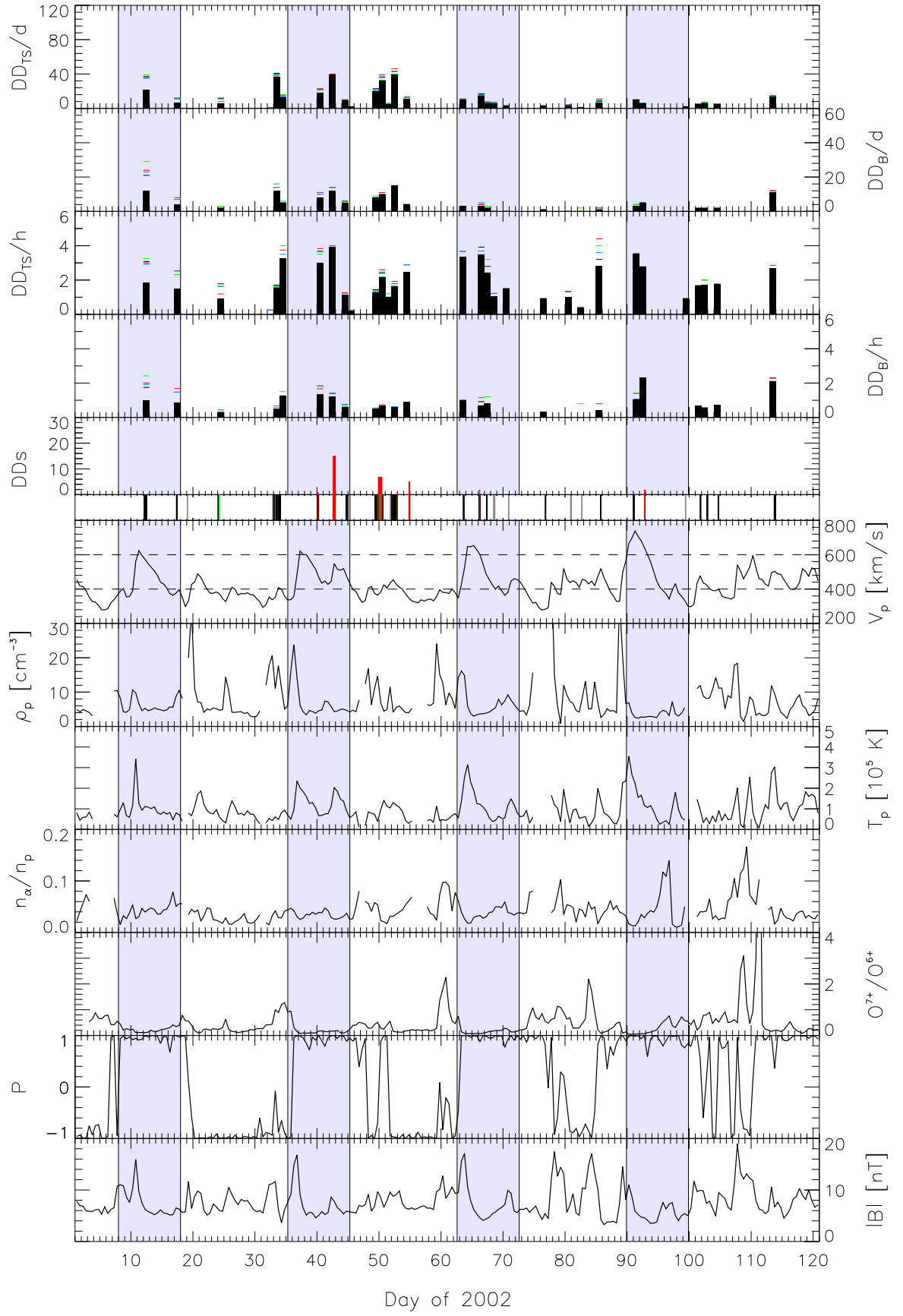


Figure 6.12: Same as Figure 6.11 for 2002. The blue shaded areas indicate repetitive fast solar wind streams.

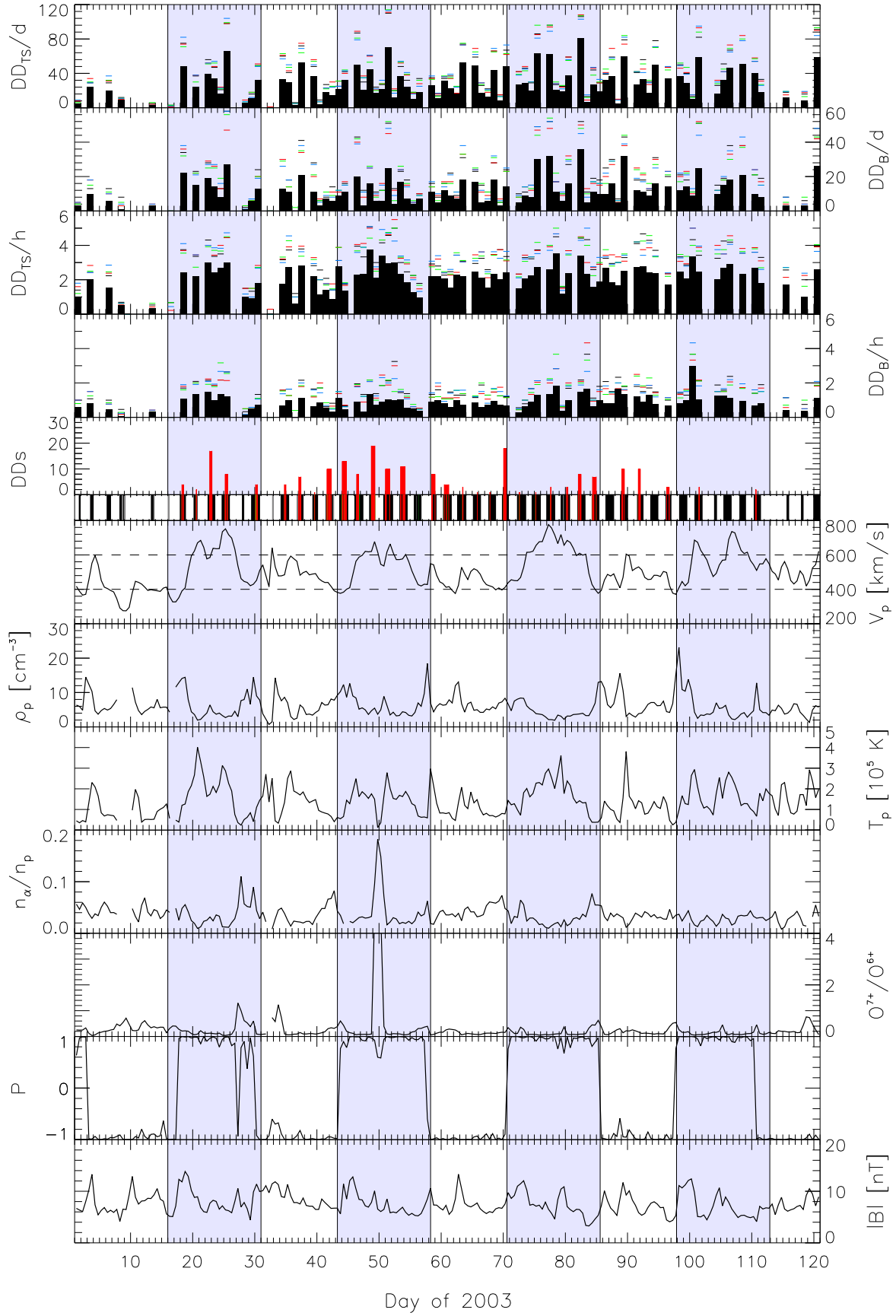


Figure 6.13: Same as Figure 6.12 for 2003.

are observed. However, they are low in amplitude, relatively short in duration and not in period with the rotation of the Sun. Some of these may be associated with temporary small coronal holes on the Sun, others with transient events. For example the fast stream around day 47 is characterised by a relatively low α -particle to proton ratio (hard to see because of the gap in the data), relatively low ratio O^{7+}/O^{6+} and a more or less unipolar magnetic field. Therefore, this stream might map back to a coronal hole. In contrast, the fast streams towards the end of the shown period are characterised by large values of n_α/n_p and O^{7+}/O^{6+} and frequent polarity changes. Hence, we consider those streams as being associated with transient events on the Sun. Note that the majority of DDs selected for further analysis (panel 5) is located predominantly in particularly slow solar wind regions, probably emanating from active regions on the Sun.

In contrast, the ACE data observed in 2002 and 2003 show very different features. The shown periods are characterised by very large amplitude, broad, quasi-repetitive streams of high-speed solar wind. This is a common observation during the declining phase close to solar minimum when a “tongue” of a large polar coronal hole crosses the solar equator. The blue shaded areas roughly indicate the four fast streams visible in Figures 6.12 and 6.13.² The four marked intervals are equal in length (10 d in 2002 and 15 d in 2003) and are equally spaced. One shaded interval starts exactly 27.3 d after the beginning of the preceding interval. In other words, the time difference between two consecutive intervals equals one Carrington rotation, i.e., the rotation period of the Sun as seen from Earth. The repetitive occurrence of the four fast streams follows this periodicity remarkably well. Furthermore, the long duration (≈ 10 d in 2003) of each fast stream is relatively constant. These features alone strongly indicate a coronal hole, persisting over at least four rotations, as the source of the fast streams. Nevertheless, we provide further illustration for agreement between these streams and a coronal hole on the Sun below and in the following three sections (6.5.3-6.5.5).

Note that the interaction of slow and fast solar wind causes compression to high plasma densities at the leading edge of the high-speed streams [Schwenn, 1990]. These density increases are visible in Figures 6.11-6.13.

Indications for coronal hole flows in 2003

Because of the poor statistics and the fact that the majority of DDs is in slow solar wind in 2002 we only consider the fast streams of 2003 in our attempt to unambiguously identify DDs in coronal hole solar wind. The procedure is exemplified in the following:

Solar wind originating from coronal holes is characterised by its steadiness and by low density. Furthermore, the helium abundance is relatively steady with the helium to hydrogen ratio n_α/n_p in the range 0.02 to 0.05 [Bame *et al.*, 1977; Neugebauer and Alexander, 1991]. Another difference to the solar wind originating from active regions is that the O^{7+}/O^{6+} ion ratio is lower for coronal hole flows. Neugebauer *et al.* [2002] find that the O^{7+}/O^{6+} ratio is $\lesssim 0.3$ for solar wind from coronal holes near solar maximum whereas von Steiger *et al.* [2000] find a ratio of < 0.03 in polar coronal holes near solar minimum. Finally, coronal

²Note that the intention here is not to exactly mark the fast streams. The shaded areas only serve as an orientation.

hole streams are usually associated with a magnetic sector of unique polarity. Crossing of a sector boundary often occurs slightly ahead of the leading edges of the high-speed streams [Schwenn, 1990].

All four characteristics of coronal hole flows are observed in the fast streams in Figure 6.13: After the increase in the stream-stream interaction region the density decreases to typically $\approx 4 \text{ cm}^{-3}$, and both the helium to hydrogen ratio n_α/n_p and the $\text{O}^{7+}/\text{O}^{6+}$ ion ratio are within the expected ranges. In particular the polarity is unique in an interval around the duration of the fast streams.

Note that there is one exception: In the middle of the second fast stream around day 50 the density increases to $\approx 9 \text{ cm}^{-3}$, the temperature drops, a sharp peak in the ratios n_α/n_p and $\text{O}^{7+}/\text{O}^{6+}$ is observed and a dip in polarity occurs. These observations are indicative of *Coronal Mass Ejections* (CMEs) (see Neugebauer *et al.* [2002] and references therein).

However, apart from this isolated case of a transient event the criteria for coronal hole flows are well satisfied. Figure 6.14 shows as an example a zoom of the first fast stream (FS I) with 2h averages, where the above characteristics can be seen more clearly. Note that here also the grey shaded intervals and DDs marked by green lines are visible (panel 2). The DDs that we consider as being in coronal hole flows are marked by drawn through red lines. Apart from the above criteria another requirement for selection as “coronal hole event” (i.e., a DD in a coronal hole flow) is that the flow velocity is high ($\gtrsim 600 \text{ km/s}$). We also inspect the corresponding plots for the other fast streams and proceed as demonstrated for FS I. Thereby we identify a considerable number of DDs which clearly satisfy the above criteria. Others are dropped from our list of “coronal hole events” because they do not seem to be in coronal hole flow. We also discard those events being very close to the CME in FS II. Note, however, that we only drop all DDs found on day 49. This leaves some ambiguous events, namely the remaining DDs in the vicinity of the CME. These are the events found on day 48 and those in the interval following the CME, i.e., day 51. Another group of ambiguous DDs are those at the leading edge of FS II (day 46). Although these events are most likely in coronal hole flow (they definitely are in fast solar wind), the ambient plasma originates from a region very close to the border of a coronal hole. Therefore, it is unclear how much influence the stream-stream interaction region has on the properties of these events.

In addition to the *in situ* measurements from the ACE spacecraft we also utilise remote sensing measurements to confirm the association of the fast streams observed in 2003 with coronal holes. In particular we use: (1) Coronal hole predictions of the *Wang-Sheeley potential-field source-surface* model that utilises synoptic observations of the photospheric magnetic field; (2) Extreme Ultra Violet (EUV) images of the Sun’s atmosphere; and (3) the helium I 1083 nm absorption line.

These observations are presented in the following three subsections.

6.5.3 Wang-Sheeley model

A *potential-field source-surface* model can be used to determine the magnetic field configuration in the region between the Sun’s photosphere and the so-called *source-surface* [Schatten

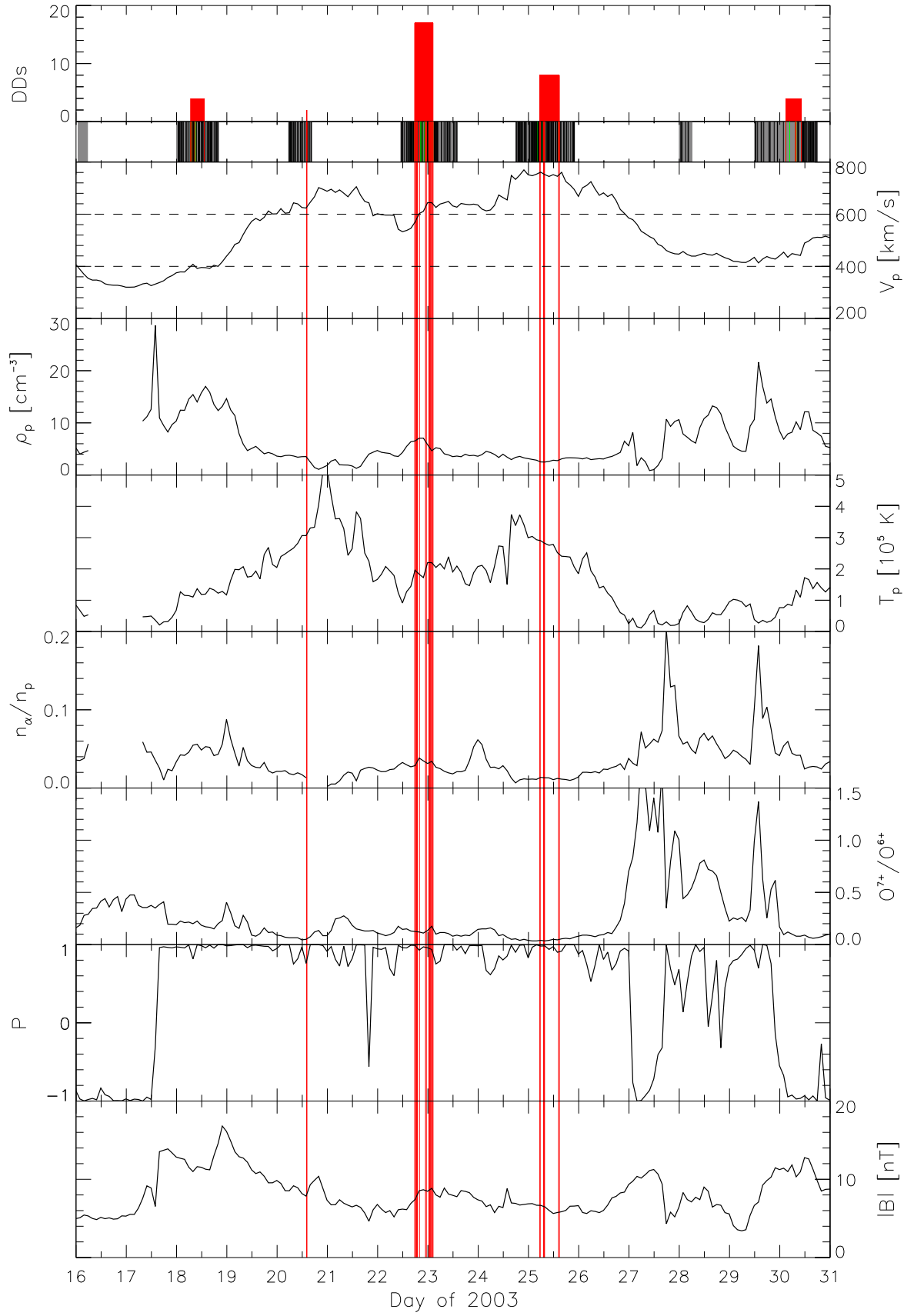


Figure 6.14: FS I from Figure 6.13, 2h averages. The first four panels of Figure 6.13 are dropped. DDs potentially originating from coronal holes are marked by drawn through red lines.

et al., 1969; Wang and Sheeley Jr., 1992]. The source-surface is a spherical reference surface of constant potential in the corona where magnetic field lines are assumed to be radial. The radius of the source-surface is usually taken to be 2-3 solar radii (R_s). For the computation the photospheric magnetic field needs to be known. It is taken from line-of-sight synoptic observations for example provided by the Wilcox Solar Observatory (WSO) [Arge and Pizzo, 1998]. The potential-field source-surface model by Wang and Sheeley [Wang and Sheeley Jr., 1992] also yields a forecast for the solar wind speed. The speed to which the solar wind is accelerated is thought to be regulated by the amount by which magnetic flux tubes expand from the base of the photosphere to the source-surface: The greater the flux tube expansion, the more the available energy is spread out and the slower the resulting flow speed. An *expansion factor* f_s at any point P on the source-surface is determined by comparing the computed local field strength at P with the associated value on the photospheric surface, as tracked back along the field line passing through P . The solar wind speed is then obtained by an empirical relation between f_s and the flow velocity, established by Wang and Sheeley Jr. [1990].

We use the predictions of the Wang-Sheeley model to verify that the high-speed streams observed in the ACE data indeed map to coronal holes on the Sun. To that purpose, we map the data measured at ACE back to the time t_{sun} when the plasma left the source-surface. We use a mapping technique previously used by Neugebauer *et al.* [2002], where t_{sun} is given by $t_{sun} = t_{ACE} - R/V_{sw}$. t_{ACE} is the time of observation at ACE, R the solar distance and V_{sw} the measured solar wind speed. This means, we assume a radial flow at constant speed. This simple technique gives rise to occasional ambiguities which are disregarded here. (For a justification of the technique see Neugebauer *et al.* [2002].)

Figure 6.15 shows as an example the mapped ACE data of the first fast stream in 2003 (bottom) compared to the predictions of the Wang-Sheeley model (top) [Arge and Pizzo, 1998]. All six panels are shown for one Carrington rotation, i.e., from Carrington longitude 240° of Carrington rotation 1998 until 240° of Carrington rotation 1999. The abscissa is the Carrington longitude in degrees. Also shown are Carrington rotation numbers. The most recent data are located at the far left of the map. To the right of the map, the data get progressively older. Note that the abscissa of the mapped ACE data is given in day of 2003. This time corresponds to the time given on top of the first panel. The crosses mark the daily position of the sub-Earth point on the maps (Sun). Since the Sun's rotation axis is inclined 7.25° to the ecliptic, over the course of a year the sub-Earth point varies (in latitude) from $+7.25^\circ$ to -7.25° below the Sun's equator. From top to bottom the panels show: (1) The synoptic map of the radial photospheric magnetic field distribution delivered from the WSO. (2) Derived coronal hole areas. Coloured dots represent photospheric foot-points of open field lines, with different colours used to indicate the expansion factors f_s (or solar wind speed V_{sw}) associated with the flux tubes. Areas shaded light grey (dark grey) are closed field lines with $B_r > 0$ ($B_r < 0$). The black lines identify the connectivity between the outer (open) boundary (i.e. $2.5 R_s$) and the source regions of the solar wind at the photosphere. (3) Predicted radial field strength B_r at $R = 5R_s$. The yellow line indicates where $B_r = 0$ gauss (i.e., the heliospheric current sheet). (4) Solar wind speed at the source surface ($R = 5R_s$). (5) Polarity from panel 8 in Figure 6.14 and (6) velocity from panel 3 in Figure 6.14 mapped back to the source surface. The red lines roughly indicate the time when the plasma containing the DDs marked as drawn through lines in Figure 6.14 left the source surface.

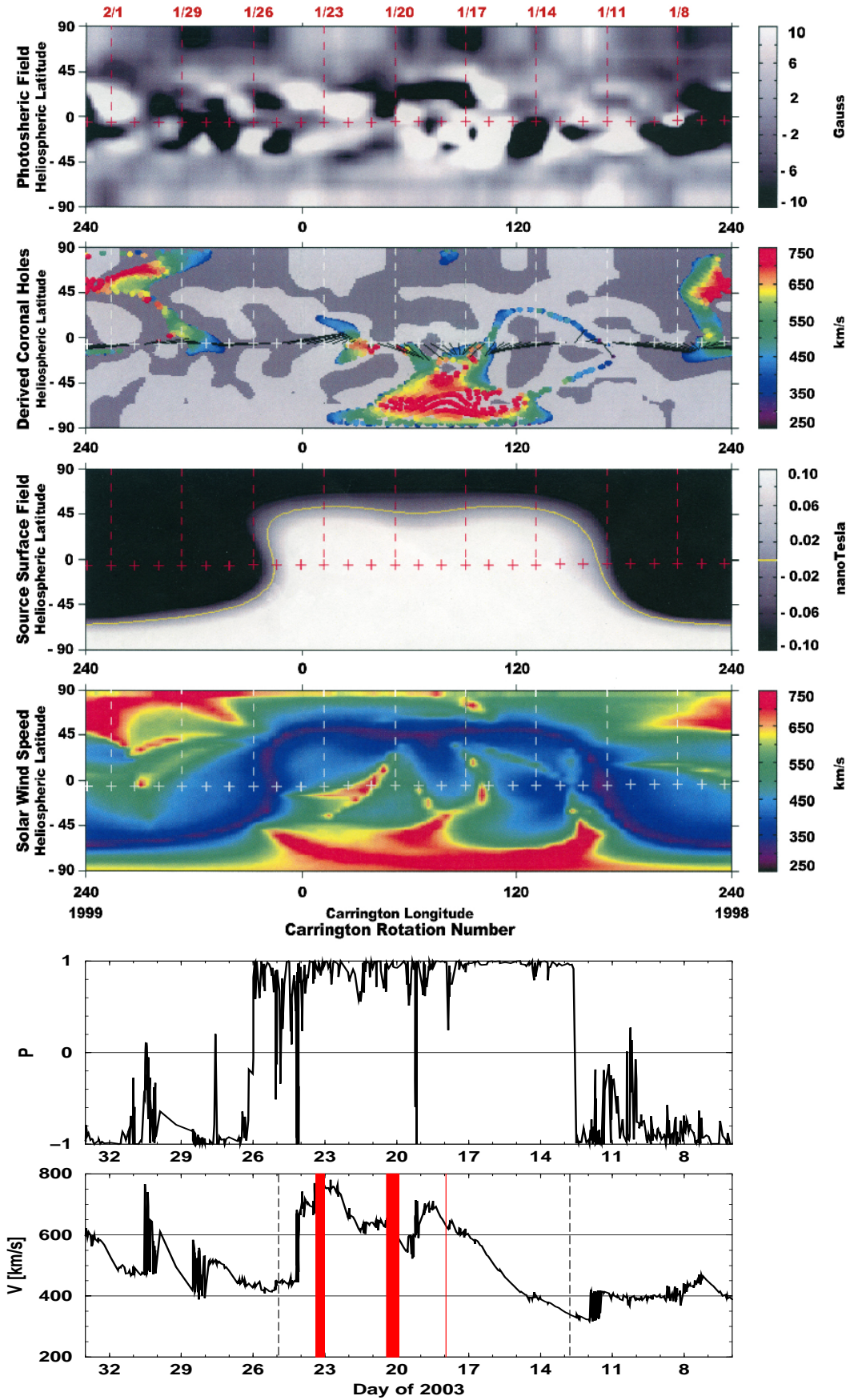


Figure 6.15: Comparison of the Wang-Sheeley model predictions (panels 1-4) with the mapped back hourly averages of polarity and velocity of FS I measured at ACE (panels 5 and 6). The top part of the Figure (Wang-Sheeley model) is taken from <http://solar.sec.noaa.gov/ws/>.

The Wang-Sheeley model predicts a large southern trans-equatorial coronal hole. The dashed lines in the bottom panel mark the boundaries of that coronal hole at $2.5 R_s$. The coincidence between the fast stream and the coronal hole boundaries is satisfactory. Another issue that needs to be tested in order to confirm the association of the fast stream with the derived coronal hole is whether the polarity measured at ACE matches that determined from the photospheric observations of the coronal hole. Comparison of panels 3 and 5 shows that the polarities are the same. Both the field predicted for the source surface and the measured interplanetary field point away from the Sun. Also the polarity changes coincide well. Note, however, that the two heliospheric current sheet (HCS) crossings are retarded by approximately one day at the mapped ACE data. Nevertheless, the general agreement is good.

As a side note we may add that the HCS is located at mid-latitudes during this and the other Carrington rotations in 2003 relevant for this study. This is in contrast to solar minimum where the HCS is generally found to be near the equator.

Finally, also the predicted solar wind speed for the source surface coincides well with the observations at ACE. Hence, the overall agreement between the predicted fast stream associated with the coronal hole and the observed stream FS I is satisfactory.

6.5.4 Extreme ultra violet imaging

Whereas hot dense plasma is trapped by the closed magnetic field lines within active regions, the plasma pours outward from coronal holes where the field lines stretch out radially and do not arch directly back to the Sun. Therefore, coronal holes are cool low density regions and appear as dark areas seemingly devoid of radiation at extreme ultraviolet (EUV) and X-ray wavelengths.³ In contrast, the most intense EUV and X-ray emission comes from within active regions. Hence, a common way to detect coronal holes is to image the Sun's atmosphere in EUV or X-ray wavelengths.

We inspect EUV images taken from the Extreme UV Imaging Telescope (EIT) [Delaboudinière *et al.*, 1995] on board the SOHO satellite. Launched on 2 December 1995, SOHO is (as ACE) in a halo orbit around the L1 Lagrangian point and is designed to study the internal structure of the Sun, its extensive outer atmosphere and the origin of the solar wind [Domingo *et al.*, 1995].

The top part of Figure 6.16 shows EIT images at a wavelength of $\lambda = 28.4$ nm which is the emission line from Fe XV at a temperature near $T = 2 \times 10^6$ K. The bright areas are active regions and the dark areas correspond to coronal holes. The nine images shown are taken on consecutive days covering the interval day 97 until day 105, i.e., approximately the time when the plasma of the fourth fast stream in Figure 6.13 left the Sun. The evolution in time follows that of a typewriter, i.e., the top row shows from left to right day 97-99, the second row shows day 100-102 and the bottom row shows day 103-105. A large trans-equatorial southern polar coronal hole in geo-effective position is clearly visible. According to the solar rotation, the visible structures move from left to right as time proceeds.

³Typical coronal temperatures are 1.0 to 1.5×10^6 K and 2 to 4×10^6 K within coronal holes and within active regions, respectively, and the density in coronal holes is less than 10% of that found in active regions.

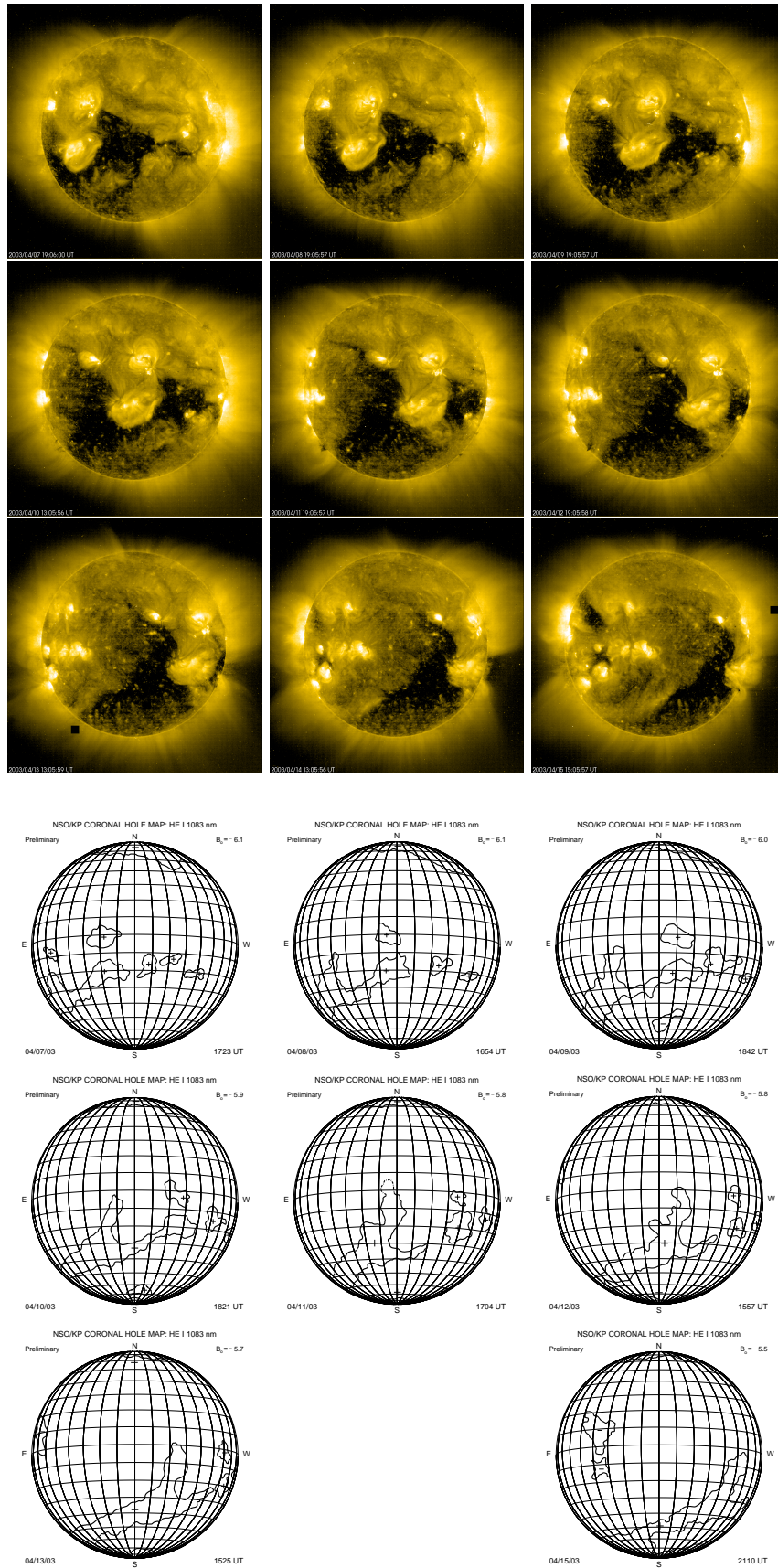


Figure 6.16: Top: SOHO EIT 284 images. Any black areas on the solar disc are likely coronal holes. Taken from <http://sohowww.nascom.nasa.gov/data/summary/gif/>. Bottom: Coronal hole map derived from the HeI 1083nm absorption line produced at NSO, Kitt Peak. Source: ftp://nsokp.nso.edu/kpvt/coronal_holes/. Daily images (maps) from 07.04.03-15.04.03 (corresponding to FS IV) are shown.

We also inspect the EIT images at the corresponding times when the plasma of the other three fast streams left the Sun. In accordance with our assumption of a persistent coronal hole being the source of the fast streams we find similar images at these three prior Carrington rotations (not shown). We also observe that the coronal hole extends with time from one rotation to the next. We check whether the onset and the end of each mapped back fast stream coincides with start and end time of geo-effectiveness of the observed coronal hole. The agreement is very good. Also note that the imaging result agrees well with the coronal hole derived by the Wang-Sheeley model. Furthermore, we test whether the observation time of the individual DDs corresponds to the geo-effective coronal hole.

We choose to present the EIT images corresponding to the fourth fast stream because of the particularly interesting structure of an active regions reaching into the large coronal hole: A tongue of an active region passes the sub-Earth point, i.e., the fast stream emanating from the coronal hole is expected to be interrupted for a couple of days, exactly as is observed in the ACE data (see Figure 6.13 \approx doy 102-105). This remarkable coherence underlines the association of the observed streams at ACE with the observed regions of open respectively closed field lines on the Sun.

6.5.5 The helium I 1083 nm absorption line

Another common way to identify flow from coronal holes is to utilise the helium I (He I) 1083 nm absorption line [Neugebauer and Alexander, 1991; Neugebauer *et al.*, 2002]. The He I line at 1083 nm is formed by electron transitions between the two lowest energy levels of the triplet states of the helium atom (ortho-helium). Hence, in order to have He I absorption an electron must be in the lowest triplet state. This can be populated either by photoionisation by UV and EUV radiation from the corona and subsequent cascading back (PR mechanism), or by direct excitation by collisions from the ground state of para-helium. The PR mechanism is effective only in regions with temperatures $T < 10000$ K, whereas collisional excitation becomes important at $T > 20000$ K [Andretta and Jones, 1997].

The lowest metastable energy levels of ortho-helium are populated rather poorly in the solar photosphere. Therefore, the absorption occurs in upper chromospheric regions (about 2000-2400 km above the photosphere) [Brajša *et al.*, 1996] where the PR mechanism dominates. Thus, helium images of the Sun are, in fact, excellent images of the chromosphere [Brajša *et al.*, 1996]. The coronal radiation is assumed to penetrate inward into the upper chromosphere, causing sufficient helium ionisation to populate the lower level of the He I 1083 nm line, resulting in an optically thin absorption of the photospheric continuum at 1083 nm. The amount of absorption, which is proportional to the optical thickness of the upper chromosphere in the 1083 nm line, depends on the density and geometrical thickness of the upper chromosphere. Absorption is increased in active regions, and reduced in coronal holes since the coronal back radiation is reduced in coronal holes. Hence, the He I 1083 nm absorption line is very shallow in coronal holes [Brajša *et al.*, 1996].

We use coronal hole maps derived from the He I 1083 nm absorption line produced at the

National Solar Observatory (NSO) vacuum telescope located on Kitt Peak, Arizona.⁴ The bottom part of Figure 6.16 shows the maps for the same days when the EUV images above were made. Although the details of the derived contours differ from the contours found in the EUV images, the general observation is the same. Apparently, the He I absorption line techniques also identifies a coronal hole on the southern hemisphere. The derived contours of coronal holes satisfactory agree with those seen in the EUV images. In particular, the “nose” of the active region can be observed.

We also plot the coronal hole boundaries obtained from the He I absorption line as a function of Carrington longitude as in Figure 6.15 and compare them to the coronal hole derived by the Wang-Sheeley model (panel 2 in Figure 6.15). The observed agreement is excellent (not shown). Since in turn the Wang-Sheeley model coincides well with the observed fast streams at ACE (see Figure 6.15), consistency between all applied methods to confirm coronal holes as the source of the four high-speed flows in 2003 is found. Also note that the polarity is consistent. Hence, together with the issues discussed according to the *in situ* solar wind measurements at ACE we unambiguously identify solar wind originating from a large coronal hole on the Sun.

6.5.6 DDs in coronal hole flow

The analysis presented above results in 83 DDs that are identified to be in coronal hole flow in 2003, i.e., 41% of the 204 DDs in the set DD_{2003} . For the purpose of the ensuing discussions we denote this subset of DD_{2003} as DD_{2003CH} . All 27 DDs in FS I marked as drawn through lines in Figure 6.14 are contained in DD_{2003CH} . We have 48 candidates in FS II, but we discarded 10 events (all events from day 49) because they are too close to the transient event around day 50, i.e., FS II contributes 38 “coronal hole events”. The remaining DDs in DD_{2003CH} are found in FS III (15 DDs) and FS IV (3 DDs). The solar wind speed is slowest in FS II compared to the other fast streams (see Figure 6.13). Sporadically $V_{sw} < 600$ km/s is observed. However, $V_{sw} = 600$ km/s is not used as a strict cut-off velocity. Also note that of the 38 events in FS II, 27 must be regarded as “unclear”. Although the ambient solar wind of these DDs is most likely from a coronal hole, it is unclear to what extent the CME, respectively the stream-stream interaction region, affects the properties of these DDs. However, the remaining 56 events in DD_{2003CH} are unambiguously in a steady coronal hole flow.

Figure 6.17 gives an overview of the field and plasma properties observed at Cluster in the vicinity of the selected DDs in 2003. The distribution of the field magnitude, the proton density and the proton velocity of DD_{2003CH} (red) are compared to the total set DD_{2003} (black). Whereas magnetic field measurements from all four spacecraft are used the plasma data are taken only from Cl 1. The number of DDs considered in the plasma data distributions is reduced to 191 because of data gaps.

The field magnitude distributions are similar for the two sets and are typical for the solar wind at 1 AU. The distribution for the coronal hole set appears to be somewhat narrower and

⁴The boundaries of coronal holes and their magnetic polarities are available online at ftp://nsokp.nso.edu/kpvt/coronal_holes/.

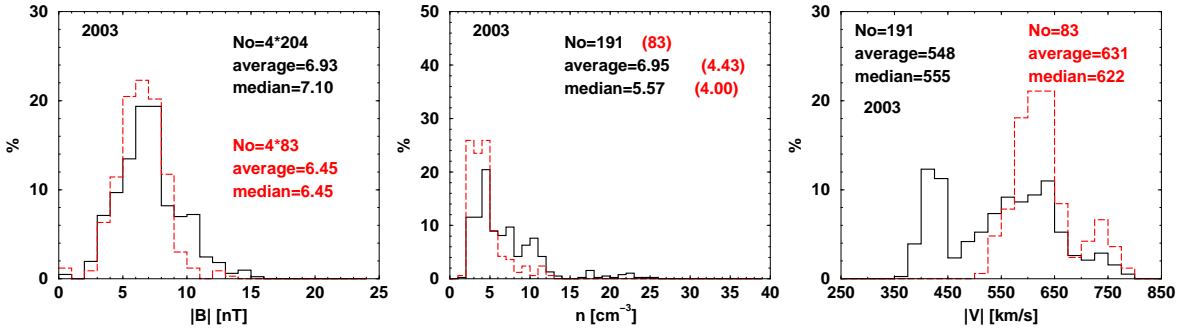


Figure 6.17: Distributions of the magnetic field and plasma parameters observed with Cluster in the vicinity of the selected DDs in 2003. Values just before and just after DDs are considered. From left to right: Field magnitude, proton density and proton velocity. The black distributions correspond to the total set DD_{2003} and the coronal hole subset is in red.

the observed magnitudes are slightly smaller. Whereas the densities are mainly in the range 2 to 5 cm $^{-3}$ (i.e., typical fast stream values) for the subset DD_{2003CH} , the density distribution considering the whole set DD_{2003} is wider with another peak around 10 cm $^{-3}$, a value typical for slow solar wind from active regions. The velocity distribution shows that DD_{2003CH} indeed only contains DDs in fast streams. The distribution of the total set is bimodal with another peak around 425 km/s.

The DDs found in 2001 are most likely embedded in solar wind from active regions on the Sun. Therefore, it will be interesting to compare the results, e.g. according to DD classification, we obtain for the sets DD_{2001} , DD_{2003} and DD_{2003CH} . In particular the test of the hypothesis of high RD abundances in coronal hole streams is of considerable interest, and can be easily performed after the thorough preparatory work presented in this section.

In summary we have shown that different types of solar wind are present during the intervals we use for DD observation. In particular we have clearly identified high-speed coronal hole flows. We have defined a subset DD_{2003CH} of all DDs selected in 2003 which only contains DDs identified within solar wind from coronal holes. According to earlier observations and theories this set should contain mainly RDs. In the following chapters this hypothesis will be tested exploiting the enhanced possibilities of the Cluster mission.

DETERMINATION OF DISCONTINUITY NORMALS

The determination of the surface normal is a key issue in analysing MHD discontinuities. This chapter describes techniques to compute the normals. Both single-spacecraft methods (the *minimum variance analysis* and the *cross product method*) and a multi-spacecraft *triangulation method* are discussed.

In a nutshell, minimum variance analysis (MVA) uses the fact that the normal is the direction with smallest variations of the magnetic field (as B_n is a constant). The cross-product method works only for TDs; then the normal is the vector perpendicular to the two magnetic field vectors on either side of the discontinuity. The triangulation method is the most accurate, but requires four spacecraft: the normal is geometrically determined based on the relative timing of the crossing of the four spacecraft through the DD.

The analysis of the differences between these three methods provides the foundation for our conclusions in the reminder of this thesis. There we claim that MVA produces normals that are inconsistent between the four spacecraft, whereas the triangulation method provides accurate normal estimates. Furthermore, to discern TDs and RDs by analysis of the magnitude of the normal component of the magnetic field requires accurate normals and estimates of their precision.

Sections 7.1 gives an overview of normal determination techniques. Sections 7.2 - 7.4 contain detailed descriptions and error analyses of the MVA, cross product and triangulation methods, respectively.

7.1 Overview of normal determination techniques

Most analyses of discontinuities are based on data from a single spacecraft. Common single-spacecraft methods to determine the surface normals exploit the jump conditions across the discontinuities (see section 3.1). The continuity of the normal component of the magnetic field (equation 3.2) is most useful as the magnetic field data is usually the most accurate and with relatively high time resolution.

Ideally, applications of the jump conditions would involve simultaneous measurements on both sides of the discontinuity using two independent measuring platforms. If the data stems from a single satellite collecting data as it passes through the DD, one has to assume that the external conditions do not change with time, i.e. time stationarity is assumed. The common techniques either use observations taken well up- and downstream of the transition or use the variations within the transition of the DD.

In the first case the normal to a planar surface can be determined if two vectors which are parallel to the surface can be found. If the type of discontinuity is known beforehand, and it is identified to be a shock, the *coplanarity theorem* can be used. The coplanarity theorem, deduced from the jump conditions, states that the magnetic field on both sides of the shock and the shock normal are in the same plane (e.g. *Colburn and Sonett [1966]*). Therefore, $(\mathbf{B}_1 \times \mathbf{B}_2)$ is perpendicular to \mathbf{n} (\mathbf{B}_1 and \mathbf{B}_2 are the field vectors measured on opposite sides of the shock). Because of the continuity of the normal magnetic field also $(\mathbf{B}_1 - \mathbf{B}_2)$ is tangential to the boundary. Hence, the shock normal can be calculated as $\mathbf{n} = \pm((\mathbf{B}_1 \times \mathbf{B}_2) \times (\mathbf{B}_1 - \mathbf{B}_2)) / |(\mathbf{B}_1 \times \mathbf{B}_2) \times (\mathbf{B}_1 - \mathbf{B}_2)|$. This method is most widely used since only the magnetic field is needed. If the discontinuity is identified to be a TD, then the normal is simply given by $\mathbf{n} = \pm(\mathbf{B}_1 \times \mathbf{B}_2) / |\mathbf{B}_1 \times \mathbf{B}_2|$ (see equation 7.8 in section 7.3).

Techniques that use variations within the transition are referred to as minimum (or maximum) variance analysis methods. In principle *minimum* variance analysis can be applied to quantities that theoretically possess a constant normal component across the discontinuity. For 1-D discontinuities these are the magnetic field (equation 3.2) and the mass flux (equation 3.3). The normal is then identified as the direction in which the variation of the magnetic field [*Sonnerup and Cahill, 1967; Sonnerup and Scheible, 1998*] or of the mass flux [*Sonnerup et al., 1987; Sonnerup and Scheible, 1998*] is minimised.

In practice, due to relatively large uncertainties in the plasma measurements and a relatively poor time resolution, minimum variance analysis using mass flux has a larger uncertainty than the magnetic field minimum variance analysis. Even more important, mass flux conservation holds in the frame moving with the discontinuity. Hence, the measured plasma velocity must be translated into the moving frame with the *a priori* unknown speed of the discontinuity relative to the spacecraft frame. For a TD the discontinuity speed is simply given by $U = \mathbf{V}_{sw} \cdot \mathbf{n}$, where \mathbf{V}_{sw} is the solar wind speed. For an RD the discontinuity speed must be obtained separately because there is a net mass flux across an RD. *Sonnerup and Scheible [1998]* suggest an iterative solution to this problem. As a consequence of these problems the magnetic field minimum variance (in the following referred to as MVA), has become the most widely applied tool for finding normals of discontinuities of unknown type.

We will discuss this method and its limitations in detail in the following section. Here we only note that by choosing the frame of reference such that the z -axis is parallel to $[\mathbf{B}]$, \mathbf{n} must lie in the x - y plane. After this transformation the search for \mathbf{n} is confined to a plane. This method is called BMVA [Söding, 1999]. For TDs and for RDs in an isotropic plasma (i.e., constant density across the RD) the frame of reference can also be chosen such that the z -axis is parallel to the difference vector of the plasma velocity; then the normal component of the velocity is also constant. This method is referred to as VMVA [Söding, 1999]. A more sophisticated technique which incorporates several conservation laws in one grand optimisation has been proposed in Kawano and Higuchi [1996]. Besides \mathbf{n} this method also determines the speed of the discontinuity along \mathbf{n} . While promising in principle, such approaches are affected by the limited quality of the plasma data. It is important that any such procedure should allow greater weight to be placed on quantities that are well determined with less weight on quantities that are less well determined. Note that the above methods apply only to 1-D discontinuities. Söding and Neubauer [1999]; Söding [1999] developed a minimum variance technique for 2-D structures applicable to events observed at two spacecraft.

An alternative to the *minimum* variance analysis is the *maximum* variance analysis. Instead of utilising the conservation of the *normal* component of physical quantities, it is used that the *tangential* electric field is constant (see section 3.1) in the latter [Sonnerup *et al.*, 1987]. Analogous to the minimum variance analysis of the magnetic field, the discontinuity normal is along the maximum variance direction of the electric field. The electric field data for the analysis can be obtained from either direct measurements of the electric field or the convective electric field derived from the magnetic field and plasma velocity measurements according to the frozen-in condition, or $\mathbf{E} = -\mathbf{V} \times \mathbf{B}$. It is important to note that the electric field must be measured in a frame of reference moving with the discontinuity. In the spacecraft frame one obtains a tangential electric field change due to the motion of the spacecraft relative to the boundary. To account for this effect, one has to transfer the electric field into a frame in which the discontinuity is at rest. As for the mass flux minimum variance analysis one suffers from the problem that the discontinuity speed has to be known before the normal of the discontinuity is determined. Sonnerup *et al.* [1987] developed an iterative method to solve this problem. Because of these problems and the generally lower quality of the plasma measurements, the magnetic field minimum variance analysis is more reliable in most cases. However, the electric field maximum variance analysis can be used as an alternative in cases when MVA has a large uncertainty (see the following section).

Multi-spacecraft methods

The use of multiple spacecraft facilitates the application of more advanced techniques based on less assumptions. Denskat and Burlaga [1977] use magnetic field and solar wind velocity data from the Explorer 33 and Explorer 35 spacecraft to study Alfvénic fluctuations in the interplanetary medium. If only two spacecraft are used, a further condition besides the time lag between wave front occurrence is needed. Denskat and Burlaga [1977] use the conservation of the magnetic field normal component: $(\mathbf{B}_2 - \mathbf{B}_1) \cdot \mathbf{n} = 0$. In addition they also need the solar wind speed measured at one of the two spacecraft. Neglecting the propagation speed of the wave front they use $(\mathbf{r}_{12} - \mathbf{V}_{sw}t_{12}) \cdot \mathbf{n} = 0$, where \mathbf{r}_{12} is the separation vector between

the two spacecraft and t_{12} the time lag. Hence, the wave front normal can be determined as $\mathbf{n} = \pm((\mathbf{B}_2 - \mathbf{B}_1) \times (\mathbf{r}_{12} - \mathbf{V}_{sw}t_{12})) / |(\mathbf{B}_2 - \mathbf{B}_1) \times (\mathbf{r}_{12} - \mathbf{V}_{sw}t_{12})|$. Applying this technique they find a strong discrepancy between the minimum variance direction and the timing derived normals. The distribution of the angle between these two directions has a peak between 40° and 50° . Whereas the MVA normals are mostly aligned with the magnetic field, the timing derived normals tend to be perpendicular to the magnetic field. *Denskat and Burlaga [1977]* conclude that MVA does not give a good estimate of the phase front direction and that the discrepancy is due to a misinterpretation of the significance of the minimum variance direction. *Horbury et al. [2001a]* confirm this conclusion. ACE magnetic field and velocity data are used to predict the arrival time at the Wind spacecraft of sharp southward turnings of the interplanetary magnetic field in order to compare the accuracy of various methods of estimating the normals. They find that of the 70% of events observed at ACE that could be identified at Wind, 93% of arrival times were predicted within 10 minutes using the cross product of the field immediately up- and downstream of the discontinuity, compared to only 56% using MVA. The poor performance of MVA is even more remarkable noting that 67% of the arrival times were predicted within 10 minutes when simply assuming a sunward normal.

When data from three spacecraft are available the discontinuity normal can be calculated without use of any jump condition. However, besides the timing information between the pairs of spacecraft the plasma velocity measured at one of the spacecraft is needed. Applying this triangulation technique to the Explorers 33, 34 and 35 *Burlaga and Ness [1969]* find normals of interplanetary discontinuities which are in good agreement with the normals determined by the cross product of the field immediately up- and downstream of the discontinuity. *Burlaga and Ness [1969]* conclude that the six discontinuities investigated are TDs. Utilising the inter-spacecraft timings between Geotail, Wind and IMP 8 *Horbury et al. [2001b]* find that MVA results in many normal estimates lying far from the timing-derived normals, in agreement with *Denskat and Burlaga [1977]*. *Horbury et al. [2001b]* conclude that the poor performance of MVA is due to surface waves on the discontinuities.

Finally, using four spacecraft only the timing information between the pairs of spacecraft is needed to determine the discontinuity normal as is detailed in section 7.4. With the four coordinated spacecraft of the Cluster mission equipped with state of the art instruments we significantly contribute to the developing understanding of the limitations of MVA. Our results, in particular concerning the reliability of MVA, are so far the clearest and most plausible (*Knetter et al. [2003]*, *Knetter et al. [2004]* and in detail the present work).

7.2 Sonnerup-Cahill minimum variance analysis

This section gives a detailed description of the Sonnerup-Cahill minimum variance analysis (MVA) method and a critical discussion of the quality of the obtained discontinuity normals. MVA is the most widely used single-spacecraft tool for this purpose, in particular if the type of discontinuity is not *a priori* known. It is frequently applied to interplanetary waves and directional discontinuities as well as to magnetopause crossings. However, we have shown that recent multi-spacecraft studies indicate fundamental deficiencies of this method.

7.2.1 Description of the method

The Sonnerup-Cahill MVA [Sonnerup and Cahill, 1967] is applied to magnetic field vector data measured during a spacecraft traversal of a discontinuity. It is based on an idealised 1-D model of the surface. Choosing a (*a priori* unknown) local Cartesian coordinate system such that its z -axis points along the sought-after discontinuity normal vector \mathbf{n} , i.e. $\partial_x = \partial_y = 0$, it follows from the solenoidality of the magnetic field (see also section 3.1): $\nabla \cdot \mathbf{B} = \partial_z B_z = 0$.

Application of this condition to discontinuities of finite thickness involves that the idealised 1-D model includes the assumption that the radius of curvature and the characteristic length for lateral changes of its structure are much larger than its thickness.

The high time resolution available in many magnetometer experiments allows many vector measurements \mathbf{B}^i ($i = 1, \dots, N$) to be made during a traversal. The minimum variance analysis approximates an estimate for the discontinuity normal \mathbf{n} as the direction in space along which the field-component set $\{\mathbf{B}^i \cdot \mathbf{n}\}$ ($i = 1, \dots, N$) has minimum variance, i.e., \mathbf{n} is determined by minimisation of

$$\sigma^2 = \frac{1}{N} \sum_{i=1}^N |(\mathbf{B}^i - \langle \mathbf{B} \rangle) \cdot \mathbf{n}|^2 \quad (7.1)$$

where $\langle \mathbf{B} \rangle = \frac{1}{N} \sum_{i=1}^N \mathbf{B}^i$ is the average over the N field vectors [Sonnerup and Cahill, 1967]. Using a Lagrange multiplier λ the minimisation of σ^2 with the constraint $|\mathbf{n}| = 1$ can be formulated as an eigenvalue problem:

$$\mathbf{M}^B \mathbf{n} = \lambda \mathbf{n} \quad (7.2)$$

where \mathbf{M}^B is the magnetic covariant matrix which reads in component form

$$M_{\mu\nu}^B = \langle B_\mu B_\nu \rangle - \langle B_\mu \rangle \langle B_\nu \rangle \quad (7.3)$$

The allowed λ values are the eigenvalues $\lambda_1 \geq \lambda_2 \geq \lambda_3$ of \mathbf{M}^B . Since \mathbf{M}^B is symmetric all eigenvalues are real and the corresponding eigenvectors \mathbf{x}_1 , \mathbf{x}_2 and \mathbf{x}_3 are orthogonal. The three eigenvectors represent the direction of maximum, intermediate and minimum variance of the field component along each vector and the corresponding eigenvalues λ_1 , λ_2 and λ_3 represent the actual variances in those field components and are therefore non-negative [Sonnerup and Scheible, 1998].

The eigenvector \mathbf{x}_3 , corresponding to the smallest eigenvalue λ_3 , approximates the discontinuity normal and λ_3 itself represents the variance of the magnetic field component along the estimated normal. The eigenvectors \mathbf{x}_1 and \mathbf{x}_2 are tangential to the discontinuity and the set $\{\mathbf{x}_1, \mathbf{x}_2, \mathbf{x}_3\}$ arranged as a right-handed orthonormal triad provides a convenient natural coordinate system for the analysis [Sonnerup and Scheible, 1998].

Deficiencies of the MVA method

For an ideal 1-D structure, $\sigma^2 = 0$ in the normal-field component. In that case MVA yields $\lambda_3 = 0$. For real discontinuities in space one usually finds $\lambda_3 > 0$, i.e., $\sigma^2 \neq 0$ along the

direction of minimum variance. Several reasons can account for this discrepancy to an ideal 1-D structure. First, the discontinuity may not be strictly 1-D, it might have 2-D or 3-D internal structures. Second, since the field vectors are not measured simultaneously, time stationarity needs to be assumed. In reality there could be temporal fluctuations in the orientation of the discontinuity normal which may occur during the spacecraft traversal time. Third, random and systematic measurement errors may occur. For modern magnetometers, the former are usually negligible compared to other uncertainties but the latter can sometimes arise in form of a zero-level offset. Note that a constant offset does not influence the normal determination. However, a problem arises for satellites that rotate around a spin axis. Since the spin axis magnetometer remains unmodulated by the satellite rotation the calculated normal vector is likely to tend to coincide with the satellite spin axis rather than with the true normal direction [Sonnerup and Cahill, 1967]. If for example the true magnetic field variations perpendicular to the spin axis are zero, then due to the spin modulation one observes a non-zero component.

Assuming that all the effects mentioned above are negligible, another model straightforwardly explaining $\lambda_3 > 0$ can be thought of. Namely, an ideal stationary 1-D structure observed with negligible measurement errors that is superposed by other fluctuations and wave fields. Since MVA is incapable of separating the variations of the true 1-D structure from those of other origin, any kind of superposed fluctuations, with non-zero variance of the field-component normal to the 1-D structure, results in a non-zero value of λ_3 . Note that if those superposed fluctuations are purely isotropic, then the determination of \mathbf{n} is not affected. However, a serious problem occurs when the superposed fluctuations or waves are anisotropic. For example, if the magnetic perturbations within the 1-D structure are mainly along the true normal of the 1-D discontinuity, the minimum variance direction may not be the normal direction of the discontinuity. This will be detailed at the end of this section.

Degeneracies of the variance ellipsoid

For MVA to be applicable one needs at least three measured field vectors. If the used data set consists of exactly three vectors, then the variation can only take place in the plane perpendicular to \mathbf{x}_3 and one always finds $\lambda_3 = 0$. If in addition the difference vectors are aligned, one also finds $\lambda_2 = 0$ because the variation then takes place in only one direction. In this case the covariant matrix is said to be degenerate, and all that can be said about \mathbf{x}_2 and \mathbf{x}_3 is that they are perpendicular to \mathbf{x}_1 , i.e., the normal of the structure could be anything perpendicular to the direction of maximum variance.

The problem of degeneracy is also of major importance when a large number of field vectors within the transition are available, especially in the context of superposed fluctuations and waves. It can be addressed conveniently in terms of the *variance ellipsoid* [Sonnerup and Scheible, 1998] shown in Figure 7.1. The principal axes half lengths of the variance ellipsoid are $\sqrt{\lambda_1}$, $\sqrt{\lambda_2}$ and $\sqrt{\lambda_3}$, and the distance along an arbitrarily chosen direction, from the origin to the intersection of a line along that direction with the ellipsoid surface, represents the standard deviation of the magnetic field component along the chosen direction [Sonnerup and Scheible, 1998].

Three types of (near) degeneracy are possible [Sonnerup and Scheible, 1998]. First, $\lambda_1 \approx$

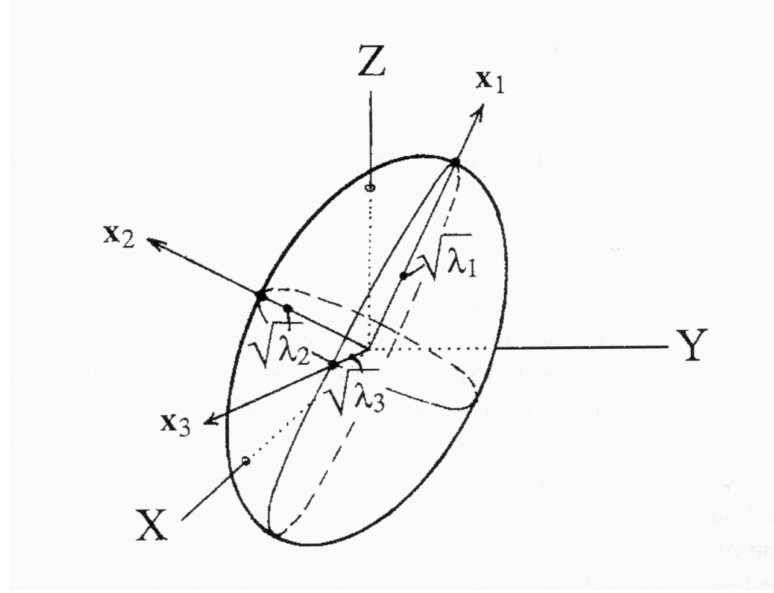


Figure 7.1: Variance ellipsoid. The three eigenvectors \mathbf{x}_1 , \mathbf{x}_2 and \mathbf{x}_3 are shown in the frame of reference in which the magnetic field data are given. Taken from Sonnerup and Scheible [1998].

$\lambda_2 \approx \lambda_3$, i.e. a nearly spherical variance ellipsoid. In this case no information about directions normal or tangential to a discontinuity can be obtained. Second, $\lambda_1 \approx \lambda_2$. Provided that $\lambda_3 \ll \lambda_1 \approx \lambda_2$ this corresponds to a discus-shaped (oblate) variance ellipsoid and the discontinuity normal is well determined via MVA.

However, for interplanetary discontinuities the third case of degeneracy, i.e. $\lambda_2 \approx \lambda_3$, is frequently observed (see section 8.3.1). In this case the variance ellipsoid is cigar-shaped (prolate) with the minimum and intermediate variance directions being constrained to be perpendicular to \mathbf{x}_1 but otherwise arbitrary. Provided that $\lambda_1 \gg \lambda_2 \approx \lambda_3$ (as typically observed for interplanetary DDs) the only statement that can be made using MVA is that the normal lies in the plane perpendicular to the well-determined direction of maximum variance (\mathbf{x}_1).

For $\lambda_2 \approx \lambda_3$ or equivalently λ_2/λ_3 being small, the minimum variance direction is extremely sensitive to superposed fluctuations or wave fields. If these magnetic perturbations are anisotropic and not aligned with \mathbf{x}_1 the direction of minimum variance will be basically determined by the superposed fluctuations. In extreme cases, the orientation of the intermediate and minimum variance directions may trade places, corresponding approximately to a 90° rotation of \mathbf{x}_2 and \mathbf{x}_3 around \mathbf{x}_1 , in response to a minor adjustment of the number of data points or the data filtering used in the analysis [Sonnerup and Scheible, 1998].

Eigenvalue ratio as estimator for uncertainty and further deficiencies

For these reasons the eigenvalue ratio λ_2/λ_3 is commonly used as an indicator for the reliability of the minimum variance direction as an estimator for the discontinuity normal. In order to ensure significant MVA results a minimum value (lower limit) $(\lambda_2/\lambda_3)^L$ is used. Assuming that for eigenvalue ratios greater than $(\lambda_2/\lambda_3)^L$ the interpretation of the minimum variance direction as the discontinuity normal is justified all discontinuities with $\lambda_2/\lambda_3 \geq (\lambda_2/\lambda_3)^L$

are used, and those with $\lambda_2/\lambda_3 < (\lambda_2/\lambda_3)^L$ are discarded. Commonly, $1.5 \leq (\lambda_2/\lambda_3)^L \leq 2.5$ is used: For example, *Sonnerup and Cahill* [1967] and *Söding* [1999] use $(\lambda_2/\lambda_3)^L = 1.5$, *Neugebauer et al.* [1984] and *Horbury et al.* [2001b] use $(\lambda_2/\lambda_3)^L = 2.0$ and *Smith* [1973a] use $(\lambda_2/\lambda_3)^L = 2.5$. The choice of such apparently small lower limits is believed to be justified by a numerical study of ideal discontinuities in the presence of *isotropic* noise [*Lepping and Behannon*, 1980], to be discussed in the following section.

However, *Lepping and Behannon* [1980] also identify another parameter that considerably determines the reliability of MVA, namely the discontinuity spreading angle ω , i.e., the angle between the magnetic field vector upstream and downstream of the discontinuity. The larger this angle, the smaller the error [*Lepping and Behannon*, 1980]. This is rather obvious since for large ω the discontinuity will be more clearly distinguished from the natural noise and superposed wave fields. However, the importance of ω has often been disregarded. *Lepping and Behannon* [1986] use $(\lambda_2/\lambda_3)^L = 2.0$ and in addition $\omega^L = 30^\circ$ as a lower limit for the spreading angle, and *Lepping et al.* [2003] use $\omega^L = 90^\circ$. Note that the present work will reveal that the lower limits for the eigenvalue ratio used in past studies as presented above are overly optimistic and confirm that ω is important.

The example of a magnetopause crossing presented in *Sonnerup and Scheible* [1998] showing that the removal of only one data point at each end of the data interval leads to an exchange of the minimum and the intermediate variance direction, points towards another general problem associated with MVA: In principle, one may select many different time intervals for the MVA, and each of them provides a different normal. Because of the statistical nature of MVA a large number of field vectors minimises the uncertainty. However, one should avoid selecting the interval too large, i.e., larger than the transition, because then too much weight on the fields on the two sides is put, and the minimum variance direction would also be determined by the wave activity upstream and downstream of the discontinuity. High resolution measurements generally yield many field vectors within the transition. On the one hand this increases the statistical significance of MVA (see next section), however, on the other hand, as the resolution increases, one may be able to resolve the wave activity within the discontinuity. As said above, these waves may cause an uncertainty in the determination of the normal direction as well. Filtering the data to pass only frequencies consistent with the thickness of the structure helps reducing the uncertainty of the normal determination.

Further comments

Before continuing the discussion of the uncertainties in more detail in the following section we may add three more comments on MVA: (1) The calculation of the covariant matrix (and thus MVA itself) is independent of the temporal order of the measured field vectors used. (2) MVA can be applied to all kinds of discontinuities. In particular there are no restrictions for the normal component of the magnetic field. However, it is most useful for RDs, since it has a large uncertainty for TDs as we will discuss in the following section. With the additional constraint $\langle \mathbf{B} \rangle \cdot \mathbf{n} = 0$, MVA can be modified to give better results for TDs [*Sonnerup and Cahill*, 1968]. However, then the type of discontinuity needs to be known *a priori*. (3) Whenever we refer to “MVA” we mean the Sonnerup-Cahill minimum variance method as

described in this section. This is important to note since there is another minimum variance technique referred to as “Siscoe MVA” [Siscoe *et al.*, 1968] which is formally similar to the Sonnerup-Cahill MVA. Siscoe *et al.* [1968] minimise the sum of the squares of the individual normal field components. In other words, they drop the second term in equation 7.1. Therefore, “Siscoe MVA” can be applied only when the field vectors rotate in the discontinuity plane from the pre-event direction to the post-event direction, i.e., the direction of minimum variance coincides with the discontinuity normal only if the discontinuity is a TD.

7.2.2 Summary of past error analysis approaches

The following error analysis of MVA is imperative for the interpretation of any results derived from this method. In particular to discern RDs and TDs by analysis of the magnetic field normal component the uncertainty needs to be known.

The uncertainties in the orientations of the eigenvectors are generally a sum of a statistical error and a systematic error. Whereas the statistical error can be estimated by use of standard analytical tools or by use of computational techniques, the systematic part, as e.g. a lack of stationarity or one-dimensionality, is not easy to assess.

Several authors have suggested approaches to estimate the error associated with MVA [Sonnerup, 1971; Lepping and Behannon, 1980; Hoppe *et al.*, 1981; Kawano and Higuchi, 1995; Khrabrov and Sonnerup, 1998; Sonnerup and Scheible, 1998]. In the following we only illustrate the basic concepts presented in Lepping and Behannon [1980], Khrabrov and Sonnerup [1998] and Sonnerup and Scheible [1998]; the other approaches are given in appendix C. Here we focus on discussing the major problems.

Empirical error estimate

Lepping and Behannon [1980] carry out a computer simulation of discontinuities with strictly known characteristics. The artificially created ideal discontinuities are simulated by a rotation of the tangential magnetic field by an angle ω while the normal field component B_n is strictly constant. The field magnitude B_p of the ideal discontinuities is also kept constant. The number of field vectors is chosen to be proportional to the angle change ω . To these ideal configurations is added *isotropic* noise. For a given noise amplitude these simulated DDs (for fixed input values ω , B_n and B_p) are then used as input for MVA. For each input value of the standard deviation of the noise distribution this procedure is repeated 100 times. For a given set of ideal DD properties the program loops through an adjustable number of noise levels, creating a full suite of sets from “quiet” to “noisy”. The process is repeated for another set of ideal DD properties (different B_n and ω), and so on, until a reasonable spectrum of DDs is created. An empirical error estimate for the relative normal component is proposed for the ranges $30^\circ < \omega < 120^\circ$ and $1 < \lambda_2/\lambda_3 < 5.6$:

$$\frac{\Delta|B_n|}{B} = \frac{3}{4} \left[\exp \left(\frac{120^\circ - \omega}{120^\circ} \right)^3 \right] \sin(\beta) \Lambda^{3.60+2.44 \log \Lambda} \quad (7.4)$$

where $\beta = \cos^{-1}(|B_n|/B)$ and $\Lambda = \lambda_3/\lambda_1 + \lambda_3/\lambda_2$. Note that this error estimate depends on the eigenvalue ratios and on ω and β . Since the eigenvalue ratio λ_1/λ_3 is usually considerably larger than λ_2/λ_3 , λ_2/λ_3 is the ratio of greatest concern in this error analysis, i.e., $\Lambda \approx \lambda_2/\lambda_3$ in most cases of interest. The β -dependence implies that for given ω and noise level, the B_n estimate is on average worse for TDs than for RDs. *Lepping and Behannon* [1980] find that resulting error values are greater by a factor of 2 or more for TDs relative to RDs. This is of considerable interest for this and related works, since it complicates the problem of proving a DD to be a TD by means of vanishing B_n .

In accordance with *Sonnerup* [1971] (see appendix C) they also find that the directional error is larger in the \mathbf{x}_2 - \mathbf{x}_3 plane than in the \mathbf{x}_1 - \mathbf{x}_3 plane. *Lepping and Behannon* [1980] further propose that using $(\lambda_2/\lambda_3)^L = 2$ as a minimum allowed value of λ_2/λ_3 is a sufficient criterion in the majority of cases to at least prevent incorrect interpretation. However, they also state that in some cases (less than 10% of the total cases studied) this criterion did not work, and that in these cases ω was small ($< 40^\circ$). Therefore, *Lepping and Behannon* [1980] suggest to also avoid such small-angle cases. The latter has, however, not been adopted by the community. As stated in the previous section the most common criterion is to use $(\lambda_2/\lambda_3)^L = 2$ as a lower limit.

Another result of *Lepping and Behannon* [1980] is that only 5% of the TDs have errors as large as $0.3 |B_n|/B$ according to their error analysis, where in this case $\Delta B_n = B_n$. Conversely, all DDs whose $|B_n|/B$ exceeds 0.3 are with 95% certainty RDs. Therefore they suggest to use this value, instead of 0.4 as proposed by *Smith* [1973a] (see also section 3.1.2), as an upper bound on the relative normal component value for TDs that can be used to separate them from RDs in studies using only magnetic field data from a single spacecraft.

However, in order to adequately interpret these results, the assumptions made must be scrutinised. First, the number of field vectors within the transition being proportional to ω is not what we observe for interplanetary discontinuities. We find thin DDs (small number of field vectors) with large ω , but also thick DDs with small ω . From our experience (we have not quantified this) we believe MVA yielding better normal estimates in the first case. One can argue that the assumption of one-dimensionality is more likely to be fulfilled for thin DDs possessing a large angular change of the field vectors than for thick DDs with the same ω . Second, and this is probably more important, the model of 1-D structures being superposed by *isotropic* noise may not be justified. The fluctuations and wave fields that are superposed to real interplanetary discontinuities are more likely to be anisotropic. We remind that the addition of isotropic noise indeed changes the variance ellipsoid (in the extreme case when the noise to signal ratio is very large the ellipsoid approaches a sphere), but the eigenvectors remain unchanged. In contrast, anisotropic noise does change the eigenvectors, particularly \mathbf{x}_3 . Therefore, we believe the estimate for the angular uncertainty of \mathbf{x}_3 and thus the estimate for the uncertainty of B_n to be overly optimistic. Also, we suggest that $\lambda_2/\lambda_3 > 2$ does not imply reliable MVA normals. Yet, the conclusion that the MVA error is largest for TDs remains valid. The same holds for the conclusion that the error is also dependent on ω .

Statistical error

Assuming that no systematic errors are present, a non-zero value of λ_3 is solely due to the statistical error. Assuming further that the noise is stationary, isotropic and spatially uncorrelated, this statistical part of the error can be calculated from first principles [Khrabrov and Sonnerup, 1998]. Khrabrov and Sonnerup [1998] note explicitly that in most applications this approach is a radical idealisation prompted by a lack of knowledge of the actual properties of the physical and instrumental noise. Therefore the resulting error estimates must be regarded as a strictly *a priori* assessment of the uncertainty. Khrabrov and Sonnerup [1998] perform a perturbation analysis on the eigenvector equation 7.2:

$$(M^* + \Delta M)(\mathbf{x}_i^* + \Delta \mathbf{x}_i) = (\lambda_i^* + \Delta \lambda_i)(\mathbf{x}_i^* + \Delta \mathbf{x}_i) \quad (7.5)$$

where the unknown noise-free state is denoted by an asterisk, and $i = 1, 2, 3$ correspond to maximum, intermediate and minimum variance associated with M^* , respectively. In the linear approximation this ansatz yields the angular error estimates [Khrabrov and Sonnerup, 1998]:

$$|\Delta \phi_{ij}| = |\Delta \phi_{ji}| = \left[\frac{\lambda_3(\lambda_i + \lambda_j - \lambda_3)}{(N-1)(\lambda_i - \lambda_j)^2} \right]^{\frac{1}{2}}, \quad i \neq j \quad (7.6)$$

where $|\Delta \phi_{ij}|$ denotes the expected angular uncertainty of eigenvector \mathbf{x}_i for rotation toward or away from eigenvector \mathbf{x}_j . Note that this estimate of the noise component decreases as $N^{-1/2}$ as expected for the purely statistical part of the error. Again, the error depends on the eigenvalues. Except for very small values of $\lambda_3/(N-1)$, the uncertainty becomes large for the nearly degenerate case, $\lambda_i \approx \lambda_j$. This is an expected and desirable property, but the linear analysis used in producing the error estimate then breaks down [Khrabrov and Sonnerup, 1998]. Since, for interplanetary discontinuities, $\lambda_1 - \lambda_3$ is generally much larger than $\lambda_2 - \lambda_3$ it follows that $|\Delta \phi_{32}|$ is considerably larger than $|\Delta \phi_{31}|$.

Assuming the error associated with the variance λ_3 and the two uncertainties associated with the angular error estimates for \mathbf{x}_3 to be independent, Sonnerup and Scheible [1998] write the composite statistical error estimate for $\langle \mathbf{B} \rangle \cdot \mathbf{x}_3$ as

$$|\Delta(\mathbf{B} \cdot \mathbf{x}_3)| = \left[\frac{\lambda_3}{N-1} + (\Delta \phi_{32} \langle \mathbf{B} \rangle \cdot \mathbf{x}_2)^2 + (\Delta \phi_{31} \langle \mathbf{B} \rangle \cdot \mathbf{x}_1)^2 \right]^{\frac{1}{2}} \quad (7.7)$$

Note that for small noise-to-signal ratios no assumptions about the probability distribution of the noise are required to calculate the angular uncertainty of \mathbf{x}_3 [Khrabrov and Sonnerup, 1998].

Finally, Sonnerup and Scheible [1998] point out that, because the conditions of a real observation of a discontinuity differ from the idealised model, a rule of thumb for reliability of the minimum variance direction for common practice should be that $\lambda_2/\lambda_3 \geq 10$ for $N < 50$. Note that this value is by a factor of 5 larger than that proposed by Lepping and Behannon [1980] which has been frequently used. Our multi-spacecraft analysis will show that this rather intuitive estimate by [Khrabrov and Sonnerup, 1998] appears to be plausible.

Comparison and discussion of the error estimates

Sonnerup and Scheible [1998] compare the results of several approaches to assess the MVA error for a specific magnetopause crossing. They find that the empirical method proposed by *Lepping and Behannon* [1980], the *bootstrap method* (see appendix C) and the purely statistical approach by *Khrabrov and Sonnerup* [1998] yield comparable error values.

Furthermore, they show, according to *Kawano and Higuchi* [1995], that the errors predicted by *Sonnerup* [1971] (see appendix C) exhibit a $N^{-1/4}$ dependence instead of the $N^{-1/2}$ dependence expected for stationary random noise. They argue that the weaker dependence on N found for this method may perhaps be justified when significant systematic errors are present in addition to the noise, but for stationary isotropic noise, equation 7.6 has better theoretical justification. *Sonnerup and Scheible* [1998] also claim that equations C.7 [*Hoppe et al.*, 1981] do not contain N at all. Hence, these error estimates would not approach zero as $N \rightarrow \infty$, as expected for time-stationary statistical fluctuations.

The discussion regarding statistical error versus systematic error is of considerable interest. We disagree with the reasoning of *Sonnerup and Scheible* [1998] that a larger number of data points inevitably leads to better normal estimates, as the following physical implications of large datasets may outweigh the statistical advantages: A large number of data points is generally related to relatively thick discontinuities, and with increasing thickness the assumption of one-dimensionality is increasingly difficult to justify. Furthermore, realising a larger number of data points by a higher time resolution physically leads to the problem of resolving high-frequency wave activity within the transition which may not be directly connected to the actual discontinuity one is interested in. Only a large number of field vectors due to a slow motion of the discontinuity relative to the spacecraft implies no physical drawbacks.

Note that applying their method to a magnetopause crossing, *Khrabrov and Sonnerup* [1998] find that the uncertainty actually increases with increasing N in that example. They presume that this effect is the result of spatial and/or temporal inhomogeneity. *Sonnerup and Scheible* [1998] admit that when data of high time resolution are used, the $N^{-1/2}$ dependence may lead to the underestimation of uncertainties, and also that additional systematic errors not described by 7.6 and 7.7 may influence the estimate.

We further claim that methods that require certain properties of the noise such as isotropy, as equation 7.4 and partially equation 7.6 do, are probably unrealistic and thus underestimate the error. Since the error-formula proposed by *Lepping and Behannon* [1980] yields results comparable to the statistical approach presented by *Khrabrov and Sonnerup* [1998] and the bootstrap method, the results of *Lepping and Behannon* [1980] may serve as a reference for our own analysis in this work.

The four Cluster spacecraft penetrate a discontinuity at four nearby locations. Assuming a planar surface on the Cluster separation scale non-collinear MVA normals indicate poor performance of MVA, and the deviations between the individual normals may be used to quantify the uncertainty of MVA. The results we obtain by this simple comparison are detailed in chapter 8. They will demonstrate that the assumptions made by most of the presented approaches for assessing the error, as for example that the disturbance field is isotropic, cannot account

for real interplanetary discontinuities.

As a final note we may add that a simple and efficient method to test the reliability of the estimated MVA normal is to perform MVA for several different time intervals and to compare the results. Experience indicates that if the results are essentially the same for several neighbouring nested data segments centred at or near the middle of the discontinuity, they are perhaps believable.

7.3 Cross product method for TDS

If a discontinuity is known to be a TD or has a vanishing normal component of the magnetic field, it is possible to find the normal to the surface by simply noting that both upstream and downstream magnetic field vectors are parallel to the discontinuity plane and, unlike the case of a perpendicular shock, are not in general parallel to one another. Hence the normal is given by the cross product of the upstream and the downstream magnetic field:

$$\mathbf{n} = \pm \frac{\mathbf{B}_1 \times \mathbf{B}_2}{|\mathbf{B}_1 \times \mathbf{B}_2|} \quad (7.8)$$

The uncertainty associated with normals determined by this method is relatively small. It stems from imprecision in \mathbf{B}_1 and \mathbf{B}_2 that are subject to fluctuations in the vicinity of the TD. The uncertainty increases with increasing collinearity of \mathbf{B}_1 and \mathbf{B}_2 . Similar to timing methods and in contrast to MVA, the cross product method is completely independent of the discontinuity fine structure, i.e., of superposed fluctuations *within* the transition.

However, it has to be checked *a priori* that the discontinuity is a TD.

Several authors have applied this method to interplanetary discontinuities [Horbury *et al.*, 2001a; Burlaga and Ness, 1969; Burlaga, 1969a; Denskat and Burlaga, 1977]. When data from more than one spacecraft was available considerable agreement with timing-related methods have been found [Horbury *et al.*, 2001a; Burlaga and Ness, 1969].

We will use the cross product method only as a third reference.

7.4 Triangulation - multi-spacecraft technique using relative timings

One of the important objectives of the four-spacecraft Cluster mission is to allow determination of the orientation and speed of discontinuities without use of single-spacecraft techniques. The use of relative timings between the four spacecraft results in an enormous increase in the estimate reliability. This technique is referred to as triangulation. The discontinuity must be observed at least at three positions for triangulation to be applicable [Burlaga and Ness, 1969; Horbury *et al.*, 2001b]. However, without requiring additional input as the solar wind speed, four spacecraft are necessary.

7.4.1 Description of the method

The timing method for determining discontinuity normals and velocities used in this work is simple and was first presented by *Russell et al.* [1983] who applied it to interplanetary shocks. It has been reviewed recently by *Harvey* [1998], *Schwarz* [1998] and *Chanteur* [1998] and has become a frequently used tool in the interpretation of magnetopause and bow shock data from the four Cluster spacecraft (e.g., *Haaland et al.* [2004]; *Maksimovic et al.* [2003]; *Horbury et al.* [2002]). The method is based on the assumption that each of the four spacecraft crosses a locally planar discontinuity that moves at a constant speed. If the spacecraft α crosses the plane at time t_α and its position vector is \mathbf{r}_α at that moment, then for each pair α and β ,

$$(\mathbf{U}(t_\alpha - t_\beta)) \cdot \mathbf{n} = (\mathbf{r}_\alpha - \mathbf{r}_\beta) \cdot \mathbf{n} \quad (7.9)$$

where \mathbf{U} is the constant velocity of the discontinuity relative to the spacecraft array and \mathbf{n} the discontinuity normal.

Figure 7.2 illustrates this. Note that only the time differences $t_{\alpha\beta} = t_\alpha - t_\beta$ and the difference vectors $\mathbf{r}_{\alpha\beta} = \mathbf{r}_\alpha - \mathbf{r}_\beta$ of the four spacecraft positions are used. Also note that the positions of the four spacecraft, taken for each of them at the time when it crosses the discontinuity, form a tetrahedron that does not correspond to any instantaneous configuration of the array.

Taking for instance Cl 1 as the reference spacecraft and defining $\mathbf{P}_1 = (\mathbf{r}_{12}, \mathbf{r}_{13}, \mathbf{r}_{14})$ and $\mathbf{t}_1 = (t_{12}, t_{13}, t_{14})$, the normal \mathbf{n} and the speed along this normal $U = \mathbf{U} \cdot \mathbf{n}$ can be calculated as

$$\frac{\mathbf{n}}{U} = \mathbf{P}_1^{-1} \mathbf{t}_1 \quad (7.10)$$

where \mathbf{P}_1^{-1} is the inverse of \mathbf{P}_1 . Note that a necessary condition for a solution (i.e., for \mathbf{P}_1^{-1} to exist) is that $|\mathbf{P}| \neq 0$. Therefore, the third constraint for applicability besides planarity and constant velocity is that the four spacecraft are not coplanar. In reality, this mathematical condition is replaced by a more physical condition which compares \mathbf{P}_1 with the standard error in the relative spacecraft positions as determined from the orbit analysis, and the standard error of the experimental measurements themselves. Indeed, as we will show at the end of this section and in chapter 9, the precision of triangulation considerably depends on the shape of the spacecraft tetrahedron. To ensure this third constraint to be fulfilled we have introduced a cut-off value P_c for the planarity in chapter 5.

The required timing information can be obtained from any quantity measured at sufficient time resolution by all four spacecraft, provided a well-defined change in that quantity occurs at the discontinuity. In this work, we use magnetic field measurements from the four Cluster spacecraft. The sharp rotation of the field vector indicates the crossing time. Figure 7.3 shows an example of an interplanetary discontinuity observed by Cluster. Whereas the field magnitude remains constant (as is the case for the majority of DDs) the rotation of the field vector is clearly visible in the sharp jumps of the components. The order of passage of the transition is Cl 2, Cl 1, Cl 3 and finally Cl 4. The time lags are determined by shifting the individual time series until the jumps are aligned (right side of Figure 7.3). For the shown example we find $t_{12} = 0.3$ s, $t_{13} = -0.7$ s and $t_{14} = -2.7$ s. In section 9.2 we show histograms of all observed timings (Figure 9.6). The maximum time lags we observe are 33 s in 2003, 6.4 s in 2001 and 0.5 s in 2002, the average values are 5.11 s, 1.23 s and

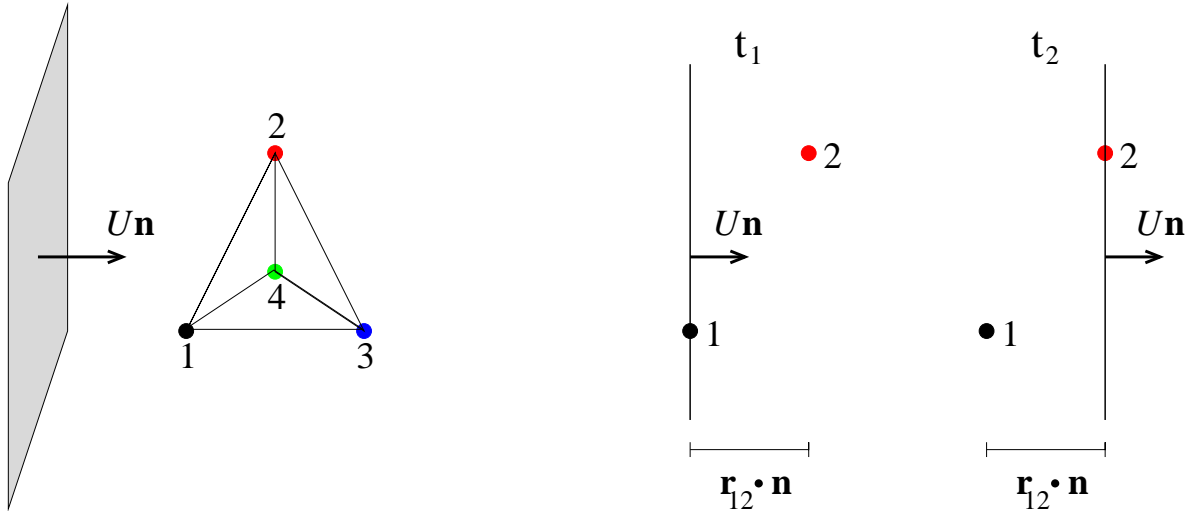


Figure 7.2: Illustration of the triangulation technique. A planar discontinuity with normal \mathbf{n} moves relative to the Cluster array with constant velocity U . The spacecraft cross the discontinuity plane at times t_α ($\alpha = 1, 2, 3, 4$). On the right projections at time t_1 and t_2 are shown. Clearly, $U t_{12} = \mathbf{r}_{12} \cdot \mathbf{n}$.

0.12 s, respectively. To optimise the procedure of finding the relative timings, we eliminate undesirable high-frequency fluctuations. To this purpose, a low-pass filter is applied to the data from each spacecraft by application of sliding averages. We use 1 s and 4 s averages depending on the width of the transition and the type of fluctuations to be eliminated. The thickness of the transition shown in figure 7.3 is approximately 1.5 s.¹ Thus applying 4 s sliding averages in this specific case would considerably smooth the actual discontinuity signature. Furthermore, the background field is rather quiet in this example. In general, however, especially when strong superposed fluctuations are present, we inspect both the high resolution data and sliding averages in order to determine precise time lags.

Note that alternatively a cross-correlation technique to determine the time differences could be used (e.g., *Haaland et al.* [2004]; *Maksimovic et al.* [2003]). Although this technique is more automated than ours, it suffers from the need to identify suitable data intervals for cross-correlation. Based on comparison of a few test cases we believe that our timing estimates are not worse than timings determined by cross-correlation.

Conditions for applicability

The assumption of constant velocity is problematic for the magnetopause and the bow shock. There, the crossing time often varies significantly from spacecraft to spacecraft. In two recent papers, *Dunlop et al.* [2001; 2002] have concluded from studies of Cluster magnetopause events that the magnetopause speed was usually not constant during an event but could change drastically over timescales of a minute or less, whereas the thickness showed more modest variations. It is also well known that the bow shock can rapidly change velocity; indeed, it

¹Histograms of the thickness of all DDs studied are shown in section 8.7. On average the duration of the transition is about 9 s. Also note that we have discussed the relation between the DD thickness and the size of the Cluster array at the end of section 5.5.

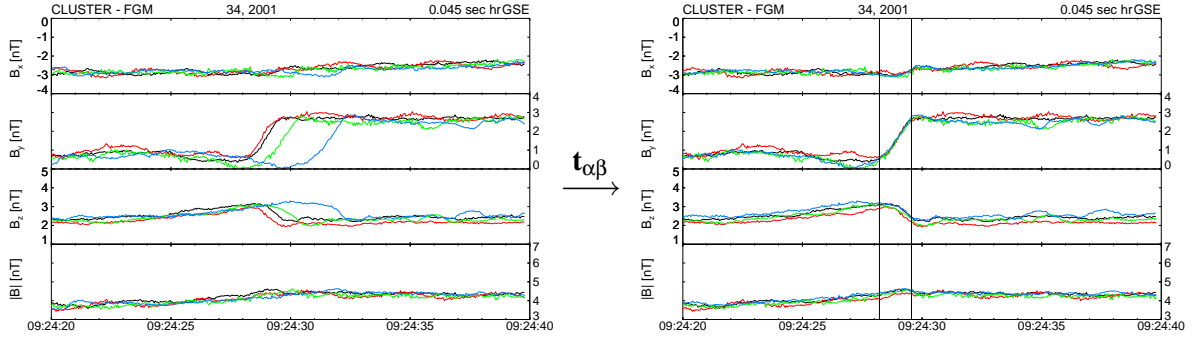


Figure 7.3: High resolution magnetic field data for one example DD from the set DD₂₀₀₁. The original four time series are shown on the left hand side. The time lags between the pairs of spacecraft are obtained by shifting the time series until they are aligned (right side). The standard colour code is used (Cl 1: black, Cl 2: red, Cl 3: green, Cl 4: blue). The vertical lines indicate the transition.

has been observed to reverse direction within the Cluster formation [Horbury *et al.*, 2001c]. Assuming constant motion, as we do, this of course leads to considerable errors when the boundary normals are determined. However, for interplanetary discontinuities the situation is different. Here, the assumption of a constant velocity is well justified. Whereas the magnetopause and the bow shock are highly dynamic and move in and out due to changing solar wind conditions, around a stable average position, interplanetary discontinuities are structures embedded in the solar wind that pass the Cluster array at comparatively high speeds. Thus, relative velocity changes from one spacecraft to the other affecting the normal determination are unlikely. In general, we do not observe considerable differences in crossing times at the four satellites, either. Consequently the assumption of constant motion is justified.

The second assumption is that the observed structure is planar over the width of the Cluster array. For the discontinuities considered in this work, the typical Cluster inter-spacecraft separation ranges from 100 km in 2002 to 4000 km in 2003 (see table B.1). This is much less than the usual estimate for the large-scale curvature of interplanetary discontinuities; Lepping *et al.* [2003] estimate an average of the radius of curvature to be 380 R_E . In addition, our subsequent analysis of Cluster data using single-spacecraft tools provides more evidence for interplanetary discontinuities being in fact planar over the used tetrahedron scales. Thus, we can argue with good cause that the conditions for the application of triangulation are indeed satisfied.

Techniques to determine motional and geometrical properties of discontinuities

By combining MVA with relative timings more detailed motional and/or geometrical properties of the discontinuity can be determined. This method and its underlying assumptions are described in Dunlop *et al.* [1997]; Dunlop and Woodward [1998]. It is referred to as the *discontinuity analyzer*. Within this technique the boundary normals are solely obtained by MVA. In the case of planar structures (inferred from collinearity of the MVA normals) a constant acceleration can be determined. As discussed above, this is of considerable interest for magnetopause or bow shock crossings generally comprising non-constant motion. In the case

of non-coplanar MVA normals the discontinuity analyzer yields information about curvature. There have also been earlier theoretical approaches addressing the local geometry of a surface crossed by a group of satellites, e.g. *Mottez and Chanteur* [1994]. All these methods share the necessity of using single-spacecraft techniques to determine local normals, with MVA as the most common. For the outcome to be meaningful these normals need to be known precisely. Our main results, that in most cases MVA does not yield well-defined boundary normals, is a serious caution for the application of such techniques.

Generalised formalism using the volumetric tensor

Harvey [1998] criticises that the method we use (equation 7.10) is incapable of handling relative time differences determined independently between each of the six different pairs of spacecraft; these time differences may be subject to experimental errors and therefore, in the mathematical sense, they will be mutually inconsistent. Furthermore, *Harvey* [1998] notes that the method cannot be generalised to more than four spacecraft and that there is a lack of symmetry selecting one reference satellite, despite the fact that the four spacecraft are identical. In order to overcome these criticisms *Harvey* [1998] presents a treatment of the problem which is formulated by means of the volumetric tensor (equation 5.5 chapter 5). It is a homogeneous least squares method applicable to four or more spacecraft. See appendix D for more details on this method.

7.4.2 Barycentric formalism - error analysis

In the following we present a third treatment of the problem of ($N = 4$) spacecraft crossing a planar discontinuity in uniform motion. The formalism of *barycentric coordinates* and *reciprocal vectors*, first applied to a multi-spacecraft problem by *Chanteur and Mottez* [1993], is especially helpful as it allows to theoretically derive analytical expressions for the uncertainties associated with the relative timing method we use. The derivation of these expressions and in particular their discussion is the aim of this section.

Barycentric coordinates and reciprocal vectors are well-known tools in applied mathematics but not in space physics. Also due to their importance in numerous topics that can be addressed by a four-spacecraft mission, it is worthwhile to present this formalism. A self-contained and detailed description is given in *Chanteur* [1998]. Here we provide a summary of definitions and fundamental properties needed later.

Again, $\alpha = 1, 2, 3, 4$ denote the vertices of an irregular tetrahedron and \mathbf{r}_α their position vectors. *Chanteur* [1998] introduces the barycentric coordinates considering the linear interpolation of a naturally occurring scalar field $u(\mathbf{r})$ or a vector field $\mathbf{v}(\mathbf{r})$ that is known only by the values $u_\alpha = u(\mathbf{r}_\alpha)$ or $\mathbf{v}_\alpha = \mathbf{v}(\mathbf{r}_\alpha)$ measured at the vertices α . The linear interpolation of these values in the vicinity of the cluster requires four basic interpolating functions μ_α which are linear scalar functions of the position vector \mathbf{r} , and which satisfy the constraints $\mu_\alpha(\mathbf{r}_\beta) = \delta_{\alpha\beta}$.

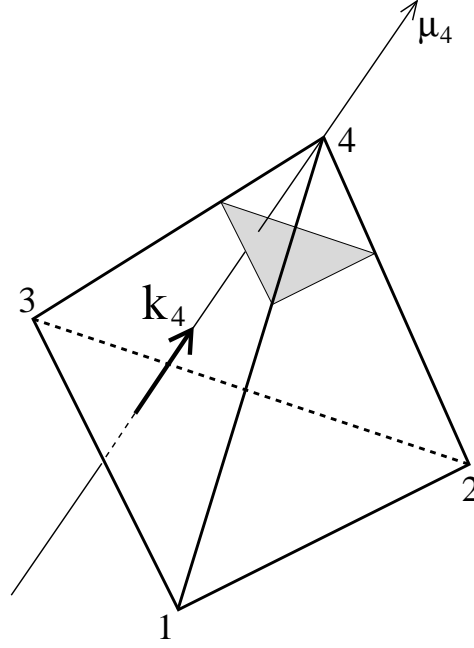


Figure 7.4: Illustration of the barycentric coordinates and the reciprocal vectors. The reciprocal vector \mathbf{k}_4 , defined by equation 7.14, points towards vertex 4 and is the gradient of the barycentric coordinate μ_4 which is constant on any plane parallel to the face 1-2-3; the shaded plane, perpendicular to the axis μ_α , is an iso-value surface of μ_α .

Let the linearly interpolated field, denoted by $L[u]$, be given by

$$L[u](\mathbf{r}) = \sum_{\alpha=1}^4 u_\alpha \mu_\alpha(\mathbf{r}) \quad (7.11)$$

The four values μ_α are the barycentric coordinates of the point \mathbf{r} . They can be expressed as $\mu_\alpha(\mathbf{r}) = v_\alpha + \mathbf{k}_\alpha \cdot \mathbf{r}$, where the v_α and \mathbf{k}_α are respectively scalar and vector constants to be determined. Using the constraints $\mu_\alpha(\mathbf{r}_\beta) = \delta_{\alpha\beta}$ one can deduce

$$\mu_\alpha(\mathbf{r}) = 1 + \mathbf{k}_\alpha \cdot (\mathbf{r} - \mathbf{r}_\alpha) \quad (7.12)$$

$$\mathbf{k}_\alpha \cdot (\mathbf{r}_\beta - \mathbf{r}_\gamma) = \delta_{\alpha\beta} - \delta_{\alpha\gamma} \quad (7.13)$$

Equation 7.13 shows that \mathbf{k}_α is normal to Π_α , the face of the tetrahedron opposite to vertex α . Thus, for example, by making use of $\mathbf{r}_{\beta\gamma} = \mathbf{r}_\gamma - \mathbf{r}_\beta$, \mathbf{k}_4 can be written

$$\mathbf{k}_4 = \frac{\mathbf{r}_{12} \times \mathbf{r}_{13}}{\mathbf{r}_{14} \cdot (\mathbf{r}_{12} \times \mathbf{r}_{13})} \quad (7.14)$$

It is proportional to the area of the face of the tetrahedron opposite to vertex 4 and inversely proportional to the volume of the tetrahedron. Expressions for \mathbf{k}_1 , \mathbf{k}_2 and \mathbf{k}_3 are obtained through cyclic permutations of the indices. *Chanteur* [1998] calls the \mathbf{k}_α the reciprocal vectors of the tetrahedron. Figure 7.4 illustrates the definitions above. The barycentric coordinates have the following properties. (1) $\mu_\alpha(\mathbf{r})$ is constant in a plane parallel to Π_α , (2) $\mu_\alpha(\mathbf{r}) = 0$ for all points lying in Π_α , (3) $\mu_\alpha(\mathbf{r}) < 0$ in the half space, relative to Π_α not containing vertex α , (4) $\mu_\alpha(\mathbf{r}) > 0$ in the half space, relative to Π_α containing vertex α and (5) $0 < \mu_\alpha(\mathbf{r}) < 1$ for all points lying inside the tetrahedron.

In the following, two properties of the reciprocal vectors will be useful. First,

$$\sum_{\alpha=1}^4 \mathbf{k}_\alpha = \mathbf{0} \quad (7.15)$$

From equation 7.12 the reciprocal vectors satisfy $\mathbf{k}_\alpha = \nabla \mu_\alpha$. Thus, taking the gradient of both sides of $\sum_{\alpha=1}^4 \mu_\alpha(\mathbf{r}) = 1$, which straightforwardly follows from the linear interpolation of a constant scalar field, equation 7.15 follows. Second, by taking the gradient of $\mathbf{A} \cdot \mathbf{r}$, where \mathbf{A} is a constant vector,

$$\mathbf{A} = \sum_{\alpha=1}^4 (\mathbf{r}_\alpha \cdot \mathbf{A}) \mathbf{k}_\alpha \quad (7.16)$$

is obtained, because \mathbf{r} itself is a linear field and can thus be written $\mathbf{r} = L[\mathbf{r}] = \sum_{\alpha=1}^4 \mathbf{r}_\alpha \mu_\alpha(\mathbf{r})$.

We are now able to formulate the problem of $N = 4$ spacecraft crossing a planar discontinuity in uniform motion by means of the reciprocal vectors (see *Chanteur* [1998]). Again, t_α denotes the time when spacecraft α crosses the surface through point P_α , the position of which is \mathbf{r}_α^0 at some arbitrary time t_0 . Then,

$$\mathbf{r}_\alpha(t_\alpha) = \mathbf{r}_\alpha^0 + \mathbf{U}(t_\alpha - t_0), \text{ for } \alpha = 1 \text{ to } 4 \quad (7.17)$$

The scalar product of this equation with the (unknown) normal \mathbf{n} gives

$$\mathbf{n} \cdot \mathbf{r}_\alpha(t_\alpha) = \mathbf{n} \cdot \mathbf{r}_\alpha^0 + \mathbf{n} \cdot \mathbf{U}(t_\alpha - t_0) \quad (7.18)$$

Multiplying this equation by \mathbf{k}_α and summing over the four values of α yields

$$\sum_{\alpha=1}^4 \mathbf{k}_\alpha \mathbf{n} \cdot \mathbf{r}_\alpha(t_\alpha) = \sum_{\alpha=1}^4 \mathbf{k}_\alpha \mathbf{n} \cdot \mathbf{r}_\alpha^0 + \sum_{\alpha=1}^4 \mathbf{k}_\alpha \mathbf{n} \cdot \mathbf{U}(t_\alpha - t_0) \quad (7.19)$$

Due to the planarity assumption all scalar products $\mathbf{n} \cdot \mathbf{r}_\alpha^0$ are equal. Hence, using equation 7.15 one obtains

$$\sum_{\alpha=1}^4 \mathbf{k}_\alpha \mathbf{n} \cdot \mathbf{r}_\alpha(t_\alpha) = U \sum_{\alpha=1}^4 \mathbf{k}_\alpha t_\alpha \quad (7.20)$$

Note that the reciprocal basis presently considered is the one associated to the fictitious tetrahedron built by the four spacecraft at positions $\mathbf{r}_\alpha(t_\alpha)$ which does not correspond to any instantaneous configuration of the cluster. Hence, using equation 7.16 the left hand side of the above equation is equal to \mathbf{n} , which is eventually given by

$$\mathbf{n} = U \mathbf{Q} \quad (7.21)$$

where

$$\mathbf{Q} = \sum_{\alpha=1}^4 \mathbf{k}_\alpha t_\alpha \quad (7.22)$$

The normal component of the relative velocity between the cluster of spacecraft and the discontinuity is given by the condition $\mathbf{n} \cdot \mathbf{n} = 1$, i.e.

$$U = (\mathbf{Q} \cdot \mathbf{Q})^{-\frac{1}{2}} \quad (7.23)$$

Note that this result contains relative spacecraft positions but absolute crossing times. Once \mathbf{n} and U have been computed with equations 7.21 - 7.23 the consistency of the four equations 7.18 can be tested. As discussed earlier, significant inconsistencies imply that at least one of our assumptions is not valid.

Using equations 7.21 - 7.23 the covariances of \mathbf{n} and U can be calculated [Chanteur, 2003]. Differentiating equation 7.22 yields

$$\delta \mathbf{Q} = \sum_{\alpha=1}^4 \delta t_{\alpha} \mathbf{k}_{\alpha} + \sum_{\alpha=1}^4 t_{\alpha} \delta \mathbf{k}_{\alpha} \quad (7.24)$$

The deviations $\delta \mathbf{k}_{\alpha}$ of the reciprocal vectors can be obtained from the deviations $\delta \mathbf{r}_{\alpha}$ of the position vectors, which are defined as the difference between the true position $(\mathbf{r}_{\alpha})_{true}$ and the nominal position \mathbf{r}_{α} [Chanteur, 1998; 2003]. However, as we will discuss in chapter 9 the positional uncertainty can be neglected. Hence²

$$\langle \delta \mathbf{Q} \delta \mathbf{Q}^T \rangle = \sum_{\alpha=1}^4 (\delta t_{\alpha})^2 \mathbf{k}_{\alpha} \mathbf{k}_{\alpha}^T \quad (7.25)$$

Differentiating equation 7.21 yields after some straightforward calculation

$$\langle \delta \mathbf{n} \delta \mathbf{n}^T \rangle = U^2 (\mathbf{I} - \mathbf{n} \mathbf{n}^T) \langle \delta \mathbf{Q} \delta \mathbf{Q}^T \rangle (\mathbf{I} - \mathbf{n} \mathbf{n}^T) \quad (7.26)$$

where \mathbf{I} is the unit tensor. The angular uncertainty of \mathbf{n} in any direction \mathbf{e} perpendicular to \mathbf{n} (see Figure 7.5) is then given by

$$(\delta \theta)^2 = \mathbf{e}^T \langle \delta \mathbf{n} \delta \mathbf{n}^T \rangle \mathbf{e} \quad (7.27)$$

Finally, from equation 7.23 one obtains

$$(\delta U)^2 = U^4 \mathbf{n}^T \langle \delta \mathbf{Q} \delta \mathbf{Q}^T \rangle \mathbf{n} \quad (7.28)$$

Discussion of the uncertainties of \mathbf{n} and U

Equations 7.25 - 7.28 identify the parameters contributing to the error values of \mathbf{n} and U . These are:

(1) The uncertainties δt_{α} in the determination of the crossing times (equation 7.25). Note that the presented method of crossing times can be modified to use time delays between spacecraft as we do [Chanteur, 2003]. In that representation the uncertainties δt_{α} of the absolute crossing times in equation 7.25 are replaced by the uncertainties of the time delays. These need to be related to the characteristic size L of the tetrahedron since the reciprocal vectors are inversely proportional to L (equation 7.14). Generally the correlation between the four time series decreases and thus the uncertainty of the time delays increase with increasing spacecraft separations. However, we find that the increase of the timing uncertainty is less than

²Dyadic notation is used: \mathbf{a}^T denotes the transpose of the column vector \mathbf{a} , and the dyad $\mathbf{a} \mathbf{b}^T$ is a tensor of rank two. The expectation value of a random variable X is noted $\langle X \rangle$.

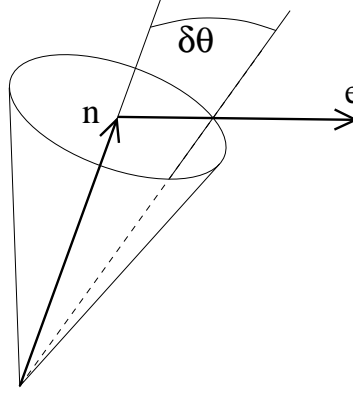


Figure 7.5: Cone of uncertainty.

linear in the separation distances. Therefore, the precision of our timing method increases with increasing spacecraft separations for the range of distances considered here.

(2) Both the angular uncertainty of \mathbf{n} (equation 7.27 with equation 7.26) and the uncertainty of the velocity U (equation 7.28) explicitly depend on U . Whereas $\delta\theta$ depends linearly on U , the dependence is quadratic for δU . Albeit the fact that $U = \mathbf{U} \cdot \mathbf{n}$ is the normal component of the discontinuity velocity and that \mathbf{n} can in principle be arbitrarily oriented with respect to the solar wind velocity \mathbf{V}_{sw} , it is apparent that the velocity of the moving plasma frame in which the discontinuity is embedded is generally a crucial parameter determining U . Therefore, the determination of \mathbf{n} and U is generally more accurate in slow solar wind as compared to fast solar wind streams.

(3) The geometry and orientation of the tetrahedron. These are implied by the right side of equation 7.25, which for $\delta t_1 = \delta t_2 = \delta t_3 = \delta t_4 = \delta t$ reads $(\delta t)^2 K$, where $K = \sum_{\alpha=1}^4 \mathbf{k}_\alpha \mathbf{k}_\alpha^T$ is the so-called *reciprocal tensor*. It can be shown [Chanteur and Harvey, 1998] that K is related to the volumetric tensor R , which provides information about the global shape of the tetrahedron (see chapter 5): $K = \frac{1}{4}R^{-1}$. A simple geometrical consideration demonstrates the impact of the tetrahedron properties: Deforming a regular tetrahedron by moving vertex 4 along the axis \mathbf{k}_4 towards the face Π_4 (see e.g. Figure 7.4) the planarity P increases from zero (regular tetrahedron) to unity (vertex 4 lies in the plane defined by face Π_4), and the reciprocal vectors \mathbf{k}_1 , \mathbf{k}_2 and \mathbf{k}_3 rotate about the axis defined by the intersection of the plain containing face Π_1 , Π_2 and Π_3 , respectively with the plain containing face Π_4 until \mathbf{k}_1 , \mathbf{k}_2 and \mathbf{k}_3 are parallel to each other and antiparallel to \mathbf{k}_4 . Since the volume of the tetrahedron approaches zero whereas the area of the sides remain positive, $|\mathbf{k}_\alpha| \rightarrow \infty$ ($\alpha = 1, 2, 3, 4$), for vertex 4 approaching face Π_4 (or $P \rightarrow 1$), generally yielding large errors according to equation 7.25. Therefore, the precision of triangulation decreases with increasing planarity P . Furthermore, since the components of \mathbf{k}_1 , \mathbf{k}_2 and \mathbf{k}_3 perpendicular to \mathbf{k}_4 vanish, and the components antiparallel to \mathbf{k}_4 dominate, the angular uncertainty on \mathbf{n} is largest in the direction given by \mathbf{k}_4 , which coincides with the normal to planarity. Hence, the angular uncertainty is largest in the direction normal to planarity. This means that the cone of uncertainty as shown in Figure 7.5 is unrealistic in the general case of an irregular tetrahedron and needs to be replaced by an asymmetric figure. Finally, considering the projections of $\langle \delta \mathbf{Q} \delta \mathbf{Q}^T \rangle$ onto $\mathbf{l} - \mathbf{n} \mathbf{n}^T$ (equation 7.26) and onto \mathbf{n} (equation 7.28) it is clear that the precision depends on

the orientation of the tetrahedron relative to the discontinuity normal \mathbf{n} .

In summary, for the subsequent analysis we need to keep in mind that we achieve best estimates for \mathbf{n} and U when the spacecraft separations are large, the solar wind velocity is low and when the shape of the cluster is close to a regular tetrahedron. We need to be aware that due to the large ratio $\delta t / (\text{spacecraft separation})$ the triangulation results are the least reliable in 2002. Also, due to the poor statistics (only 33 events) in this year the contribution of the set DD_{2002} regarding multi-spacecraft techniques is of minor importance. The most meaningful triangulation results are obtained in 2003, where the separations are largest. However, as discussed in chapter 5, care needs to be taken of strongly flattened spacecraft configurations in this year. Using only those events with a suitable spacecraft geometry ($P < P_c = 0.8$ as defined in chapter 5) we still retain a large data set of 191 events with excellent estimates of \mathbf{n} and U . In chapter 9 we will demonstrate that $P_c = 0.8$ is a reasonable cut-off value.

In chapter 9 we use an empirical method to estimate the uncertainties which gives the maximum possible deviation from the measured normal \mathbf{n} (denoted as dn) and the maximum possible difference to the measured velocity U (denoted as dU) within the experimentally observed uncertainty δt . A detailed error analysis for the specific events investigated will be carried out in that chapter. Among others the importance of the identified factors affecting the triangulation accuracy will be discussed in detail. For typical values of δt we obtain on average (see table 9.1): $dn = 5^\circ$ and $dU = 25$ km/s in 2003, $dn = 10^\circ$ and $dU = 75$ km/s in 2001 and $dn = 35^\circ$ and $dU = 500$ km/s in 2002. Note that in our analysis the angle θ_{Bn} between the magnetic field \mathbf{B} and the discontinuity normal \mathbf{n} is of particular interest. Due to the anisotropy of the angular uncertainty, $d\theta_{Bn}$ is in general considerably smaller than dn . As a final remark we point out that in our error analysis (here and in chapter 9) we neglect the possibility of DDs being non-planar or in non-constant motion on the Cluster scale.

STATISTICAL ANALYSIS OF DISCONTINUITIES AT 1AU

This chapter contains the majority of results of our statistical study on interplanetary discontinuities.

First, we establish that the ensemble of DDs investigated in this study does not differ statistically from those in previous studies: Our results are consistent with previous studies if analysed and interpreted as single-spacecraft measurements and using established analysis tools such as MVA (section 8.1).

We then present the seminal result that four-spacecraft analysis with discontinuity normal estimates based on the triangulation method yields strikingly different results than one-spacecraft analysis with normals from MVA (section 8.2). This result implies a radically different physical picture of the solar wind micro-structure. Much of the following analysis is devoted to solving the observed discrepancy.

We provide evidence for MVA being much less reliable than previously thought, yielding poor estimates in many cases (section 8.3). Given that MVA is a widely used data analysis technique applied in a variety of fields in space plasma physics, this result has drastic implications beyond this project.

We define circumstances that are likely to favour erroneous MVA normal estimates, and we propose a physical model for interplanetary discontinuities that accounts for these observations. According to the discussion in the previous chapter (section 7.2) the accuracy of MVA mainly depends on the eigenvalue ratio λ_2/λ_3 and the discontinuity spreading angle ω . The analysis presented in section 8.3 is hence mainly based on these two parameters.

Simple but effective consistency tests presented in section 8.4 prove that, in contrast to MVA, the triangulation method yields reliable normal estimates.

Being aware of the deficits associated with MVA, further problems can be tackled. In section 8.5 we discuss geometrical properties of DDs. Propositions for the large scale curvature of DDs have been made in earlier studies (e.g. *Lepping et al.* [2003]). These are based on MVA normal estimates made at two or more widely separated spacecraft. The four Cluster spacecraft flying in formation only a few hundred or thousand kilometres apart are used to help interpreting such results in section 8.5.

Another macroscopic quantity to be investigated is the orientation of the DDs in the interplanetary medium (section 8.6).

In order to determine the discontinuity thickness from the transition time, the relative velocity between DD and spacecraft needs to be known. Whereas the velocity had to be derived from plasma data in earlier studies it is directly computed by the triangulation technique in this study. Also, because of the high time resolution of the FGM instrument on board Cluster, we are able to resolve very thin DDs (section 8.7).

Note that the analysis presented in sections 8.1-8.7 is solely based on magnetic field data from the FGM instrument on board Cluster. In section 8.8 we come back to the classification analysis, approaching the problem from a different side. Whereas in section 8.2 only the normal component and the change of magnitude of the magnetic field are used, the polarisation relation, the density jump and the propagation relative to the ambient plasma are investigated in section 8.8 aiming to distinguish RDs from TDs. Not being misled by erroneous normal estimates (as all earlier studies based on MVA were) we can analyse the question of which type of solar wind is most likely to host RDs. This in turn is strongly related to the long standing question of identifying possible generation mechanisms of interplanetary discontinuities.

Some of the results presented in this chapter have already been published [*Knetter et al.*, 2003; 2004]. These publications contain a fractions of the results using magnetic field data from 2001 only.

8.1 Single spacecraft analysis

In order to demonstrate that the ensemble of DDs investigated in this work does not differ statistically from those in previous studies we use each satellite as a separate mission and apply established single-spacecraft analysis tools.

We have already identified some characteristics of our sets of DDs indicating representative ensembles in section 6.3 where we discussed the occurrence statistics. In accordance with earlier studies we find: (1) The number density of identified DDs is not constant in time but fluctuates strongly from day to day. (2) These fluctuations are correlated to the fluctuations of the solar wind speed. (3) The tendency of DDs to occur in clusters is also visible within one day, and (4) a frequency of one (B-method) and two (TS-method) DDs per hour is observed on average. Further characteristics are discussed below.

It is found that the distribution of the discontinuity spreading angle ω follows an exponential

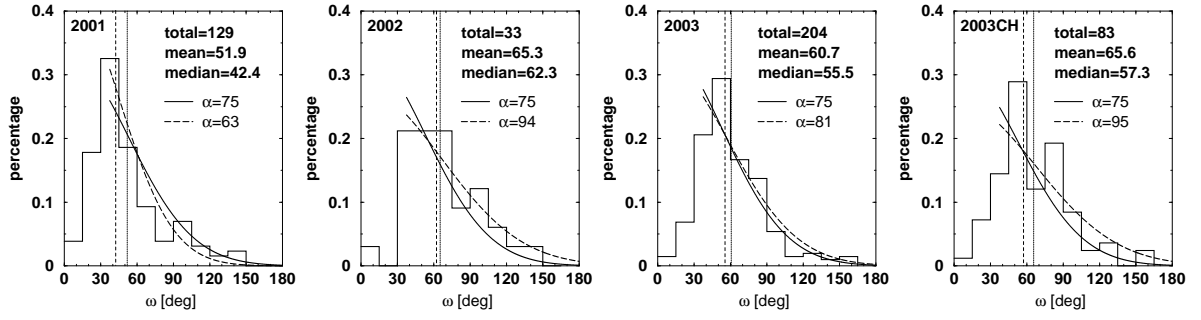


Figure 8.1: Histogram of ω obtained from Cl 1. All DDs are considered. The solid line shows a fit with $\alpha = 75^\circ$, the dashed line the best fit. The vertical dashed and dotted lines indicate the median and mean value, respectively.

decrease for $\omega > 30^\circ$:

$$\text{Number of DDs}(\omega) \propto e^{\left(\frac{\omega}{\alpha}\right)^2} \quad (8.1)$$

with $\alpha = 75^\circ$ at 1 AU [Burlaga, 1969a; Burlaga et al., 1977]. This means that the distribution rapidly decreases and that the majority of DDs have a small spreading angle ω . Burlaga [1971b]; Mariani et al. [1973]; Barnstorf [1980] find similar distributions. Barnstorf [1980] states that one half of all DDs have a spreading angle less than 50° .

We find that ω is almost the same at the position of all four spacecraft.¹ Figure 8.1 shows the distributions we obtain from Cl 1 separately for all four sets (DD_{2001} , DD_{2002} , DD_{2003} and DD_{2003CH}). Note that as discussed in section 6.2 the distribution is artificially biased due to the selection criteria used. Effectively, discontinuities with $\omega \lesssim 30^\circ$ are disregarded. However, since for the determination of ω high resolution FGM data are used, $\omega < 30^\circ$ is possible in Figure 8.1. The ω distributions we find are consistent with the distributions found in earlier studies. We fit each of the four distributions to equation 8.1 for $\omega > 30^\circ$ (dashed line). Best fits are obtained for $\alpha = 63^\circ$, $\alpha = 94^\circ$ and $\alpha = 81^\circ$ in 2001, 2002 and 2003, respectively. Especially in 2003, where most events contribute to the distribution, the fitting parameter is close to $\alpha = 75^\circ$, as found by Burlaga [1969a]; Burlaga et al. [1977]. A weighted average over all three years yields $\alpha = 76^\circ$. In accordance with Barnstorf [1980], we observe median values around 50° . Hence we add to our above list: (5) The distribution of the spreading angle ω is consistent with distributions found for sets used in earlier studies.

Note that the distribution of ω is different for the four sets. Apparently the decrease is steepest in 2001 (smallest α). In this period of observation, where we mostly identified slow solar wind from active regions, the spreading angle is smallest (also compare the different average values given in Figure 8.1). A comparison of α and the mean value between DD_{2003} and DD_{2003CH} confirms that ω tends to be larger in fast solar wind originating from coronal holes.

For our purpose the most important indicator of consistency with earlier studies is the single-spacecraft classification result, i.e., the percentages RD:TD:ED:ND obtained using MVA. We have discussed the classification results in section 3.2 found so far. We have shown that these results vary. Whereas some authors find more TDs than RDs, the majority of studies claim a dominance of RDs. There is general agreement that the abundance of RDs increases in fast solar wind, and to our knowledge no published study does not find a clear RD at all. In

¹This will be discussed in more detail in section 8.3.4.

Table 8.1: *RD:TD:ED:ND Percentages. Deviations from 100 are due to truncation errors.*

Author	Mission	DDs	MVA	Triangulation
			RD:TD:ED:ND (R/T)	RD:TD:ED:ND
<i>Smith</i> [1973a]	Mariner5	118	37:15:47:1 (2.5)	-
<i>Lepping and Behannon</i> [1980]	Mariner10	163	38:18:38:6 (2.1)	-
<i>Neugebauer et al.</i> [1984]	ISEE3	473	56:12:32:1 (4.7)	-
<i>Horbury et al.</i> [2001b]	Wind (I8, G)	35	57:11:26:6 (5.2)	9:14:74:3
<i>DD</i> ₂₀₀₁	Cluster	432/4	35:16:47:2 (2.1)	0:16:83:2
<i>DD</i> ₂₀₀₂	Cluster	113/4	42: 6:48:4 (6.7)	3: 6:91:0
<i>DD</i> ₂₀₀₃	Cluster	698/4	42: 9:48:1 (4.5)	0:10:90:0
<i>DD</i> _{2003CH}	Cluster	282/4	37:11:49:3 (3.3)	0:14:86:0
<i>DD</i> _{2003CHS}	Cluster	185/4	45: 6:47:1 (7.0)	0:10:90:0

other words, all previous studies conclude that “unambiguously” identified RDs represent a significant fraction of all observed discontinuities, so they must be considered an important interplanetary phenomenon.

The classification results strongly depend on details in selection and on the rules applied for classification. Therefore, we directly compare our results to studies that use the same classification principles that we choose to adopt, namely a classification based on the magnetic field component normal to the DD and the field magnitude jump across the transition (see Figure 3.3 in section 3.1.2).² Four studies that are relevant in this regard are listed in Table 8.1. Note, however, that *Smith* [1973a] and *Lepping and Behannon* [1980] use slightly different thresholds. Table 8.1 shows from left to right: The authors, the spacecraft used, the number of DDs investigated and the classification result (RD:TD:ED:ND) found using MVA. The number in brackets (R/T) is the direct ratio of RDs to TDs. The rightmost column is not relevant for the discussion in this section and can be ignored for the moment. The top part of Table 8.1 shows the results found in the literature. The results from our own analysis are presented in the bottom part. These results are obtained by performing MVA with the data from each spacecraft separately and subsequent calculating $|B_n|/B_{max}$ according to the derived normal estimate. Following common practice (see section 7.2) we use $(\lambda_2/\lambda_3)^L = 2$ as a lower limit, i.e., all DDs with $\lambda_2/\lambda_3 \leq 2$ are discarded. The data shown in Table 8.1 represent the results obtained at the individual spacecraft that satisfy the constraint. This means that if $\lambda_2/\lambda_3 > 2$ at all four spacecraft, the corresponding DD appears four times in the statistic. The individual results for each spacecraft can be viewed in appendix B (Table B.2).

Table 8.1 shows that our single-spacecraft results agree very well with the percentages found in literature. Excellent consistency is found between our 2001 result and the classifications determined by *Smith* [1973a] and *Lepping and Behannon* [1980]. *Neugebauer et al.* [1984] reason that the enhanced percentage of RDs that they find is caused by the high solar wind velocity prevailing during the time interval of their investigation. The results we obtain for *DD*₂₀₀₃ and *DD*₂₀₀₂, where the solar wind speed is also enhanced compared to 2001, are consistent with *Neugebauer et al.* [1984], although we find a higher ratio of EDs to RDs. In

²Note that this only accounts for this part of the work. Later we will also apply other criteria.

particular the ratio R/T is in excellent agreement for DD_{2003} (which is the largest of our sets). The result obtained by *Horbury et al.* [2001b] is similar to that of *Neugebauer et al.* [1984], although their statistics are worse. Also in agreement with other single-spacecraft studies is that the relative number of RDs increases with increasing solar wind speed (The ratio R/T found in 2003 is roughly twice as large as in 2001).

In order to study the dependence on solar wind type in more detail, we repeat the analysis for the set DD_{2003CH} , i.e., the subset of DD_{2003} containing only those DDs that are found in fast streams presumably from coronal holes on the Sun (see section 6.5). We are surprised to find relatively fewer RDs in the coronal hole subset than in the total set, contradicting earlier results. Therefore we investigate the set DD_{2003CH} in more detail. As one would expect for coronal hole flow, the magnitude changes are all moderate with $|[B]|/B_{max} \lesssim 0.3$ for all 83 DDs. Further, only 11 out of the 83 DDs have $|[B]|/B_{max} > 0.2$, and using MVA we identify only 7, 9, 9 and 7 TDs at Cl 1, Cl 2, Cl 3 and Cl 4, respectively. It turns out, that the vast majority of these TDs in DD_{2003CH} belong to the 27 DDs in FS II identified as being “unclear” (see section 6.5), because either they are in the vicinity of the CME on \approx day 50 or very close to the border of the fast stream where the stream-stream interaction region might have some influence on the properties of the DDs. To be more precise, most TDs identified in the set DD_{2003CH} are observed on day 46, 48 and 51. This explains the relatively large magnitude changes ($|[B]|/B_{max} \in [0.2, 0.3]$) observed for these DDs. The set $DD_{2003CHS}$ in Table 8.1 is the subset of DD_{2003CH} where the 27 “unclear” events are removed. This set contains only DDs unambiguously found in steady coronal hole flow. Of the remaining 56 DDs in $DD_{2003CHS}$ only 3 DDs are identified as TDs with $|[B]|/B_{max}$ only barely exceeding the threshold 0.2. As can be viewed in Table 8.1, an increased ratio R/T is found for this subset as compared to the total set DD_{2003} . Hence, altogether our single-spacecraft classification results coincide very well with earlier studies.

Note that, although statistically the individual analyses using each of the four spacecraft yields similar classification results, the normals derived by MVA at the location of the four spacecraft are always different for the traversal of a DD. Sometimes the angle between the four individual MVA normals is small, and in other cases it is large, sometimes even 90° . (Figure 8.17 in section 8.5 gives an overview.) In fact, the deviating normals often lead to a DD being identified as an ED at the location of one spacecraft and as an RD at the location of another spacecraft. Because of the small separations between the Cluster satellites this remarkable disagreement between the four MVA results is indicative of a considerable uncertainty associated with the MVA normal determination. This will be detailed in the following sections.

As a final test for consistency we compare the average MVA eigenvalue ratio λ_2/λ_3 , the spreading angle ω and the discontinuity thickness separately found for RDs, TDs and EDs according to the classification above. We only exemplarily present our results of 2001. An important result for the following discussion is the consistent observation that λ_2/λ_3 is significantly smaller for RDs than for TDs and EDs on average. We find $\langle \lambda_2/\lambda_3 \rangle = 4.8$ for RDs, $\langle \lambda_2/\lambda_3 \rangle = 11.1$ for TDs and $\langle \lambda_2/\lambda_3 \rangle = 12.2$ for EDs for the set DD_{2001} . The corresponding values obtained by *Lepping and Behannon* [1986] are: $\langle \lambda_2/\lambda_3 \rangle = 4.9, 8.5$ and 8.8 . *Söding* [1999] finds the same tendency, although the differences are not as pronounced, and

the eigenvalue ratios are generally larger. The latter is probably due to the different time resolution used: Whereas *Lepping and Behannon* [1986] and we use high resolution magnetic field data (0.040 s and 0.045 s, respectively), *Söding* [1999] uses WIND and IMP 8 data averaged to 3 and 1.28 s, respectively.

Also relevant for the subsequent discussion is that ω is found to be smaller for RDs than for TDs and EDs on average. We find $\langle \omega \rangle = 40^\circ$, 62° and 64° for RDs, TDs and EDs, respectively, which compares well to the values found by *Söding* [1999] (40° , 65° and 60°).

Finally, the average thickness we observe agrees well with earlier studies at 1 AU. We find similar values for RDs and TDs (2600 km and 2100 km, respectively). *Burlaga et al.* [1977]; *Lepping and Behannon* [1986] and *Söding* [1999] also find similar values, although the DDs analysed by *Burlaga et al.* [1977] are rather thin (1200 km and 1300 km, respectively) and those found by *Söding* [1999] are rather thick ($\approx 4000 - 6000$ km, depending on the spacecraft used, for both types of DDs). Hence, the average thicknesses we find for the set DD_{2001} are somewhere in-between and compare well to those found by *Lepping and Behannon* [1986] (2600 km for both types). Note also that the determination of the DD thickness is influenced by the time resolution.

In summary, we have shown by comparison of several statistical properties that the set of DDs used in our analysis is consistent with those used in earlier studies. In particular the classification result is consistent when the normals are estimated using MVA, and a significant number of RDs is found. Hence, apart from the alarming observation of diverging MVA normals at the locations of the four Cluster spacecraft, we confirm many physical properties of interplanetary discontinuities gained in the last four decades. This first step of our analysis is of great importance, since it puts the results of the following section in the right light.

8.2 Classification result from triangulation compared to MVA

Apart from the important observation that the four MVA normals are inconsistent among each other for many DDs, the results obtained in the previous section are solely based on single-spacecraft techniques. Using Cluster as a true multi-spacecraft mission we can determine the discontinuity normals by utilising the time lags between the four spacecraft (see section 7.4). Application of this triangulation technique yields surprising results.

Figure 8.2 shows the distribution of DDs in the classification diagram introduced in section 3.1.2 (Figure 3.3) for each of the four sets DD_{2001} , DD_{2002} , DD_{2003} and DD_{2003CH} separately. The MVA results (black diamonds) are obtained from the FGM data of Cl 4. Note that only those DDs are shown for which $\lambda_2/\lambda_3 > 2$. To allow for better comparison the triangulation results (red squares) are also shown only for these DDs, and the change in field magnitude for triangulation is adopted from the FGM data of Cl 4. Thus, the value of $||[B]||/B_{max}$ is the same for the red squares as for the black diamonds for each DD in Figure 8.2.

Strong differences between the MVA and the triangulation results are found for the values of $|B_n|/B_{max}$ which are determined by the normal estimates. The scatter obtained using MVA compares very well to similar plots in earlier studies (see e.g. *Smith* [1973a]; *Lepping and*

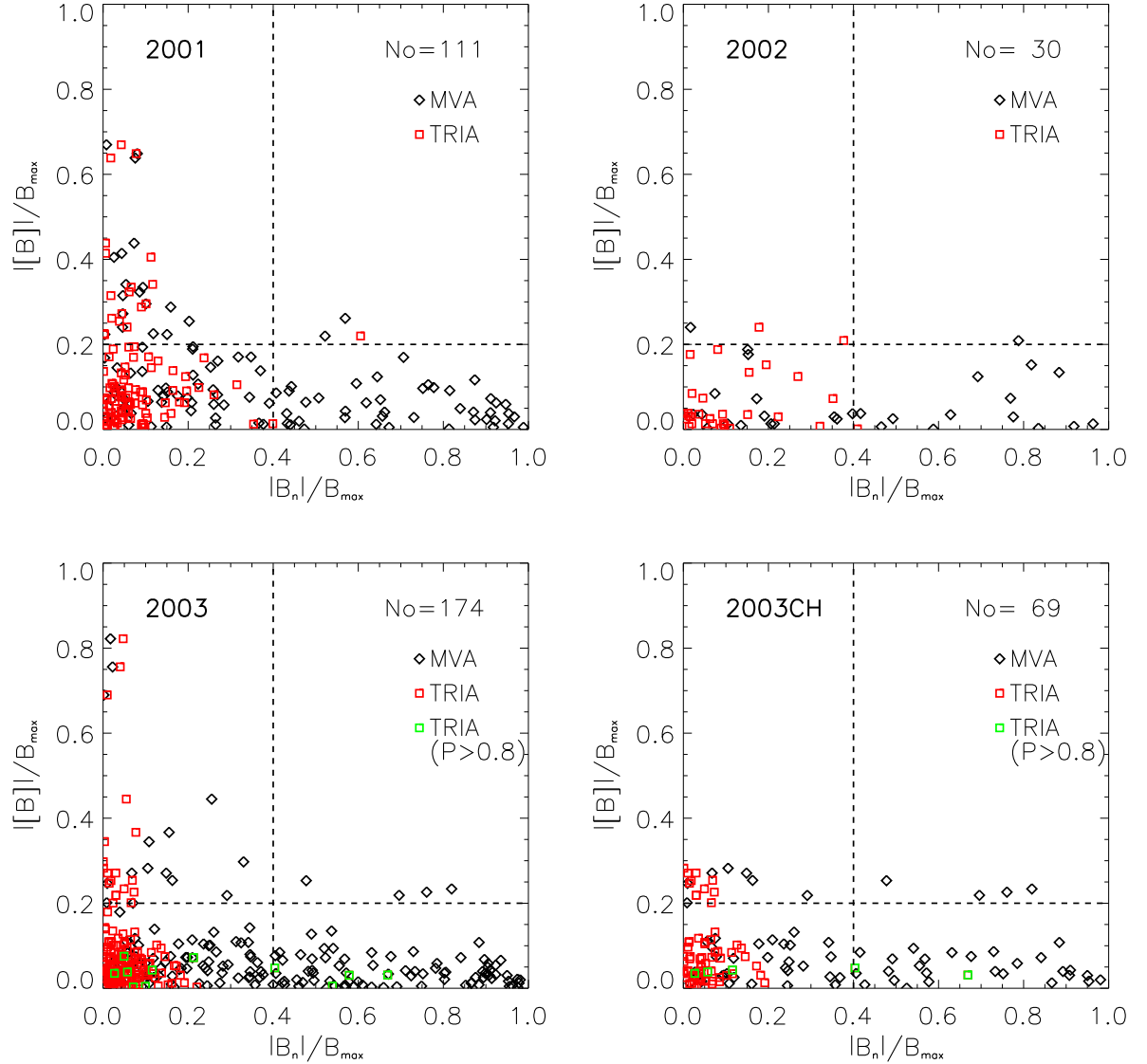


Figure 8.2: Scatterplots based on normal estimates from triangulation (red squares) and Cl 4 MVA (black diamonds). Uncertain triangulation results, i.e., $P > 0.8$ (only 2003) are green. Top row: 2001 and 2002. Bottom row: 2003 and 2003CH. Only those DDs are shown for which $\lambda_2/\lambda_3 > 2$ at the location of Cl 4.

Behannon [1980]), confirming the result of the previous section. In particular, a huge number of RDs is found.

However, application of triangulation yields a completely different picture. The timing-derived normals yield much smaller normal components of \mathbf{B} , i.e., B_n . Especially when the magnitude change is small ($|[B]|/B_{\max} < 0.2$) a major difference between the two methods is apparent. For the majority of DDs, $|B_n|/B_{\max} < 0.1$ is obtained when the normals are estimated via relative timings, and the RD category remains almost completely devoid. Considering all 366 DDs only one event is classified as an RD according to the criteria applied here. This event is found in 2002 (see upper right of Figure 8.2), where the spacecraft separations are very small and thus the triangulation performance is worst. In addition, with $|B_n|/B_{\max} = 0.4093$ this event is very close to the border between EDs and RDs.

In fact, the small values of $|B_n|/B_{max}$ found when triangulation is applied even decrease with increasing quality of the relative timing method. As discussed earlier (sections 5.5 and 7.4) the accuracy of the relative timing normal estimates increases with increasing spacecraft separations. Due to the small separations, and thus small time lags, the derived normals in 2002 must be handled with great care. In contrast, the normal estimates in 2003, where the separations are largest, can be regarded as excellent. The triangulation results in 2001 are intermediate. Commensurate with these different accuracies, the observed normal components of the magnetic field decrease with increasing spacecraft separations. Whereas the scatter of $|B_n|/B_{max}$ is largest in 2002 and intermediate in 2001, the observed values of $|B_n|/B_{max}$ are all close to zero in 2003 when triangulation is applied.

The accuracy of normal determination also strongly depends on the geometrical properties of the tetrahedron built by the four spacecraft. We have pointed out in section 5.5 that the tetrahedron can become very flat in 2003 yielding large uncertainties for the relative timing method. DDs observed with extremely flat tetrahedra (planarity $P > P_c = 0.8$) are marked green in Figure 8.2 (bottom). Note that some of these events are identified as being RDs. They are marked as black crossed in the E - P diagram of Figure 5.8. Obviously, triangulation yields large values of $|B_n|/B_{max}$ only when its performance is worst. In these cases, however, the uncertainty in normal determination is too large to consider the results as meaningful. In fact, errors as large as 90° are found (see chapter 9).

We have demonstrated with great care that the set DD_{2003} contains a considerable number of DDs in fast coronal hole streams (see section 6.5) where past studies and thereof deduced theories expect to find a huge abundance of RDs. Hence, whereas the absence of RDs in 2001 could be argued to be connected to the prevailing slow solar wind from active regions, this type of argumentation fails for the set DD_{2003} . In order to emphasise this issue we also show the scatterplot containing only the set DD_{2003CH} (lower right in Figure 8.2). No clear RD is identified in this subset of DDs in coronal hole flow when triangulation is used.

However, in contrast to the total set DD_{2003} , this subset does not contain many clear TDs either. No DD with a large change in field magnitude is observed. As discussed in the previous section, the few cases with $|[B]|/B_{max}$ barely exceeding the threshold 0.2 are predominantly those DDs that are found in the vicinity of the CME or near the fast stream border. The point of major importance, however, is that the absence of any cases with large values of $|B_n|/B_{max}$ is independent of solar wind type. The observed differences of the triangulation results in the four sets of DDs as presented in Figure 8.2 only correlate with the varying precision of normal determination.

The classification results obtained using triangulation are summarised in Table 8.1 (rightmost column). Note that the percentages presented are based on all selected DDs, apart from the 13 cases in 2003 where the spacecraft configuration is too far from a regular tetrahedron ($P > 0.8$). However, no eigenvalue ratio restrictions are applied. The number of DDs considered are: 129 (DD_{2001}), 33 (DD_{2002}), 191 (DD_{2003}), 76 (DD_{2003CH}) and 49 ($DD_{2003CHS}$). The most striking difference compared to the MVA results is that no clear RD is found, aside from the one in 2002. Commensurate with the absence of RDs, the number of EDs is increased. The relative number of clear TDs is about the same as for the single-spacecraft analysis. This means that all of the DDs “unambiguously” identified as RDs by MVA are found to be EDs

when triangulation is used. Hence, the vast majority of DDs are identified to be EDs.

Note that in contrast to MVA, the triangulation classification results are remarkably stable. The result is almost the same in all three periods of observation.

Apparently, the basic result presented in *Horbury et al.* [2001b] and our result are similar (see Table 8.1). *Horbury et al.* [2001b] also find many DDs being identified as RDs by MVA to be EDs when relative timings are used, although their result is not as extreme as ours.

As pointed out earlier in this work, the study presented in *Horbury et al.* [2001b] is quite distinct from our study in several aspects. First, they use only three spacecraft. Thus, in order to determine the discontinuity normal, they need the measured plasma velocity. If four spacecraft are available, as in the present study, only magnetic field data are needed. Hence, the techniques are quite different. Second, the three spacecraft used in *Horbury et al.* [2001b] are from three different missions and they are thus not coordinated as the four Cluster spacecraft are. Different magnetometers with different time resolutions may introduce additional error. Third, the distance between the three spacecraft in *Horbury et al.* [2001b] is typically 2×10^5 km. The distance between the four Cluster spacecraft is typically 1000 km, which is of the order of ten thermal proton gyro-radii in the solar wind. Thus, two clearly distinct scales are observed in the two studies. Whereas the assumption of planar structures on the length scale of gyro-radii seems to be reasonable, it is not clear *a priori* whether the same assumption holds for distances 200 times larger. Finally, the much larger number of events (366 in the present work compared to 35 in *Horbury et al.* [2001b]) contributes to a higher level of confidence. Note that *Horbury et al.* [2001b] still find a considerable number of RDs. It is not clear to what extent this difference can be attributed to the difficulties mentioned above.

Note that when we say, we do not find any RDs when triangulation is used, this means no RDs found according to the classification rules applied. Apart from the fact that the large group of EDs may contain RDs, the classification criteria are somewhat arbitrary. In order to test whether the small values of $|B_n|/B_{max}$ found are consistent with $|B_n| = 0$, i.e., whether the DDs in question are consistent with TDs, one has to compare these values with the error associated with the determination of $|B_n|/B_{max}$. This is done in chapter 9.

Having a closer look at the distributions of DD_{2001} and DD_{2003} in Figure 8.2, one realises that some DDs in the ED-section have larger normal components than those in the TD-section ($|B_n|/B_{max} \gtrsim 0.1$). This might indicate that these events are RDs with small but finite $|B_n|/B_{max}$. In order to determine the true nature of these DDs, we use plasma data (section 8.8).

Nevertheless, the triangulation results presented in this section for the first time open up the possibility that indeed no RDs are present in the solar wind at 1 AU. At least one might argue that the solar wind is dominated by TDs and not by RDs. This possible conclusion would be of great importance for the micro-structure of the solar wind, since TDs separate distinct plasma regions which are not magnetically connected. This in turn might have dramatic impact on energetic particle diffusion. Certainly, this finding is also relevant for possible generation processes and the stability of interplanetary discontinuities. Not finding any RDs probably contains information about what non-linear dynamical processes are relevant in the solar wind plasma. For instance, the proposed phase-steepening of Alfvén waves as a source

for RDs (see section 3.3) becomes questionable when no RDs are observed in the solar wind. Even if all (or some) EDs were RDs, new perspectives would be given. In that case the question arises, why do all RDs have such small normal magnetic field components. This is also related to the issue of generation processes and the stability of DDs.

Since the selected ensemble of events is representative in the sense that single-spacecraft analysis is consistent with earlier studies, the strong discrepancy between the RD:TD ratios must be a result of the different methods used. One might argue that the small spacecraft separations and the resulting short time lags between occurrences at the four spacecraft yield uncertainties in the triangulation method. However, the consistency tests and the detailed error analysis, as discussed below, demonstrate that the timing-derived normals are indeed reliable. Aside from that, *Horbury et al.* [2001b] find similar results using timing-derived normals with typical inter-spacecraft separations of about two orders of magnitude larger than the distances in the present study. Thus, spacecraft separations and associated uncertainty arguments are not maintainable. Instead, we presume that non-isotropic fluctuations cause a bias away from the true normals and hence cause inaccurate MVA estimates even if $\lambda_2/\lambda_3 > 2$ is required.

Indicative of unreliable MVA normals are the deviations observed between the four spacecraft. Another indication is the cases that simultaneously have large $||B||/B_{max}$ and large $|B_n|/B_{max}$. Whereas $|B_n|/B_{max} < 0.1$ for all DDs with $||B||/B_{max} > 0.2$ when triangulation is applied (2003), $|B_n|/B_{max}$ also takes large values when MVA is used for the same DDs (see the scatter of DD_{2003} , i.e., lower left of Figure 8.2). In particular MVA identifies NDs where triangulation finds clear TDs. Note that using triangulation only one ND is found (in 2001), and this event is probably a weak shock.

Provided our assumption is correct, and the discrepancy between the classifications from MVA and triangulation is indeed caused by inaccurate MVA normals, then it should be possible to find a subset of DDs for which both methods agree, for instance those DDs for which the four individual MVA estimates are consistent. Since MVA results generally gain reliability with increasing λ_2/λ_3 and/or ω , the MVA normal estimates should converge towards the triangulation estimates when the lower limits $(\lambda_2/\lambda_3)^L$ and/or ω^L are increased. Note that *Horbury et al.* [2001b] find no dependence of their results on the eigenvalue ratio λ_2/λ_3 . However, they only have a small statistic and do not investigate this issue systematically.

In the following we prove the existence of subsets of DDs for which the two methods agree very well. These subsets indeed happen to consist of those DDs for which MVA is most reliable, i.e., when $(\lambda_2/\lambda_3)^L$ or ω^L are large. In the following section we analyse the dependence of the normal estimates on these two parameters and its consequences for the ratio RD:TD.

8.3 Reexamination of MVA - consequences

Because the strong deviations between the MVA normals observed at the different spacecraft are hard to explain by means of motional or geometrical DD properties, we assume that inaccurate MVA normal estimates are responsible for the extremely different classification

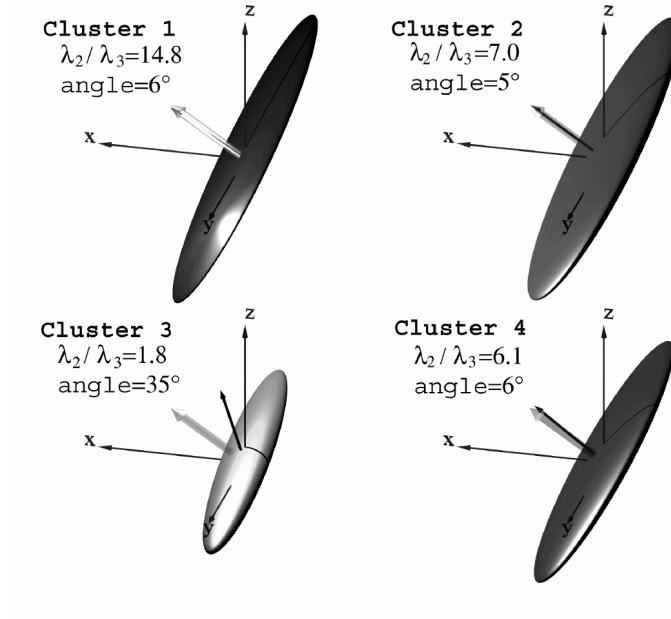


Figure 8.3: Variance ellipsoids obtained from the magnetic field data of the example discontinuity presented in Figure 7.3 for each of the four Cluster spacecraft separately. The ellipsoids are shown in GSE coordinates. Note that the direction of maximum variance is compressed by a factor of ten. The four respective MVA normal estimates are indicated by the thin arrows. The triangulation normal is shown as a thick partly transparent vector. To allow for better comparison this vector is attached to each of the four ellipsoids. The corresponding values of λ_2/λ_3 and the respective angle between the MVA normal and the triangulation normal are displayed.

results discussed in the previous section. This section contains a systematic statistical analysis confirming this hypothesis.

We successively increase $(\lambda_2/\lambda_3)^L$ and ω^L and study how the differences between the two methods evolve as a function of this limitation. It turns out that MVA is much less reliable than previously assumed. In particular, we demonstrate that using the lower limit $(\lambda_2/\lambda_3)^L = 2$ is by no means sufficient to ensure reliable MVA normal estimates.

Before presenting the statistical analysis, we illustrate the basic idea by means of the example presented in Figure 7.3 (section 7.4). Since the global structure (in particular the thickness) of the DDs appears very similar at the four spacecraft, we always pick an interval of equal length for the application of MVA at all four spacecraft. This interval is selected after the time series are shifted such that they are aligned. The vertical lines in Figure 7.3 (right) mark this interval. The corresponding variance ellipsoids are shown in Figure 8.3.

The ellipsoids obtained from the data of spacecraft 1, 2 and 4 have a shape comparable to flat surfboards. This is reflected in the relatively large values of λ_2/λ_3 . Here the MVA normals are well defined and coincide well with the triangulation normal.

At the position of Cl 3 the eigenvalue ratio is small ($\lambda_2/\lambda_3 = 1.8$) and the corresponding variance ellipsoid is “cigar-shaped”. In this case the MVA normal estimate can be anything perpendicular to the direction of maximum variance. As a consequence the MVA normal derived at Cl 3 deviates from the triangulation normal.

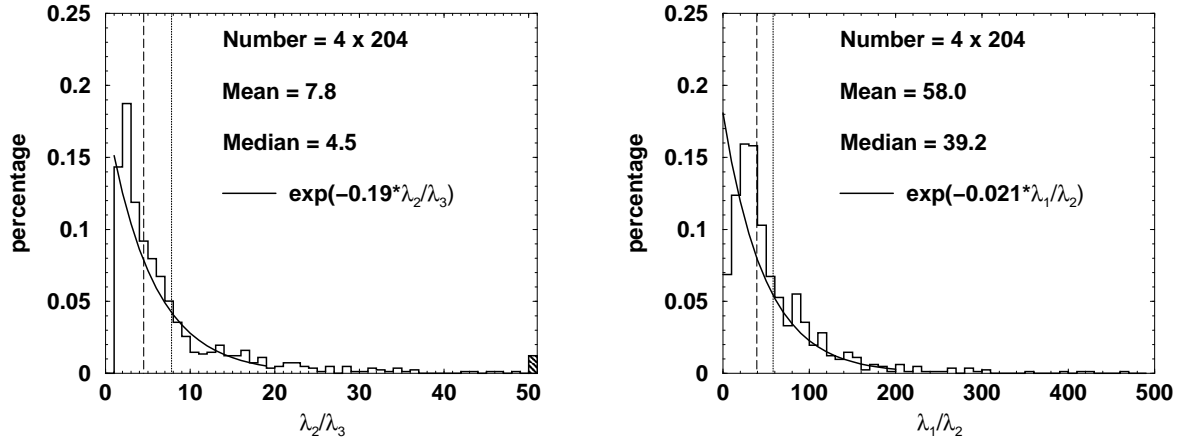


Figure 8.4: Distribution of λ_2/λ_3 (left) and λ_1/λ_2 (right) obtained from all four Cluster satellites. All DDs in the set DD_{2003} are considered. The solid line shows a fit to $p \propto \exp(-\beta \lambda_2/\lambda_3)$, respectively $p \propto \exp(-\beta \lambda_1/\lambda_2)$. The median and the mean values are also plotted (vertical dashed and dotted line).

Note that $\lambda_2/\lambda_3 = 1.8$ is in the vicinity, or even exceeds, the lower limit used for the application of MVA in almost all past studies (see section 7.2) and also in this study when producing Figure 8.2 and the corresponding classification results.

The example presented in Figure 8.3 clearly confirms our assumption stated above. The following systematic analysis provides evidence on a statistical basis.

8.3.1 Parameters affecting the precision of MVA

In this section the distributions of the parameters affecting the precision of MVA are presented. The distribution of ω has already been discussed in section 8.1 where we have found an exponential decrease. The distributions of λ_2/λ_3 and λ_1/λ_2 are very similar in the three periods of observation. Figure 8.4 shows the distributions of these two eigenvalue ratios for the set DD_{2003} . Both distributions can be fitted to an exponential function with a fitting parameter β (see caption). Note that the λ_2/λ_3 distribution (left) compares quite well to the distribution found by *Lepping and Behannon* [1986]. Unfortunately for the application of MVA the majority of events have a small eigenvalue ratio λ_2/λ_3 with a most probable value of $\lambda_2/\lambda_3 = 2.5$. The distribution then rapidly decreases with $\beta = 0.19$. Only about 18% of the events lie above $\lambda_2/\lambda_3 = 10$. Hence, attempting to improve the performance of MVA by increasing the lower limit $(\lambda_2/\lambda_3)^L$ results in a dramatic reduction of events suitable for the analysis. Physically, the small λ_2/λ_3 ratios found for interplanetary discontinuities indicate deviations from 1-D structures. However, it is unclear whether the actual discontinuity is not 1-D or whether $\lambda_3 \neq 0$ is caused by fluctuations superposed to a 1-D discontinuity.

In contrast to λ_2/λ_3 the ratio of largest to intermediate eigenvalue λ_1/λ_2 decreases slowly ($\beta = 0.021$). Generally λ_1/λ_2 is found to be rather large ($\lambda_1/\lambda_2 = 58$ on average). The values found for λ_1/λ_2 are almost ten times the value of λ_2/λ_3 , yielding strongly elongated variance ellipsoids. In other words, the “surf boards” or “cigars” as shown for the example in

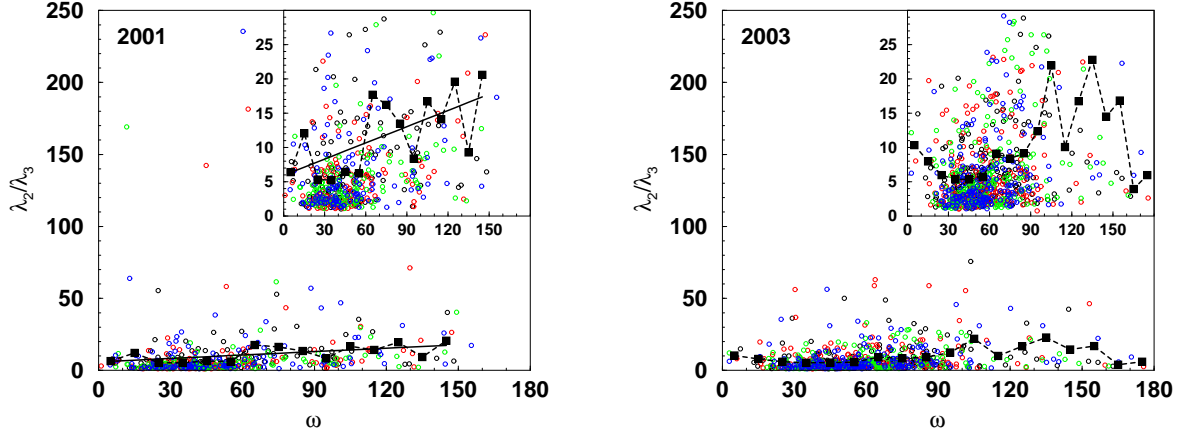


Figure 8.5: Relationship between λ_2/λ_3 and ω . Left: DD_{2001} . Right: DD_{2003} . The values found at each spacecraft are plotted. The standard colour code is used.

Figure 8.3 are extremely long. This is important to know since it indicates that the direction of maximum variance is generally well defined. Hence, a reasonable normal estimate must be perpendicular to this direction. We apply this necessary condition to the triangulation normals in order to confirm their reliability (section 8.4). Physically, the maximum eigenvalue being considerably larger than the intermediate eigenvalue indicates that the field change across the discontinuity takes place mostly in one direction, i.e., linearly polarised waves.

The corresponding distributions for the coronal hole subset DD_{2003CH} (not shown) are similar to the eigenvalue distributions of the total set DD_{2003} .

For the accuracy of MVA the two most important parameters are λ_2/λ_3 and ω . In Figure 8.5 we plot λ_2/λ_3 versus ω , in order to examine how these two parameters are related. All DDs found in DD_{2001} (left) and DD_{2003} (right) are shown. The values found at each spacecraft are shown. Since the spreading angle ω is almost the same at the location of the four spacecraft one can see that λ_2/λ_3 differs strongly at the four positions in many cases. The differences can be extreme for individual DDs. This discrepancy is the subject of later discussions.

Figure 8.5 shows an accumulation of DDs in the region $\lambda_2/\lambda_3 < 5$ and $30^\circ < \omega < 60^\circ$. Also shown are values of λ_2/λ_3 averaged over 10° intervals (black squares connected by the dashed line). A least squares fit of these averages indicates a weak linear trend in the 2001 data. Increasing ω by 10° yields an increase of λ_2/λ_3 by 0.08. For the set DD_{2003} no such linear trend is observed. Also comparing the weak trend to the enormous scatter around the fit in 2001, the linear coherence is rather meaningless. Plenty of small- ω DDs with large eigenvalue ratios are observed. Thus, it is legitimate to claim that the two parameters are independent.

Obviously there are regions in Figure 8.2 where triangulation and MVA results are consistent and regions where enormous discrepancies are observed. In order to get a first clue as to how this is related to the corresponding eigenvalue ratios and ω values, we examine how these parameters are distributed over the classification diagram. In Figure 8.6 the results obtained by MVA for all DDs with $\lambda_2/\lambda_3 > 2$ are shown individually for each of the four spacecraft for the set DD_{2001} . The colour indicates the value of λ_2/λ_3 (left) and ω (right)

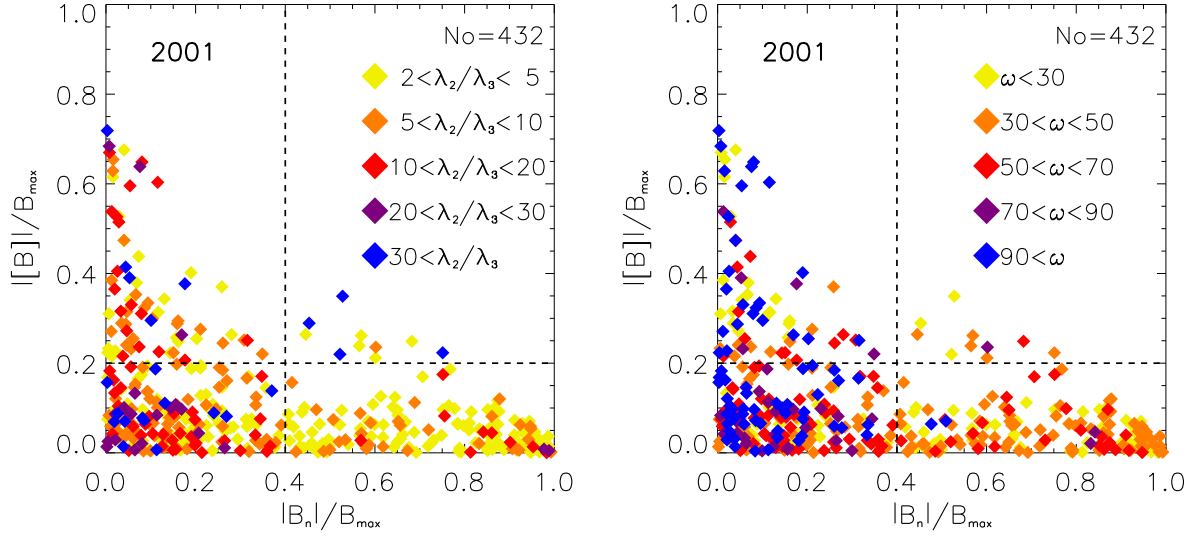


Figure 8.6: Distributions of λ_2/λ_3 (left) and ω (right) for the set DD_{2001} . All four spacecraft are considered. Only DDs with $\lambda_2/\lambda_3 > 2$ are plotted.

for the corresponding DD. Obviously the smallest eigenvalue ratios are observed when the MVA results deviate most from the triangulation results, namely in the RD-category. Here the majority of DDs have $\lambda_2/\lambda_3 < 5$, whereas those events where MVA and triangulation are consistent (i.e., those with small $|B_n|/B_{max}$) happen to have larger values of λ_2/λ_3 .

Analogous results are found for the ω distribution (right hand side of Figure 8.6). Almost all DDs with $\omega > 90^\circ$ are in the TD or the ED category, whereas the RD category is dominated by discontinuities with $\omega < 50^\circ$. Again, those DDs for which the normals are determined with highest accuracy using MVA the two methods are closest to each other. In other words, RDs are predominantly found when the performance of MVA is worst.

The corresponding distributions for the sets DD_{2002} and DD_{2003} (not shown) yield qualitatively the same picture. Also the average values of λ_2/λ_3 and ω separately computed for RDs, TDs and EDs are similar for these two years. The observation of small eigenvalue ratios and spreading angles in the RD section as compared to EDs and TDs can be regarded to be well established (see also the discussion in section 8.1).

The qualitative impression gained from Figure 8.6 is quantified in the following section by successively increasing $(\lambda_2/\lambda_3)^L$ and ω^L and observing how the differences between the two methods evolve as a function of this limitation.

8.3.2 Dependence on the eigenvalue ratio λ_2/λ_3

In this section we study how the results of MVA and triangulation evolve as a function of the lower limit $(\lambda_2/\lambda_3)^L$. Figure 8.7 shows from top to bottom the average angle between the MVA and the triangulation normals, the average difference $\langle \Delta(|B_n|/B_{max}) \rangle$ between the MVA-derived values of $|B_n|/B_{max}$ and those obtained from triangulation and the remaining number of DDs as a function of $(\lambda_2/\lambda_3)^L$. The results are shown for all three years of ob-

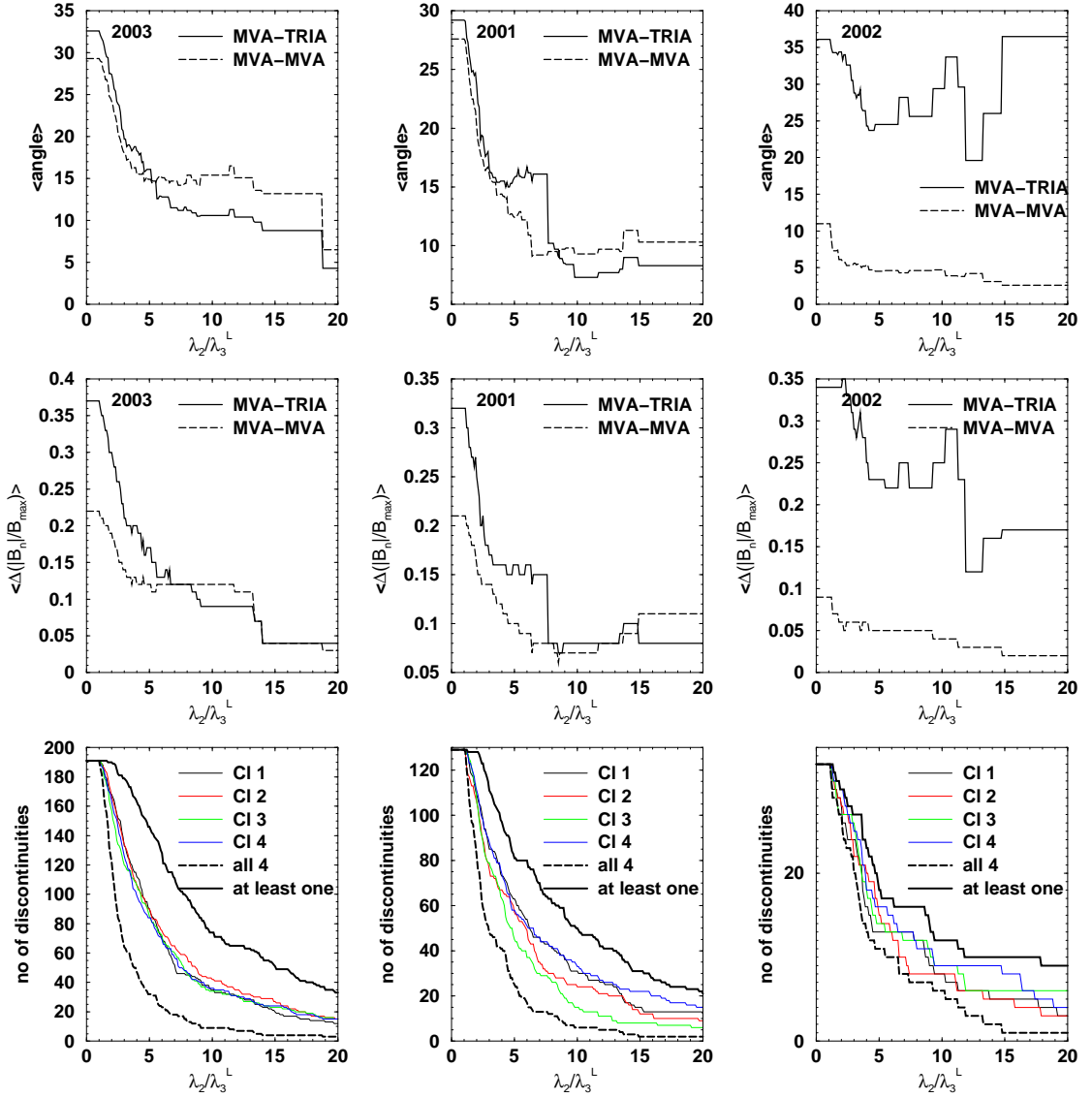


Figure 8.7: Dependence on $(\lambda_2/\lambda_3)^L$. Top: Average angle between the four MVA normals and the triangulation normal (solid line) and average angle between the MVA normals among each other (dashed line). Middle: Average non-negative difference of $|B_n|/B_{\max}$. Bottom: Number of DDs remaining when $\lambda_2/\lambda_3 > (\lambda_2/\lambda_3)^L$ is enforced. The thin coloured lines correspond to the scenario when each spacecraft is treated separately. The thick dashed line is generated when all four spacecraft are required to satisfy $\lambda_2/\lambda_3 > (\lambda_2/\lambda_3)^L$ simultaneously, and the thick solid line represents the case when at least one satellite accomplishes the requirement. For the upper and middle panels we require all four satellites to satisfy the eigenvalue restriction simultaneously. From left to right the sets DD_{2003} , DD_{2001} and DD_{2002} are shown, i.e., in decreasing order of the prevailing spacecraft separations. Note that in DD_{2003} only those DDs are considered for which $P < 0.8$.

servation separately. From left to right the sets DD_{2003} , DD_{2001} and DD_{2002} are shown, i.e., in decreasing order of the prevailing spacecraft separations. Apparently, the results obtained in 2003 (left) and 2001 (middle) are quite similar, whereas a different picture is obtained in 2002. We start by discussing the typical characteristics found in 2003 and 2001 before pointing out differences between the three periods of observation.

The average values shown in Figure 8.7 are produced as follows. For each DD the average angle between the timing-derived normal and the four MVA normals is calculated. Then the average over all discontinuities satisfying $\lambda_2/\lambda_3 > (\lambda_2/\lambda_3)^L$ is determined (solid line). Note, that in the representation shown only those DDs are considered for which the MVA eigenvalue ratios at all four satellites are simultaneously sufficiently large.

Apparently, the angle between the normals strongly depends on the eigenvalue ratio. The average angle between the MVA normals and the triangulation normal of the DDs in the set DD_{2003} decreases from 32.5° for $(\lambda_2/\lambda_3)^L = 1$ to 4° when only DDs with $\lambda_2/\lambda_3 > 20$ are considered. Accordingly, the maximum value for $(\lambda_2/\lambda_3)^L = 1$ is 29° in 2001 which decreases to 7° for $(\lambda_2/\lambda_3)^L = 10$.

Also plotted is the average angle between the six pairs of MVA normals (dashed line). This average angle is calculated by determining the angle between each pair of the four MVA normals from a single DD crossing, yielding an average angle for each DD. Then the average over all DDs satisfying $\lambda_2/\lambda_3 > (\lambda_2/\lambda_3)^L$ is computed (as above).

Again, a strong decrease with $(\lambda_2/\lambda_3)^L$ is observed. Moreover, the two curves (i.e., the solid and the dashed curve) are indeed very similar to each other. In particular, the agreement between the MVA normals among each other is hardly better than between the MVA normals and the timing-derived normal. Note that in 2003 (2001) the two curves intersect at $(\lambda_2/\lambda_3)^L \approx 5.5(8)$, i.e., for $(\lambda_2/\lambda_3)^L \gtrsim 5.5(8)$ the agreement between the four MVA normals and the triangulation normal is even better than the agreement between the MVA normals among each other. This could be realised for instance by MVA normals scattered around the (true) normal determined by triangulation.

These observations clearly support the hypothesis that the deviations between the two methods are substantially caused by inaccurate MVA normal estimates. If we consider only discontinuities with well defined MVA normals, i.e., with large λ_2/λ_3 values, MVA is self-consistent and consistent with triangulation.

Important for the classification into RDs and TDs is the fraction of magnetic field threading the discontinuity plane, i.e. $|B_n|/B_{max}$. The middle panel of Figure 8.7 shows the average difference $\langle \Delta(|B_n|/B_{max}) \rangle$ between the MVA-derived values of $|B_n|/B_{max}$ and those obtained from triangulation (solid line). Again the average difference between the MVA values among each other is displayed by the dashed line. The averaging procedure is the same as described above. Note that $\Delta(|B_n|/B_{max})$ denotes the absolute value of the respective differences.

The dependence on $(\lambda_2/\lambda_3)^L$ is qualitatively similar to that observed for the average angle. When no restriction on λ_2/λ_3 is enforced, a mean difference of $\langle \Delta(|B_n|/B_{max}) \rangle = 0.37(0.32)$ is found between the triangulation and the MVA values in 2003 (2001). This reflects the unacceptable situation presented in Figure 8.2, where we have two methods yielding two completely distinct RD:TD ratios. For $(\lambda_2/\lambda_3)^L = 14(8)$ the difference between the two methods is down to $\langle \Delta(|B_n|/B_{max}) \rangle = 0.04(0.08)$ in 2003 (2001). In that case no significant discrepancies would be reflected on the RD:TD ratios.

Comparing the values of $|B_n|/B_{max}$ arising from MVA among each other, an average difference of $\langle \Delta(|B_n|/B_{max}) \rangle = 0.22(0.21)$ is found when $(\lambda_2/\lambda_3)^L = 1$ in 2003 (2001). In many

cases this inevitably leads to discontinuities being classified as clear RDs by one spacecraft and as possible TDs by another one. Only for large eigenvalue ratios can a consistent classification result be expected at the different spacecraft, according to Figure 8.7.

The bottom panel of Figure 8.7 shows the number of DDs remaining when $\lambda_2/\lambda_3 > (\lambda_2/\lambda_3)^L$ is enforced. The four coloured thin solid lines correspond to the single-spacecraft scenario, i.e., when the eigenvalue restriction needs to be satisfied only at the individual satellite separately. The thick dashed line gives the number of events remaining when all four satellites have to satisfy $\lambda_2/\lambda_3 > (\lambda_2/\lambda_3)^L$ simultaneously, i.e., this curve represents the number of events contributing to the averages shown in the top and the middle panel of Figure 8.7. Finally, the thick solid line represents the case when only at least one of the four satellites accomplishes the requirement. In the single-spacecraft scenario the observed decrease is exponential in $(\lambda_2/\lambda_3)^L$. In contrast, the decrease of the number of remaining DDs is much steeper when the requirement is enforced at all four spacecraft simultaneously, indicating that λ_2/λ_3 varies considerably at the distinct spacecraft locations. This important issue is the subject of section 8.3.4. There we particularly demonstrate that this variability depends on the spacecraft separation. Here we point out that applying the λ_2/λ_3 restriction simultaneously to all four spacecraft is a much stronger requirement than for the single-spacecraft case.

The curves describing the angle between the various normals and the differences between the observed magnetic field normal components as a function of $(\lambda_2/\lambda_3)^L$ show drastically changed characteristics when only a small number of events is left. The rapid strictly monotonic decrease observed for small $(\lambda_2/\lambda_3)^L$ values turns into a more discontinuous characteristic. This is particularly apparent in 2002 where *a priori* only a small number of events is available. The comparison between the MVA normals and the triangulation normal shows the expected characteristic only for $\lambda_2/\lambda_3 \lesssim 4.2$. Beyond that point strong fluctuations are observed. Note that only 12 DDs satisfy the restriction $\lambda_2/\lambda_3 > 4.2$. At about the same number of events (corresponding to $(\lambda_2/\lambda_3)^L = 8.8$ in 2003 and $(\lambda_2/\lambda_3)^L = 7.7$ in 2001) the rapid strict monotonic decrease also ends in 2003 and 2001. Hence, the rather unexpected behaviour is most likely due to the poor statistics when $(\lambda_2/\lambda_3)^L$ is large. In addition to the small number of events, one has to account for the fact that the triangulation normals can be inaccurate in 2002 because of small spacecraft separations. Therefore, the poor performance in 2002 is likely to be contaminated by erroneous triangulation normals contained in the small remaining subset of DDs when $(\lambda_2/\lambda_3)^L$ is large.

Another noticeable result is that apparently the MVA normals are well aligned among each other in 2002. Even when no restrictions on λ_2/λ_3 are imposed, good agreement between the four MVA normals is observed. However, we do not interpret this alignment as an indicator of reliable MVA normals. Instead, we suggest that the superposed fluctuations, that are responsible for the direction of minimum variance not coinciding with the discontinuity normal, do not differ strongly between the spacecraft locations when they are only 100 km apart. When the DDs are observed at larger separated locations (as in 2003 and 2001) the anisotropic superimposed fluctuations may have different minimum variance directions at the four spacecraft positions. This issue is the subject of following sections.

More important for the discussion in this section is the conclusion, drawn from the observations in 2001 and 2003, that inaccurate MVA normals are responsible for the discrepancy

between the two methods, and that by increasing $(\lambda_2/\lambda_3)^L$ a subset of DDs can be found for which the four MVA normals are consistent among each other and with triangulation.

Classification results

Figure 8.8 demonstrates that the classification result strongly depends on the choice of $(\lambda_2/\lambda_3)^L$ when MVA normal estimates are used. On the left the percentages of RDs, TDs and EDs are shown as a function of $(\lambda_2/\lambda_3)^L$ obtained by both MVA and triangulation. The MVA results are based on the data from Cl 1. Note that the λ_2/λ_3 criterion needs to be satisfied only at Cl 1. The middle and the right part of Figure 8.8 show the ratio RD:TD obtained from MVA, found at each spacecraft separately. Whereas the plot in the middle, analogous to the left plot, is obtained by enforcing $\lambda_2/\lambda_3 > (\lambda_2/\lambda_3)^L$ only for the corresponding spacecraft, all four spacecraft need to satisfy the requirement simultaneously in the rightmost plot. We show only the results for DD_{2001} here. The number of DDs available in 2002 is too small for that kind of analysis, and the results found for DD_{2003} are similar to those presented in Figure 8.8. Any differences are discussed below.

The striking impact of the lower limit $(\lambda_2/\lambda_3)^L$ is obvious. Figure 8.8 (left) shows that the triangulation results are rather independent on $(\lambda_2/\lambda_3)^L$. The same holds for the percentage of TDs obtained by MVA. However, the relative number of RDs identified using MVA decreases with increasing $(\lambda_2/\lambda_3)^L$, whereas the percentage of EDs increases correspondingly. The MVA results approach the results obtained by using relative timings. If only DDs with $\lambda_2/\lambda_3 \gtrsim 10$ are considered, both methods agree well, and for $(\lambda_2/\lambda_3)^L = 14$ MVA yields exactly the same result as triangulation. This means that simply by ensuring good quality MVA results (large eigenvalue ratios) a subset of DDs can be found for which the MVA-derived and the triangulation-derived classification results are consistent. Note that according to Figure 8.7 this subset coincides with the DDs for which the four MVA normals are also consistent among each other.

From Figure 8.8 (middle) it can be seen that particularly the ratio RD:TD considerably depends on the chosen value of $(\lambda_2/\lambda_3)^L$. Without enforcing a restriction on λ_2/λ_3 , the ratio is between 2.6 and 3.1 depending on the spacecraft considered. With increasing $(\lambda_2/\lambda_3)^L$ the value of RD:TD decreases dramatically. For $(\lambda_2/\lambda_3)^L = 2$ the RD to TD ratio is ≈ 2 (see also Table 8.1). However, with a selection criterion $\lambda_2/\lambda_3 > 5$ the observed incidences of RDs and TDs are balanced, i.e. $RD:TD = 1$, and the decrease continues in this manner. Hence, the choice of $(\lambda_2/\lambda_3)^L$ is definitely decisive for the classification result that one obtains. Since we have not found physical arguments explaining the coherence between the eigenvalue ratio and the ratio RD:TD, but many arguments (both theoretical and observational) proving the correlation between $(\lambda_2/\lambda_3)^L$ and the error cone angle associated with MVA, we conclude that the RD:TD ratio approaches the true value with increasing $(\lambda_2/\lambda_3)^L$. For $(\lambda_2/\lambda_3)^L = 13, 23, 9, 20$ the triangulation result $RD:TD = 0$ is reached at Cl 1, 2, 3 and 4, respectively.

Note that there are a few events with large eigenvalue ratios included in the RD category, for instance when data from Cl 2 or Cl 4 are used. The set DD_{2003} also contains such cases (not shown). However, these events are all very weak with a small spreading angle ($\omega \approx 30^\circ$).

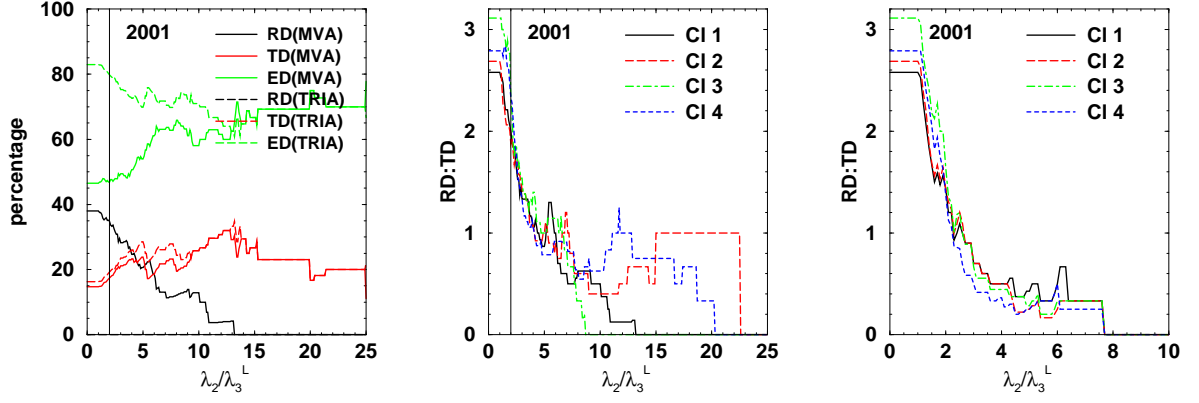


Figure 8.8: Dependence of the classification result on $(\lambda_2/\lambda_3)^L$. Only data from 2001 are shown. Left: Percentages of RDs (black), TDs (red) and EDs (green). Results obtained from MVA applied to CI 1 data (solid lines) and from triangulation (dashed lines) are shown. Note that the line representing the RD percentage found from triangulation coincides with the horizontal axis. Middle and right: Ratio RD:TD for each satellite separately. For the left and middle panels the lambda criterion needs to be satisfied only at the individual spacecraft. The vertical line indicates $(\lambda_2/\lambda_3)^L = 2$. In the right panel all four spacecraft are enforced to satisfy $\lambda_2/\lambda_3 > (\lambda_2/\lambda_3)^L$ simultaneously. The number of remaining DDs can be extracted from Figure 8.7.

Also note that when the much stricter requirement of simultaneously enforcing $\lambda_2/\lambda_3 > (\lambda_2/\lambda_3)^L$ is applied the ratio RD:TD decreases even more rapidly, and no RDs are observed when $(\lambda_2/\lambda_3)^L > 8$ (right of Figure 8.8). This is particularly apparent in 2003 (not shown).

So far we have clearly demonstrated a correlation between the classification result and the reliability of MVA. If $(\lambda_2/\lambda_3)^L$ is chosen large enough, the MVA normals are almost collinear. In this case MVA yields the same picture as triangulation, namely a solar wind dominated by discontinuities with small values of $|B_n|/B_{max}$, which appears to be closest to the truth. Note, however, that we cannot exclude the possibility that “real RDs” have smaller eigenvalue ratios than TDs or EDs (i.e., DDs with small values of $|B_n|/B_{max}$) and we thus introduce a bias favouring TDs by selecting only events with high eigenvalue ratios. The question is whether it is an intrinsic property of RDs to have small eigenvalue ratios or whether some DDs are simply identified as RDs by MVA because they have small eigenvalue ratios. We suggest the latter to be the correct answer. Of course we cannot guarantee that we do not pre-select the results by increasing the lambda ratio, but there are at least two arguments against this: (1) Triangulation yields small values of $|B_n|/B_{max}$ for all events regardless of $(\lambda_2/\lambda_3)^L$. One advantage of this multi-spacecraft method is that it is independent of the inner DD structure and thus independent of λ_2/λ_3 . (2) For 1-D structures, deviations from $\lambda_3 = 0$ can occur only due to superposed fluctuations. The DDs we omit have $\lambda_2 \approx \lambda_3$, with λ_3 distinct from zero, i.e., there are superposed fluctuations present (assuming the actual discontinuities to be 1-D in nature). There is no reason for RDs to be distinct from TDs in this respect. Further arguments will follow.

The observations presented above entail serious practical consequences. For $(\lambda_2/\lambda_3)^L = 5$ only approximately 50% of the DDs in the original sets remain (see Figure 8.7). However, in order to achieve satisfactory MVA normal estimates, we suggest to use $(\lambda_2/\lambda_3)^L \approx 10$ as a lower limit. In that case only approximately 25% of the total number of events persist,

dramatically reducing the number of DDs suitable for studies using MVA. In order to pursue this issue a little further, we ask how many DDs remain when we demand a certain average angle between the MVA normals. Therefore, we plot the number of DDs versus the average angle for the different subsets arising from varying $(\lambda_2/\lambda_3)^L$ (not shown). The observed coherence is linear: Number of DDs ($\langle \text{angle} \rangle$) $\propto k \langle \text{angle} \rangle$, with $k = 7.3$ (11.3) using DD_{2001} (DD_{2003}). In other words, in order to increase the average MVA accuracy by 10° , one has to abandon 73 out of the 129 DDs (57%) in 2001 and 113 out of the 204 DDs (55%) in 2003.

More evidence for the poor performance of MVA and for $|B_n|/B_{max}$ being small

Figure 8.9 provides further evidence for the poor performance of MVA in the low lambda ratio regime. Moreover we demonstrate that the apparently true DD normals appear to be indeed perpendicular to \mathbf{B} . The left hand side of Figure 8.9 shows various distributions of the angle θ_{Bn} between the derived normal \mathbf{n} and the average magnetic field \mathbf{B} . The top panel shows the results for DD_{2001} and the middle panel the results for DD_{2003} . The θ_{Bn} distribution obtained from MVA is shown for different subsets. These subsets are selected according to the values of λ_2/λ_3 . Counting all DD traversals of each individual spacecraft, we have 4×129 and 4×204 DD crossings in 2001 and 2003, respectively. Of these, all traversals with $\lambda_2/\lambda_3 \in [1, 3]$ are put in one group, regardless of the particular spacecraft (light blue). The same is done for the ranges $\lambda_2/\lambda_3 \in (3, 8]$ (magenta) and $\lambda_2/\lambda_3 > 8$ (dark blue). A further group is built by the DDs where all four spacecraft simultaneously satisfy $\lambda_2/\lambda_3 > 8$ (green). As a reference we also plot the theoretical θ_{Bn} distribution that one obtains for uniformly distributed vectors on a unit sphere, i.e. $P(\theta_{Bn} \in [l, u]) = \int_l^u \sin(\theta_{Bn}) d\theta_{Bn}$. This distribution would be obtained when the normal vector is chosen at random for each transition with any direction having equal probability. The other reference plotted is the θ_{Bn} distribution obtained from triangulation. The bin width is 5° .

The distributions shown are qualitatively the same in 2001 and in 2003. In both plots (upper left and middle left of Figure 8.9) a considerable change of the MVA distributions with increasing accuracy (lambda ratio) is found. The distribution according to the worst MVA normals ($\lambda_2/\lambda_3 \in [1, 3]$) remarkably well resembles the random distribution. In other words, MVA normal estimates in the low eigenvalue regime yield the same result as randomly chosen directions would give.

With increasing values of λ_2/λ_3 the MVA-derived distributions differ more and more from the random distribution and approach the distribution from triangulation. This means that the relative number of DDs with large θ_{Bn} increases. Note that the strongest restriction, i.e., the “green group”, leads to the absence of DDs with $\theta_{Bn} < 50^\circ$ in 2003.

Apparently triangulation always yields normals close to being perpendicular to the magnetic field, i.e. $\theta_{Bn} \approx 90^\circ$. We have shown above that with increasing quality this result is also approached using MVA. It is of considerable interest that apparently also the θ_{Bn} distributions obtained from relative timings are different for different accuracies. This is shown in the bottom left plot of Figure 8.9. Here the distributions according to the triangulation normals are shown separately for each year. With increasing spacecraft separations (i.e., increasing accuracy) the respective distributions more clearly resemble a δ -distribution at $\theta_{Bn} = 90^\circ$.

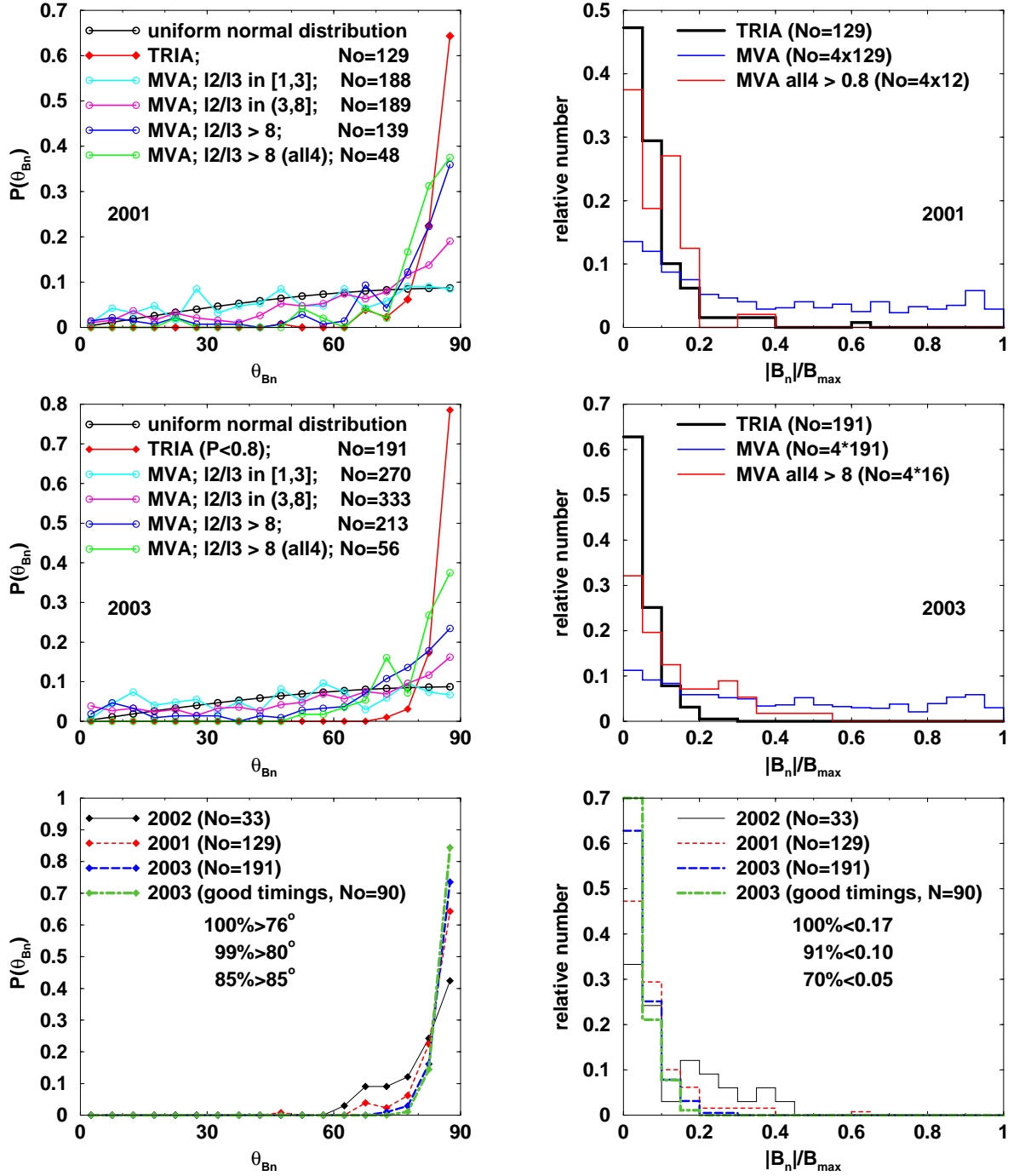


Figure 8.9: Left (top and middle): Probability distribution of $\theta_{Bn} = \angle(\langle \mathbf{B} \rangle, \mathbf{n})$ obtained from MVA for different ranges of λ_2/λ_3 compared to the distribution obtained from uniformly distributed vectors on the unit sphere (black) and the distribution obtained from triangulation (red). Data from 2001 (top) and 2003 (middle) are shown. In the bottom panel the triangulation results for all three years are compared. Right: Distributions of $|B_n|/B_{max}$. For the triangulation results only DDs with $P < 0.8$ are considered.

Whereas the poorly estimated normals in 2002 occasionally yield relatively small angles, the normals obtained with larger separations in 2001 and particularly in 2003 are always nearly perpendicular to \mathbf{B} . As a further test we selected all DDs in the set DD_{2003} for which the relative timings are identified to be particularly well known³. Certainly, for this subset (90

DDs) the determined normals are most accurate. The distribution of this “best estimates” - set is represented by the green line. Indeed, the trend towards $\theta_{Bn} = 90^\circ$ with increasing reliability of the normals can be confirmed. All but one DD ($\theta_{Bn} = 76^\circ$) are found in the last two bins, i.e., for 99% of the DDs the angle between the normal and the magnetic field is greater than 80° ; and 85% of the normals are identified to be perpendicular to \mathbf{B} within only 5° .

It is tempting to conclude from these observations that the true normals of the DDs investigated are in fact perpendicular to \mathbf{B} . In terms of the magnetic field normal component this means $|B_n|/B_{max} = 0$.

The corresponding distributions of $|B_n|/B_{max}$ are presented on the right hand side of Figure 8.9. The colour code for the respective sets in the lower panel is the same as for the θ_{Bn} distribution. The largest normal component found in the “best estimates” - set is $|B_n|/B_{max} = 0.17$. For 91% of the DDs $|B_n|/B_{max}$ is less than 0.1, and for 70% $|B_n|/B_{max}$ is even below 0.05. With increasing uncertainty, the resulting values of $|B_n|/B_{max}$ increase. The largest normal components are found in 2002 where the spacecraft separations are extremely small. Here a considerable number of DDs have normalised normal components between 0.15 and 0.45. In chapter 9 we compare the measured normal components to the uncertainty of triangulation, in order to prove that the found values are indeed consistent with $|B_n|/B_{max} = 0$.

The top and the middle panel on the right hand side of Figure 8.9 show the $|B_n|/B_{max}$ distributions obtained from MVA compared to the triangulation-derived distributions. In the distribution represented by the blue line all 129 DDs in 2001 (top), respectively all 191 DDs with $P < 0.8$ in 2003 (middle) are considered. The normal components are almost uniformly distributed with a slight increase towards small $|B_n|/B_{max}$ values. Considering only relatively well determined MVA normals ($\lambda_2/\lambda_3 > 8$ simultaneously at all four spacecraft), the distribution (red) approaches that found by triangulation (black).

In summary, we have demonstrated the existence of a subset of DDs for which MVA and triangulation yield consistent classification results. This subset coincides with those DDs for which the MVA normals are also consistent among each other, i.e., when λ_2/λ_3 is large. We conclude that MVA is inadequate to determine reliable normal estimates when λ_2/λ_3 is small. In particular the choice of $(\lambda_2/\lambda_3)^L = 2$ is overly optimistic. Using such a small lower limit yields fallacious classification results. Moreover, we find that the more precisely the normals are determined the more they tend to be perpendicular to the magnetic field. This is true both for MVA and for triangulation. This observation may suggest that perhaps all DDs in our representative set are TDs. At least they may all be consistent with being TDs.

8.3.3 Dependence on the spreading angle ω

The other parameter affecting the accuracy of MVA is the spreading angle ω . Since λ_2/λ_3 and ω are two independent parameters, finding another subset of DDs with consistent normals by increasing ω^L would certainly confirm our conclusions from the previous section.

³For instance because of a particularly quiet background field.

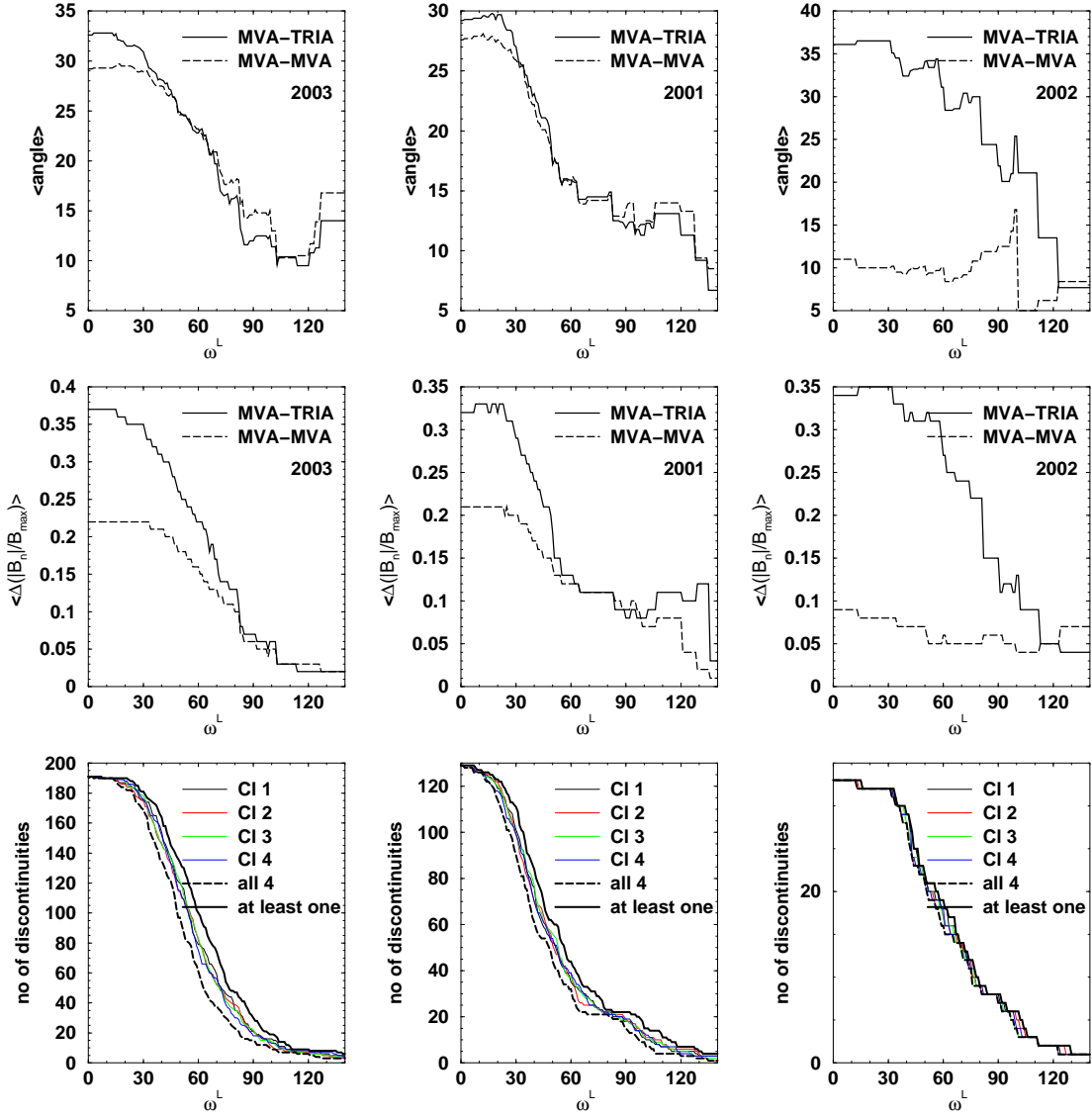


Figure 8.10: Same as Figure 8.7 for ω^L .

The procedure is the same as above. Basically only the parameter $(\lambda_2/\lambda_3)^L$ is replaced by ω^L . Figures 8.10 and 8.11 are analogous to Figures 8.7 and 8.8, respectively.

Apparently the average angle between the various normals and the average difference between the values of $|B_n|/B_{max}$ also strongly depend on ω^L (see Figure 8.10). Both quantities dramatically decrease with increasing values of ω^L . As for $(\lambda_2/\lambda_3)^L$, the two curves representing the angle between the MVA normals among each other and the angle between the MVA normals and the triangulation normal intersect. For $\omega^L \gtrsim 60^\circ$ the MVA normals agree on average better with the triangulation normal than among each other. Note that the two curves are even closer together than in Figure 8.7, indicating that mainly poor MVA estimates are responsible for the discrepancy between the two methods. Again, considering only DDs with well defined MVA normals, MVA is self-consistent and consistent with triangulation. Comparing the results obtained for the set DD_{2002} (right) one may conclude that in addition to MVA, the triangulation results gain accuracy with increasing ω whereas stricter requirements regarding λ_2/λ_3 only affect the MVA normals. Whereas for large λ_2/λ_3 cases

the decrease of $\langle \Delta(|B_n|/B_{max}) \rangle$ is less clear, and the angle between MVA and triangulation normals even increases with increasing $(\lambda_2/\lambda_3)^L$, the agreement between the two methods continuously improves with increasing ω^L . However, we need to keep in mind the poor statistics in 2002.

The differences between the measured normal components of the magnetic field almost vanish when only DDs with large spreading angles are considered. This value goes down to $\langle \Delta(|B_n|/B_{max}) \rangle \approx 0.02$ in 2003 and 2001. This means that considering only DDs with a large spreading angle identical classification results are expected.

The observations above confirm that ω is indeed an important parameter for the accuracy of MVA, as already pointed out by *Lepping and Behannon* [1980]. Unfortunately this coherence has not been adopted by the community so far. Commonly only a lower limit of $(\lambda_2/\lambda_3)^L \approx 2$ is used in order to ensure reliable MVA normals, and ω is disregarded (see the discussion in section 7.2). Although the proposed value of $\omega^L = 40^\circ$ [*Lepping and Behannon*, 1980] appears to be overly optimistic (Figure 8.10 rather suggests to use $\omega^L \approx 90^\circ$, or perhaps $\omega^L \approx 60^\circ$ in connection with an additional requirement on λ_2/λ_3 to ensure consistent MVA normals), the principle finding of *Lepping and Behannon* [1980] to consider ω is certainly important.

The bottom panel of Figure 8.10 points to an important difference between the two parameters λ_2/λ_3 and ω . The number of DDs remaining as a function of $(\lambda_2/\lambda_3)^L$ strongly depends on how the restriction is enforced (see bottom panel of Figure 8.7). If we require that at least one satellite satisfies $\lambda_2/\lambda_3 > (\lambda_2/\lambda_3)^L$, many more DDs are left over than when all four satellites have to satisfy the requirement. Even in the single-spacecraft scenario, where each satellite is treated separately, differences occur. On the other hand, all six curves are almost the same when ω^L is increased (bottom panel of Figure 8.10). Apparently the macroscopic observable ω is the same at the positions of the four spacecraft, whereas λ_2/λ_3 , which strongly reflects the inner structure of the DDs, varies considerably at the distinct locations. This issue will be detailed in section 8.3.4.

Classification results

Analogous to the analysis in the previous section we investigate the dependence of the classification result on the choice of ω^L . Figure 8.11 is similar to Figure 8.8. The left and the middle panel show the percentages of RDs, TDs and EDs as a function of ω^L in 2001 and 2003, respectively. Again, the solid lines indicate the MVA classification results and the dashed lines those obtained from triangulation. An additional requirement is that also $\lambda_2/\lambda_3 > 2$, such that the initial results (on the left) correspond to the classifications obtained in earlier studies. All four satellites are enforced to satisfy the ω criterion simultaneously. However, since ω is almost the same at the position of the four spacecraft, this specification is not particularly relevant. The right panel shows the ratio RD:TD obtained for the set DD_{2003} . The vertical lines indicate the value $\omega^L = 30^\circ$. Because most of the selected DDs according to the B- and the TS-method have spreading angles $\omega > 30^\circ$ (see section 6.2), the classification results are almost constant left of this line.

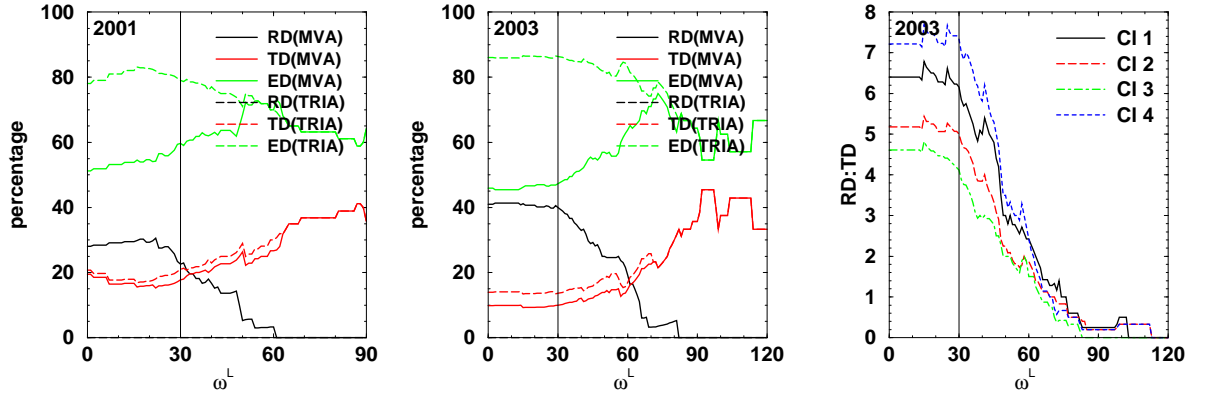


Figure 8.11: Dependence of the classification result on ω^L . Similar to Figure 8.8. Left and middle: Percentages for RDs (black), TDs (red) and EDs (green) obtained from CI 1 (MVA) in 2001 (left) and from CI 4 (MVA) in 2003 (middle). Note that the line representing the RD percentage found from triangulation coincides with the horizontal axis. Right: Ratio RD:TD for each satellite separately (data from 2003). In all three plots the ω^L criterion needs to be satisfied at all four spacecraft simultaneously. In addition $\lambda_2/\lambda_3 > 2$ is applied for the left and the middle plot. The vertical line indicates $\omega^L = 30^\circ$. The number of remaining DDs can be extracted from Figure 8.10.

The principle characteristics of the ω^L dependence observed in Figure 8.11 are the same as for the $(\lambda_2/\lambda_3)^L$ dependence (Figure 8.8). Also the results are almost the same in 2001 and in 2003. With increasing ω^L the percentage of RDs found using MVA decreases whereas the relative number of EDs increases correspondingly. For $\omega^L \gtrsim 60^\circ$ (80°) MVA yields the same results as triangulation in 2001 (2003). Hence, the classification result also strongly depends on the choice of ω^L , and the MVA results approach those obtained from triangulation.

In addition to the decrease of RDs and the increase of EDs, there is a superposed tendency towards more TDs, independent of the method used. Obviously discontinuities showing a change in magnitude also have a larger spreading angle ω .

The dependence of the percentage of EDs on ω^L found using MVA is particularly interesting. Initially the relative number of EDs increases corresponding to the decrease of RDs. The maximum of the ED curve is reached approximately at the value of ω^L for which MVA and triangulation agree. A further increase of ω^L then yields a decreasing number of EDs in favour of TDs. In contrast, the relative number of EDs found using triangulation is almost a strictly monotonic decreasing function of ω^L .

The partially increased relative number of TDs found by triangulation as compared to MVA (in the low ω regime) accounts for the NDs identified by MVA. Those DDs are identified as TDs when triangulation is applied (also see Figure 8.2). This also applies to the left hand side of Figure 8.8.

From the right hand side of Figure 8.11 it can be seen that the ratio RD:TD also strongly depends on ω^L . Without enforcing a restriction on ω , this ratio ranges between ≈ 4.5 and ≈ 7 in 2003. For $\omega^L \gtrsim 30^\circ$ the ratio dramatically decreases with increasing lower limit ω^L , and is unity for $\omega^L \approx 70^\circ$. Finally, for $\omega^L \approx 80^\circ - 110^\circ$ (depending on the spacecraft considered) MVA identifies no RDs either.

Moreover, the classification results considerably differ at the individual spacecraft when all DDs are considered. With increasing accuracy of MVA this discrepancy decreases, i.e., good quality MVA normals yield consistent classification results among each other. Note that no restrictions on λ_2/λ_3 are enforced for the right panel of Figure 8.11.

As in the case of the λ_2/λ_3 criterion, the number of DDs identified to be suitable for proper MVA application is dramatically reduced. Therefore, single-spacecraft studies give a choice between rather poor statistics with good quality MVA normals or good statistics with poorly estimated normals.

Analogous to the discussion in the previous section we cannot exclude the possibility of “real RDs” having, in fact, only small spreading angles. However, it would require a remarkable coincidence for “real RDs” to be always characterised by parameters for which MVA performs poorly, i.e., small lambda ratios and small ω . It is more reasonable to conclude that DDs in this parameter regime have small normal components in reality, as triangulation suggests, and that MVA identifies them as “clear RDs” simply because of a huge error cone angle.

The main conclusions of this and the previous section can be summarised as follows: Increasing the reliability of MVA by separately increasing two independent parameters, i.e., $(\lambda_2/\lambda_3)^L$ and ω^L , we find the same result. In both cases subsets can be identified for which the MVA results are consistent among each other and the two different methods are also consistent (i.e., for $\lambda_2/\lambda_3 \gtrsim 10$ and $\omega \gtrsim 70^\circ$, respectively). Thus we conclude that the different classification results found initially are simply due to the poor performance of MVA in well defined circumstances (small values of λ_2/λ_3 and/or ω). We further conclude that the solar wind is dominated by DDs with a small magnetic field normal component, perhaps TDs.

For practical reasons concerning future single-spacecraft investigations we point out that besides λ_2/λ_3 , also ω is an important parameter affecting the accuracy of MVA (see also *Leping and Behannon* [1980]). In order to *a priori* ensure reasonable MVA results a preselection of events with $\omega \gtrsim 60^\circ$ appears adequate. Further quality tests (much stricter than in common practice) must then be done by inspecting the eigenvalue ratio λ_2/λ_3 after MVA is performed.

8.3.4 Variability of λ_2/λ_3 and ω

In the previous sections we have noted that, whereas similar values of ω are observed at the positions of the four spacecraft, λ_2/λ_3 varies strongly at the distinct locations where a DD is traversed. This is explicitly shown in Figure 8.12. On the left the distributions of

$$\Delta(\lambda_2/\lambda_3)/(\lambda_2/\lambda_3)_{\max} = ((\lambda_2/\lambda_3)_{\max} - (\lambda_2/\lambda_3)_{\min})/(\lambda_2/\lambda_3)_{\max}$$

are presented, where $(\lambda_2/\lambda_3)_{\max}$ is the maximum and $(\lambda_2/\lambda_3)_{\min}$ the minimum of the λ_2/λ_3 values observed at the four spacecraft. The right hand side shows the distributions of the correspondingly defined values of $\Delta\omega/\omega_{\max}$. From top to bottom the results for DD_{2002} , DD_{2001} and DD_{2003} (i.e., in the order of increasing spacecraft separations) are shown.

Apparently λ_2/λ_3 differs strongly at the positions of the four spacecraft. In many cases the observed difference $\Delta(\lambda_2/\lambda_3)$ between the maximum and the minimum of the four λ_2/λ_3

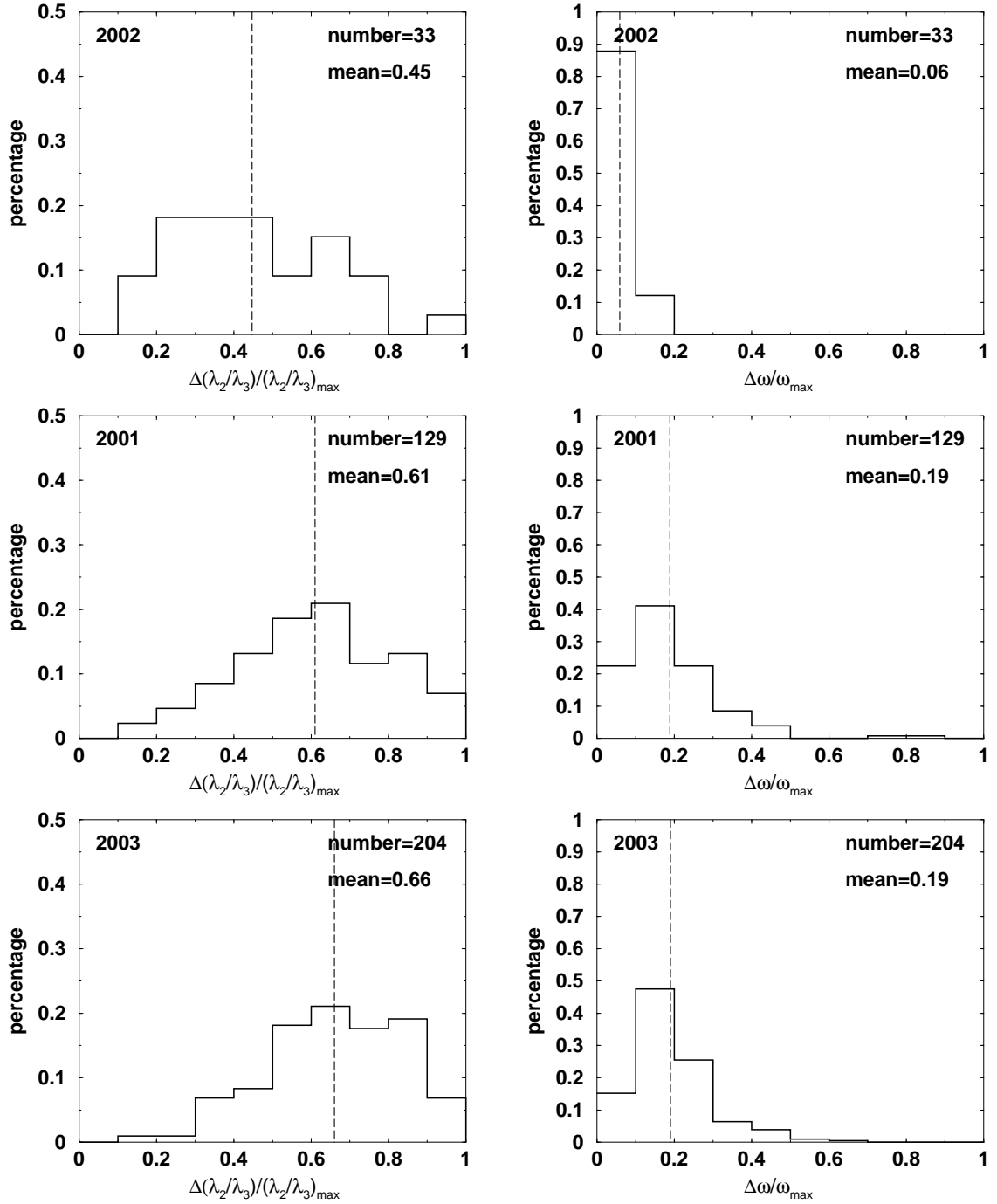


Figure 8.12: Distributions of $\Delta(\lambda_2/\lambda_3)/(\lambda_2/\lambda_3)_{\max}$ (left) and $\Delta\omega/\omega_{\max}$ (right). Note the different ranges of the ordinate. From top to bottom: 2002, 2001, 2003.

values is almost as large as the maximum value $(\lambda_2/\lambda_3)_{\max}$ itself. In contrast, the spreading angle is similar at all four spacecraft. Note that we have used high resolution data to determine ω (i.e., ω is the angle between the first and the last high resolution magnetic field vector of the DD). Hence, the results are hampered by high frequency fluctuations. Certainly the agreement would be even better if average values were used.

In sections 8.4 and 8.5 we use 20 s average field vectors immediately upstream and downstream of the DDs to estimate the normals via the cross product of these vectors. The excellent agreement between the cross product normals (see section 8.5) indicates that the averaged

upstream and downstream field vectors also coincide at the positions of the four spacecraft. Hence, macroscopic observables determined by quantities requiring measurements on the two sides of the DDs, such as ω , generally agree very well at the locations of the four spacecraft. Consequently, methods estimating discontinuity normals independently of the inner structure of the DDs, such as the triangulation method or the cross product method, agree very well, even if λ_2/λ_3 is small (see sections 8.4 and 8.5). We conclude that the actual discontinuity does not differ at the positions of the four spacecraft.

In contrast to ω , the eigenvalue ratio λ_2/λ_3 depends strongly on the inner structure of the DDs. The individual values of λ_2/λ_3 being extremely different at the four positions indicates a considerable variability of the superposed fluctuations or high frequency wave fields on the length scales given by the spacecraft separations. Furthermore, this observation indicates that the superimposed fluctuations are non-isotropic.

Considering that the measured eigenvalues and corresponding eigenvectors account for the sum of the measured variances, which are composed of both the pure undisturbed discontinuity and the superimposed fluctuations, the variability of λ_2/λ_3 can then be explained by a varying spatial orientation of the non-isotropic perturbation field related to the actual discontinuity. For instance, the total eigenvalue ratio is generally large when the minimum variance direction of the superimposed fluctuations coincides with the minimum variance direction of the actual discontinuity. This way $(\lambda_2/\lambda_3)_{max}$ could be realized at one spacecraft. At another spacecraft the wave vector of the superimposed fluctuations might be oriented such that the minimum variance direction of the undisturbed discontinuity coincides with the maximum variance direction of the perturbation, yielding a large total value of λ_3 and thus generally a small value of λ_2/λ_3 . Hence, non-isotropic fluctuations or waves, superposed on the ideal discontinuity and thus modifying the undisturbed variance ellipsoids differently at different positions, are a likely reason for observing different MVA normal estimates at the distinct positions of the four satellites.

Dependence on the spacecraft separation

From Figure 8.12 it can be seen that the observed variability of λ_2/λ_3 and ω depends on the spacecraft separations. Whereas not much difference between the sets DD_{2001} and DD_{2003} are found, the values of λ_2/λ_3 and ω are considerably closer together in 2002 where the spacecraft separations are small.

To visualise the spatial dependence we plot the average values of $\Delta(\lambda_2/\lambda_3)/(\lambda_2/\lambda_3)_{max}$ and $\Delta\omega/\omega_{max}$ (marked as vertical lines in Figure 8.12) versus the average spacecraft separation in the three periods of observation (Figure 8.13). Although only four distances are considered, Figure 8.13 bares information of considerable interest. Both quantities strictly monotonically increase when the spacecraft separations are small. However, although the maximum available average distance is still relatively small (≈ 4000 km in 2003), both $\Delta(\lambda_2/\lambda_3)/(\lambda_2/\lambda_3)_{max}$ and $\Delta\omega/\omega_{max}$ appear to saturate: The variability of ω is almost the same at an average separation of 900 km as at 4000 km, and the rate of increase of $\Delta(\lambda_2/\lambda_3)/(\lambda_2/\lambda_3)_{max}$ almost vanishes for distances > 900 km. Note, however, that we can only address the spacecraft separations given by Cluster. It would be interesting to see how the quantities evolve for larger

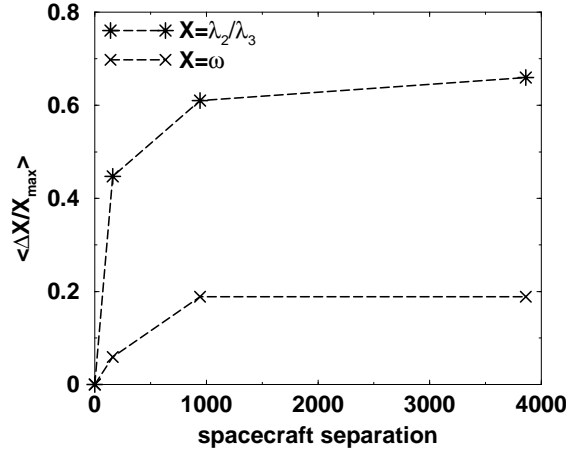


Figure 8.13: Average values of $\Delta X/X_{\max}$ ($X = \lambda_2/\lambda_3, \omega$) versus average spacecraft separation in the corresponding period of observation. We added the theoretical values $\Delta X/X_{\max}(0) = 0$.

separations, e.g. 2 or 3 magnitudes larger.

Of particular interest is the dramatic increase of $\Delta(\lambda_2/\lambda_3)/(\lambda_2/\lambda_3)_{\max}$ observed for small separations. Strong discrepancies between the eigenvalue ratios are found already at an average separation of only ≈ 100 km. From the discussion above one may conclude that the length scales on which the superimposed high frequency fluctuations are spatially correlated is rather small. It would be certainly interesting to pursue this issue further, for instance by also examining λ_1/λ_2 .

We point out that we assume the variability of λ_2/λ_3 to be solely related to fluctuations superimposed on the actual discontinuity. To test this it would be interesting to repeat the analysis for magnetic field data intervals not containing any DDs. Certainly, this type of multi-spacecraft analysis is also relevant for studies related to solar wind turbulence, but this is beyond the scope of the present work.

Whereas the small separations in 2002 appear to be still within the segment of the curve where the spatial variability of λ_2/λ_3 sharply increases with distance, the separations in 2001 and 2003 are already in the region of moderate increase. Hence, the spacecraft separations in 2002 (≈ 100 km) may be small enough for the minimum variance directions of the disturbance field to be well aligned at the four positions. Therefore, the error associated with the interpretation of the minimum variance direction of the total signal as the true normal of the discontinuity is similar at all four spacecraft. As a consequence, the four individual MVA normal estimates agree fairly well in 2002 (see preceding sections).

We conclude that the non-isotropic high frequency disturbances may be correlated on length scales observed in 2002 for many DDs and are generally rather uncorrelated on length scales $\gtrsim 900$ km (as observed in 2001 and 2003), yielding aligned minimum variance directions in 2002 and deviating normal estimates in 2001 and 2003.

8.3.5 Superposed wave fields - one example

The observations and conclusions presented in the previous sections imply that an appropriate model for discontinuities in interplanetary space is a 1-D structure, that is planar on the Cluster separation scale, superposed by non-isotropic fluctuations or wave fields. The superposed fluctuations could be MHD waves, independently existing in the solar wind, or the discontinuities could generate these wave modes of their own. The example we present in this section confirms that the above model indeed coincides well with the observations. Furthermore, we discuss the nature and possible origins of the superposed fluctuations.

The procedure we apply consists of subtracting the superposed fluctuations from the observed total structure and subsequently analysing the DD and the fluctuations separately. In addition we examine the fluctuations in a quiet (not containing a DD) interval in the vicinity of the DD to study whether the fluctuations within and outside the DD are interrelated.

The example shown in Figure 8.14 is taken from the set DD_{2001} . The DD, identified as an RD by MVA and as an ED using triangulation, is observed on day 44 at 03:07 UTC. It is extreme in the sense that it represents a rather weak DD ($\omega \approx 30^\circ$) superposed by strong fluctuations. It is characterised by large MVA eigenvalue ratios ($\lambda_2/\lambda_3 = 11, 23, 8, 20$ at Cl 1, Cl 2, Cl 3 and Cl 4, respectively) and well aligned MVA normals (see Table 8.2). Apart from the small spreading angle, one could thus assume that MVA performed rather well. However, this particular event attracts our attention, because in spite of good eigenvalue ratios and the consistent MVA results, the triangulation normal is almost perpendicular to the MVA normals (see Table 8.2). Certainly the time gaps between the spacecraft are difficult to evaluate, because of the strongly fluctuating field. Hence, this is probably one of the cases where triangulation performs relatively poor. However, using low pass filtered data, i.e., 4 s sliding averages, timings can be found which permit a reasonable normal estimate. In any case, the associated triangulation error cone angle is well below 90° .

In order to investigate the influence of the superposed fields we subtract a model $\{\mathbf{B}_{disc}^{(m)}\}$ for the actual discontinuity from the observed field $\mathbf{B}^{(m)} = \mathbf{B}_{disc}^{(m)} + \mathbf{B}_{fluc}^{(m)}$. The remaining signature $\{\mathbf{B}_{fluc}^{(m)}\}$ then solely consists of the superimposed wave fields.⁴

The difficulty of such an approach is to find a suitable model $\{\mathbf{B}_{disc}^{(m)}\}$ for the actual discontinuity. Trigonometric functions may be useful in this regard. For instance *Schröder* [2002] uses the arc tangent function. However, the mean characteristic of the particular event in Figure 8.14 resembles rather a simple linear ramp. In a first step we low pass filter the data using 4 s sliding averages. Figure 8.14 shows that even the filtered data comprise waves,

⁴The brackets $\{\}$ denote the set of the individual field vectors $\mathbf{B}^{(m)}$, $\mathbf{B}_{disc}^{(m)}$ or $\mathbf{B}_{fluc}^{(m)}$, respectively.

Table 8.2: Angles between the four MVA normals among each other (left) and between the MVA normals and the triangulation normal (right), in degrees.

1-2	1-3	1-4	2-3	2-4	3-4	T-1	T-2	T-3	T-4
5.3	3.2	1.2	8.3	6.5	2.6	87.5	83.8	88.4	88.6

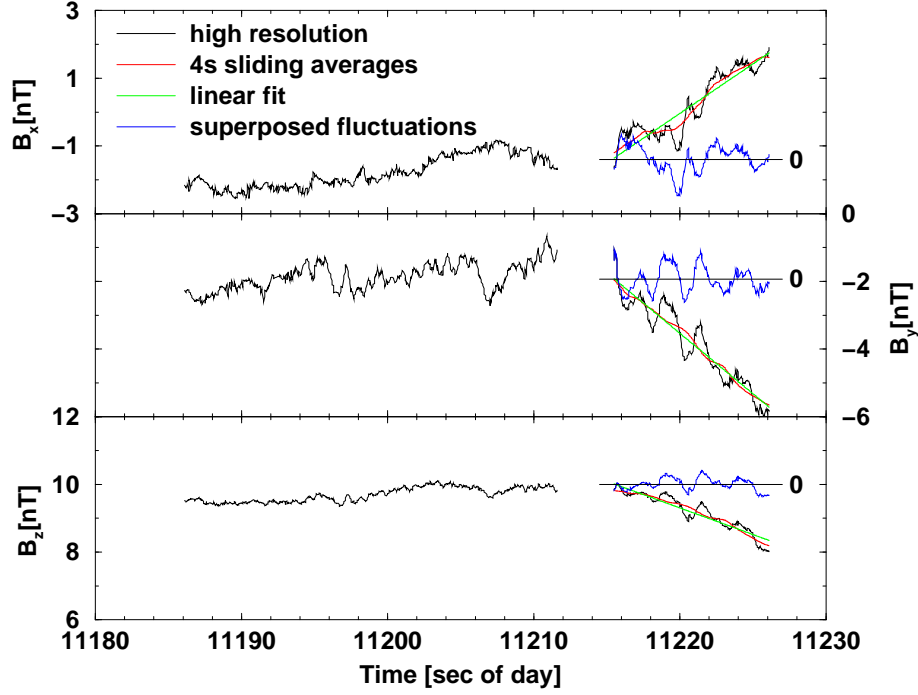


Figure 8.14: Cl 3 data of a DD observed on doy 44 at 03:07 UTC. The components are shown in GSE coordinates. The high resolution FGM data are represented by the black line. Besides the discontinuity (11216-11226) a quiet interval before the DD is shown (11186-11212). The red line represents 4 s sliding averages and the green line a linear fit to these averages. The blue line represents the difference between the DD in high resolution data and the linear fit. Note that for better visibility we moved the zero-point of that time series. The horizontal lines indicate zero in each component.

indicating relatively low frequency fluctuations. It can be seen that the actual transition between the upstream and the downstream field can be best fitted by a linear function in each component. Both the high resolution and the 4 s averages fluctuate around that fit, indicating that the linear approach is indeed justified.

The next step is to perform a minimum variance analysis separately for the total structure and for the superposed fluctuations $\mathbf{B}_{fluc}^{(m)} = \mathbf{B}^{(m)} - \mathbf{B}_{disc}^{(m)}$ (blue line in Figure 8.14). In addition we analyse a “quiet” interval (second 11186-11212), which is clearly outside the DD, to compare the fluctuations within the DD with those in the ambient magneto-plasma.

The analysis reveals that the direction of minimum variance is almost the same for the fluctuations $\{\mathbf{B}_{fluc}^{(m)}\}$ as for the total structure $\{\mathbf{B}^{(m)}\}$. The angle between the two respective directions of minimum variance is 10° , 3° , 3° and 5° for the data from Cl 1, Cl 2, Cl 3 and Cl 4, respectively. Table 8.3 summarises the MVA results for Cl 3 in detail. First, it can be seen that besides the eigenvector \mathbf{x}_3 , corresponding to the minimum eigenvalue λ_3 , \mathbf{x}_1 and \mathbf{x}_2 are also similar for the field vector sets $\{\mathbf{B}_{fluc}^{(m)}\}$ and $\{\mathbf{B}^{(m)}\}$. Second, the extracted fluctuations have almost exactly the same lowest and intermediate eigenvalues λ_3 and λ_2 as the total structure. Note that λ_3 is always slightly smaller when only the fluctuations are considered; this is also true for the other three spacecraft. The only difference is that the maximum eigenvalue λ_1 is an order of magnitude larger for the total DD.

Table 8.3: Comparison of the Cl 3 MVA results for the total structure (DD) and for the superposed fluctuations (FL). Top: Eigenvectors in GSE coordinates and angle (AN) between the respective vectors in degrees. Bottom: Corresponding eigenvalues and eigenvalue ratios.

	\mathbf{x}_1	\mathbf{x}_2	\mathbf{x}_3
DD	(-0.5785, 0.7460, 0.3293)	(0.8153, 0.5171, 0.2604)	(0.0237, 0.4195, -0.9074)
FL	(-0.6795, 0.6920, 0.2438)	(0.7320, 0.6167, 0.2896)	(0.0500, 0.3752, -0.9256)
AN	7.7	7.6	3.2

	λ_1	λ_2	λ_3	λ_1/λ_2	λ_2/λ_3
DD	2.4519	0.0990	0.0130	24.8	7.6
FL	0.2111	0.0994	0.0125	2.1	8.0

These observations confirm the idea that interplanetary discontinuities consist of an ideal 1-D structure that is superposed by non-isotropic fluctuations and illustrate the associated difficulties regarding MVA. The linear fit of the actual discontinuity implies that $\lambda_2 = \lambda_3 = 0$; i.e., with the superposed fluctuations being subtracted from the net signal the covariant matrix is degenerated. Only the direction of maximum variance \mathbf{x}_1 is defined, whereas the minimum variance direction could be anything perpendicular to \mathbf{x}_1 . The positive values of λ_2 and λ_3 are solely contained in the superimposed fluctuations. Apparently, with an eigenvalue ratio $\lambda_2/\lambda_3 = 8$ these fluctuations are highly non-isotropic. This means, in cases similar to the example where the actual discontinuity is linearly polarised, or at least close to that, the direction of minimum variance is purely determined by superposed fluctuations, provided they are non-isotropic. Therefore, extreme caution must be exercised when interpreting the direction of minimum variance to be the discontinuity normal.

The agreement between the two sets regarding λ_2 and λ_3 is slightly weaker for the other three spacecraft (not shown). This is because the directions of maximum variance for $\{\mathbf{B}_{fluc}^{(m)}\}$ and $\{\mathbf{B}^{(m)}\}$ are not so well aligned as is the case for the Cl 3 data. If they were in fact parallel to each other, the total DD and the fluctuations would have exactly the same intermediate and smallest eigenvalues. Whenever the directions of maximum variance are tilted, λ_3 of the superposed fluctuations must be smaller than for the total structure (as is observed) since the additional variance of the discontinuity causes the variance ellipsoid to change orientation.

We point out that by choosing a linear fit to model the actual transition we pushed the results presented above to a certain extent. However, the linear fit appears to be adequate, and in addition small non-linearities would not change the principle result.

Note that the four directions of minimum variance obtained for the extracted fluctuations are almost aligned among each other, indicating that the superposed fluctuations are spatially correlated over the spacecraft separation scale. This large correlation length causes the four MVA normals of the total structure to be aligned also.

The agreement among the four minimum variance directions is also excellent for the quiet interval outside the DD. They are aligned within 5° . Furthermore, these fluctuations have a similar direction of minimum variance as the extracted fluctuations within the discontinuity. They only deviate by 5° - 15° at the respective satellites. Hence, the fluctuations within and outside the DD may be interrelated.

As stated above, the only reliable information on the actual discontinuity obtained from MVA is the direction of maximum variance. Hence, the true discontinuity normal should be perpendicular to that direction. We find the angle between the triangulation normal and \mathbf{x}_1 to be 81.2° . Therefore the relative timing result is at least consistent with the maximum variance direction obtained from MVA, although the time lags are difficult to determine for the example event.

It is interesting to note that (as usual) according to triangulation a vanishing normal component is computed ($|B_n|/B_{max} = 0.003$). In contrast, the minimum variance direction is almost aligned with the magnetic field ($|B_n|/B_{max} = 0.98$). This is the typical discrepancy we observe between the two methods for many DDs with small ΔB and moderate ($\approx 30^\circ$) spreading angle (such as the DD in Figure 8.14). The analysis above reveals that, in fact, the wave-vector of the superposed fluctuations is parallel to the mean field (the angle between \mathbf{B} and \mathbf{x}_3 is only 4° for $\{\mathbf{B}_{fluc}^{(m)}\}$). Provided that λ_2/λ_3 is small for the actual discontinuity this causes the minimum variance direction of the total structure (discontinuity plus waves) to be also aligned with the mean field.

To answer questions regarding the nature and particularly the origin of these apparently important superimposed waves, an extended study, including the investigation of more DDs, would be necessary. We do not further pursue this. However, previous studies (both theoretical and observational) already suggest interesting answers. According to *Hollweg* [1982], *Horbury et al.* [2001b] conclude that the superposed wave fields are surface waves on and around the discontinuity surface. *Hollweg* [1982] discusses MHD surface waves on TDs and shows that a variety of waves could be supported, but argues that compressive surface waves would be damped, leaving a population of non-compressive modes whose wave-vectors would lie parallel to the mean field, not to the discontinuity normal (as in our example). Furthermore, *Hollweg* [1982] finds that the surface waves bear a resemblance to the usual Alfvén mode in a uniform medium.

The occurrence of correlated field and velocity changes across TDs has already been observed by *Denskat and Burlaga* [1977]. They assume that the static structures are surrounded by MHD waves. The static structures will move with the solar wind, and the waves will generally move past them or possibly even interact with them. However, the possibility that the TDs might support a wave mode of their own has first been raised by *Hollweg* [1982]. As discussed in chapter 3, the Alfvénic nature of these fluctuations led several authors (e.g., *Neugebauer et al.* [1984]) to conclude that the static structures were consistent with RDs.

To conclude, both the deviation of the minimum variance direction from the discontinuity normal due to surface waves or other field-perpendicular fluctuations and the Alfvénic appearance of these waves are likely reasons for mistakenly identifying TDs as RDs. Furthermore, the example presented in this section shows that large ratios λ_2/λ_3 are only a necessary condition for reliable MVA normal estimates, not a sufficient one.

8.3.6 New classification criteria for single-spacecraft studies

Assuming interplanetary discontinuities to be planar on the scale of the Cluster array, the only reason for the relative normal component $|B_n|/B_{max}$ having different values at the positions of the four spacecraft is the inaccuracy of MVA. Hence, $\Delta(|B_n|/B_{max})$ can be used as an indicator for the error associated with MVA normal estimates, which is important for ascertaining an appropriate criterion to discern RDs from TDs in studies using only magnetic field data from a single spacecraft.

For TDs, $B_n = 0$ is required. In order to say that a DD is most likely not a TD, one can introduce a threshold b_{nc} such that if $|B_n|/B_{max} > b_{nc}$, the corresponding DD is not tangential. Some attempts have been carried out to estimate b_{nc} so far (see section 7.2). *Smith* [1973a] established this method and quantified $b_{nc} = 0.4$. Although this was only a sophisticated guess, this value has been applied often in related studies, as we do in parts of this work. A more profound analysis has been carried out by *Lepping and Behannon* [1980], where $b_{nc} = 0.3$ is determined by numerical simulations of ideal discontinuities superposed by isotropic noise.

Using magnetic field data from the four coordinated Cluster spacecraft we are in the unique position to determine b_{nc} empirically as follows: For each DD traversal we compute the pairwise differences between the values of $|B_n|/B_{max}$ measured at the four spacecraft, provided that $\lambda_2/\lambda_3 > (\lambda_2/\lambda_3)^L$ at both spacecraft. The threshold b_{nc} for the particular $(\lambda_2/\lambda_3)^L$ is then identified as the value exceeding 95% of all measured $\Delta(|B_n|/B_{max})$ values. We therefore assume the true value of $|B_n|/B_{max}$ to be inside an interval of width b_{nc} with a probability of 95%. Since a TD has a normal component of zero, this means that for 95% of the TDs the measured value of $|B_n|/B_{max}$ is below b_{nc} . Conversely, if $|B_n|/B_{max} > b_{nc}$ is found, the corresponding DD is not a TD with 95% confidence.

As discussed in section 8.3.4, aligned MVA normal estimates do not indicate that the direction of minimum variance indeed coincides with the discontinuity normal when the spacecraft separations are as small as in 2002. For that reason we use only the sets DD_{2001} and DD_{2003} to estimate b_{nc} . Note, however, that collinear minimum variance directions do not necessarily guarantee reliable normal estimates, even if the spacecraft are ≈ 1000 km apart (see the example presented in the previous section). Therefore, even by using only DDs from 2001 and 2003 we probably still underestimate the value of b_{nc} .

Figure 8.15 shows distributions of $\Delta(|B_n|/B_{max})$ for subsets of DD_{2003} with different restrictions on λ_2/λ_3 . All pairs of spacecraft with $\lambda_2/\lambda_3 > (\lambda_2/\lambda_3)^L$ are considered. The values of b_{nc} are marked by the vertical lines. As one would expect from the results presented previously, the width of the distribution decreases with increasing strength of the requirements on λ_2/λ_3 . Table 8.4 summarises the values of b_{nc} we obtain for various lower limits $(\lambda_2/\lambda_3)^L$ and ω^L . Besides the decrease of b_{nc} with increasing $(\lambda_2/\lambda_3)^L$ and ω^L , it can be seen that we determine similar values of b_{nc} for both sets (DD_{2001} and DD_{2003}). Note that b_{nc} is even smaller in 2003 than in 2001 for some lower limits, although the spacecraft separations are larger.

We remind the reader that the most commonly used value of b_{nc} is 0.4 in connection with

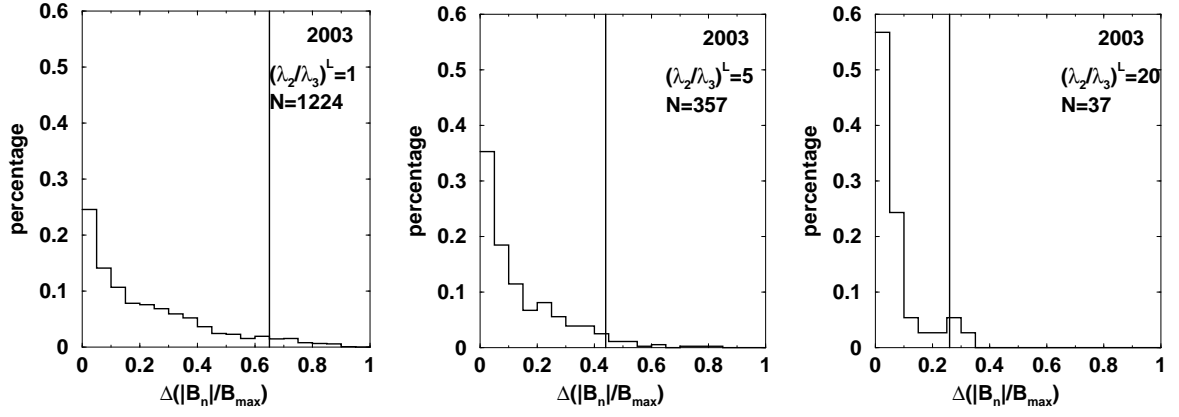


Figure 8.15: Distributions of $\Delta(|B_n|/B_{\max})$ for different subsets of DD_{2003} . Only pairs of spacecraft with $\lambda_2/\lambda_3 > (\lambda_2/\lambda_3)^L$ are considered. From left to right $(\lambda_2/\lambda_3)^L = 1$ (i.e., the total set), $(\lambda_2/\lambda_3)^L = 5$ and $(\lambda_2/\lambda_3)^L = 20$. The vertical lines indicate the value of b_{nc} . N denotes the number of pairs considered.

$(\lambda_2/\lambda_3)^L = 2$. Our results show that this is definitely overly optimistic; $b_{nc} = 0.6$ appears to be more adequate. Conversely, Table 8.4 suggests that using $b_{nc} = 0.4$, meaningful classification results may be found when only DDs with $\lambda_2/\lambda_3 \gtrsim 5$ or $\omega \gtrsim 60^\circ$ are considered. The threshold $b_{nc} = 0.3$ suggested by *Lepping and Behannon* [1980] appears reasonable when requiring $(\lambda_2/\lambda_3)^L \approx 10$ or $(\omega)^L \approx 90^\circ$. Note, however, that as discussed above the thresholds we suggest are only lower limits for b_{nc} . Hence, to assure not to mistakenly identify too many DDs as “clear RDs” by means of the normal magnetic field component using MVA, we suggest to enforce even stricter requirements on λ_2/λ_3 and ω .

The analysis presented in this section confirms that MVA is much less reliable than previously thought to determine the correct type of interplanetary discontinuities, yielding a large number of fallaciously identified “clear RDs”. Our results in earlier sections suggest that this dramatic underestimation of the error is supported by the assumption of isotropic fluctuations superposing the discontinuities (also see the discussion in section 7.2). For instance, we assume that the simulations carried out by *Lepping and Behannon* [1980] would yield a larger value of b_{nc} if non-isotropic fluctuations were considered.

Table 8.4: Values of b_{nc} for different restrictions $(\lambda_2/\lambda_3)^L$ (top) and ω^L (bottom). The number of pairs used is given in brackets.

$(\lambda_2/\lambda_3)^L$	1	2	5	10	20
2001	0.66 (774)	0.58 (572)	0.33 (241)	0.29 (80)	0.23 (31)
2003	0.65 (1224)	0.62 (924)	0.44 (357)	0.35 (125)	0.26 (37)
ω^L	60°	90°	120°		
2001	0.37 (205)	0.30 (100)	0.28 (24)		
2003	0.44 (449)	0.23 (108)	0.11 (41)		

8.4 Consistency tests for triangulation

In previous sections we have shown that the discrepancy between the classification results obtained from triangulation and MVA is caused mainly by inaccurate MVA normals and can be resolved when only DDs are considered for which MVA performs well. The purpose of this section is to affirm, by means of simple consistency tests, that the triangulation results in turn generally provide reliable normal estimates and thus reliable magnetic field normal components. A detailed error analysis for the relative timing method follows in chapter 9.

The most striking feature of the triangulation normals is that they all tend to be perpendicular to the magnetic field. Before showing the tests for consistency we demonstrate with a thought experiment that the relative timing method does not *a priori* exclude the possibility of large magnetic field normal components: Triangulation determines the normal solely on the basis of the time lags between magnetic field variations observed at the four spacecraft. Let us assume that triangulation is performed and $|B_n|/B_{max} = 0$ is found. Adding a constant field, aligned with the computed normal, would not change the orientation of the normal, since adding a constant field does not affect triangulation. This way any positive value of $|B_n|/B_{max}$ can be realised, and any orientation of \mathbf{n} relative to \mathbf{B} is possible without limitations.

In the following, two independent consistency tests for the triangulation normals are presented. The first test is based on the fact that the direction of maximum variance is generally well determined (see e.g. section 8.3.1). Hence, a necessary condition for the true discontinuity normal is that it is perpendicular to the direction of maximum variance. The second test we perform makes use of the observation that the triangulation normals tend to be perpendicular to the magnetic field. If a discontinuity is indeed tangential, or has a vanishing normal component, then the normal can also be calculated by the cross product of the upstream and the downstream magnetic field vector (see section 7.3): $\mathbf{n} = \pm(\mathbf{B}_1 \times \mathbf{B}_2)/(|\mathbf{B}_1 \times \mathbf{B}_2|)$. Consequently, the triangulation normals should coincide with the cross product normals.

Figure 8.16 shows the distributions of the angle between the triangulation normal and the direction of maximum variance (left) and the distributions of the angle between the triangulation normal and the cross product normal (right) for the sets DD_{2002} , DD_{2001} and DD_{2003} . The histograms are presented from top to bottom in increasing order of the prevailing spacecraft separations. Also shown are the distributions for the subset of DD_{2003} containing those DDs for which the relative timings can be determined best (bottom). Since we have four maximum variance directions and four cross product normals for each DD, the total number of angles contributing to each statistic is four times the number of DDs in the corresponding set. To determine \mathbf{B}_1 and \mathbf{B}_2 for the cross product, we average over 450 magnetic field vectors, i.e., ≈ 20 s on either side of the DD. This interval is assumed to be long enough to eliminate fluctuations and short enough to be not too far away from the DD.

Maximum variance direction

Apparently both tests are successful. A clear tendency for the timing-derived normals to be perpendicular to the maximum variance direction can be seen in Figure 8.16. Furthermore,

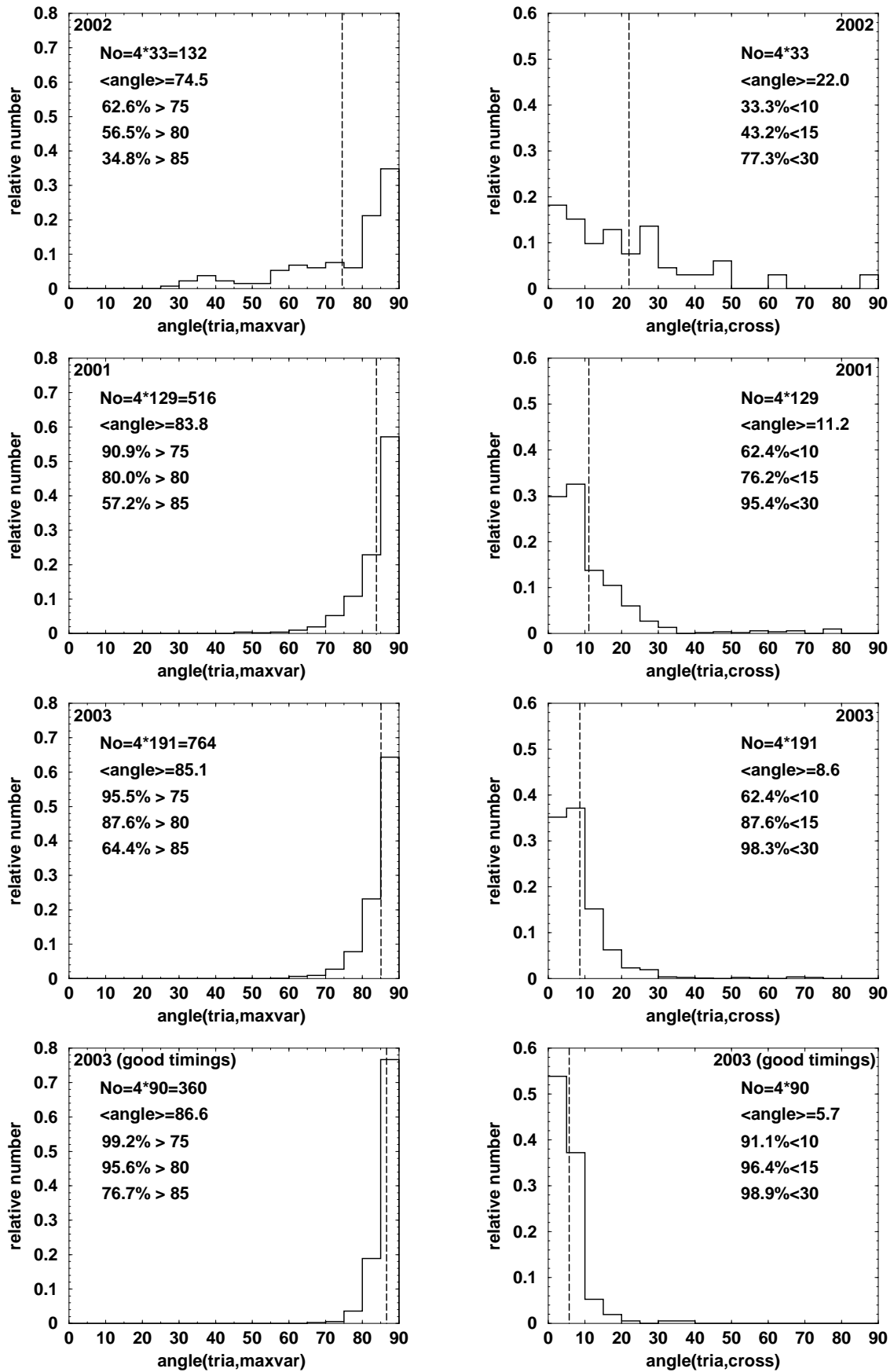


Figure 8.16: Distributions of the angle between the triangulation normal and the direction of maximum variance (left) and the angle between the triangulation normal and the cross product normal (right). From top to bottom: DD_{2002} , DD_{2001} , DD_{2003} and the subset of DD_{2003} containing those DD s for which the relative timings can be determined best. Only DD s with $P < 0.8$ are considered. The vertical lines indicate the average angle.

the ideal distribution (δ -function at 90°) is approached with increasing accuracy of the triangulation normals (from top to bottom). As pointed out earlier, the relative timing estimates are worst in 2002, corresponding to a comparatively broad distribution in Figure 8.16. However, the triangulation normal is perpendicular to the maximum variance direction within 10° for more than half of the DDs (57%) even for the set DD_{2002} . The same percentage of triangulation normals is perpendicular to the maximum variance direction within only 5° in 2001, and in 91% of all cases a deviation of less than 15° is observed. On average the triangulation normals are only 6° away from being perpendicular to the maximum variance direction for the set DD_{2001} . Excellent agreement with the expected distribution for exact methods is found for the set of DDs for which we expect triangulation to perform best, i.e., the subset DD_{2003} (good timings). Almost all of the triangulation normals of these DDs (99%) are perpendicular to the maximum variance direction within 15° , and 77% are perpendicular within 5° . On average the expected result is achieved within about 3° . Note that the maximum variance direction is not accurate, either.

As a side-note we may add that, since the direction of minimum variance is by definition perpendicular to the maximum variance direction, the triangulation normal and the MVA normal both lie in the plane perpendicular to the maximum variance direction (see also Figure 8.3). A remaining difficulty is to distinguish the minimum from the intermediate variance direction. In order to make this task tractable the ratio λ_2/λ_3 must be sufficiently large.

Cross product normal

The right hand side of Figure 8.16 shows that generally the triangulation normal coincides well with the cross product normals. As is the case for the first consistency test, the required result for exact triangulation and cross product normals under the assumption that all DDs are TDs is approached with increasing accuracy of the relative timing method, i.e., from top to bottom. The average angle between the two methods decreases from 22.0° for the set DD_{2002} and 11.2° for DD_{2001} to 8.6° for DD_{2003} . Considering only those DDs in DD_{2003} for which triangulation performs best the average angle goes down to 5.7° . In that case the angle between the triangulation normal and the cross product normals is less than 30° for almost all DDs (99%), and it is less than 10° for 91% of the DDs. For more than half of the events (54%) the two methods even agree within 5° .

To provide a reference we may recall that the average angle between the triangulation normal and the MVA normals is $\approx 30^\circ$ when the same DDs as in Figure 8.16 are considered. Considering only the few DDs for which MVA performs best, the agreement between triangulation and MVA is similar to the average angle between triangulation and cross product normals (see Figure 8.7). Also note that the average angles between triangulation and cross product normals compare quite well with the average angular errors associated with triangulation that we compute for the respective sets (see table 9.11 in chapter 9).

Accounting for the fact that also the cross product method is subject to errors, the agreement between the two methods is very good. Note that the cross product method works only for TDs, and we do not exclude the possibility that there are some DDs with small but finite $|B_n|/B_{max}$. The other source of error for the cross product method is that \mathbf{B}_1 and \mathbf{B}_2 are not

known precisely. For instance, the 20 s interval we average over on both sides of the DD may contain real trends or variations that make the determination of the upstream and the downstream state imprecise. Another problem are zero-level offsets of the fluxgate magnetometers. Whereas MVA and triangulation are not affected by this offset, the cross product method considerably depends on accurate zero-levels.

We point out that just as for the relative timing method, the cross product method is independent of the inner structure of the DDs. Hence, superimposed fluctuations within the transition do not affect the cross product normals, in contrast to MVA.

To summarise, both tests for consistency carried out above were successful. We conclude that triangulation performs very well and that with considerable confidence $|B_n|/B_{max}$ is, in fact, very small for all DDs in the representative ensemble considered here. However, since any method to determine DD normals is subject to some error it is impossible to claim that all events are TDs, i.e., $|B_n|/B_{max} = 0$. The new perception is that all DDs are, in fact, consistent with being TDs (see also chapter 9). Since in addition the majority of events have only small field magnitude changes across them, they could as well be RDs propagating almost perpendicular to the magnetic field (i.e., almost static structures). Hence, in order to determine the true type of these EDs, the use of plasma data is necessary. Jump conditions that require plasma data will be examined in section 8.8.

8.5 Surface curvature on the Cluster scale and beyond

Another subject of multi-point observations is to study the geometrical properties of boundary layers. The statistical considerations presented in this section demonstrate that attempts to assess surface curvature are strongly affected by the imprecision of MVA.

For practical reasons one generally assumes DDs to be infinitely extended planar structures. This assumption simplifies for instance the determination of the DD normal. Also studies on the interaction of DDs with planetary magnetospheres generally use this simple model. However, because the source region of DDs (on or near the Sun) is limited in size and because the solar wind is a highly dynamic medium it is more reasonable to assume that interplanetary discontinuities have a finite transverse extent and that they are curved on large scales.

The first observational indication for curved DD surfaces was given by *Burlaga and Ness* [1969]. They suggested that DDs may have significant surface curvature on spacecraft separation scales ranging from $< 10 R_E$ to $\approx 135 R_E$. To be more specific, they studied a small number (7 events) of DDs which they identified as TDs. Comparing the normals computed by the cross product technique at three spacecraft they determined that TD surface curvature is likely, but they did not estimate the typical degree of curvature. An extensive study on the degree of 2-D curvature of DD surfaces at 1 AU was carried out by *Lepping et al.* [2003]. They used data from the IMP-8 and the WIND spacecraft which were on average separated by $\approx 130 R_E$ (i.e., $\approx 10^6$ km) during the investigation. Using MVA normals, *Lepping et al.* [2003] estimated an average radius of curvature of $380 R_E$, and a most probable value of 290

R_E . Furthermore, they found that 56% of the events have concave surfaces as viewed from the Sun and 44% have convex surfaces.

For that type of analysis it is crucial to have good estimates of the local surface normals. *Lepping et al.* [2003] point out that the assumption they made that a change in a DD normal from one position to the other is due exclusively to DD surface curvature may be incorrect. They suggest the possibility that waves on the DD surface are partly or fully responsible for a change in the normal.

In view of the large radii of curvature found by *Lepping et al.* [2003], it appears as if the comparatively tiny side lengths of the Cluster tetrahedron are unsuitable to contribute to the issue of DD surface curvature. For instance, a radius of curvature of $R_c = 300 R_E$ corresponds to a change in normal from one spacecraft to the other of less than 0.1° for typical tetrahedra sizes in 2003. This is certainly far beyond the capability of MVA. For that reason, we do not present a detailed analysis on surface curvature. Instead, a simple statistical treatment is given. The main result is that the deviations between MVA normals at different spacecraft are statistically similar at the Cluster separation scales (about 1000 km) as at 10^6 km.

Figure 8.17 (top) shows the distributions of the angle between the four MVA normals for each year. Only DDs are considered for which $\lambda_2/\lambda_3 > 2$ simultaneously at all four spacecraft. The enormous discrepancies between the normals measured at the closely spaced Cluster satellites are hard to explain by means of curved DD surfaces or perhaps rigid rotations of the surface between the four traversals. As stated earlier these differences even cause a DD to be identified as an RD at one spacecraft and as a possible TD at another one in many cases. *Lepping et al.* [2003] also observe such “changes of type” between the widely separated WIND and IMP-8 spacecraft. They suggest that these “changes of type” might be real. In fact, $|B_n|/B_{max}$ may be different at the location of widely spaced spacecraft when the DD surface is curved. However, a significant real change of $|B_n|/B_{max}$ within a time gap of the order of 1 to 10 seconds (as observed with Cluster) is hard to imagine. We have concluded earlier that the discrepancy between the spacecraft is most likely due to poorly performing MVA. We further suggested that the relatively good alignment found in 2002 is caused by similar MVA errors at the four positions when the spacecraft are close together.

In the previous section we have demonstrated that in turn the cross product method yields reasonable normal estimates, because the normal magnetic field component is generally very small for all DDs investigated. The bottom part of Figure 8.17 shows the distributions of the angle between the four cross product normals. Note that no quality selection is carried out, i.e., all DDs are considered in each set. Almost perfect collinearity between the four cross product normals is observed. The angle between these normals is less than 10° for nearly all DDs in the entire ensemble and it is less than 5° for the vast majority of events. On average the angle between the four cross product normals is 1.5° , 3.7° and 4.1° in 2002, 2001 and 2003, respectively. Hence, accounting for the error associated with the cross product method, no DD surface curvature on the scale of the Cluster array is needed to explain these vanishing discrepancies. The assumption of planar structures on that length scales appears reasonable. However, we remind the reader that caution must be exercised when interpreting the cross product normals, because the type of DD must be known to be tangential before application of that method. Note that the superposed fluctuations we have identified as the source for

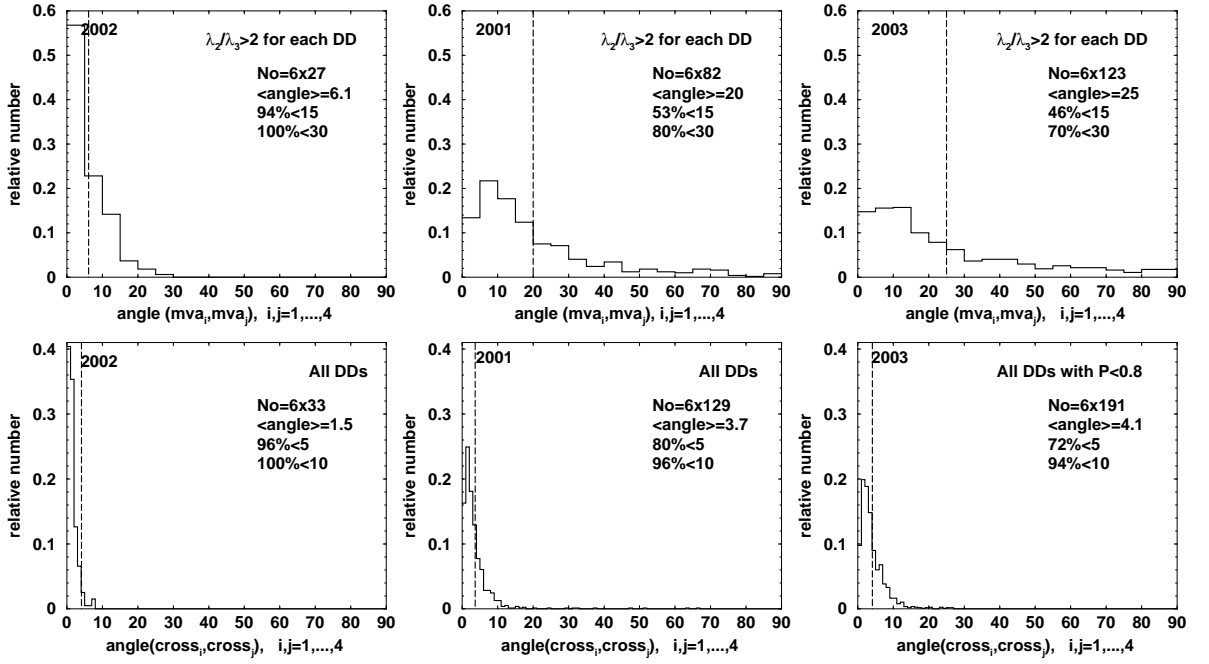


Figure 8.17: Average angle between normals determined from single-spacecraft analysis methods. Top: MVA. Only DDs with $\lambda_2/\lambda_3 > 2$ simultaneously at all four spacecraft are considered. Bottom: Cross product method. From left to right the sets DD_{2002} , DD_{2001} and DD_{2003} are shown.

the poor performance of MVA do not affect the cross product method. Most likely this is the reason for finding deviating MVA normals and well aligned cross product normals.

Figure 8.18 shows the dependence of the average angle between the four MVA normals on the average spacecraft separation prevailing in the three periods of observation (left). On the right hand side $\langle \Delta(|B_n|/B_{max}) \rangle$ is shown. As in Figure 8.13 a fourth point (0, 0) is added. The dependence is shown for different restrictions on ω . Also plotted is the average angle between the four cross product normals.

The behaviour of the individual curves is similar to that found for $\Delta(\lambda_2/\lambda_3)/(\lambda_2/\lambda_3)_{max}$ (see Figure 8.13). A strong increase of the average angle and $\langle \Delta(|B_n|/B_{max}) \rangle$ at small distances is followed by almost stagnating values when the separations become larger. This behaviour is especially apparent when the requirements on ω are rather strict. The value of $\langle \Delta(|B_n|/B_{max}) \rangle$ even decreases with distance for $\omega^L = 90^\circ$ and $\omega^L = 120^\circ$ as does the average angle between the MVA normals for $\omega^L = 90^\circ$. Note, however, that the statistics are poor for large values of ω^L . For instance, only around 15 events remain in each of the three sets for $\omega^L = 90^\circ$. Furthermore, we point out that different DDs in different solar wind conditions are compared at the three average separations.

Although the angles are much smaller when the cross product is used to estimate the normals, the general behaviour as a function of separation is the same. The average angle appears to saturate.

Certainly, using only the relatively small Cluster arrays our conclusions are restricted to a limited spatial scale. However, we can easily augment our data set by the observations made by *Lepping et al.* [2003] using widely spaced spacecraft. In order to ensure high quality MVA normal estimates, *Lepping et al.* [2003] use $\omega^L = 90^\circ$ as a lower limit. They find an average

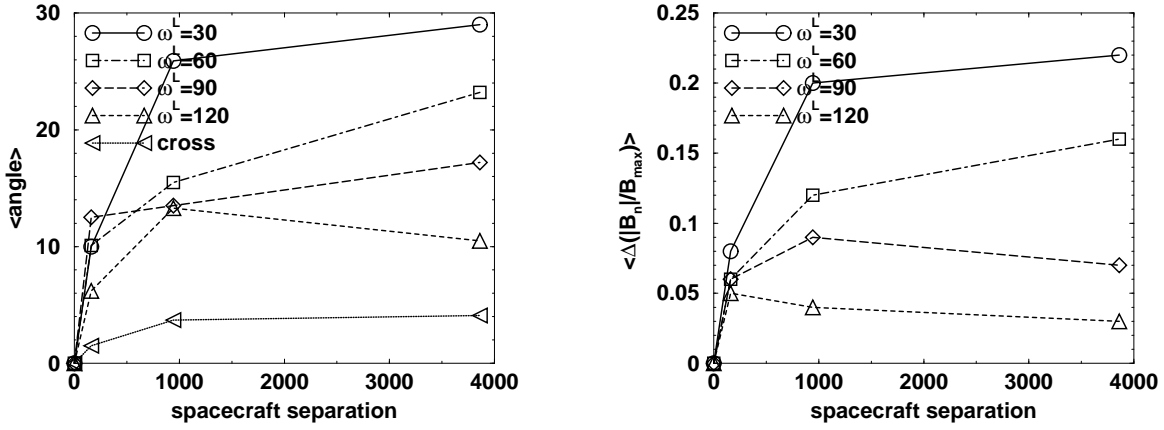


Figure 8.18: Dependence of the average angle between single-spacecraft normals (left) and derived average differences between $|B_n|/B_{max}$ (right) as a function of spacecraft separation.

angle between the MVA normals determined at IMP-8 and WIND of 12.5° at an average separation of $\approx 10^6$ km. This is the same angle we find for $\omega^L = 90^\circ$ at a separation of only 100 km, i.e., four orders of magnitude smaller. Hence, adding the point (10^6 km, 12.5°) determined by *Lepping et al.* [2003] to the left hand side of Figure 8.18, the observation of a saturating average angle can be expanded to an average spacecraft separation of 10^6 km. Moreover, we compare the distribution of the angle found by *Lepping et al.* [2003] (Figure 7 in their paper) to the distributions we obtain for $\omega^L = 90^\circ$ (not shown). In spite of the enormous difference in spacecraft separation the distributions are quite similar to each other. Note, however, that in addition to the requirement $\omega > 90^\circ$ *Lepping et al.* [2003] carefully inspect the ratio λ_2/λ_3 . They do not use DDs with $\lambda_2/\lambda_3 < 5.5$, and for most DDs in their statistics the lambda ratio is greater than 10. Therefore, their normal estimates are probably better than those used in Figure 8.18.

Let us assume for a moment that the angles between the normals measured at the four Cluster spacecraft are not caused by errors associated with MVA, but are indeed caused by real surface curvature. We then use the average angles together with the average spacecraft separations in the three periods of observation to roughly estimate “typical radii of curvature”. We find $R_c \approx 2000$ km, 6000 km, 14000 km for the three sets DD_{2002} , DD_{2001} and DD_{2003} , when the lower limit $(\lambda_2/\lambda_3)^L = 10$ is used. These hypothetical radii of curvature appear exceedingly small, particularly compared to $\langle R_c \rangle = 380 R_E$ found by *Lepping et al.* [2003]. Moreover, the “radius of curvature” dramatically increases with increasing spacecraft separation. Conversely this means that the average angle between the individual normals does not increase strong enough with distance (in this simplified statistical treatment) to yield consistent typical curvatures in the three periods of observation. Let us assume that $R_c \approx 14000$ km (i.e., the result for set DD_{2003}) is a reliable estimate for the typical curvature. Then, provided that the DDs found in 2001 and 2002 have similar characteristics, the average angle between the normals would be expected to be only 3.7° and 0.6° , respectively, and not 9.3° and 4.7° as observed. These considerations of the average properties indicate that it is difficult to distinguish whether real curvature or poor MVA estimates cause the normals to deviate.

To determine the rough estimates of R_c presented above we make a lot of simplifying assumptions. For instance, instead of the average side length of the tetrahedra one actually

must use the lateral distance between the spacecraft in the DD plane (for more details see *Lepping et al.* [2003]). Furthermore we stress that we only consider average properties and compare totally different DDs observed in different years with different solar wind conditions. The considerations above strictly speaking can only be applied when a single DD is observed simultaneously at spacecraft separated on various length scales. However, the aim in this section is not to cover all the details necessary for a conscientious analysis. Instead, we aim to demonstrate that statistically similar deviations between MVA normals are found at separation scales ranging from $\approx 10^2$ km to $\approx 10^6$ km, and this complicates the determination of large scale DD surface curvature.

To conclude, our results indicate that *Lepping et al.* [2003] may not measure large scale curvature properties. They explicitly allow for the possibility that waves on the DD surface are responsible for the two MVA normals not to be aligned. The Cluster results show that the deviations are more likely due to fallacious MVA normal estimates, although we must keep in mind that *Lepping et al.* [2003] carefully select the used DDs to ensure reasonable MVA normals. Perhaps DDs are less curved on large scales than proposed by *Lepping et al.* [2003], but have a corrugated structure on a smaller scale. We point out that we do not propose planar structures on large scales. We only claim that MVA may not be appropriate to determine a typical degree of DD surface curvature. In other words, it is difficult to distinguish between true large scale curvature, inaccurate MVA normals or ripples on otherwise planar structures. The finding of *Lepping et al.* [2003] that the ratio of concave to convex curvature as seen from the Sun is balanced may also indicate a rather random mechanism, such as inaccuracies or small scale structures, to be responsible for the specific normals to deviate.

As a final note we add that, also supported by the well-aligned cross product normals, the assumption of planar DDs on the Cluster separation scale appears to be well justified. Note that this is an important prerequisite for triangulation to be applicable.

8.6 Distribution of the discontinuity normals in space

The awareness of MVA normal estimates being highly inaccurate in many cases requires a revision of the previously established idea (based on single-spacecraft studies) of how interplanetary discontinuities are oriented in space.

The orientation of discontinuities in the solar wind (at 1 AU) has been the subject of a considerable amount of literature [*Burlaga*, 1969a; 1971b; *Burlaga et al.*, 1977; *Turner and Siscoe*, 1971; *Mariani et al.*, 1973; *Smith*, 1973b; *Barnstorf*, 1980; *Lepping and Behannon*, 1986; *Söding*, 1999]. *Burlaga* [1969a; 1971b]; *Mariani et al.* [1973] use the cross product method to estimate the normal \mathbf{n} . They consistently find that the ecliptic component of \mathbf{n} tends to be perpendicular to the average magnetic field direction given by the Parker spiral [*Parker*, 1958]. Whereas *Burlaga* [1969a; 1971b] observe a strong tendency of \mathbf{n} to be directed away from the ecliptic plane, *Mariani et al.* [1973] find no clear preference for the normal to be oriented either in or at a large angle to the ecliptic plane. Note, however, that the direction of $\mathbf{B}_1 \times \mathbf{B}_2$ is *a priori* perpendicular to the local magnetic field and does not necessarily coincide with the DD normal.

The majority of studies use MVA to estimate the normals. Often the distributions are presented separately for RDs and TDs, determined by means of the normal magnetic field component. According to our results presented in previous sections, this separation is rather meaningless. Nevertheless, it is interesting to revisit these earlier results on normal distributions in the light of our new findings.

The general result is that the MVA normals of TDs tend to be perpendicular to the spiral average magnetic field direction and close to but somewhat out of the ecliptic plane (i.e., similar to the cross product results), while the normals of RDs are more randomly scattered (see *Burlaga et al.* [1977] and references therein). *Burlaga et al.* [1977] confirm this general pattern, i.e., an isotropic distribution of the RD normals in the ecliptic and a preference of the TD normals perpendicular to the Parker spiral. However, *Burlaga et al.* [1977] also find that most DDs (both TDs and RDs) have a normal inclined to the ecliptic plane by an angle $\theta \approx 30^\circ$. *Smith* [1973b] finds that the orientation of RDs show no statistically significant preference for any direction, i.e., the normals are randomly scattered.

Barnstorf [1980]; *Lepping and Behannon* [1986]; *Söding* [1999] compare the DD normals to the local magnetic field. All three report essentially the same observation: Whereas the RD normals tend to be aligned with the local magnetic field, the ecliptic component of the TD normals tend to be perpendicular to the local field. The normals of both types of DD are found to be close to the ecliptic plane. Whereas *Lepping and Behannon* [1986] and *Söding* [1999] compute the local field only from the measurements within the DD transition zone for each of the events, *Barnstorf* [1980] in addition uses an hourly average field value centred at the DD, to exclude local effects. However, the results as described above remain unchanged.

Söding [1999] concludes that the distribution of the normals is not correlated with the macroscopic magnetic field (Parker spiral) in detail, but that it is essentially determined by the local magnetic field. The RD normals being aligned with the local magnetic field are interpreted by all three authors to confirm that RDs are associated with phase steepened Alfvén waves propagating along the magnetic field.

These earlier observations are hampered by the fact that the normal estimates are based on single-spacecraft methods. The DDs identified as RDs most likely have a large normal magnetic field component, because MVA performs poorly in these cases. We suggest that the normals of the events being identified as field parallel propagating steepened Alfvén waves are aligned with the magnetic field, because the superimposed fluctuations have a wave vector parallel to \mathbf{B} , not the discontinuity itself. Caution must be exercised also when interpreting the distributions of $\mathbf{B}_1 \times \mathbf{B}_2$. This direction coincides with the DD normal only if it is a TD.

In the following we present our own results obtained from triangulation. In order to have a reference, and for better comparison with the earlier results, we also present the distribution of our MVA normals. As in the other single-spacecraft studies, we use $(\lambda_2/\lambda_3)^L = 2$ to provide consistency.

The distributions of n_ϕ and n_θ derived from triangulation and MVA are shown in Figure 8.19. As illustrated in Figure 4.2, θ is the angle between the normal and its projection in the ecliptic plane (positive angles point northwards), and ϕ is the angle between the projection and the Earth-Sun line ($\phi = 0^\circ$ means that the ecliptic component of \mathbf{n} points towards the Sun). We

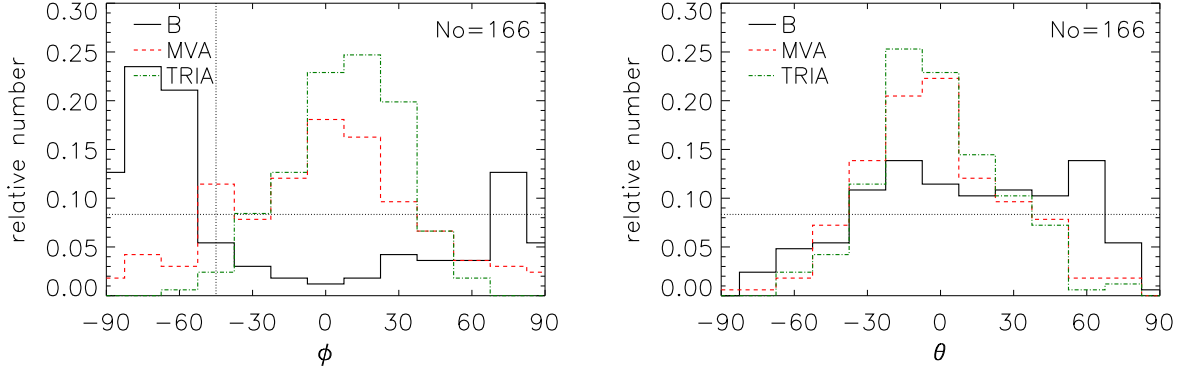


Figure 8.19: Distributions of the normals in space (left: ϕ , and right: θ). Only DD_{2003} is presented. The horizontal line corresponds to a uniform distribution. The vertical line indicates ϕ_P .

choose the orientation of all normals such that they point in the sunward half space. Different from the definition in section 4.2, the sign of ϕ is the same as the sign of the GSE y -component and thus ranges from -90° to $+90^\circ$. Note that the Parker spiral angle is $\phi_P \approx -45^\circ$ at 1 AU in this representation.

Since the distributions are very similar for all sets⁵, we only show DD_{2003} as a representative example. The distribution of n_ϕ derived from triangulation (green) has a maximum at about 15° . The corresponding distribution for the MVA normals (red) is quite similar, but it is considerably broader.

Also plotted is the distribution of the average magnetic field within the transition zone of each DD. Note that this distribution differs from the expected azimuthal field direction according to the Parker spiral ($\phi_P \approx -45^\circ$). Several reasons can be responsible for this discrepancy. First, the Parker angle is generally only visible on long term averages. On shorter time scales (days, or weeks) the field direction varies. Second, the average fields within DDs may be different from long term averages due to local effects associated with the DDs themselves. Third, the maximum of the distribution being shifted by 30° from ϕ_P towards the GSE y -axis can well be related to our selection process that accounts for foreshock activity. In section 6.4 we pointed out that certain field configuration cause Cluster to be within the foreshock region. Particularly when the major semi-axis of the Cluster orbit is along the Earth-Sun line, i.e., around March each year, an interplanetary magnetic field parallel to the GSE y -axis yields longer intervals with Cluster in the undisturbed solar wind. Towards the end of each solar wind period (around May) an IMF orientated almost perpendicular to ϕ_P is necessary to find Cluster outside the foreshock region. Hence, the distribution of $\langle \mathbf{B} \rangle$ is probably biased by our foreshock selection, and thus probably also the distribution of \mathbf{n} .

However, this possible bias does not affect the relation between the local magnetic field and the preferred orientation of DDs. Figure 8.19 (left) shows that the triangulation normals tend to be perpendicular to the local magnetic field in the ecliptic plane. This is the same result that Barnstorf [1980]; Lepping and Behannon [1986]; Söding [1999] find for their TDs. Many of our MVA normals show the same tendency. However, there is a subset of DDs for which the MVA normals are parallel to the local field. These are the events classified as RDs.

⁵In particular the coronal hole set DD_{2003CH} shows similar characteristics as the total set DD_{2003} .

In agreement with most previous studies, the normals are near the ecliptic in most cases, regardless of the method used (right hand side of Figure 8.19).

A frequently used representation of the DD orientation in space is shown in Figure 8.20 for DD_{2001} (left) and DD_{2003} (right). We generated these plots by determining the intersections of the normal vectors placed at the origin of a unit sphere and the surface of that sphere. The left hand side shows the calculated intersection point density integrated over θ as a function of ϕ , i.e., the distribution in the ecliptic plane. The right hand side shows the density integrated over ϕ as a function of θ , i.e., the distribution perpendicular to the ecliptic. The particular sections in Figure 8.20 comprise an angle of 15° and the respective radius of each sector is proportional to the density for that interval. The semicircle (dotted line) represents a uniform distribution of normal vectors.

The distributions are quite similar for the two years. One difference is that θ tends to be positive for the triangulation normals in 2001 and negative in 2003. However, in both years θ is rather small, and we assume that this difference is likely a statistical effect. The distributions of θ for the MVA normals show the same tendency as the respective distributions of the triangulation normals. However, the scatter around $\theta = 0^\circ$ is stronger when MVA is applied.⁶

Also the direction perpendicular to the Earth-Sun line in the ecliptic plane is almost devoid of normals. Only a few MVA normals point in that direction. Note that the triangulation-derived distributions of n_ϕ are almost the same in the two years. In agreement with *Barnstorf* [1980]; *Lepping and Behannon* [1986]; *Söding* [1999], the maximum is perpendicular to the ecliptic component of the local magnetic field (see Figure 8.19). However, contradicting *Burlaga* [1969a; 1971b]; *Mariani et al.* [1973]; *Barnstorf* [1980], the most probable azimuthal direction is not perpendicular to the Parker spiral, indicating that the local magnetic field is more important than large scale properties of the IMF, as suggested earlier by *Söding* [1999].

Although broader, the distribution of the MVA normals in the ecliptic plane is similar to that found using triangulation. However, there is one systematic difference between the two methods which is particularly apparent in 2003: Whereas for almost no triangulation normal $\phi = \phi_P$ is observed, this direction is populated by a considerable number of normals when MVA is used. This population consists of RDs in previous studies. Note that for the coronal hole subset DD_{2003CH} the number of these DDs is less significant (not shown), contradicting the hypothesis of phase steepened Alfvén waves. In other respects, particularly regarding triangulation, the distributions for DD_{2003CH} are very similar to the distributions for DD_{2003} .

In conclusion, statistically the distributions of \mathbf{n} obtained from MVA and triangulation are quite similar. However, for a subset of the DDs the MVA normals tend to be aligned with the magnetic field in the ecliptic plane. This subsets consists of those DDs for which MVA performs poorly.

The observations from earlier studies that the orientation of RDs is either uniformly distributed [*Smith*, 1973b] or tends to be aligned with the local magnetic field [*Barnstorf*, 1980;

⁶Note that the statistics are poor when θ is close to 90° . Using MVA we find only one DD with $\theta > 82.5^\circ$ in 2001 and one DD with $\theta < -82.5^\circ$ in 2003. But since the surface of the unit sphere above 82.5° (or below -82.5°) is small, a large density is determined in the respective sections. Aside from these two events strongly inclined normals according to the ecliptic plane are sparse.

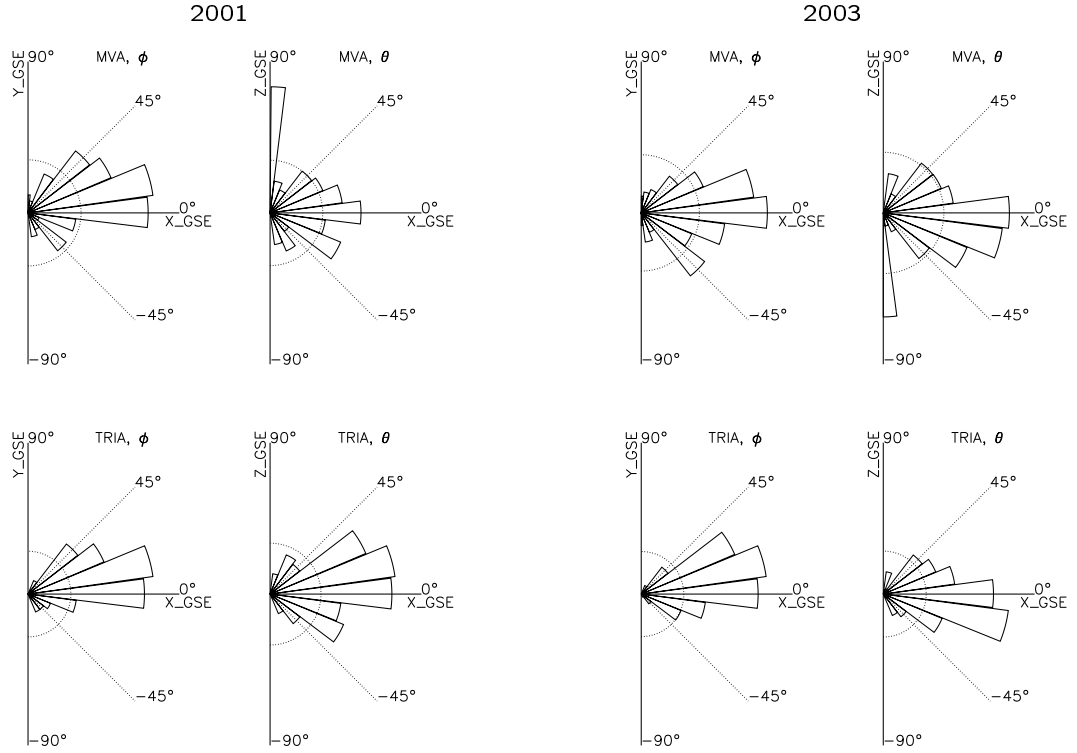


Figure 8.20: Spatial distribution of normal estimates derived from MVA (top) and triangulation (bottom) in GSE coordinates. On the left the respective distributions in the ecliptic plane are shown and on the right the distributions normal to the ecliptic plane. The results for DD_{2001} (left) and DD_{2003} (right) are shown.

[Lepping and Behannon, 1986; Söding, 1999] very well confirms our conclusions in previous sections. We suggest that the MVA normal estimates are highly inaccurate for those DDs identified as RDs by means of the normal magnetic field component. This yields a random distribution with a tendency to be aligned with the magnetic field, because the minimum variance direction of the superimposed fluctuations tends to be parallel to \mathbf{B} (see section 8.3.5). We do not believe that phase steepened Alfvén waves are the reason for the observed distribution, as is generally assumed. If only well defined MVA normals (or triangulation normals) are considered, this RD part of the distribution disappears, leading to a reduced spread of the normals in space. The remaining distribution is comparable to that found for TDs (i.e., those DDs for which MVA performs well) in previous studies.

In agreement with most previous studies we find that the normals tend to be in the ecliptic plane.

We propose that the ‘true’ DD normals are near the ecliptic plane and tend to be perpendicular to the local magnetic field in that plane. In the particular case of the DDs selected in this thesis, this results in an orientation approximately radially away from the Sun. However, there may be a bias due to the selection criteria accounting for the foreshock region. Therefore, we suggest that the most likely azimuthal direction is perpendicular to the Parker spiral in general.

8.7 Discontinuity thickness

In this section we study the width of interplanetary discontinuities. By using the four Cluster spacecraft, the thickness can be more accurately determined than in previous single-spacecraft studies. We confirm earlier observations, in particular that the thinnest DDs found have a width of a few proton gyro-radii.

Early observations already show that DDs are rather thin structures. For instance, *Siscoe et al.* [1968] find that the time needed for the DDs to pass a spacecraft is generally less than 10 s which corresponds to a width of few proton Larmor radii. Hence, the kinetics of the involved particles are important.

Predictions from theory

Assuming that the plasma is collisionless over the small scales in the boundary layer and that particles interact only with the magnetic and electric fields, *Lemaire and Burlaga* [1976] solve the Vlasov's equation and the Maxwell's equations for stationary 1-D boundary layers.⁷ They study several boundary conditions that can be realised by TDs. Besides a change in the field direction some discontinuities include a change in magnitude, others do not. *Lemaire and Burlaga* [1976] find that two kinds of boundary layers are possible. In one the current within the layer is carried by electrons, and in the other the current is carried by protons. The thickness of the electron boundary layers would be on the order of a few electron Larmor radii. However, *Lemaire and Burlaga* [1976] propose that the electron boundary layers broaden and that the electron velocity distribution function reaches rapidly an equilibrium state where it is nearly isotropic and where the electrons no longer carry the electric current. They suggest that the electron boundary layers may be destroyed in a time interval less than the transit time of the solar wind between the Sun and 1 AU.

In contrast, the proton boundary layers are found to be stable, and their thickness is always on the order of a few proton Larmor radii, as one expects because the currents are due to gyrating protons [*Lemaire and Burlaga*, 1976].

Hence, *Lemaire and Burlaga* [1976] propose that the thickness of DDs observed in the solar wind is always a few to several proton gyro-radii, and not as thin as several electron gyro-radii.

Complementary to the analytic approach, *Cargill* [1990]; *Cargill and Eastman* [1991] use 1-D hybrid simulations to compute the TD equilibrium structure. Assuming that electron physics may not be important, they choose an ion kinetic description where the ions are treated as simulation particles and the electrons as a massless fluid. The simulations are started with an infinitesimally thin TD in pressure equilibrium, which is then allowed to evolve in time. Imposing different plasma and field conditions on either side of the TDs, *Cargill* [1990]; *Cargill and Eastman* [1991] find that the structure of a TD strongly depends on the initial conditions. The final width of the TDs is between 2 and 5 thermal proton gyro-radii, consistent with the analytic solutions from *Lemaire and Burlaga* [1976].

⁷Their work is an extension of the work of *Sestero* [1964] who considers only the case in which the magnitude of the magnetic field changes while the direction remains constant.

Observations - transition time

In situ observations of the thickness of interplanetary discontinuities has been the subject of a considerable amount of literature [Siscoe *et al.*, 1968; Burlaga *et al.*, 1977; Tsurutani and Smith, 1979; Barnstorff, 1980; Lepping and Behannon, 1986; Söding, 1999]. It is generally found that the transition time τ needed for the DDs to pass the spacecraft is less than 10 s in most cases (see e.g. Siscoe *et al.* [1968]; Burlaga *et al.* [1977]; Tsurutani and Smith [1979]; Söding [1999]). For instance, Burlaga *et al.* [1977] find that 70% of the durations are less than 10 s, and 98% are less than 15 s (for TDs). The relative number of DDs with transition times longer than 10 s is found to decrease rapidly.

The thickness distributions depend strongly on details in the analysis. The criteria to select DDs are not the same in all studies, and also the choice of the start and end time of the discontinuities is rather subjective. Moreover, the available time resolution of the magnetic field data plays an important role. If for instance the sampling rate is less than, say, 1 s^{-1} , the thinnest DDs can probably not be resolved. For these reasons the average thicknesses observed vary.

By using high-resolution magnetic field measurements from Explorer 43 with a sampling rate of 14 s^{-1} Burlaga *et al.* [1977] can resolve the structure of even the thinnest DDs in their sample. On average they find a transition time of 5 s. In contrast, Söding [1999] finds $\tau = 15 \text{ s}$ using IMP-8 data (time resolution = 1.28 s) and $\tau = 20 \text{ s}$ using WIND data with a time resolution of 3 s.

Although the sampling rate of the FGM instruments on board the Cluster spacecraft is higher (22 s^{-1}) than for the magnetometer on board Explorer 43 we find an average transition time of $\approx 9 \text{ s}$. Figure 8.21 shows the distributions we obtain for the four sets DD_{2001} , DD_{2002} , DD_{2003} and DD_{2003CH} . The average and median values are indicated by the vertical lines. In agreement with previous studies, the transition time is less than 10 s for most DDs. The DDs in our sets are somewhat thicker than those found by Burlaga *et al.* [1977], and thinner than those found by Söding [1999].

The distributions are quite similar in all four sets. However, there are more DDs with very short transition times (less than 4 s) in 2001 (slow solar wind) than in the other sets where the most likely value is 5 s.

Observations - thickness

In order to calculate the actual width d of the transition, besides the transition time τ , the surface normal \mathbf{n} and the DD velocity \mathbf{U} relative to the spacecraft need to be known. The thickness is then given by

$$d = (\mathbf{U} \cdot \mathbf{n})\tau \quad (8.2)$$

When only a single spacecraft is available, \mathbf{U} needs to be determined as $\mathbf{U} = \mathbf{V}_{sw} + \mathbf{V}_A - \mathbf{V}_{s/c}$, where \mathbf{V}_{sw} is the local solar wind velocity, \mathbf{V}_A the propagation velocity of the DD relative to the ambient plasma and $\mathbf{V}_{s/c}$ the spacecraft velocity. Therefore, the determination of d is subject to a considerable amount of errors in single-spacecraft studies. First, \mathbf{n} is usually

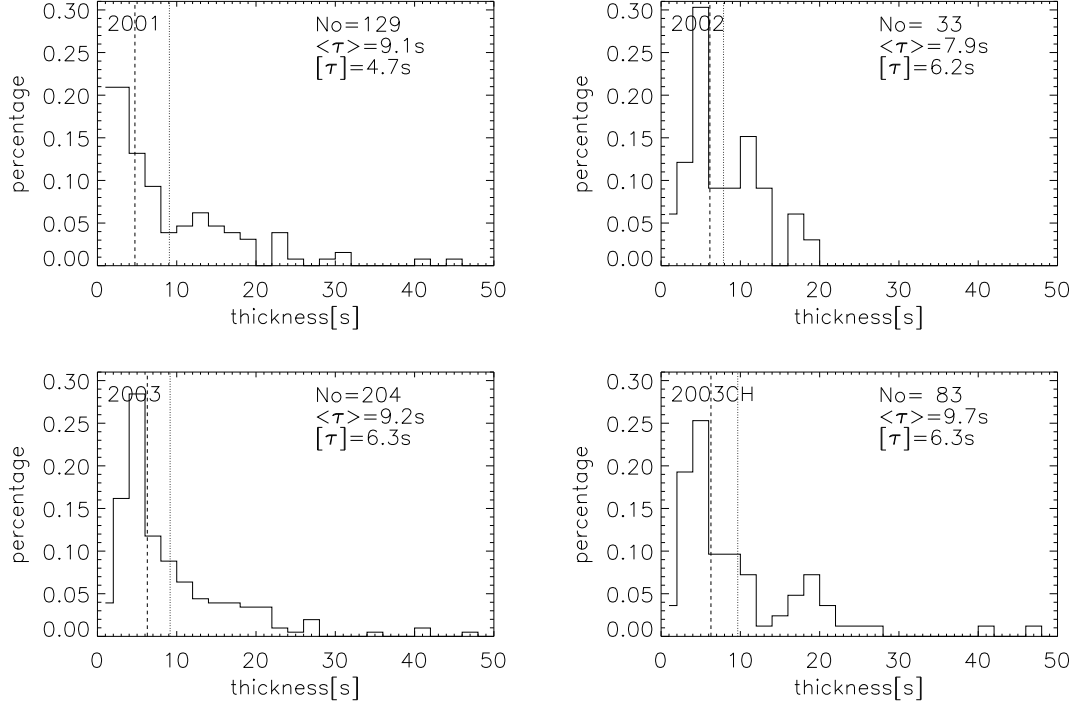


Figure 8.21: Histograms of the discontinuity thickness in s. All DDs are considered. The vertical lines indicate the average value (dotted line) and the median value (dashed line). From left to right: Top: DD_{2001} , DD_{2002} , Bottom: DD_{2003} , DD_{2003CH} .

poorly determined due to the dependence on MVA. Second, the direction and magnitude of propagation need to be computed. The direction of propagation is usually determined by testing whether \mathbf{B} and \mathbf{V}_{sw} are correlated or anti-correlated. The magnitude of the propagation velocity is set to zero for TDs and equals the Alfvén velocity V_A for RDs. To compute V_A , the plasma density is needed (see equation 3.9), introducing further uncertainties. Moreover, all or many of the RDs are likely to be EDs which, if at all, propagate extremely slow. Therefore, previous estimates of the DD thickness need to be revisited.

Using the relative timings between the four Cluster spacecraft, \mathbf{n} is determined more precisely, and we do not need to make assumptions regarding propagation, since $U = \mathbf{U} \cdot \mathbf{n}$ is calculated by triangulation. Figure 8.22 shows the distributions that we obtain for our four sets. Again, the average and median values are shown. Note that the distributions are somewhat different for the four sets. Whereas almost half of all DDs in DD_{2001} (44%) are within the first bin (1000 km) and the average thickness is 2773 km, the other sets, containing fast solar wind streams, show a tendency towards thicker DDs. For instance, the average thickness is almost 1.5 times larger in 2003 than in 2001 and only a small percentage of DDs is thinner than 1000 km (6%). The maximum of the distributions moves even more towards a larger thickness when only the coronal hole events are considered (DD_{2003CH}). These observations may suggest that the DDs are thicker in fast solar wind streams than in slow solar wind. Note, however, that due to the higher flow velocity, \mathbf{n} and U are less accurately determined for the DDs in DD_{2003CH} (see section 7.4). Because of the small separations, the thickness is determined least accurately in 2002.

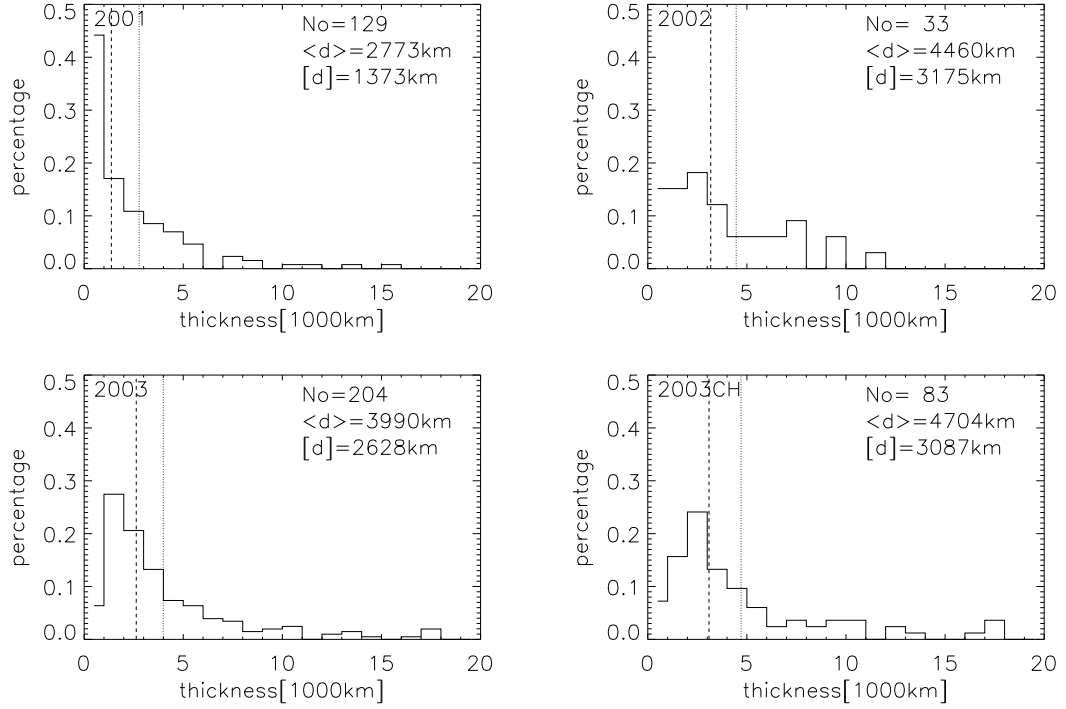


Figure 8.22: Histograms of the discontinuity thickness in km. All DDs are considered. From left to right: Top: DD_{2001} , DD_{2002} , Bottom: DD_{2003} , DD_{2003CH} .

In previous studies the distributions are often presented separately for RDs and TDs (see also section 8.1). Since the population of the RDs is most likely a consequence of erroneous MVA normals, we only compare our results to the TD distributions found previously. Average values found for the TD thickness at 1 AU are: 1300 km (14 s^{-1}) [Burlaga *et al.*, 1977], 2450 km (4 s^{-1}) [Barnstorf, 1980], 2640 km (25 s^{-1}) [Lepping and Behannon, 1986] and 4001 km (0.78 s^{-1}) [Söding, 1999]. The numbers in brackets denote the sampling rate used. Apparently, Söding [1999] finds larger thicknesses than the other studies. This is probably related to the lower sampling rate used in that work. Whereas the average thickness we obtain for the set DD_{2001} compares well to those found by Barnstorf [1980] and Lepping and Behannon [1986], the average thickness found in 2003 is almost the same Söding [1999] finds using the IMP-8 data. This is surprising, because due to the high time resolution of the Cluster FGM one would expect the widths to compare well with those found by the other authors listed above. Thus, perhaps the deficiencies of single-spacecraft analysis cause an underestimation of the DD thickness which is “compensated” by the low time resolution in the case of Söding [1999].

In the light of the theoretical predictions presented at the beginning of this section the discontinuities thickness is often given in units of the thermal proton gyro-radius r_L . Burlaga *et al.* [1977] find that the thickness ranges from $1.5 r_L$ to $82 r_L$ and that on average $d = 12 r_L$. Hence, although the thickness distribution overlaps the thickness of the theoretical current sheets [Lemaire and Burlaga, 1976; Cargill, 1990; Cargill and Eastman, 1991], the average observed thickness is higher than that found theoretically.

It is also interesting to note that Barnstorf [1980]; Söding [1999] find that, contrary to the

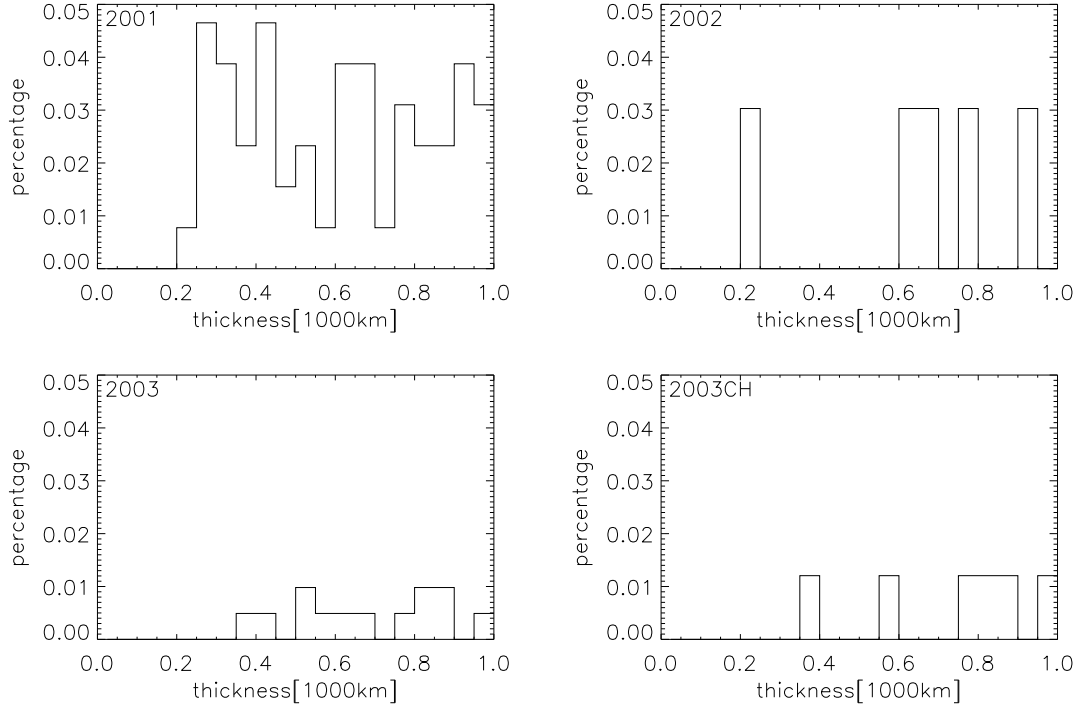


Figure 8.23: Same as Figure 8.22, but only in the range $d = 0 - 1000$ km. The bin width is 50 km.

theoretical prediction, the average thickness in terms of the thermal proton gyro-radius decreases as a function of solar distance. However, *Lepping and Behannon* [1986] find that d in units of r_L is constant between 0.46 and 1 AU.

In order to confirm the prediction that electron boundary layers are absent at 1 AU, one is interested in very thin DDs. The thinnest DD found by *Burlaga et al.* [1977] has a width of 1.5 thermal proton gyro-radii, confirming the theoretical result. However, because of the large uncertainties associated with this single-spacecraft study, we revisit this issue making use of the four Cluster spacecraft.

Figure 8.23 shows only the first bin (i.e., 0 – 1000 km) of the respective distributions presented in Figure 8.22. The bin width is reduced to 50 km. Apparently, no DDs thinner than 200 km are observed. Particularly in 2001 the distribution drops rapidly at this value. We point out that even these thinnest DDs can be fully resolved by the high-resolution FGM data. Table 8.5 shows the transition time τ , the number of data points within the transition, the thickness d in km, the local thermal proton gyro-radius r_L and the thickness in units of r_L for the thinnest DD observed in each of the three periods of observation. The number of data points indicates that practically we could resolve thinner DDs, even on the order of a few electron gyro-radii (the expected width of electron boundary layers [*Lemaire and Burlaga*, 1976]). However, the thinnest DDs we observe are on the order of 2 – 4 r_L , i.e., even thicker than the thinnest boundary found by *Burlaga et al.* [1977]. Hence, our results confirm previous predictions and observations.

In summary, we find that the distribution of the DD thickness obtained from triangulation compares quite well to those found in earlier single-spacecraft studies, although the DDs

Table 8.5: *Properties of the thinnest DD found in each period of observation.*

Year	τ [s]	data points	d [km]	r_L [km]	$d [r_L]$
2001	0.76	18	212.7	67.8	3.1
2002	0.71	17	228.0	63.4	3.6
2003	0.53	14	360.4	165.2	2.2

in 2003, where fast solar wind streams are prevailing, appear to be somewhat thicker than previously assumed. For the theory of discontinuities it is of interest that no DDs as thin as a few thermal electron gyro-radii are found.

8.8 Using plasma data to identify possible RDS

In this section we come back to the problem of classifying DDs into RDs and TDs. In sections 8.2-8.4 we have shown that $|B_n|/B_{max}$ is small for all DDs in our ensemble, and in chapter 9 we will demonstrate that indeed all events are consistent with being TDs. Since the only certain indication for unambiguously identifying an RD is a magnetic field normal component larger than its uncertainty would allow for a TD, our sample contains no clear RDs. However, because most DDs also have a small change in magnitude $||B|/B_{max}$ across the boundary (see Figure 8.2) and we cannot prove $B_n = 0$ exactly, it is still possible that the majority (or even all) of the EDs are RDs with tiny magnetic field normal components. Since about 90% of all events are identified as EDs, these somewhat special RDs could theoretically constitute the major fraction of interplanetary discontinuities.

Besides $B_n > 0$ we have derived further necessary conditions for RDs (section 3.1). Using these criteria, which requires plasma data, we seek to identify possible candidates that are consistent with RDs (sections 8.8.4-8.8.7). In agreement with previous studies (e.g. *Neugebauer et al.* [1984]), one of the conditions (the polarisation relation) is found not to be satisfied by the majority of DDs. Being aware that all of our DDs are consistent with TDs, this result is discussed from a new perspective.

In addition to the criteria that can be applied using a single spacecraft, we are able to test whether or not the DDs propagate relative to the ambient plasma (section 8.8.6). No indication for RDs are found this way.

In contrast to previous studies, the DDs that satisfy the necessary RD conditions are not found predominantly in fast solar wind streams from coronal holes (section 8.8.7). This result is of considerable interest for identifying possible generation mechanisms for RDs.

In the following two sections we specify the conditions to be tested and introduce the data set. Before performing the tests we demonstrate that the anisotropies measured by the CIS instrument aboard Cluster are unrealistically high, which complicates the analysis (section 8.8.3).

8.8.1 Necessary conditions for RDs to be tested

We use the moments (density ρ , velocity \mathbf{V} and temperature T) calculated from the proton distribution function measured by the CIS HIA instrument aboard Cl 1. The moments of the 3-D distributions have a time resolution of 4 s, i.e., the spin period of the satellite (see section 4.3.2). Note that the protons are treated as a single fluid with the moments calculated by integration over the entire proton distribution. Often, however, the solar wind has two proton beams: a slower, denser primary beam plus a faster, less dense secondary beam with less energy flux [Feldman *et al.*, 1973; Marsch *et al.*, 1981]. Also note that we do not account for contributions from alpha particles and electrons. A detailed study, also incorporating a secondary proton beam and alpha particles, is done by Neugebauer *et al.* [1984]. They find that the inclusion of alpha particles does not change the basic results.

The plasma moments are difficult to determine, and they are therefore subject to considerable uncertainty. This is particularly true for the computation of the thermal anisotropy. As stated in section 3.1 the degree of anisotropy is often given in terms of the firehose factor A :

$$A = 1 - \frac{(p_{\parallel} - p_{\perp})\mu_0}{B^2}$$

The subscripts \parallel and \perp refer to directions relative to the local magnetic field. Burlaga *et al.* [1977] find that $\sqrt{A} = 0.9 \pm 0.1$ in the solar wind. Therefore an isotropic plasma is often assumed in related studies. Being aware of the experimental problems associated with the determination of T_{\parallel} and T_{\perp} , we also assume $A = 1$ in a first approach. The related results can be used as a reference. In a second step we utilise the measured quantities T_{\parallel} and T_{\perp} to determine A .

The necessary conditions for RDs to be tested in the following are summarised in Table 8.6 (see also section 3.1). Following Neugebauer *et al.* [1984], the polarisation relation (condition 2) is tested in two steps. In a first step the collinearity of $[\mathbf{V}]$ and $[\mathbf{B}/\rho]$ is tested (condition 2.1), and in a second step the magnitudes of $[\mathbf{V}]$ and $[\mathbf{B}/\rho]$ are compared (condition 2.2). For the latter we define the ratios R_{VB}^{iso} and R_{VB} which are expected to equal unity for RDs.

For TDs the change in velocity and the change of the magnetic field vector are not necessarily related. Also, the density (or ρA) can change arbitrarily across the boundary. Note, however, that TDs can satisfy conditions 1 and 2, although this is not required according to MHD theory. Therefore, it is important to point out that conditions 1 and 2 are necessary but not sufficient conditions for RDs.

In order to test conditions 1 and 2, only one spacecraft is needed, and our results essentially confirm previous findings (e.g. Neugebauer *et al.* [1984]).

Condition 3 states that RDs propagate with the Alfvén velocity. Since TDs are convected structures that do not propagate, the right side of condition 3 must be zero for TDs. Note that testing this condition is tractable, because the DD velocity U relative to the spacecraft array is accessible due to our relative timing analysis. By using only data from a single spacecraft U remains unknown, unless one makes assumptions regarding propagation. However, the Alfvén velocity V_A is typically 40 km/s in the solar wind near 1 AU. In addition, \mathbf{n} is usually almost perpendicular to \mathbf{B} . Hence, one expects the right side of condition 3 to be very small

Table 8.6: Necessary conditions for RDs to be tested.

Condition	Isotropic ($A = 1$)	Anisotropic (A from data)
1.	$[\rho] = 0$	$[\rho A] = 0$
2.	$[\mathbf{V}] = \pm \left(\frac{1}{\mu_0 \rho} \right)^{\frac{1}{2}} [\mathbf{B}]$	$[\mathbf{V}] = \pm \left(\frac{\rho A}{\mu_0} \right)^{\frac{1}{2}} [\mathbf{B}/\rho]$
2.1	$[\mathbf{V}] \parallel [\mathbf{B}]$	$[\mathbf{V}] \parallel [\mathbf{B}/\rho]$
2.2	$R_{VB}^{iso} = (\mu_0 \rho)^{\frac{1}{2}} \frac{ [\mathbf{V}] }{ [\mathbf{B}] } = 1$	$R_{VB} = \left(\frac{\mu_0}{\rho A} \right)^{\frac{1}{2}} \frac{ [\mathbf{V}] }{ [\mathbf{B}/\rho] } = 1$
3.	$(\mathbf{V} - \mathbf{U}) \cdot \mathbf{n} = \left(\frac{1}{\mu_0 \rho} \right)^{\frac{1}{2}} \mathbf{B} \cdot \mathbf{n}$	$(\mathbf{V} - \mathbf{U}) \cdot \mathbf{n} = \left(\frac{A}{\mu_0 \rho} \right)^{\frac{1}{2}} \mathbf{B} \cdot \mathbf{n}$

for possible RDs, making it difficult to distinguish between propagating and non-propagating structures.

In section 8.2 we have noted that a small sub-group of the EDs is found for which the normal magnetic field components are larger than for the DDs in the TD category which usually have $|B_n|/B_{max} \lesssim 0.1$ in 2003 and $|B_n|/B_{max} \lesssim 0.15$ in 2001 (see the scatter diagram 8.2 for DD_{2001} and DD_{2003}). In the following sections we also seek to find out whether the DDs in this sub-group are more likely to satisfy the RD conditions than the others. Therefore, we split the group of EDs into those with $|B_n|/B_{max} \leq 0.1$ (0.15) and those with $|B_n|/B_{max} > 0.1$ (0.15) in 2003 and (2001). The first sub-group will be referred to as ED^* and the latter as RD^* . Note, however, that the number of RD^* s is small. Of those DDs in DD_{2001} for which plasma data are available only 11 fall into the RD^* category (12%), and 28 DDs (15%) would be classified as RD^* in DD_{2003} . Therefore, the statistics are probably too poor to support any fundamental conclusions. Moreover, $|B_n|/B_{max}$ is still small for the RD^* s. According to our error analysis they are consistent with TDs. Therefore, it is important not to confuse this new category with the traditional RD category which was believed to contain clear RDs. For these reasons the subdivision of the EDs into ED^* s and RD^* s is certainly of minor importance and can be regarded as a desperate attempt to identify at least some DDs that are rotational according to MHD theory.

8.8.2 Data coverage and selection of intervals

Since the data coverage of the CIS instrument is generally worse than that of the FGM instrument, plasma data are not available for all DDs in our ensemble. For the following numbers of events sufficient plasma information is available:

DD_{2001} :	91	out of	129 DDs
DD_{2002} :	32	out of	33 DDs
DD_{2003} :	191	out of	204 DDs
DD_{2003CH} :	83	out of	83 DDs

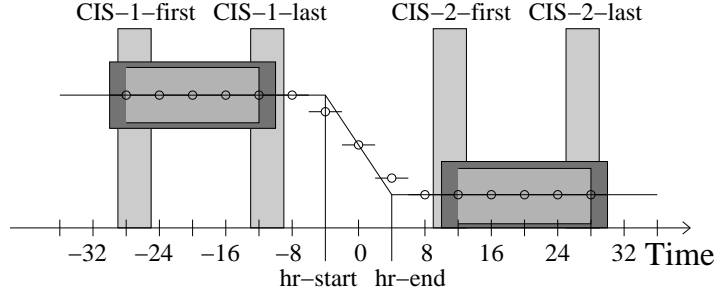


Figure 8.24: Intervals to average plasma and field data over.

In order to test the conditions 1-3 listed in Table 8.6, it is necessary to know the plasma and field properties on both sides of the DDs. Since we are interested in the state of the magnetoplasma in the immediate vicinity of the events, the interval to average over should not be too long and not too far away from the DD. On the other hand, however, caution must be exercised not to include information from within the transition.

We select the intervals to average over as shown in Figure 8.24. The solid line represents a DD in high-resolution FGM data centred at time zero. The start and end time, *hr-start* and *hr-end*, of the DD are known from our prior analysis and coincide with the borders of the interval used for MVA. Plasma data from the CIS instrument (4 s resolution) are marked by the circles. We plotted them as if they would coincide with the FGM data. This is, of course, only for the purpose to simplify the illustration. The first CIS record of the averaging interval on side 2 (right) of the DD is taken from the interval [*hr-end*+5s, *hr-end*+9s], marked by the bar named CIS-2-first. This choice definitively ensures that the averaged data do not contain any information from within the transition. The moments on side 2 are then averaged over this and the following 4 data points. Hence, the average is taken over 5 records (shaded light grey in Figure 8.24) corresponding to a time interval of length 20 s. Since we need to interrelate plasma and field data, the high-resolution magnetic field data must be averaged over the same interval. Because the time tag of each CIS record is in the centre of the 4 s measuring period, the interval over which we average the FGM data begins 2 s before the time assigned to the first CIS record and ends 2 s after the time assigned to the last of the five CIS records (dark grey in Figure 8.24). The corresponding intervals on side 1 (left) of the DD are determined accordingly.

8.8.3 Thermal anisotropy

Before performing the tests for consistency with RDs, it is instructive to get an idea of the degree of thermal anisotropy measured by the CIS instrument. Figure 8.25 shows distributions of T_{\parallel}/T_{\perp} measured just before and after the DDs (as described in the previous section) for all four sets.

The reliability of these measurements may be tested by comparing T_{\parallel}/T_{\perp} obtained from CIS measurements to earlier long-time measurements. Using Vela 3 data, *Hundhausen et al.* [1970] find generally smaller anisotropies. In particular, no such extreme values of T_{\parallel}/T_{\perp} are

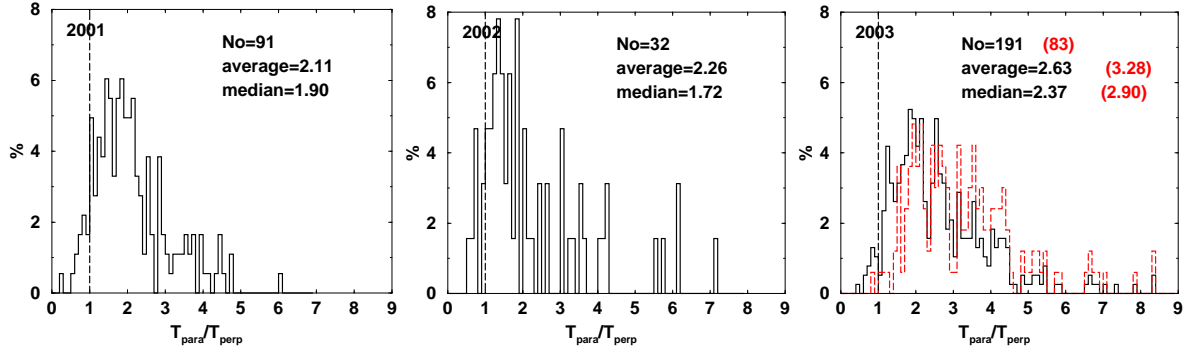


Figure 8.25: Distributions of T_{\parallel}/T_{\perp} measured in the vicinity of the DDs. From left to right: DD_{2001} , DD_{2002} , DD_{2003} . The histogram and the numbers plotted in red correspond to the set DD_{2003CH} .

found as in the CIS data. *Hundhausen et al.* [1970] find that on average $T_{\parallel}/T_{\perp} = 1.9 \pm 0.9$, a median value of 1.6 and a range of values from 1.1 to 3.4. Using Helios data between 0.9 and 1 AU, *Schwenn* [1990] finds $T_{\parallel}/T_{\perp} = 1.5$ on average. A comparison with the average and median values presented in Figure 8.25 shows that the anisotropies measured by CIS are comparatively high. The best agreement with values from the literature is obtained in 2001.

We observe a tendency towards higher anisotropies with increasing solar wind speed. The values of T_{\parallel}/T_{\perp} are particularly high in 2003 where many high speed solar wind streams are observed. Comparing anisotropies from DD_{2003} with those of DD_{2003CH} shows that indeed the highest anisotropies are found in the fast streams. Here the average value is more than twice as large as the average value found by *Schwenn* [1990]. Note that the tendency of increasing anisotropy with increasing solar wind speed also contradicts the long-time measurements. Using data taken only for solar wind speeds $V < 400$ km/s, *Schwenn* [1990] finds $\langle T_{\parallel}/T_{\perp} \rangle = 1.7$, and $\langle T_{\parallel}/T_{\perp} \rangle = 1.2$ is found for $V > 600$ km/s. *Hundhausen et al.* [1970] also find a decrease of anisotropy with increasing solar wind speed. In the light of these observations, the extreme anisotropies found in the fast streams in 2003 appear even more unrealistic.

It is difficult to say whether the high anisotropies observed by the CIS instrument (particularly in 2003) are real or whether they are subject to large errors. We tend to believe that the latter is true. Note, however, that comparison with the literature might be hampered by the fact that the data shown in Figure 8.25 are all measured in the vicinity of DDs, and it is unclear whether the discontinuities affect these average values. A better approach to test the quality of the CIS measurements would certainly be to use all available solar wind data and directly compare them to other satellites, as for instance ACE.

Note that the high anisotropies measured by the CIS instruments lead to many DDs that suffer from the firehose instability (see section 3.1). According to equation 3.16, we use $A > 0$ as a further criterion to identify RDs when T_{\parallel} and T_{\perp} are used to determine A . Consequently, a large number of events are removed from the list of possible RDs because of high anisotropies.

8.8.4 Continuity of ρA

In the limit that contributions from alpha particles and electrons and the proton anisotropy can be neglected, condition 1 can also be written as $\{n\} = 1$, where n is the proton number density and $\{n\} = \text{larger of } n_1/n_2, n_2/n_1$.

Figure 8.26 shows the distributions of $\{n\}$. Apparently, n is continuous for almost all DDs. The one DD with $\{n\} = 1.6$ in 2001 coincides with the only ND event that we find. This is probably a weak shock. The coronal hole events do not differ from the other events.

Accounting for the large error associated with the determination of n , the values found for $\{n\}$ can be regarded as being consistent with $\{n\} = 1$. Note that the conservation of n is a well established result (see e.g. *Neugebauer et al.* [1984]).

Following *Neugebauer et al.* [1984] we also present the distributions of $\{n\}$ for the different types of DDs found in 2001 and 2003 separately (middle and bottom part, respectively, of Figure 8.26). Since we do not find any clear RDs, we split the group of EDs into RD^* s and ED^* s as discussed above. No clear difference can be observed. However, it appears as if the conservation of n is indeed better satisfied for the RD^* s than for the TDs and that the distribution of the ED^* s resemble more that of the RD^* s than that of the TDs in 2003. *Neugebauer et al.* [1984] find the same result. However, accounting for the poor statistics the difference is negligible. Moreover, the conservation of n appears to be better satisfied for the ED^* s than for the RD^* s in 2001.

We conclude that, in accordance with previous studies, condition 1 for the isotropic case is satisfied for all DDs. Note that, although not required by MHD theory, n is also conserved across TDs.

Figure 8.27 shows the distributions of $\{\rho A\}$. In contrast to the isotropic approximation, considerable jumps in ρA are found across the DDs. This is particularly apparent across the coronal hole events where the abundance of RDs was assumed to be large according to previous studies. No difference is found between the three groups TDs, RD^* s and ED^* s (not shown). Since n is continuous, the large jumps of ρA correspond to jumps in the firehose factor.

There are two possibilities to interpret the discontinuity of ρA observed for the majority of events: (1) Most DDs do not satisfy condition 1 and, therefore, they are no RDs, and (2) the measured anisotropies, which are particularly high in the vicinity of the coronal hole events, are unrealistic. We tend to believe that (2) is the more likely interpretation. Note that, for instance, *Neugebauer et al.* [1984] find distributions of ρA that are similar to the results for the isotropic distribution, i.e., A is found to be rather continuous. Also note that according to the CIS data, many DDs suffer from the firehose instability. For 29, 5 and 72 DDs $A < 0$ on at least one side of the DD in 2001, 2002 and 2003, respectively, and $A < 0$ for more than half of the coronal holes events.

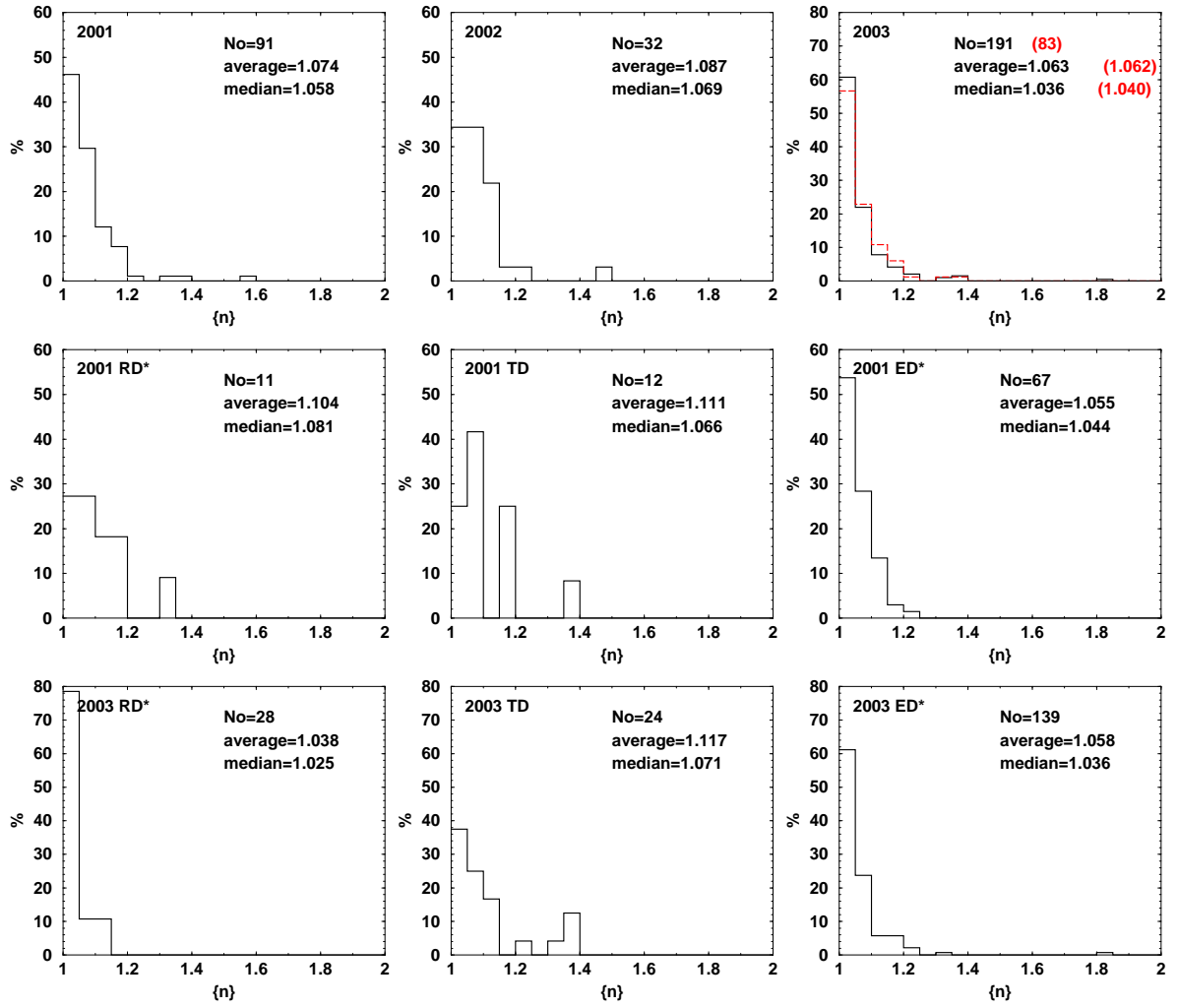


Figure 8.26: Distributions of $\{n\}$. Top: All DDs are considered. From left to right: DD₂₀₀₁, DD₂₀₀₂, DD₂₀₀₃. The distribution for DD_{2003CH} is plotted in red. Middle: DD₂₀₀₁ separately for RD*s, ED*s and TDs. Bottom: Same as middle panel for DD₂₀₀₃.

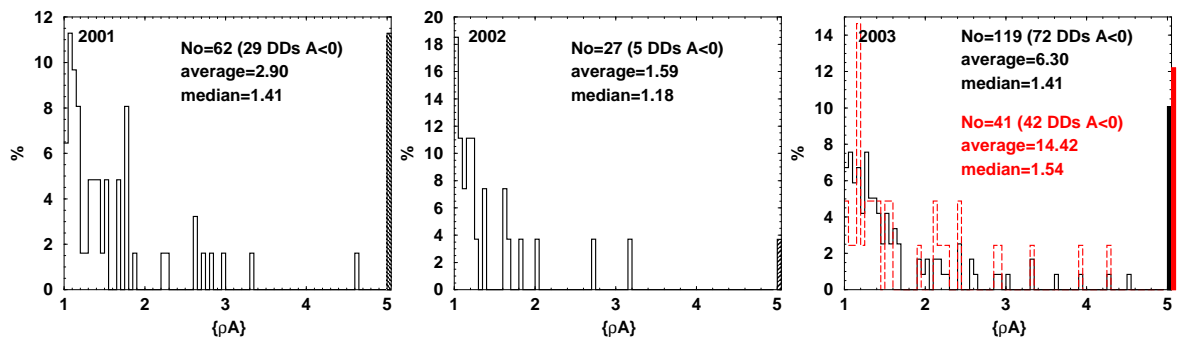


Figure 8.27: Same as upper part of Figure 8.26 for $\{pA\}$. The bars on the right side indicate the percentage of events for which $\{pA\} > 5$.

8.8.5 Polarisation relation

In this section the polarisation relation is tested. Two well established results from previous studies are confirmed: First, $[\mathbf{V}]$ and $[\mathbf{B}/\rho]$ are aligned for almost all DDs (although not required for TDs). Second, R_{VB} and R_{VB}^{iso} are generally less than unity, i.e., this necessary condition for RDs is mostly not satisfied.

Condition 2.1

We begin with condition 2.1, i.e., the collinearity of $[\mathbf{V}]$ and $[\mathbf{B}/\rho]$ required for RDs. Note that for RDs propagating outward from the Sun, the minus (plus) sign applies in condition 2 when the interplanetary magnetic field points away from (toward) the Sun. We define Θ_{VB} to be the angle between $[\mathbf{V}]$ and $[\mathbf{B}/\rho]$, where the sign of $[\mathbf{B}/\rho]$ is reversed when the IMF points toward the Sun. In this way $\Theta_{VB} \approx 180^\circ$ for RDs propagating outward from the Sun. Note, however, that the appropriate choice of sign is not always clear, especially when a DD changes the sense of the field from inward to outward, or vice versa. Also note that the accuracy of Θ_{VB} decreases with decreasing $||[\mathbf{V}]||$.

Figure 8.28 presents $||[\mathbf{V}]||$ versus Θ_{VB} in a polar scatter diagram for all four sets separately, and the corresponding percentage distributions of Θ_{VB} are shown in Figure 8.29. It can be seen that in most cases, apart from those where $||[\mathbf{V}]||$ is very small, $[\mathbf{V}]$ and $[\mathbf{B}/\rho]$ tend to be either parallel or anti-parallel. The directions of $[\mathbf{V}]$ and $[\mathbf{B}/\rho]$ are (anti-)parallel within 30° for more than 90% of the events in 2002 and 2003, whereas deviations of Θ_{VB} from 0° or 180° are more common in 2001. From Figure 8.28 it can be seen that generally $||[\mathbf{V}]||$ is larger in 2002 and 2003 than in 2001 which might explain this difference. Apart from one TD in 2001 ($||[\mathbf{V}]|| \approx 90$ km/s, $\Theta_{VB} \approx 140^\circ$) there are no DDs with large $||[\mathbf{V}]||$ at angles which are not close to 0° or 180° . Note that besides this TD, no difference between TDs and EDs (ED^*s plus RD^*s) is found. This is an interesting result, since according to MHD theory the angle Θ_{VB} is arbitrary across TDs. Also note that the only ND event in our sample (blue) deviates from the other events.

There is a strong anisotropy, with many more DDs near 180° than near 0° which is more accentuated in 2002 and 2003 than in 2001 (slow solar wind). Considering only the coronal hole events a slightly stronger anisotropy is observed than for the total set DD_{2003} , which might be indicative for the solar wind type to be important in this regard.

The dependence on solar wind speed (particularly Θ_{VB} being closer to 0° or 180° in fast streams than in slow solar wind) has been found earlier [Solodyna *et al.*, 1977]. However, Neugebauer *et al.* [1984] suggests that this result is an artefact arising from the dependence of the magnitude of $[\mathbf{V}]$ on solar wind speed combined with the inaccuracy of determining Θ_{VB} when $||[\mathbf{V}]||$ is small. Burlaga [1969b] finds that DDs with large $||[\mathbf{V}]||$ usually occur when V is high, and Turner [1973] states that the relative number of times that $||[\mathbf{V}]||$ exceeds 25 km/s is greater in high-speed streams. Neugebauer *et al.* [1984] also observe a strong correlation between $||[\mathbf{V}]||$ and V .

According to Figures 8.28 and 8.29, condition 2.1 is satisfied by nearly all events, and most

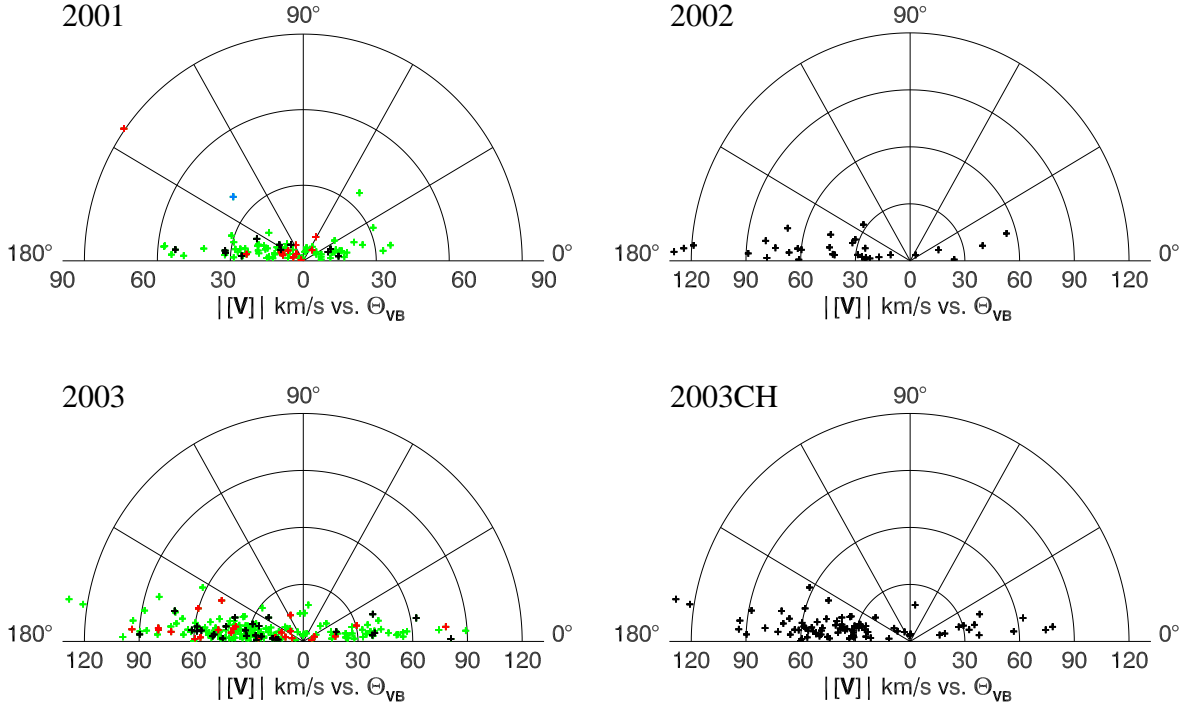


Figure 8.28: Polar scatter diagram of the change in velocity $||\mathbf{V}||$ versus the angle Θ_{VB} between $[\mathbf{V}]$ and $[\mathbf{B}/\rho]$. For the sets DD_{2001} (upper left) and DD_{2003} (lower left) the types of DDs are colour coded (red: TD, black: RD^* , green: ED^* and blue: ND).

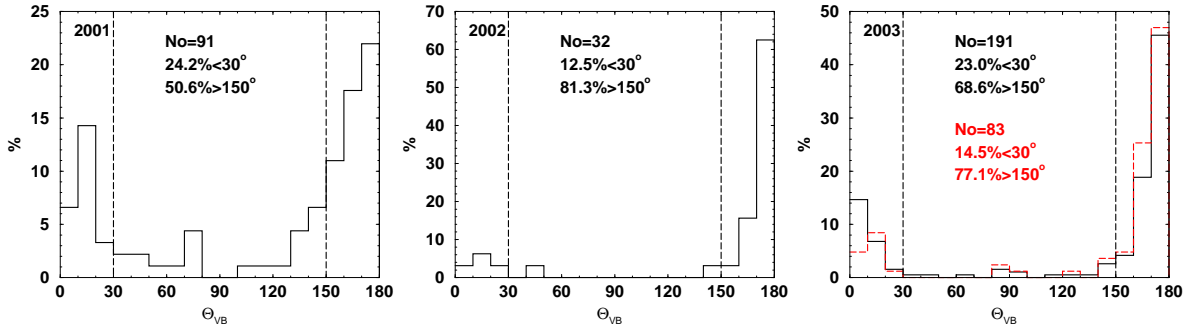


Figure 8.29: Distribution of the angle Θ_{VB} . From left to right: DD_{2001} , DD_{2002} and DD_{2003} . The distribution for DD_{2003CH} is plotted in red.

DDs are consistent with outward propagating RDs so far (at least in the isotropic limit).

Of particular interest is that the change in velocity and in the field direction are (anti-)correlated also for the TDs. We point out that this result is well established, and several authors contributed to this issue:

Neugebauer et al. [1984] suggest that the Alfvénic nature of TDs, in the sense that $[\mathbf{V}]$ is (anti-)parallel to $[\mathbf{B}/\rho]$, could have its cause in the mechanisms responsible for the generation of TDs close to the Sun, in Alfvénic changes perhaps having greater stability than other changes and thus being more likely to survive to 1 AU. Another explanation could lie in processes which alter the plasma conditions at the DD as it moves out from the Sun to 1 AU. One possibility is that the observed Alfvénic condition may be generated by interplanetary turbulence (*Neugebauer et al.* [1984] and references therein).

Neugebauer [1985] finds that the alignment of $[\mathbf{V}]$ and $[\mathbf{B}/\rho]$ across TDs is independent of the solar wind stream structure and that it occurs at all solar distances between 1 and 2.2 AU. *Neugebauer* [1985] suggests that the alignment may be caused either by Alfvénic fluctuations travelling through the plasma on the two sides of a TD or by surface waves on the TDs. Since the level of Alfvénic fluctuations strongly depends on the solar wind stream structure [*Belcher and Davis Jr.*, 1971], and *Neugebauer* [1985] finds no correlation of the alignment with stream structure, the first explanation appears unlikely. Based on the work by *Hollweg* [1982] on surface waves in a cold plasma with $[\rho] = 0$ and $[B] = 0$, it can be shown that in the limit that the amplitude of the surface wave is large compared to the underlying field change of the discontinuity, $[\mathbf{V}]$ and $[\mathbf{B}]$ are aligned [*Neugebauer*, 1985]. Note that *Horbury et al.* [2001b] suggest that also the misinterpretation of the minimum variance direction as the discontinuity normal is caused by the surface waves proposed by *Hollweg* [1982] leading to large apparent normal components in many cases (see section 8.3.5).

Surfaces at which one fluid flows past another can be subject to disruption by the Kelvin-Helmholtz instability. Using the stability criterion derived by *Sen* [1963], *Neugebauer et al.* [1986] find that TDs for which $[\mathbf{V}]$ and $[\mathbf{B}/\rho]$ are not aligned are unstable to the Kelvin-Helmholtz instability. They conclude that the alignment of $[\mathbf{V}]$ and $[\mathbf{B}/\rho]$ probably results from the destruction by the Kelvin-Helmholtz instability of TDs for which Θ_{VB} is far away from 0° or 180° .

In contrast to the explanations given above, where it is assumed that the alignment of $[\mathbf{V}]$ and $[\mathbf{B}/\rho]$ across TDs is real, other authors claim these DDs to be, in fact, RDs. For instance, *Solodyna et al.* [1977] attribute all DDs with Θ_{VB} close to 0° or 180° to RDs and the rest of the DDs to TDs. *de Keyser et al.* [1998] suggest the Alfvénic nature observed for DDs with large field magnitude changes and a small normal field component to be indicative for these structures (conventionally identified as TDs) to be, in fact, RDs, i.e., phase-steepened large-amplitude Alfvén waves [*Tsurutani et al.*, 1994] that happen to propagate quite slowly as their wave vector is nearly perpendicular to the magnetic field.

The alignment of $[\mathbf{V}]$ and $[\mathbf{B}/\rho]$ for all DDs is still a puzzle today. Moreover, condition 2.1 leads to no clear conclusion. If TDs are Alfvénic in nature, this condition cannot be used to discern RDs and TDs. In any case, according to the alignment of $[\mathbf{V}]$ and $[\mathbf{B}/\rho]$ nearly all DDs in our ensemble are consistent with RDs.

Condition 2.2

We now consider condition 2.2, addressing the relative magnitudes of $[\mathbf{V}]$ and $[\mathbf{B}/\rho]$. We begin with the isotropic limit ($A = 1$ per default). Figure 8.30 shows the distributions of R_{VB}^{iso} . In the upper panel all DDs in the four sets of DDs are considered. The middle and the bottom panel present the distributions separately for the RD^* s, TDs and ED^* s found in 2001 (middle) and 2003 (bottom).

Apparently, the theoretical value of $R_{VB}^{iso} = 1$ expected for RDs in an isotropic plasma is not observed for the majority of events. The magnitude of $[\mathbf{V}]$ is generally smaller than required from MHD theory. Condition 2.2 appears to be better satisfied in 2002 and 2003 than in

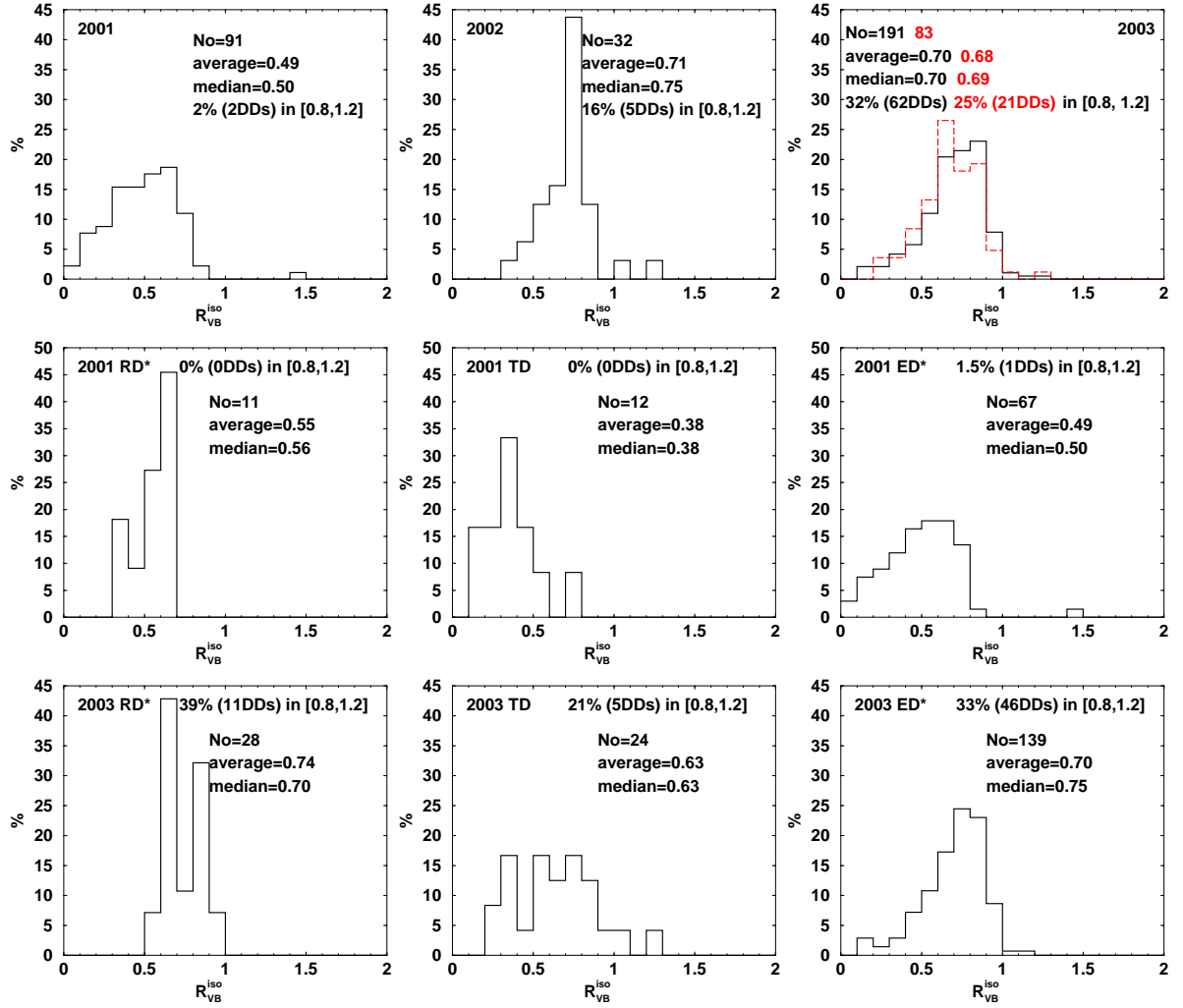


Figure 8.30: Distributions of R_{VB}^{iso} . Top: All DDs are considered. From left to right: DD_{2001} , DD_{2002} , DD_{2003} . Middle: DD_{2001} separately for RD^* s, ED^* s and TDs. Bottom: Same as middle panel for DD_{2003} .

2001. Although the statistics are poor, the distributions obtained separately for the RD^* s, TDs and ED^* s show some characteristic differences. The distributions for the TDs appear much broader than those for the RD^* s, as one would expect from theory, because R_{VB}^{iso} is arbitrary for TDs. However, in contradiction to MHD theory, R_{VB}^{iso} is not centred at unity but at ≈ 0.5 in 2001 and at ≈ 0.75 in 2003. Hence, even those DDs that are more likely RDs according to the normal magnetic field component do not satisfy condition 2.2. The distributions of the ED^* s appear to be a mixture of the TD and the RD^* distributions.

These observations coincide very well with earlier studies [Martin et al., 1973; Belcher and Solodyna, 1975; Solodyna et al., 1977; Neugebauer et al., 1984; Söding, 1999]. For instance, Solodyna et al. [1977] find $\langle R_{VB}^{iso} \rangle = 0.6$ using Pioneer 6 data and $\langle R_{VB}^{iso} \rangle = 0.73$ using data from Mariner 5 for DDs with $\Theta_{VB} \geq 140^\circ$.

Solodyna et al. [1977]; Söding [1999] find that $\langle R_{VB}^{iso} \rangle$ is closer to unity in fast solar wind streams than in slow solar wind. This is in agreement with our observation that $\langle R_{VB}^{iso} \rangle$ is larger in 2002 and 2003 than in 2001. Note, however, that R_{VB}^{iso} is not closer to unity for the coronal hole events than for the total set of DDs in DD_{2003} . Therefore, we cannot confirm a

clear association with solar wind speed. *Neugebauer et al.* [1984] find $\langle R_{VB}^{iso} \rangle = 0.59$ for their RDs.

We point out that this contradiction to MHD theory has been a major problem, because according to the magnetic field normal component, derived from MVA, a considerable number of RDs were found which were believed to be inconsistent with TDs. Therefore, the majority of these events were inconsistent with both, RDs and TDs. Using the four Cluster spacecraft, we now know that these large $|B_n|/B_{max}$ cases are an artefact caused by misinterpretation of the minimum variance directions. Since according to triangulation all DDs are consistent with TDs, we could argue that there is at most a small fraction of DDs that is consistent with RDs, and that therefore the majority of events are, in fact, TDs. For instance, R_{VB}^{iso} is in the interval $[0.8, 1.2]$ for only 2 DDs (2% of all DDs) in 2001⁸ and for only 5 DD (16%) in 2002. The corresponding number is relatively large in 2003 (62 DD, i.e., 32%) when all DDs are considered. Note that in contradiction to earlier theories this increased percentage is not found to be clearly related to the coronal hole events. Only for 25% of these DDs R_{VB}^{iso} is in the interval $[0.8, 1.2]$.

Neugebauer et al. [1984] find that the inclusion of the proton anisotropy in the calculation does not change the result. Instead of $\langle R_{VB}^{iso} \rangle = 0.59$ they find $\langle R_{VB} \rangle = 0.62$, which is not a significant improvement [*Neugebauer et al.*, 1984]. In contrast, we find a considerable improvement of the results in favour of RDs in all four sets. Figure 8.31 presents the distributions we obtain for R_{VB} , i.e., when using the thermal proton anisotropies measured by the CIS instrument. Note that a considerable number of events (detailed in the respective plots) is inconsistent with RDs, because they suffer from the firehose instability. However, for the remaining events the inclusion of the anisotropy noticeably leads to more events with R_{VB} in the vicinity of unity. Whereas the difference to the isotropic limit is marginal in 2001, about half of the events with $A > 0$ show the expected RD characteristic, i.e., $R_{VB} \approx 1$ in 2003. Whereas the sharp distribution for the RD^* s is still centred below unity (consistent with earlier works) in 2001, the majority of RD^* s indeed behave as expected for RDs from MHD theory in 2003. Note, however, that the statistics are poor and that this result is in apparent disagreement with previous observations [*Neugebauer et al.*, 1984]. It may well be that the agreement with RD theory observed for a large fraction of events in 2003 is caused by uncertain anisotropies measured by the CIS instrument. We would like to remind the reader that T_{\parallel} and T_{\perp} appear most unrealistic in the fast streams observed in 2003. Also note that the anisotropy is even so high that $R_{VB} > 1$ is observed in many cases.

Let us pursue this a little further. Using condition 2.2 one can calculate the anisotropy A that is necessary to compensate the small magnitude of $[\mathbf{V}]$ observed in the isotropic approximation. This should be on the order of the typical firehose factor near 1 AU:

$$\sqrt{A} = \sqrt{\frac{\mu_0}{\rho}} \frac{|[\mathbf{V}]|}{|[\mathbf{B}/\rho]|} \stackrel{!}{\approx} 0.9 \pm 0.1 \quad (8.3)$$

Note that for $[\rho] = 0$ the right hand side is equal to R_{VB}^{iso} . The upper panel of Figure 8.32 presents the distributions of \sqrt{A} obtained from equation 8.3. Apparently \sqrt{A} needs to be

⁸Note that one of these two DDs is the ND. With a large jump in density and field magnitude this event is unlikely to be an RD.

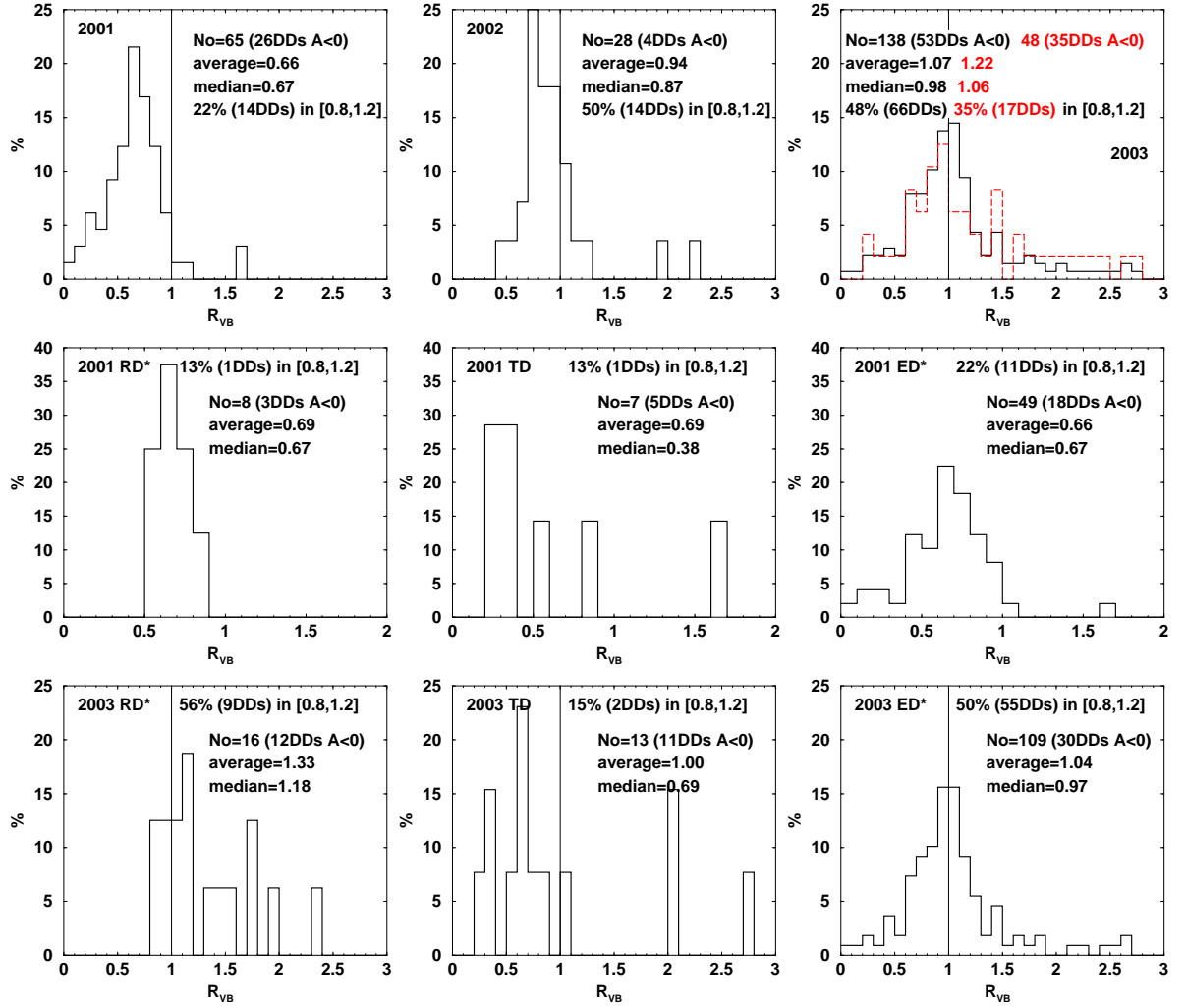


Figure 8.31: Same as Figure 8.30 for R_{VB} .

rather small for condition 2.2 to be satisfied in most cases. On average a firehose factor of $\sqrt{A} \approx 0.5$ is needed in 2001 and $\sqrt{A} \approx 0.7$ in 2003. However, the measured firehose factors are generally closer to unity, at least in 2001 and 2002 (middle panel of Figure 8.32). In agreement with earlier investigations [Burlaga, 1971b; Söding, 1999], $\sqrt{A} = 0.9 \pm 0.1$ in most cases in these two years. The discrepancy between \sqrt{A} determined from equation 8.3 and \sqrt{A} measured by the CIS instrument, which is particularly apparent in 2001, leads to $R_{VB} \neq 1$ in most cases in DD_{2001} . Surprisingly, the two values of \sqrt{A} coincide quite well in 2003, such that the measured firehose factor leads to a distribution of R_{VB} which is centred at unity (see Figure 8.31). The relatively high anisotropy measured in 2003 compensates the small magnitude of $[\mathbf{V}]$.

The direct comparison of the two values (desired \sqrt{A} from the polarisation relation and directly measured \sqrt{A}) for each individual event (bottom part of Figure 8.32) demonstrates the differences between the three sets DD_{2001} , DD_{2002} and DD_{2003} more clearly. Whereas in 2001 the desired value of \sqrt{A} (black circles) is generally very small and the measured firehose factor (red squares) is in the expected range, the two values of \sqrt{A} coincide very well in many individual cases in 2003. We point out that the latter observation is in apparent contradiction to previous results and may be due to measurement errors. Also note that the distribution of

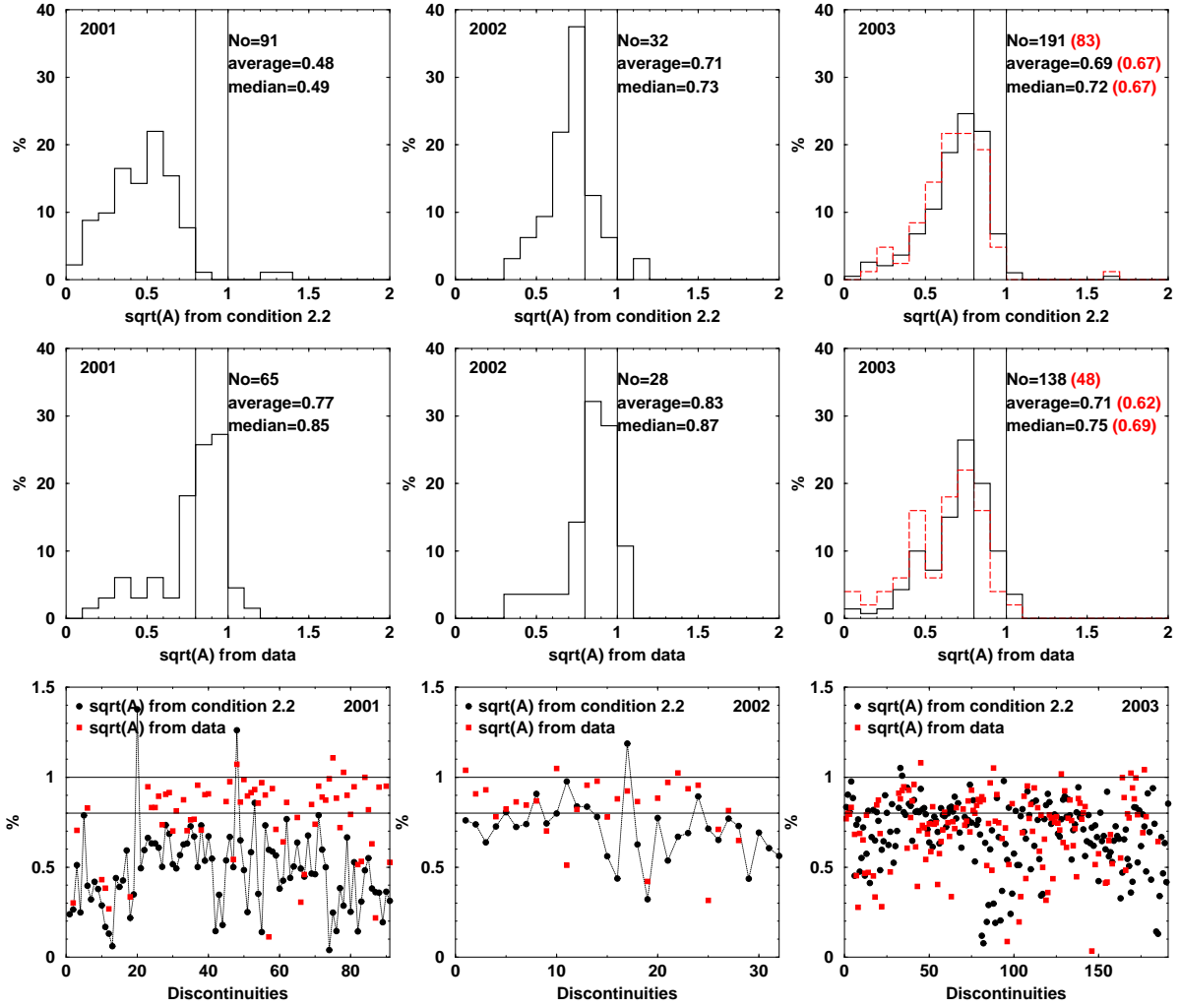


Figure 8.32: Firehose factor. Top: Calculated from condition 2.2 such that $R_{VB} = 1$. Middle: From thermal anisotropy measured by CIS. Bottom: direct comparison of the two values for each individual event. From left to right: DD_{2001} , DD_{2002} and DD_{2003} . The vertical (top and middle) and the horizontal lines (bottom) indicate the expected range of \sqrt{A} .

R_{VB} being centred around unity in 2003 fallaciously indicates consistency with RDs, because many DDs have $A < 0$, and are therefore not considered in the distribution.

Note that according to *Neugebauer et al.* [1984], besides the inclusion of anisotropy, the use of a multi-stream model and adjustment for a possible offset in the density calibration of the ISEE 3 instrument can diminish, but not eliminate, the discrepancy between observation and MHD theory. After all these adjustments *Neugebauer et al.* [1984] are still left with $\langle R_{VB} \rangle < 1$ for their RDs. Note that a similar discrepancy exists between the observed magnitudes of $\delta \mathbf{V}$ and $\delta \mathbf{B}$ in Alfvén waves in the solar wind [*Belcher and Davis Jr.*, 1971; *Belcher and Solodyna*, 1975; *Goldstein et al.*, 1995]. It appears to be a general problem which has not been fully understood, yet.

Since according to triangulation all DDs are consistent with TDs, we can argue that DDs not satisfying condition 2.2 are not consistent with RDs and are therefore TDs. However, some authors propose that there may exist mechanisms affecting the ratio R_{VB} such that it differs from the polarisation relation. For instance *de Keyser et al.* [1998] suggests that as the

RD propagation speed decreases (small $|B_n|/B_{max}$), particles need more time to drift across the layer and can be affected by other phenomena, such as deviations from planar geometry and diffusion due to micro-turbulence, resulting in a lower velocity jump magnitude than predicted from condition 2.2.

In summary, condition 2.1 is satisfied by nearly all DDs in our set, and condition 2.2 is generally not satisfied. However, particularly in 2003 we identify some events that are consistent with RDs according to conditions 1 and 2.

8.8.6 Propagation relative to the ambient plasma

The tests of conditions 1 and 2 performed in the previous sections require data from only a single spacecraft. Some DDs could be identified that are consistent with RDs. In agreement with previous studies, most of them are outward propagating. However, since according to condition 2.1 also clear TDs have the characteristics of outward propagating RDs in most cases, a definite assignment to RDs is not possible.

A direct measurement of the propagation velocity is possible only when at least four spacecraft are available. In that case the discontinuity velocity U relative to the spacecraft array can be determined from triangulation. Together with the solar wind velocity \mathbf{V} measured by the CIS instrument, the propagation with respect to the ambient plasma is then given by $(\mathbf{V} - \mathbf{U}) \cdot \mathbf{n}$. In this section we seek to differentiate between propagating and non-propagating structures by means of this quantity (condition 3).

Figure 8.33 demonstrates that this intention is complicated by small Alfvén velocities. Plotted are the percentage distributions of the normal component of the Alfvén velocity measured just after the DDs. For the vast majority of events $\mathbf{V}_A \cdot \mathbf{n}$ is less than 10 km/s, which is on the order of the errors in $\mathbf{V} \cdot \mathbf{n}$ and U . However, for some events $\mathbf{V}_A \cdot \mathbf{n}$ is larger than the error. Therefore, at least some individual DDs may be identified that propagate at Alfvén speed. Furthermore, we try to find a trend in the statistical data that might indicate propagation.

Figure 8.34 presents the relation between $\mathbf{V} \cdot \mathbf{n}$ and U for four different sets of DDs, namely DD_{2002} , DD_{2001} , DD_{2003} and the subset of DD_{2003} for which triangulation performs best (from top to bottom). Hence, the accuracy of \mathbf{n} and U determined from the relative timing method increases from top to bottom. Note that on the left hand side of Figure 8.34 we plot the solar wind velocity measured on both sides of the DDs separately. Since not much difference between $\mathbf{V} \cdot \mathbf{n}$ on the two sides is observed, we consider only $\mathbf{V} \cdot \mathbf{n}$ measured after the DDs in the probability distributions of $(\mathbf{V} - \mathbf{U}) \cdot \mathbf{n}$ on the right hand side of Figure 8.34 and in the reminder of this section.

The increasing accuracy from top to bottom is clearly reflected in the degree of agreement between $\mathbf{V} \cdot \mathbf{n}$ and U . The DD velocity U determined from triangulation is subject to huge errors in 2002 where the spacecraft separations are small. The enormous discrepancies between $\mathbf{V} \cdot \mathbf{n}$ and U cannot be related to propagation which is expected to be on the order of 10 km/s (see Figure 8.33). Therefore, the set DD_{2002} is of no use for our purpose here.

The DD velocity U is considerably better determined in 2001 where the spacecraft separa-

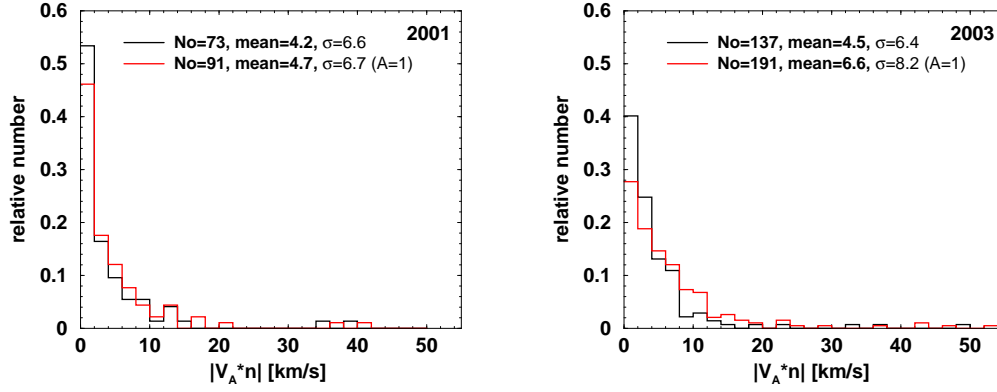


Figure 8.33: Histograms of the normal component of the Alfvén velocity $|\mathbf{V}_A \cdot \mathbf{n}|$ measured after the DDs in 2001 (left) and 2003 (right). The isotropic approximation ($A = 1$) is in red.

tions are intermediate (second panel in Figure 8.34). However, U is still far from the solar wind speed in many cases. Note that the distribution is asymmetric with a few DDs having extremely large values of U . This is an artifact caused by the triangulation method which will be explained in chapter 9.

When the spacecraft separations are large (in 2003), U is determined much more precisely. The width of the distribution is much smaller in the third panel than in the second panel of Figure 8.34. The asymmetry is diminished, but still visible.

Note that, provided the errors in U and $\mathbf{V} \cdot \mathbf{n}$ are symmetric and normally distributed, one would expect the distribution of $(\mathbf{V} - \mathbf{U}) \cdot \mathbf{n}$ to resemble a normal distribution centred at zero when all DDs are simple convected structures (TDs). In fact, we find $\langle (\mathbf{V} - \mathbf{U}) \cdot \mathbf{n} \rangle \approx 0$ in 2003. However, a new kind of asymmetry becomes apparent. Comparing the probability distribution of $(\mathbf{V} - \mathbf{U}) \cdot \mathbf{n}$ to the Gaussian-fit, which is centred at zero, one sees that the most probable value of $(\mathbf{V} - \mathbf{U}) \cdot \mathbf{n}$ is not zero, but is shifted to a positive value. Apparently, DD velocities 5 to 25 km/s below the flow speed are more likely than velocities exceeding the proton flow speed. (Note that the bin width is 10 km/s.) This asymmetry is of considerable interest since it is in the range of the Alfvén velocity. Hence, it may be related to propagation with respect to the solar wind flow. Note that $(\mathbf{V} - \mathbf{U}) \cdot \mathbf{n} > 0$ corresponds to inward propagating structures, contradicting the general belief that RDs propagate outward from the Sun (see previous section). However, in chapter 9 we will show that the shifted maximum is caused by an asymmetric error in U . Therefore, the asymmetry is probably not related to propagation, but would be expected for convected structures.

In the bottom panel of Figure 8.34 only those DDs are considered for which the relative timings between the spacecraft can be determined particularly well. For these DDs (for 85 of which also plasma data are available) \mathbf{n} and U can be regarded as highly accurate. This high precision leads to the data points of all events being very close to the solid diagonal line plotted in the scatter diagram (left). For nearly all DDs $(\mathbf{V} - \mathbf{U}) \cdot \mathbf{n}$ is less than 45 km/s and for 65% this quantity is even less than 15 km/s. The standard deviation is 16 km/s. Note that this is on the order of the error of the proton velocity determination. Fränz [2004] estimates an error of 2% in the x -component of \mathbf{V} and 50% in the y - and z -components (in GSE

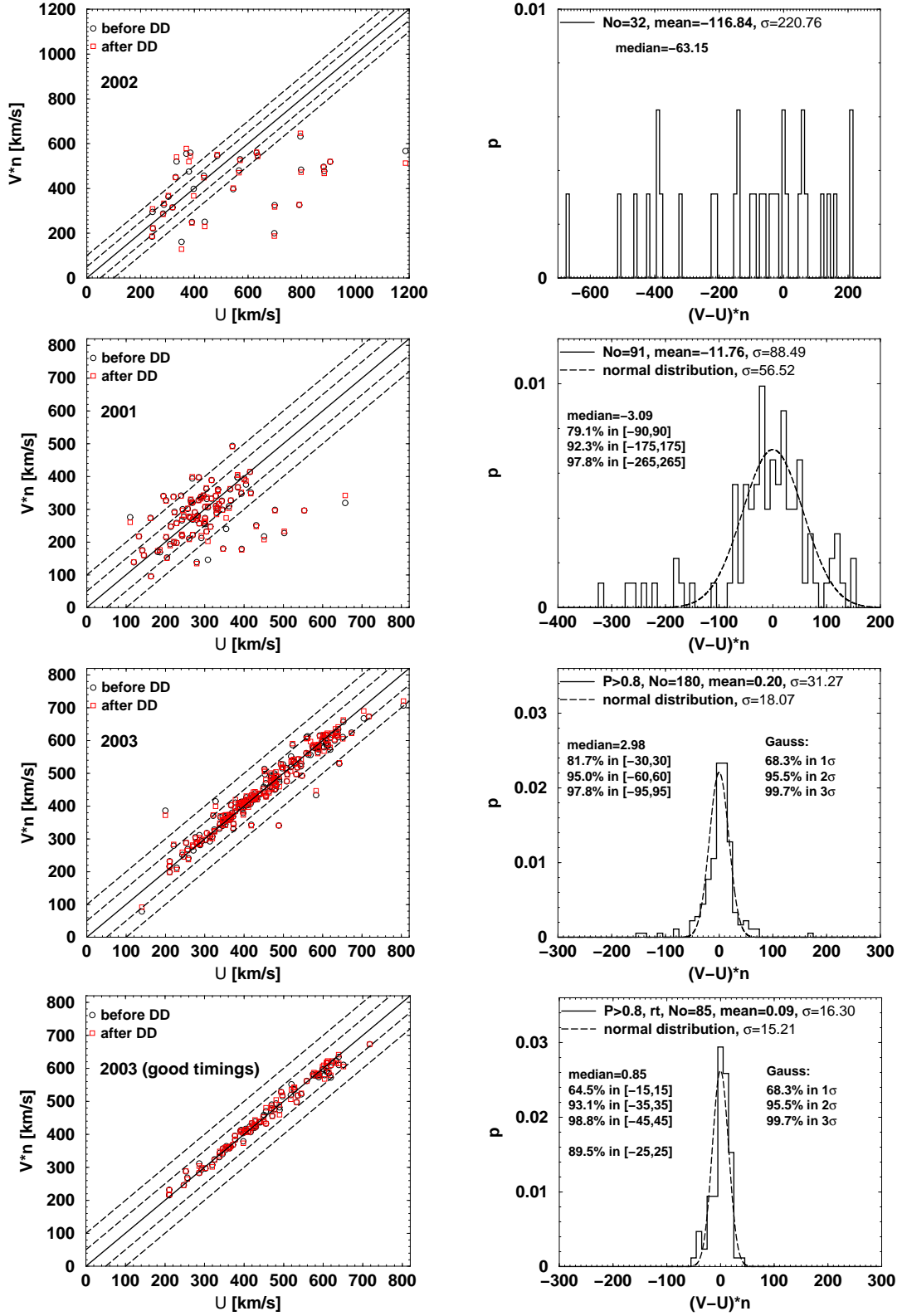


Figure 8.34: Left: $V \cdot \mathbf{n}$ versus U . Data points corresponding to convected structures are expected to lie on the solid line. DDs for which U differs from $V \cdot \mathbf{n}$ by less than 50 km/s are found within the first pair of dashed lines, and the second pair of dashed lines indicates a difference of 100 km/s. Right: Corresponding probability distributions of $(V - U) \cdot \mathbf{n}$. The dashed curve represents a fit to a centred normal distribution. From top to bottom: DD_{2002} , DD_{2001} , DD_{2003} and the subset of DD_{2003} containing those DDs for which the relative timings can be determined best. Only DDs with $P < 0.8$ are considered.

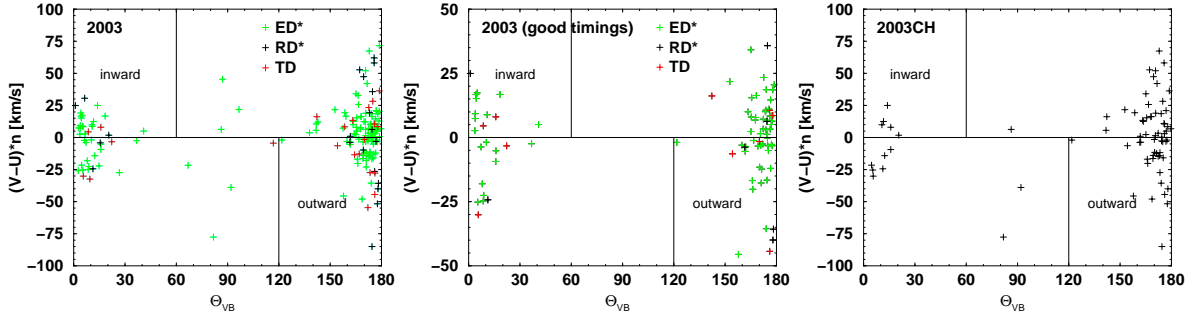


Figure 8.35: Consistency test for propagating RDs. The directly measured propagation and the propagation expected for RDs from MHD theory coincide for the events in the upper left corner (inward propagation) and for the events in the lower right corner (outward propagation). From left to right: DD_{2003} , DD_{2003} (good timings) and DD_{2003CH} . Only those DDs are considered for which $P < 0.8$. The colour code (only left and middle) indicates the type of DD.

coordinates). Since the normals of most DDs in our set (particularly in DD_{2003}) are directed nearly parallel to the Earth-Sun line (see section 8.6), the error of $\mathbf{V} \cdot \mathbf{n}$ is on the order of 10 km/s when $V = 500$ km/s is assumed. Hence, the errors are on the order of the quantity that we wish to measure.

Nevertheless, one could expect to observe at least a tendency for the measured propagation direction to coincide with the expected direction obtained from the correlation between $[\mathbf{V}]$ and $[\mathbf{B}/\rho]$, if the DDs were RDs. However, Figure 8.35 demonstrates that this is not the case. Here $(\mathbf{V} - \mathbf{U}) \cdot \mathbf{n}$ is plotted against Θ_{VB} . As noted previously, $\Theta_{VB} = 180^\circ$ corresponds to outward propagating RDs. In that case U would be larger than $\mathbf{V} \cdot \mathbf{n}$ and hence $(\mathbf{V} - \mathbf{U}) \cdot \mathbf{n} < 0$. Thus, outward propagating RDs would be consistently observed by both methods only for DDs that are in the lower right corner of Figure 8.35. Accordingly, the upper left corner corresponds to consistently identified inward propagating RDs. Apparently, no correlation between the two methods to identify the direction of propagation can be found. On the left hand side of Figure 8.35 all DDs in 2003 are considered, and only those DDs with well determined relative timings are plotted in the middle. However, no improvement of the correlation is observed. The degree of correlation is also independent of the type of DD. The sign of $(\mathbf{V} - \mathbf{U}) \cdot \mathbf{n}$ is independent of Θ_{VB} regardless of $|[\mathbf{B}]|/B_{max}$ and $|B_n|/B_{max}$. (The different types are colour coded: green: ED^* s, black: RD^* s and red: TDs.) In particular, also the RD^* s do not show a tendency toward consistency. Finally, the right hand side of Figure 8.35 shows the subset of coronal hole events, DD_{2003CH} . Again, no consistent propagation direction is found.

In a final attempt to identify a propagating RD, we plot $(\mathbf{V} - \mathbf{U}) \cdot \mathbf{n}$ against $\mathbf{V}_A \cdot \mathbf{n}$ (Figure 8.36). Theoretically, TDs (red) should all lie at the origin, and RDs should be on the diagonal line. Clearly, the error in U is too large to draw any conclusions. Even when only those DDs are considered for which triangulation performs best (not shown), no correlation can be seen. Some improvement is achieved, however, when A is not determined from CIS but is set to unity (right). Note that the correlation between $(\mathbf{V} - \mathbf{U}) \cdot \mathbf{n}$ and $\mathbf{V}_A \cdot \mathbf{n}$ appears to be even worse for the RD^* s than for the TDs and the ED^* s. This may indicate that also the magnetic field normal component is inaccurately determined for these events.

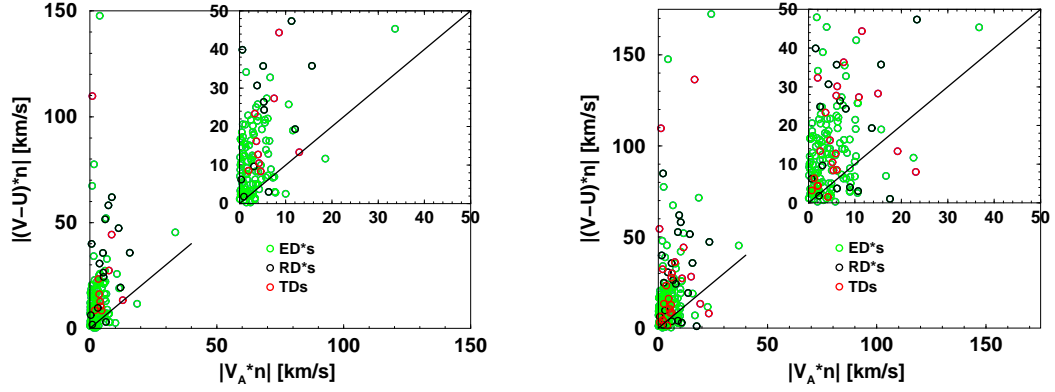


Figure 8.36: Directly observed magnitude of propagation $|(\mathbf{V} - \mathbf{U}) \cdot \mathbf{n}|$ versus the magnitude of the Alfvén speed $|\mathbf{V}_A \cdot \mathbf{n}|$ for the set DD_{2003} . On the left hand side \mathbf{V}_A is determined using the anisotropy measured by CIS, and on the right \mathbf{V}_A is determined in the isotropic limit ($A = 1$). Only those DDs for which $P < 0.8$ are considered.

It is also difficult to identify individual cases for which reasonable agreement between $(\mathbf{V} - \mathbf{U}) \cdot \mathbf{n}$ and $\mathbf{V}_A \cdot \mathbf{n}$ can be determined. Of particular interest in this regard are DDs with a relatively large Alfvén velocity on both sides. There is one ED^* with a relatively large value of $\mathbf{V}_A \cdot \mathbf{n}$ (34 km/s) for which $(\mathbf{V} - \mathbf{U}) \cdot \mathbf{n}$ (45 km/s) is close to $\mathbf{V}_A \cdot \mathbf{n}$. However, by inspecting the other side of this DD (in Figure 8.36 only the quantities after the DDs are shown), we find $\mathbf{V}_A \cdot \mathbf{n} = 4$ km/s and $(\mathbf{V} - \mathbf{U}) \cdot \mathbf{n} = 45$ km/s. Since the flow velocity must equal the Alfvén velocity on both sides of an RD in the DD rest frame, this one hopeful candidate must be dropped also. Moreover, $\Theta_{VB} = 87^\circ$ for this event, i.e., it is one of the few cases for which $[\mathbf{V}]$ and $[\mathbf{B}/\rho]$ are not aligned and can therefore not be an RD.

To conclude, we are not able to assign any DD to be rotational by means of propagation. The results are rather consistent with convected TDs. However, since even in the best cases the uncertainty in U is of the order of the Alfvén speed, no definite conclusion in favour of either of the two types is possible.

8.8.7 Properties of possible RDS

In the previous sections we have tested whether the DDs in our ensemble satisfy several necessary conditions for RDS (conditions 1-3 in Table 8.6). These tests were performed separately. However, for a DD to be consistent with an RD all these necessary conditions need to be satisfied simultaneously. In the following we aim to identify DDs that accomplish this demand. In a second step we analyse the properties of this subset of possible RDS, in order to deepen our understanding of their origin.

To do so it is necessary to establish quantitative criteria that select those DDs that satisfy the necessary conditions. We point out that the thresholds we define in the following are rather arbitrary numbers which are not based on a detailed error analysis. The resultant set of DDs must therefore be regarded as a subset of the total ensemble which is more likely to be consistent with RDS than the remaining DDs. It may well be that we over- or underestimate

the number of possible RDs. Moreover we remind the reader that all of the selected events can still be tangential.

We apply the following criteria:

$$\text{C1: } R_{VB} \in [0.8, 1.2] \text{ (A from CIS), } R_{VB}^{iso} \in [0.8, 1.2] \text{ (A = 1)}$$

$$\text{C2: } C1 + \{nA\} < 1.4 \text{ (A from CIS), } \{n\} < 1.2 \text{ (A = 1)}$$

$$\text{C3: } C2 + (\Theta_{VB} < 20^\circ) \vee (\Theta_{VB} > 160^\circ)$$

$$\text{C4: } C3 + |[B]|/B_{max} < 0.2$$

$$\text{C5: } C4 + ((\mathbf{V} - \mathbf{U}) \cdot \mathbf{n} > 0 \wedge \Theta_{VB} < 90^\circ) \vee ((\mathbf{V} - \mathbf{U}) \cdot \mathbf{n} < 0 \wedge \Theta_{VB} > 90^\circ)$$

$$\text{C6: } C5 + |(\mathbf{V} - \mathbf{U}) \cdot \mathbf{n} - \mathbf{V}_A \cdot \mathbf{n}| < 20 \text{ km/s}$$

Note that we distinguish between the isotropic approximation ($A = 1$) and the case where we determine A from the CIS data ($A \neq 1$ in general). The criterion C1 selects all DDs that satisfy condition 2.2 from table 8.6. According to the previous sections the majority of events fail this test. The remaining DDs need to additionally satisfy condition 1 (C2) and condition 2.1 from table 8.6 (C3). In the next step (C4) all DDs with large magnetic field magnitude changes are sorted out. Finally, criteria C5 and C6 test whether for the remaining events also the direction of propagation is determined consistently (C5) and whether the propagation velocity determined from triangulation coincides with the Alfvén velocity (C6).

Table 8.7 presents the number of events remaining after each step. The results for the isotropic approximation ($A = 1$) are shown on the left hand side, and the right hand side corresponds to the case where we use the CIS data to determine A . Note that for testing the criterion C1 we use ρA measured immediately before the DDs. The upper row on the right side of Table 8.7 indicates the number of events for which $A > 0$ immediately before the DDs. Also note that the events failing C2 in the anisotropic case also include those DDs for which $A < 0$ on both sides of the transition layer.

Although many DDs suffer from the firehose instability, C1 is considerably more often satisfied when A is determined from CIS than in the isotropic approximation in all three sets. However, we point out that the value of A measured by the CIS instrument is questionable.

Apart from criterion C2 in the anisotropic case, the criteria C2-C4 are satisfied for almost all events that are preselected by the criterion C1. It is particularly interesting that nearly all events selected according to C3 have only a small change in magnetic field magnitude across them (C4), i.e., they are all EDs. This means that C3 automatically rejects DDs which are likely to be tangential according to $|[B]|/B_{max}$.

Inspecting the number of possible RDs that remain after C4 is applied, a remarkable difference between the four sets of DDs is observed. Particularly in the isotropic approximation (which we believe is more meaningful) apparently more possible RDs are identified in 2002 and 2003 than in 2001. After all, 59 events (31%) remain after step C4 in 2003, whereas only 1 DD (1%) remains in 2001. This difference and its possible relation to the prevailing solar wind conditions will be discussed below.

Table 8.7: *Number (and percentage) of DDs satisfying the necessary RD-conditions.*

$A = 1$	DD_{2001}	DD_{2002}	DD_{2003}	$A \neq 1$	DD_{2001}	DD_{2002}	DD_{2003}
total	91	32	191	$A_1 > 0$	65 (71%)	28 (88%)	138 (72%)
C1	2 (2%)	5 (16%)	62 (32%)	C1	14 (15%)	14 (44%)	66 (35%)
C2	1 (1%)	5 (16%)	62 (32%)	C2	7 (8%)	11 (34%)	32 (17%)
C3	1 (1%)	5 (16%)	61 (32%)	C3	6 (7%)	11 (34%)	32 (17%)
C4	1 (1%)	5 (16%)	59 (31%)	C4	6 (7%)	11 (34%)	32 (17%)
C5	0 (0%)	4 (13%)	27 (14%)	C5	2 (2%)	9 (28%)	17 (9%)
C6	0 (0%)	0 (0%)	18 (9%)	C6	1 (1%)	1 (3%)	14 (7%)

According to the discussion in the previous section, the significance of the criteria C5 and C6 is questionable. Particularly in 2002 and 2001 the uncertainty in the determination of U is probably too large to draw any conclusion from these two criteria. Note that of those events satisfying C4 about 80% are found to have a consistent propagation direction in 2002 (small separations), and about 50% satisfy this criterion (C5) in 2003. Because of the large separations, the best results should be obtained in 2003. However, no correlation is found. Since this may well be due to the error of U generally being larger than the Alfvén speed, we attach no importance to criteria C5 and C6, and we define the DDs passing C4 as possible RDs for the following discussion. We note only that a considerable number of events from DD_{2003} (9% in the isotropic approximation) also survive C6.

Solar wind type

We now address the question why apparently many more DDs can be considered as possible candidates for RDs in 2003 (and 2002) than in 2001. The most obvious difference between these periods of observation is the presence of fast streams originating from coronal holes on the Sun in 2002 and 2003 (see section 6.5). This may suggest that coronal hole streams are indeed more likely to contain RDs than slow solar wind streams. We recall that earlier observations (mainly based on the normal magnetic field component determined by MVA) confirm this picture which is related to the idea of RDs being phase-steepened Alfvén waves (see sections 3.2 and 3.3). Utilising the relative timings between the four Cluster spacecraft, we have shown that according to $|B_n|/B_{max}$ no clear RD exists in these fast streams. Perhaps the selection of possible RDs by means of criterion C4 leads to a preference for these events to be in coronal hole streams which would confirm earlier observations and related theory at least to some extent. However, the results presented in the previous sections already indicate that this is not the case.

Assuming that the DDs satisfying criterion C4 are good candidates for possible RDs, we now investigate whether RDs are indeed more abundant in coronal hole streams than in the slow solar wind: Of the 59 DDs satisfying C4 in the isotropic limit in 2003, 39 are found in slow solar wind and only 20 are found in coronal hole streams. Hence, 36% of the 108 DDs in slow solar wind streams are possible candidates for RDs, whereas only 24% of the 83 coronal hole

events satisfy C4. This means that the probability of finding an RD in solar wind originating from coronal holes is even reduced.

When A is determined from the CIS data this trend is even more pronounced. In that case (right side of Table 8.7) only 6 out of the 32 possible RDs are in coronal hole streams. Hence, the percentage of RD candidates is 22% in the slow solar wind compared to only 7% in coronal hole streams.

Note that in section 6.5 we classified 27 of the 83 coronal hole events as “unclear”, because they might be affected by a CME or by stream-stream interaction regions. By removing these ambiguous DDs from the coronal hole events and adding them to the group of slow solar wind DDs, we get the following result: 21% of the remaining coronal hole group and 35% of the other group are possible RDs in the isotropic approximation, and when A is determined from CIS the corresponding percentages are 4% and 22%. Hence, the “unclear” events have a similar percentage of possible RDs as the low speed DDs, and the percentage of possible RDs is even smaller in the remaining coronal hole group.

We conclude that the assumed abundance of RDs in coronal hole streams can by no means be confirmed by our analysis. In fact, our results suggest that the opposite is the case, i.e., the probability of finding an RD is even lowered in coronal hole streams. Together with the $|B_n|/B_{max}$ analysis based on triangulation, it is questionable if RDs exist at all in the solar wind at 1 AU. And if they were indeed present, then they would have a vanishing magnetic field normal component. Moreover, possible RD candidates are not preferentially observed in coronal hole streams. Putting these new results together, the well accepted hypothesis of phase-steepening Alfvén waves as possible source for RDs appears at best questionable.

Since the coronal hole streams do not appear to be a plasma environment favouring RD generation, the question arises whether we are able to identify another solar wind type which is likely to contain RDs. Therefore, we mark all possible RDs as vertical lines in Figures 6.11 - 6.13 in section 6.5 (not shown) and analyse where most of these events can be found. On a qualitative level it appears as if stream-stream interaction regions have an enhanced probability of containing possible RDs. For instance, four of the six candidates found in 2001 (including the one found in the isotropic approximation) are found in the stream-stream interaction region on day 43 (see Figure 6.11). Several stream-stream interaction regions can be identified in 2002 and 2003. Most of them comprise possible RDs.

In order to further pursue this analysis, we study the distributions of the proton velocity and density in the vicinity of the RD candidates (not shown). We observe a slight enhancement of the density and slightly decreased velocities in the vicinity of these events which is consistent with the above hypothesis. However, the difference from the distributions of the other DDs is small and probably not significant.

Note that because of the rather poor solar wind coverage, this type of analysis is difficult using the Cluster spacecraft. Knowing that MVA is unreliable and that $|B_n|/B_{max}$ is generally small, only a single spacecraft is needed to test C4. Therefore, one could use a measuring platform permanently operating in the solar wind, such as ACE, to pursue this analysis. Not being misguided by fallacious MVA normals one could then use the criteria applied in this section (C4) to identify possible RD candidates, just as presented above. With a huge sample

of candidates one could then systematically investigate which type of solar wind is most likely to contain RDs.

We point out that recent hybrid simulations also identify stream-stream interaction regions as plasma regions where RD generation appears likely [Lyu, 2003]. Therefore, it appears to be worthwhile to carry out the experiment suggested above.

Statistical properties

In the following we summarise further characteristics of the DDs identified as possible RDs. Most of the parameters we consider can be obtained from a single spacecraft. Hence, this analysis could be repeated with a larger sample, for instance, acquired by the ACE spacecraft.

Essentially, the subset of DDs selected according to C4 does not differ significantly from the other DDs. For instance, the distributions of the discontinuity thickness and the spreading angle ω for the RD candidates are very similar to those found for the other DDs. Also, the average and median values are nearly the same. The eigenvalue ratios λ_2/λ_3 of the possible RDs appear to be somewhat larger than the values we usually find. This is an interesting result, because it suggests that the assumption of one-dimensionality is not less justified for the DDs satisfying C4. This result also has some relevance for our analysis presented in section 8.3.2, since it demonstrates that increasing the lower limit $(\lambda_2/\lambda_3)^L$ does not sort out possible RDs. Finally, we examine the magnetic field normal components. The finding that $|B_n|/B_{max}$ determined by MVA is the same as for the DDs not satisfying C4 (in fact, $|B_n|/B_{max}$ appears to be even slightly smaller for the possible RDs) confirms that the large values of $|B_n|/B_{max}$ determined by MVA do not justify for considering the corresponding DDs as RDs. Using the triangulation normals to determine $|B_n|/B_{max}$, we find a similar result. In particular, no dominance of RD^* s (i.e., EDs with $|B_n|/B_{max} > 0.15$ in 2001 and EDs with $|B_n|/B_{max} > 0.1$ in 2003) can be found in the sample of possible RDs according to criterion C4.

To conclude, the only definite indication for an RD is a magnetic field normal component that is larger than its uncertainty would allow for a TD. None of the DDs in our entire ensemble satisfies this condition. However, there are some DDs that satisfy several necessary RD conditions simultaneously (see Table 8.7). This sample can be regarded as being consistent with RDs. Therefore, we cannot exclude the possibility that there are some RDs with small values of $|B_n|/B_{max}$ in the solar wind at 1 AU. However, the DDs in this sample show no specific characteristics. Since RDs and TDs are two distinct types of MHD discontinuities one might expect to observe differences. Hence, it may well be that the criteria defined in this section are only incidentally satisfied, and that the selected DDs are in fact TDs.

In contradiction to earlier observations (e.g. *Neugebauer and Alexander [1991]*), possible RDs are more likely to be found in stream-stream interaction regions than in fast solar wind streams originating from coronal holes on the Sun. It is of considerable interest to relate this observation to the theory of possible generation processes for RDs. The established line of argument is to relate the abundance of non-linear Alfvén waves to the presently belief that

there is an abundance of RDs in coronal hole streams. Hence, the connection between these two solar wind features appeared obvious. In the light of our new observational results, this argumentation is hard to maintain.

On the other hand, the agreement of our observations with the recent hybrid simulations that identify the plasma conditions in stream-stream interaction regions to favour RD generation [Lyu, 2003] appears promising. On the theoretical side, further simulations may be helpful to understand the exact generation mechanisms in these plasma regions. Particularly an explanation is needed for possible RDs always having a small magnetic field normal component. Perhaps the idea of phase-steepening is still maintainable in the sense that stream-stream interaction regions provide exactly the environment needed to produce the kind of possible RDs that we observe.

To verify the observational results acquired in this section we suggest an extended investigation of interplanetary discontinuities. Since our diligent analysis presented in other parts of this work leaves no doubt that $|B_n|/B_{max}$ is generally small, the suggested investigation can take this result for granted. Hence, C4 can be tested using only a single satellite which permanently operates in the solar wind. With a huge sample of DDs the analysis presented in this section can then be repeated to verify the assumption of stream-stream interaction regions as possible source regions for RDs.

As a final comment, we may add that *Neugebauer et al.* [1984] find that according to conditions 1 and 2, their EDs have more attributes of their RDs than of their TDs. Among others, this lead *Neugebauer et al.* [1984] to conclude that the majority of EDs are, in fact, RDs. However, since their classification of RDs is based on unreliable MVA estimates, all of these events are most likely EDs, according to our new multi-spacecraft results. Hence, it is not surprising that the EDs found in *Neugebauer et al.* [1984] have similar characteristics as their RDs. Therefore, the similarities of their EDs with their RDs can not be used to argue that EDs are mostly RDs.

ERROR ANALYSIS OF THE TRIANGULATION METHOD

Normals obtained by the triangulation method (section 7.4) have an imprecision that is mostly due to uncertainty in the timing data. This chapter discusses the relationship between the error δt of the timing data and the errors dn and dU of the normal \mathbf{n} and the velocity U of the discontinuity relative to the spacecraft array. In particular, it analyses the strong dependence of this relationship on external factors, such as the geometry of the spacecraft configuration and the absolute value of U .

This discussion is imperative for the far-reaching radical results presented in chapter 8. It provides the justification for our claim that the triangulation technique yields reliable normal estimates, in contrast to the MVA technique.

Our method to estimate absolute errors of \mathbf{n} and U consists in an analysis of the spread of \mathbf{n} and U if the relative timings vary within an interval $t_{ij} \pm \delta t$ (section 9.1). In particular, we will show that a symmetric error distribution within that interval yields anisotropic distributions of errors dn and dU . This affords a simple explanation for the deviations of the distribution of $(\mathbf{V} \cdot \mathbf{n} - U)$ from the Gaussian distribution (see section 8.8.6).

In order to be aware of circumstances that are likely to produce large uncertainties, it is important to know the principle factors determining the precision of triangulation. Section 9.2 discusses how dn and dU are affected by the absolute value of U , by the geometry factor P of the spacecraft configuration and by the orientation of the spacecraft configuration. Among others, we demonstrate that $P_c = 0.8$ is a reasonable upper limit for the planarity.

Section 9.3 gives numerical values for the errors of the datasets for 2001, 2002 and 2003.

Finally, section 9.4 presents the most important conclusion of this chapter: As a consequence of this error analysis, we can confidently claim consistency of the data with vanishing normal component of the magnetic field ($|B_n|/B_{max} = 0$) and with vanishing propagation ($U = \mathbf{V} \cdot \mathbf{n}$).

9.1 Method and symmetry considerations

This section gives an analysis of the error of the triangulation method (section 7.4). The uncertainty stems mostly from the uncertainty in the relative timings t_{ij} between the spacecraft, as the only other input parameter, the satellite positions, is known with much higher precision. The uncertainty in \mathbf{n} , corresponding to the imprecision δt in the relative timings, is best visualised as a generally deformed asymmetric cone around the normal \mathbf{n} . The shape of this cone is analysed by sampling the interval $t_{ij} \pm \delta t$ of the relative timings between the four spacecraft (by 11 sample points each). We will see that the error cone often degenerates to a nearly flat *error fan*. This anisotropy and the asymmetry of the error of the relative velocity U are discussed.

Recall the method to determine relative timings (e.g., Figure 7.3): The data curves for the magnetic field at the different satellites j are, roughly, piece-wise constant with a smoothed jump at t_j when spacecraft j passes through the discontinuity. The relative timings $t_{1j} = t_j - t_1$ ($j = 2, 3, 4$) are obtained by manual alignment of the curves of CI j and the reference curve of CI 1.

The determination of t_{1j} has an ambiguity that is due to differences in shape of the curves which mostly stems from superposed fluctuations. We quantify this uncertainty in the following way: Instead of the best alignment value t_{ij} , we identify an interval of values $T_j = [t_-, t_+]$ of all those values that yield acceptable alignment. The average is $t_{ij} = (t_- + t_+)/2$ and the uncertainty is $\delta t = (t_+ - t_-)/2$. This uncertainty depends on various parameters. Most important is the level of background fluctuations superposed to the discontinuity. In particular, δt depends strongly on the spacecraft separations, since with increasing distance the correlation between the individual time series decreases. For the data sets analysed in the previous chapters we find that $\delta t \approx 0.1 t_{ij}$ on average. In contrast, the relative error in the satellite distances, approximately 1% (see chapter 5), is one order of magnitude lower. It is therefore neglected in the following discussion.

The corresponding uncertainties of the obtained normal vectors \mathbf{n} and of the velocities U are now evaluated by the following process: Each of the three intervals T_j associated with an event is sampled by 11 equidistant points. This yields $N = 11^3 = 1331$ combinations of acceptable timing values $\hat{\mathbf{t}}_1 = (\hat{t}_{12}, \hat{t}_{13}, \hat{t}_{14})$ for which normal vectors $\hat{\mathbf{n}}_i$ and velocities \hat{U}_i are calculated by the triangulation method (equation 7.10).

Plotted as unit vectors from the same origin, these N normal vectors $\hat{\mathbf{n}}_i$ form a deformed asymmetric cone. The spread of the cone is an indication of the error of \mathbf{n} . Any conceivable combination of reasonable timing values yields a normal vector contained within the error fan. Similarly, the spread of the solutions \hat{U}_i yields the error of U .

Instead of the uniform distribution of the \hat{t}_{1j} , that we use, a Gaussian distribution in T_j might be more appropriate, to account for the \hat{t}_{1j} close to t_{1j} being more likely correct. A Monte Carlo calculation then yields the statistical error. This definition yields a smaller error than ours. What we get is the maximum deviation from \mathbf{n} and U possible within δt . So, e.g., when we ask whether there is any possible solution $\hat{\mathbf{n}}_i$ within δt that is perpendicular to the magnetic field (i.e., the associated DD is consistent with a TD) our treatment is advantageous.

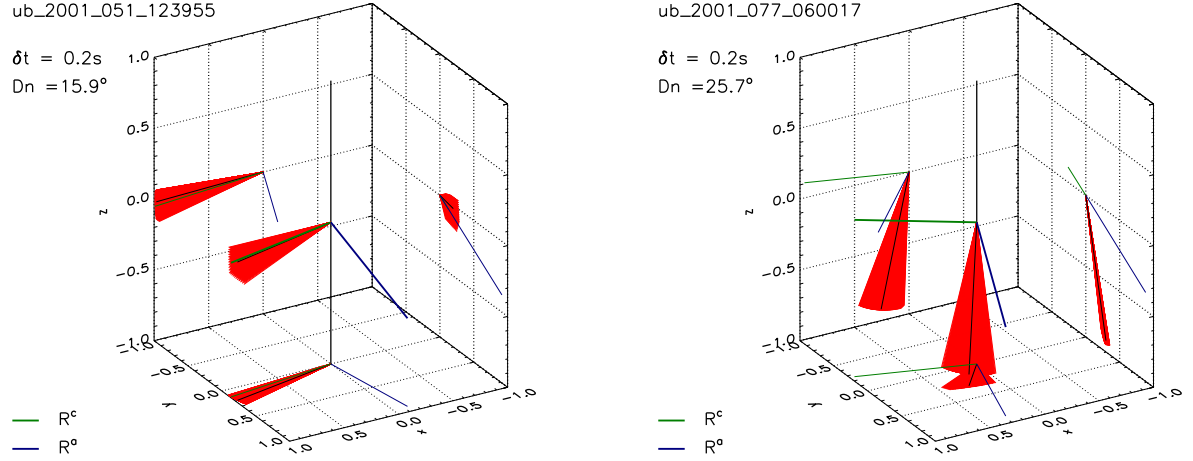


Figure 9.1: Error cone of the triangulation normal for two examples. Shown are the measured normal \mathbf{n} (black) and the 1330 $\hat{\mathbf{n}}_i$ for $\delta t = 0.2$ s (red). Also shown are \mathbf{R}^c (green) and \mathbf{R}^a (blue), and projections onto the coordinate planes. The coordinate system is GSE. The two examples are extremes of the orientation of the spacecraft configuration relative to the DD surface: \mathbf{n} and \mathbf{R}^c are almost aligned for *ub_2001_051_123955* (left) and almost perpendicular for *ub_2001_077_060017* (right). The angles between \mathbf{n} and \mathbf{R}^c are $\angle(\mathbf{n}, \mathbf{R}^c) = 4.6^\circ$ and $\angle(\mathbf{n}, \mathbf{R}^c) = 86.0^\circ$, respectively, and the angles between \mathbf{n} and the direction of elongation are $\angle(\mathbf{n}, \mathbf{R}^a) = 86.6^\circ$ and 47.3° , respectively.

This, of course, only holds within the limitation of the limited number of N different results. We cannot cover the whole continuum of possible solutions within the time uncertainty. In fact, instead of using a fixed number N , it might be better to keep the time step between two consecutive \hat{t}_{1j} constant, in order to treat various values of δt equally. Not doing so might favour larger errors for small δt as compared to larger δt , because the density of solutions is higher. However, for small ranges of δt the effect is negligible. The density of solutions is rather high even for the largest δt that we use.

Figure 9.1 shows the scatter of the $\hat{\mathbf{n}}_i$ around \mathbf{n} for two examples with $\delta t = 0.2$ s (a typical value in 2001). The normals $\hat{\mathbf{n}}_i$ in the diagram are too close to be resolved individually. These two examples¹ are particularly instructive because of the orientation of the spacecraft configuration relative to the normal: The discontinuity normal \mathbf{n} and the normal of planarity \mathbf{R}^c of the volumetric ellipsoid are nearly aligned for *ub_2001_051_123955* (left) and nearly perpendicular for *ub_2001_077_060017* (right).²

In the first case, the normals $\hat{\mathbf{n}}_i$ form a nearly circular cone, the error is *isotropic*. In the second case, the error cone degenerates to an error fan expanding in the plane defined by \mathbf{n} and \mathbf{R}^c . The projections of the cone onto the coordinate planes in Figure 9.1 elucidate this degeneracy. The anisotropy is caused by the fact that the error is largest in the direction of \mathbf{R}^c (see section 7.4.2).

¹*ub_yyyy_ddd_hhmmss* is an identification code that we use, where *yyyy* is the year, *ddd* the day of year and *hhmmss* hour, minute and second of observation of the event.

²See chapter 5 for the definitions of \mathbf{R}^a , \mathbf{R}^b , \mathbf{R}^c and planarity P .

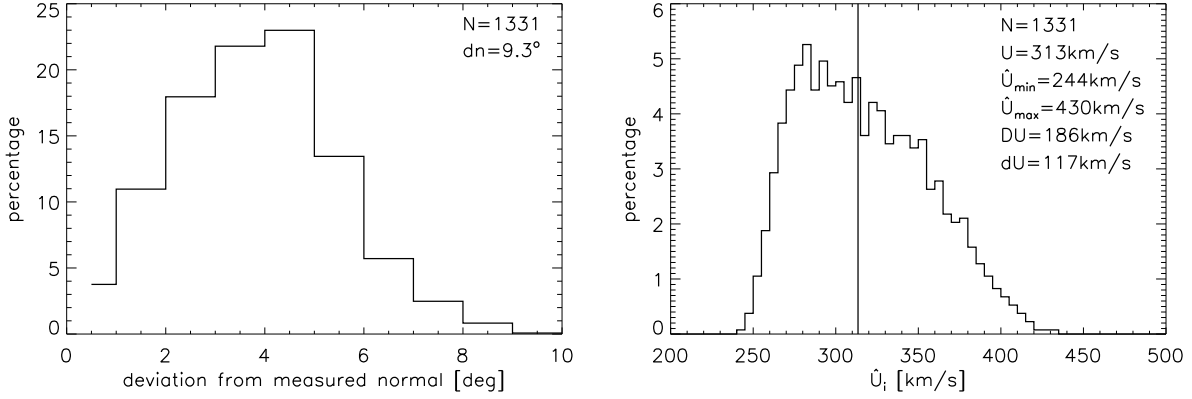


Figure 9.2: Left: Distribution of the angle between the measured normal \mathbf{n} and the 1330 normals $\hat{\mathbf{n}}_i$, and (right) distribution of the 1331 velocities \hat{U}_i for the event *ub_2001_051_123955* (left of Figure 9.1). The vertical line indicates the measured velocity U .

To characterise the deviations more quantitatively, we now discuss the distributions of the normal and speed deviations. Figure 9.2 shows distributions of the deviations of $\hat{\mathbf{n}}_i$ from \mathbf{n} and of the associated \hat{U}_i for *ub_2001_051_123955*. These statistics plus the distribution of the angle between all pairs of $\hat{\mathbf{n}}_i$ are calculated for each DD. We define the following scalar quantities to characterise the distributions:

$$Dn := \max(\angle(\hat{\mathbf{n}}_i, \hat{\mathbf{n}}_j)), \quad (9.1)$$

$$dn := \max(\angle(\hat{\mathbf{n}}_i, \mathbf{n})), \quad (9.2)$$

$$DU := \hat{U}_{\max} - \hat{U}_{\min}, \quad (9.3)$$

$$dU := \max(|\hat{U}_i - U|), \quad (9.4)$$

with $i, j = 1, \dots, 1331$ and $\hat{U}_{\max(\min)} = \max(\hat{U}_i)$ ($\min(\hat{U}_i)$). Thus, Dn and DU are the total spread of possible solutions within δt , and dn and dU are the largest deviation from the measured parameters \mathbf{n} and U . For *ub_2001_051_123955* we find $Dn = 15.9^\circ$. For a perfectly isotropic error this would be the apex angle of the error cone. In that case, dn would be exactly half of Dn . However, we find $dn = 9.3^\circ$ (see also Figure 9.2).

To account for incidental large deviations we also calculate 95% confidence intervals. The spreads within these intervals are denoted by the appendix ‘95’. For instance, 95% of the angles between \mathbf{n} and $\hat{\mathbf{n}}_i$ are less than dn_{95} .

Asymmetry of the error of U

The distribution of the \hat{U}_i is clearly not symmetric (Figure 9.2). The left side (low velocities) is steeper than the right side (high velocities). Compared to U , the maximum of the distribution is slightly shifted towards lower velocities. From there the distribution slowly decreases towards high values of \hat{U}_i . The asymmetry of the distribution is characteristic for most DDs. It is a consequence of $U \propto 1/t_{ij}$ (see equation 7.10). The \hat{t}_{ij} are distributed symmetrically around t_{ij} . The \hat{t}_{ij} with $|\hat{t}_{ij}| > |t_{ij}|$ are mapped on velocities $\hat{U}_i < U$ in a narrow codomain as compared to the codomain $\hat{U}_i > U$ of the \hat{t}_{ij} with $|\hat{t}_{ij}| < |t_{ij}|$. The $\hat{U}_i > U$ can be large, especially for \hat{t}_{ij} close to zero.

This asymmetry explains the observed asymmetric distribution of $(\mathbf{V} \cdot \mathbf{n} - U)$ (Figure 8.34): Let \tilde{t}_{ij} be the true time difference between CI i and CI j yielding the true velocity \tilde{U} . The unknown value of \tilde{t}_{ij} is assumed to be in T_j . Furthermore, it is plausible to assume that the probability distribution of the t_{ij} of the events in our ensemble is centred at \tilde{t}_{ij} . Because of $U \propto 1/t_{ij}$, the distribution of the measured velocities U around the true velocities \tilde{U} is asymmetric, following the same arguments as above. This means that the most probable velocity that we obtain from triangulation is slightly below the true velocity. Large deviations are associated with measured velocities larger than the true velocity. The latter are, however, less probable. Therefore, just by means of these uncertainty considerations one expects the distribution of $(\tilde{U} - U)$ to be asymmetric, as is qualitatively observed for the distribution of $(\mathbf{V} \cdot \mathbf{n} - U)$ in Figure 8.34. (Note that $\tilde{U} = \mathbf{V} \cdot \mathbf{n}$ for non-propagating structures).

In particular, the abundance of DDs with $(\mathbf{V} \cdot \mathbf{n} - U) \in [0, 20]$ as compared to the normal distribution (see the distribution for 2003 in Figure 8.34) caught our attention, since these DDs could also be interpreted as RDs propagating toward the Sun at Alfvén speed. However, propagation is not necessary in order to explain the observed feature of the $(\mathbf{V} \cdot \mathbf{n} - U)$ distribution. Simply convected structures, as TDs, can produce the distribution shown in Figure 8.34, provided that the discrepancies are within the error bars. Also note that extreme differences between $\mathbf{V} \cdot \mathbf{n}$ and U are predominantly observed for negative values of $(\mathbf{V} \cdot \mathbf{n} - U)$, i.e. large U , in Figure 8.34, which is also in agreement with our expectations.

Anisotropy of the error cone of \mathbf{n}

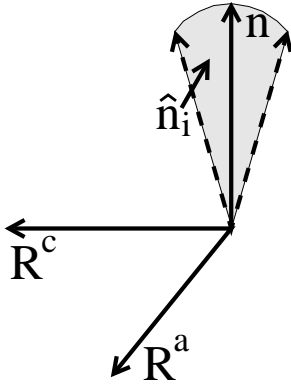


Figure 9.3: Illustration of the “error fan” when \mathbf{R}^a , \mathbf{R}^c and \mathbf{n} are perpendicular to each other.

As stated above, the distribution of the $\hat{\mathbf{n}}_i$ is anisotropic for the example *ub_2001_077_060017* (Figure 9.1). In the following we illustrate by statistical means that this observation is valid in general whenever the spacecraft configuration is anisotropic. Furthermore, we argue that this anisotropy does not introduce a bias to the measured DD normals.

The error cone being degenerated to a flat fan expanding in the plane spanned by \mathbf{n} and \mathbf{R}^c is equivalent to $(\mathbf{n} \times \hat{\mathbf{n}}_i) \perp \mathbf{R}^c \forall i$, i.e., the volume of the parallelepiped spanned by the vectors \mathbf{n} , $\hat{\mathbf{n}}_i$ and \mathbf{R}^c is zero: $S_x := (\mathbf{n} \times \hat{\mathbf{n}}_i) \cdot \mathbf{R}^x = 0 \forall i (x = c)$. This is illustrated in Figure 9.3. Since the fan is not totally flat and \mathbf{R}^a and \mathbf{R}^c are generally not perpendicular to \mathbf{n} , in reality, $S_c = 0$ is certainly not strictly to expect. However, Figure 9.4 shows that indeed $\langle S_c \rangle < \langle S_a \rangle$. Especially in 2001, $\langle S_c \rangle$ predominantly takes small values, whereas $\langle S_a \rangle$ is rather uniformly distributed, as expected.

These features are less apparent in 2003. This is because the spacecraft configuration in 2003 often resembles an almost regular tetrahedron, e.g., $P < 0.34$ for 139 events (see chapter 5). Therefore, the effect of anisotropic configurations on the error is reduced in 2003. Nevertheless, on average $\langle S_a \rangle$ is more than twice as large as $\langle S_c \rangle$. The distributions of $\langle S_a \rangle$ and $\langle S_c \rangle$ for the set of DDs in 2002 is similar to the distributions in 2001 (not shown).

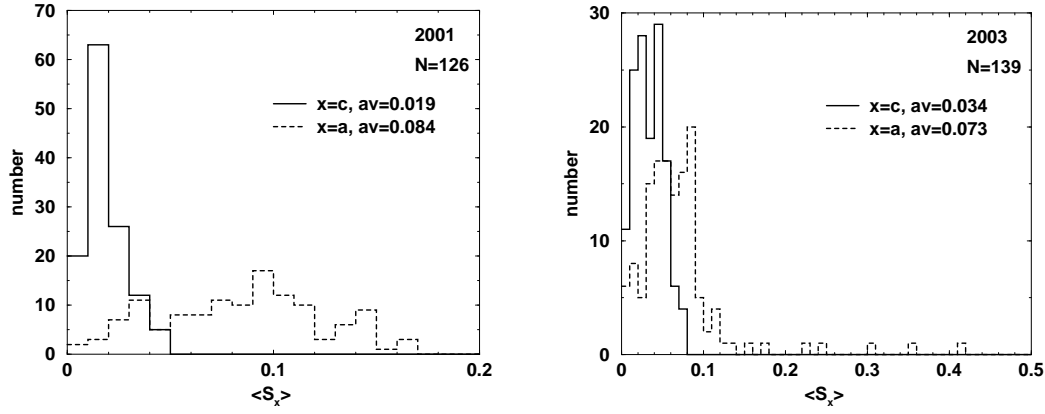


Figure 9.4: Histograms of $\langle S_x \rangle$ for 2001, $\delta t = 0.2$ s (left) and 2003, $\delta t = 0.34$ s (right). For the average values we considered only those $\hat{\mathbf{n}}_i$ for which $\angle(\mathbf{n}, \hat{\mathbf{n}}_i) > 5^\circ$ to avoid small S_x and thus inaccurate values. If for a specific event no such $\hat{\mathbf{n}}_i$ exists, this event is not considered in the histogram.

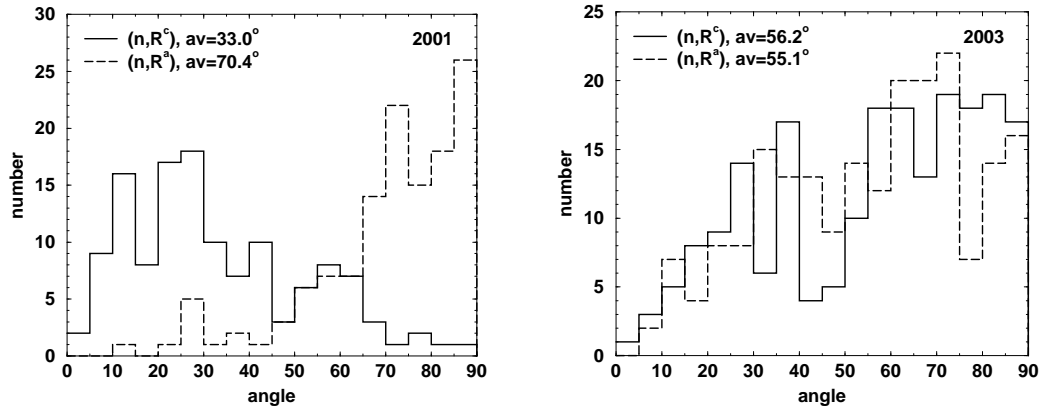


Figure 9.5: Histograms of $\angle(\mathbf{n}, \mathbf{R}^c)$ (solid line) and $\angle(\mathbf{n}, \mathbf{R}^a)$ (dashed line) for 2001 (left) and 2003 (right).

Another reason for the value of $\langle S_c \rangle$ being smaller than $\langle S_a \rangle$ could also be that $\angle(\mathbf{n}, \mathbf{R}^c)$ is possibly smaller than $\angle(\mathbf{n}, \mathbf{R}^a)$. Figure 9.5 shows that this is indeed the case in 2001: The DD normals tend to be closer to \mathbf{R}^c than to \mathbf{R}^a . However, the distributions of $\angle(\mathbf{n}, \mathbf{R}^a)$ and $\angle(\mathbf{n}, \mathbf{R}^c)$ do not differ significantly in 2003. Therefore, $\langle S_c \rangle < \langle S_a \rangle$ is, in fact, due to the anisotropy of the error.

It is important to point out that the anisotropic error does not introduce a bias for the calculation of \mathbf{n} . Whereas the most likely angle between \mathbf{n} and \mathbf{R}^c is around 30° in 2001, \mathbf{n} and \mathbf{R}^c tend to be more perpendicular to each other in 2003 (see Figure 9.5). This suggests that there is no mechanism systematically falsifying the normal calculation yielding directions ruled by the orientation of the spacecraft array. Instead, the DD normals are predominantly oriented along the Earth-Sun line (see section 8.6), regardless of the tetrahedron orientation. Therefore, the observed distributions of $\angle(\mathbf{n}, \mathbf{R}^c)$ simply reflect the orientation of the spacecraft configuration (shown in Figure 5.9), which for the vast majority of events is such that \mathbf{R}^c is scattered around the Earth-Sun line within 30° in 2001, whereas \mathbf{R}^c is predominantly perpendicular to this direction in 2003.

We will discuss further implications of the DD orientation relative to the spacecraft configuration in the next section.

9.2 Parameters affecting the error - avoiding large errors

In the last section we have demonstrated how the empirical uncertainty δt for the timing data yields error estimates for the normal \mathbf{n} and the DD velocity U . This section discusses the parameters affecting the error. Two results are of particular interest: First, particularly error-prone spacecraft constellations are identified. The $P > 0.8$ cut-off criterion for the minimal planarity can be formulated to eliminate such events from our statistics. Second, the error of the triangulation method increases with increasing solar wind speed V .

The error is different for each DD. Principal factors are: (1) the tetrahedral geometry, (2) the orientation of the configuration relative to \mathbf{n} and (3) the DD velocity U relative to the spacecraft array (see also section 7.4.2). (1) includes both, the characteristic size L and the shape of the tetrahedra. Since the configurations we use are squashed rather than elongated (see chapter 5), the planarity P is an essential parameter determining the accuracy of the triangulation method in this work. The characteristic tetrahedra sizes are discussed in chapter 5. They are different for each year of observation, largest in 2003, intermediate in 2001 and smallest in 2002. The different impacts of the above factors on the error will be discussed in this section. The aim is to identify circumstances likely to produce large errors and to avoid these if indicated.

Uncertainties of the relative timings - influence of the tetrahedra size

The only uncertain quantities that go into the calculation are the relative timings t_{ij} (assuming the relative spacecraft positions to be well known). Therefore, besides the above parameters, the choice of δt is essential.

Generally, the correlation between the four time series decreases, and thus δt increases, with increasing separation between the spacecraft. In addition, however, δt inherently depends on the actually observed field signature of the particular DD. For some DDs the background field is very quiet. In these cases δt is small. Other DDs are embedded in a strongly fluctuating field. These superposed fluctuations complicate the determination of the t_{ij} and thus yield large uncertainties. Also the thickness and the spreading angle contribute to the accuracy of the t_{ij} .

The experience in manual alignment of the four time series shows that an interval $I_{\delta t} = [\delta t^{\min}, \delta t^{\max}]$ can be estimated such that $\delta t \in I_{\delta t}$ for the majority of events. Since the correlation between the four time series depends on the spacecraft separations, $I_{\delta t}$ is different for each period of observation. We estimate $I_{\delta t} = [0.03 \text{ s}, 0.05 \text{ s}]$ in 2002, $I_{\delta t} = [0.05 \text{ s}, 0.2 \text{ s}]$ in 2001 and $I_{\delta t} = [0.1 \text{ s}, 0.4 \text{ s}]$ in 2003. Note that δt can be outside $I_{\delta t}$ for individual events.

Also note that finding reasonable estimates is most difficult in 2002 where the timing uncertainties are generally small. The δt we estimate for the DDs in 2002 are on the same order of

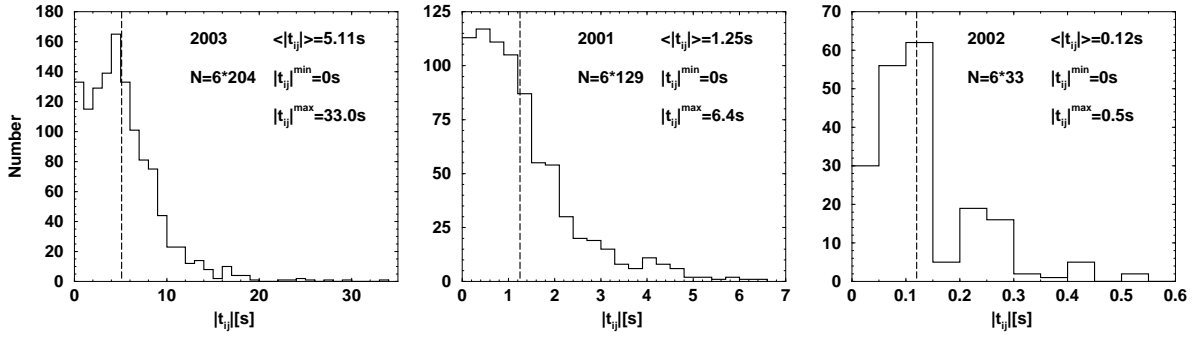


Figure 9.6: Histograms of the time differences between the spacecraft. All 6 pairs of spacecraft are considered. From left to right: 2003, 2001, 2002. The minimum value, the maximum value and the average value of $|t_{ij}|$ are shown.

magnitude as the sampling rate of the magnetic field data (22 vectors/second, i.e., $\Delta t \approx 0.045$ s). In principle, interpolation by eye allows for $\delta t < \Delta t$. However, there are of course limitations for δt . Therefore, the ratio $\delta t / |t_{ij}|$, mainly determining the size of the error, is largest in 2002, yielding large errors.

Figure 9.6 shows histograms of the relative timings t_{ij} for each year. According to the various spacecraft separations these values are clearly distinct in the three years. The respective intervals $I_{\delta t}$ are located within the first bin of the histogram in each year. The average values $\langle |t_{ij}| \rangle$ are also shown. According to the empirically determined intervals $I_{\delta t}$, the ratio $\delta t / \langle |t_{ij}| \rangle$ ranges between 2% and 8% in 2003, between 4% and 16% in 2001 and between 25% and 42% in 2002. Note that the uncertainty in evaluating the relative timings increases less than linearly with the separation distances for the range of separations that we consider. Therefore, for the spacecraft separations considered here, the accuracy generally increases with increasing tetrahedra size (see also section 7.4.2).

Error as a function of the DD velocity U relative to the spacecraft array

In order to study the error as a function of U , it is advantageous to use DD_{2001} or DD_{2002} , because the planarity is similar for all DDs in these sets, in contrast to DD_{2003} (see chapter 5). Figure 9.7 shows dU , dU/U and dn versus U for DD_{2001} . In agreement with the analytic argument presented in section 7.4.2, we observe a quadratic dependence of dU on U . The solid line in the left plot is a quadratic least-squares fit to the dU . The observed linear dependence of dU/U on U demonstrates the agreement with the theoretical prediction more clearly. The directional error dn increases linearly with U , also in agreement with theory (section 7.4.2). Thus, since U is generally related to the solar wind speed V , we can conclude that in particular for our set of DDs the error is larger in fast solar wind compared to slow solar wind.

Error as a function of planarity P

The dependence of the error on the tetrahedral shape is stronger than on the velocity. This is best exemplified by DD_{2003} because the whole range of P is covered by this set. Since

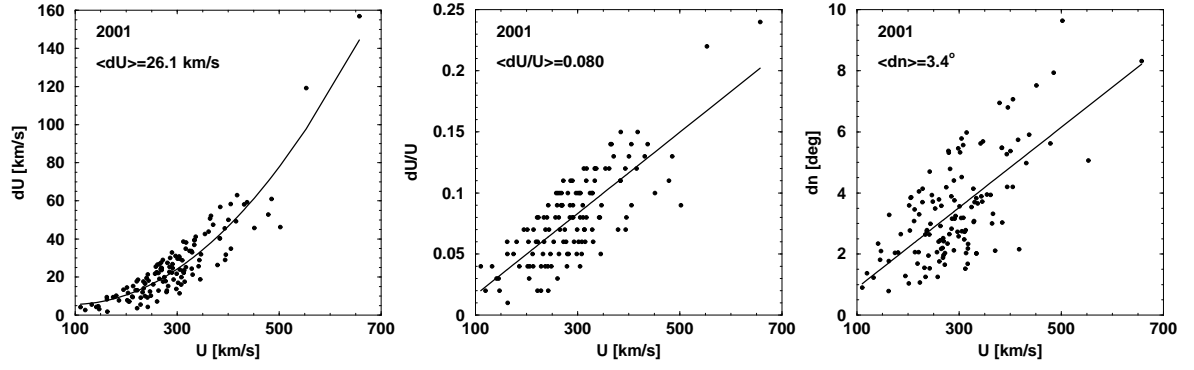


Figure 9.7: Dependence of the error on U for 2001. A quadratic least-squares fit to dU (left) and a linear least-squares fit to dU/U (middle) and dn (right) is shown. $\delta t = 0.05 \text{ s}$. The grouping of the dU/U values in lines is an artefact due to rounding.

the two error sources add together, it is instructive to plot dU and dn versus P and versus U side by side. Figure 9.8 shows this dependence for DD_{2003} for $\delta t = 0.3 \text{ s}$. On the left hand side the error is plotted versus P . The vertical dashed line indicates P_c and the thin solid lines border the range of P in 2001 and 2002. This figure clearly shows that the tetrahedral shape is of crucial importance. The error increases with increasing P . For the majority of events, $P < 0.34$ (see also chapter 5). In this regime, $dn < 10^\circ$ for all but one DD. The rate of increase is moderate for $P < 0.8$, and extremely large errors are observed for $P > 0.8$. The uncertainty of U can be as large as 350 km/s and dn reaches its maximum value of 90° .

This is the reason for choosing $P_c = 0.8$. Omitting events with $P > P_c$ prevents us from fallacious triangulation results *a priori*. Also note the average values of dn and dU shown separately for the subsets with $P < 0.8$ and $P > 0.8$.

The right hand side of Figure 9.8 demonstrates that the effect of the tetrahedral shape is stronger than the influence of U . Whereas the dependence on U is explicit in 2001 (Figure 9.7), the scatter around the least-squares fit (quadratic for dU and linear for dn) is larger in 2003, because of the superposed impact of the geometry factor P . This even holds for the shown subset of DDs with $P < P_c$. In the inserts all 204 events are shown. The 13 events with $P > P_c$ are marked by crosses. For these DDs the deviation from the quadratic, respectively linear, U dependence is particularly apparent. Regardless of U , the error is largest when P takes very large values. This confirms that $P_c = 0.8$ is a good choice for the cut-off value. At least, it must not be larger.

The values of P covered by the sets DD_{2001} and DD_{2002} indicate that no extreme errors due to planar spacecraft constellations are expected. However, the “shape-induced” error is certainly larger than for the majority of events in 2003. Apart from the larger spacecraft separations, the generally high geometrical quality of the tetrahedra in 2003 (after the restriction $P < P_c$) is decisive for the excellent quality of the results for this set of DDs. Fortunately, the majority of events used in this work are from 2003: Of the 191 DDs in 2003 with $P < P_c$ for 139 events (73%) $P < 0.34$. This is more than the total number of DDs studied in 2001 (129) and in 2002 (33). For the above reasons the interpretation of the triangulation results is most meaningful in 2003.

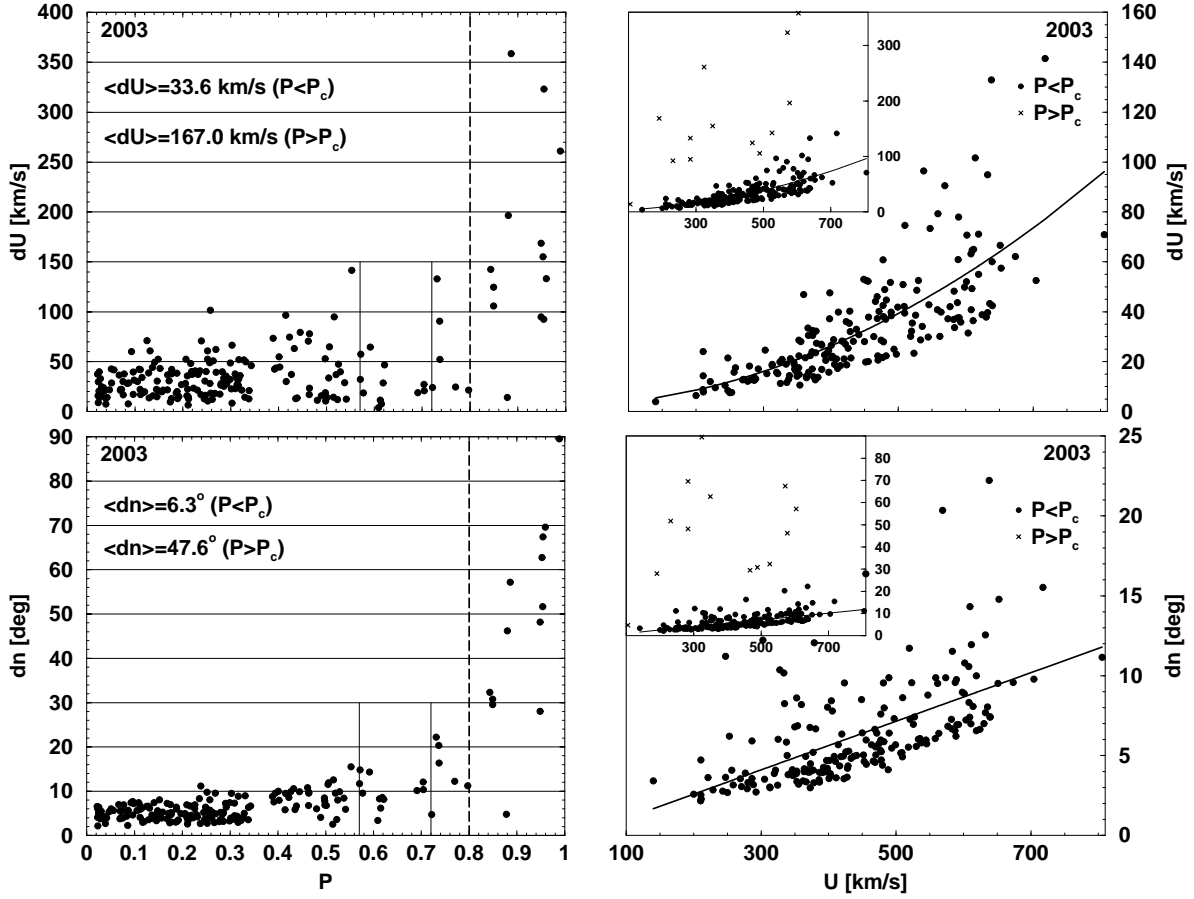


Figure 9.8: The two main parameters determining the accuracy of triangulation. (Left) planarity P and (right) DD velocity U relative to the spacecraft array. Shown are dU (top) and dn (bottom) for 2003 for $\delta t = 0.3$ s. The vertical thick dashed line indicates the cut-off value $P_c = 0.8$. For $P > P_c$ the error can be large. The two thin solid lines indicate the range of P present in 2001 and 2002. To better isolate the U -dependence the DDs are split in those with $P < P_c$ (circles) and those with $P > P_c$ (crosses). Only the inserts show both groups. $dU(U)$ is fitted to a quadratic function and $dn(U)$ to a linear function (solid line). For the fitting procedure only those DDs with $P < P_c$ are considered.

Influence of the orientation of the tetrahedra relative to \mathbf{n}

Finally, we discuss the impact of the orientation of the generally anisotropic spacecraft configuration related to the DD orientation. Equations 7.26 and 7.28 in section 7.4.2 demonstrate the influence of the orientation on the error analytically. Here, this is illustrated by the following geometrical consideration: The uncertainty of \mathbf{n} is largest in the direction \mathbf{R}^c perpendicular to planarity (section 7.4.2). Let, for instance, \mathbf{n} and \mathbf{R}^c be aligned, i.e., the DD surface and the plane defined by \mathbf{R}^a and \mathbf{R}^b are parallel. Then the direction in which the uncertainty of \mathbf{n} is largest coincides with \mathbf{n} . Consequently, the error is small. The other extreme is $\mathbf{n} \perp \mathbf{R}^c$. In that case the largest uncertainty of \mathbf{n} is perpendicular to \mathbf{n} , i.e., the directional error is large.

Figure 9.9 illustrates the two extreme cases. Let us assume $P = 1$ for simplicity, i.e., all four spacecraft are in the plane spanned by \mathbf{R}^a and \mathbf{R}^b . Then, the DD is observed simultaneously at the four locations for $\mathbf{n} \parallel \mathbf{R}^c$ (left hand side of Figure 9.9). Any change of the relative orientation of the two planes, e.g. by a rotation of the DD normal \mathbf{n} by an angle ψ , yields $t_{ij} \neq 0$ for at least one pair of spacecraft. Rotating \mathbf{n} in the opposite direction causes a change

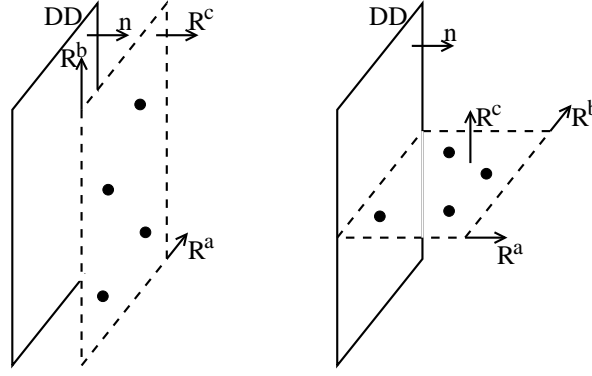


Figure 9.9: Illustration of the influence of the orientation on the error. Shown are two extreme cases for $P = 1$. The four spacecraft (circles) lie in the plane indicated by the dotted line. On the left the DD normal \mathbf{n} is parallel to the normal of planarity \mathbf{R}^c , and on the right \mathbf{n} is perpendicular to \mathbf{R}^c .

in sign; the order in which the spacecraft observe the DD is extremely sensitive to small changes of \mathbf{n} . In the initial situation (left hand side of Figure 9.9) all relative position vectors \mathbf{r}_{ij} are perpendicular to \mathbf{n} . Since $t_{ij} \propto \mathbf{n} \cdot \mathbf{r}_{ij} \propto \cos \angle(\mathbf{n}, \mathbf{r}_{ij})$, and the derivative of the cosine is maximal at 90° , t_{ij} is most sensitive regarding perturbations of \mathbf{n} when \mathbf{n} is approximately perpendicular to \mathbf{r}_{ij} , i.e., when \mathbf{n} and \mathbf{R}^c are aligned. In the contrary, this means that a given uncertainty δt_{ij} has only relatively little impact on \mathbf{n} in that case. Hence, for the case $\mathbf{n} \parallel \mathbf{R}^c$ the error in \mathbf{n} is smallest.

The other extreme is $\mathbf{n} \perp \mathbf{R}^c$ (right hand side of Figure 9.9). In that case, relatively large rotations of \mathbf{n} in the direction \mathbf{R}^c cause only relatively small changes in the t_{ij} . (Note that the sequence of spacecraft observing the DD on the right hand side of Figure 9.9 remains unchanged unless $\psi > 90^\circ$). Therefore, a given uncertainty δt_{ij} yields relatively large deviations in \mathbf{n} .

Figure 9.9 also illustrates why the uncertainty of \mathbf{n} is largest in the direction normal to planarity: Rotating the DD surface in any other direction than \mathbf{R}^c yields a larger rate of change of $\mathbf{n} \cdot \mathbf{r}_{ij}$ and thus of t_{ij} .

The relative timings t_{ij} are in general smaller when $\mathbf{n} \parallel \mathbf{R}^c$ than in the case $\mathbf{n} \perp \mathbf{R}^c$. In addition, the transversal dislocations of the spacecraft are generally smaller in the latter case, yielding smaller δt_{ij} . Therefore, the accuracy of the absolute value of the DD velocity U , which is mainly determined by the ratio $\delta t_{ij}/t_{ij}$, is best when $\mathbf{n} \perp \mathbf{R}^c$, i.e., reversed compared to the accuracy of \mathbf{n} .

For an adequate empirical analysis of the effect of the tetrahedron orientation on the error, it is again advantageous to use DD_{2001} , because the shapes of the configurations are all similar in this set of DDs. Therefore, the influence of variable P is minimised. Figure 9.10 shows dU and dn plotted versus $\angle(\mathbf{n}, \mathbf{R}^c)$. The respective trends expected as explained above are visible. However, the dominant influence of U yields a large scatter. The orientation is even less relevant in 2003 (not shown). Here, the accuracy of the DD velocity even slightly increases with increasing angle between \mathbf{n} and \mathbf{R}^c , contradicting the expectations. This is because P is the dominant parameter, and there is a tendency for increasing P with increasing $\angle(\mathbf{n}, \mathbf{R}^c)$ (not shown), i.e., P mainly determines the observed trend in 2003.

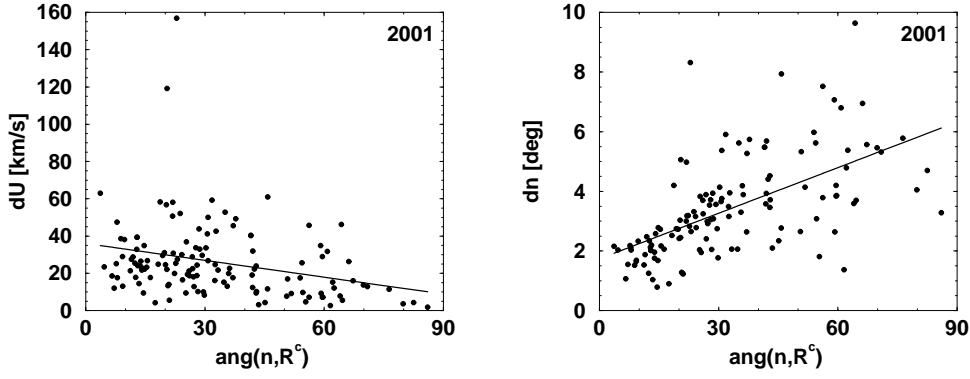


Figure 9.10: Dependence of the error on the orientation of the tetrahedron relative to the measured DD normal \mathbf{n} . 2001, $\delta t = 0.05$ s. The solid lines indicate the linear trend.

In conclusion we state that U is an important factor determining the precision of the triangulation method. Therefore, it is important to keep in mind that in the fast solar wind, e.g. originating from coronal holes, the uncertainty is expected to be larger than in slow solar wind. Since P is restricted to a small range in 2001 and 2002, U is the dominant factor for the variability of the error for the sets of DDs in these years. The orientation of the spacecraft configuration relative to the DD orientation is noticeable but not crucial. The most important factor affecting the precision of \mathbf{n} and U is the tetrahedral geometry. Therefore it is mandatory to define a cut-off value for the planarity. We have shown that $P_c = 0.8$ is a reasonable value.

9.3 Histograms and average values of the errors of \mathbf{n} and U

This section presents an overview of the error estimates of our three data sets.

In the previous section we have defined intervals $I_{\delta t}$ so that $\delta t \in I_{\delta t}$ for the majority of events for each of the three sets DD_{2001} , DD_{2002} and DD_{2003} . Figure 9.11 and Table 9.1 give an overview of the size of the error associated with the determination of the DD normal \mathbf{n} and the DD velocity U relative to the spacecraft array based on these intervals.

Figure 9.11 shows histograms of dn and dU for δt^{\min} and δt^{\max} for each year. Since the true uncertainty δt of an individual event is in-between δt^{\min} and δt^{\max} for most DDs, the distribution of the actual error values is somewhere between these extreme cases.

The uncertainties are moderate in 2001, but dn and dU can take large values in 2002 where the spacecraft separations are small. Best reliability is achieved for the DDs in 2003 (large separations). For $\delta t^{\min} = 0.1$ s, $\langle dn \rangle = 2.1^\circ$ and $\langle dU \rangle = 10.8$ km/s. For all DDs, $dn(\delta t^{\min}) < 8^\circ$ and for all but three DDs, $dn(\delta t^{\min}) < 5^\circ$. Even for $\delta t^{\max} = 0.4$ s, the error remains small: For 95% of all DDs $dn < 15^\circ$, and the most probable value is 5.5° .

The average values of all used error parameters and their standard deviations are shown in Table 9.1 for various values of δt separately for each year. The average directional error increases linearly with increasing $\delta t \in I_{\delta t}$ in 2003, and slightly stronger than linear in 2001.

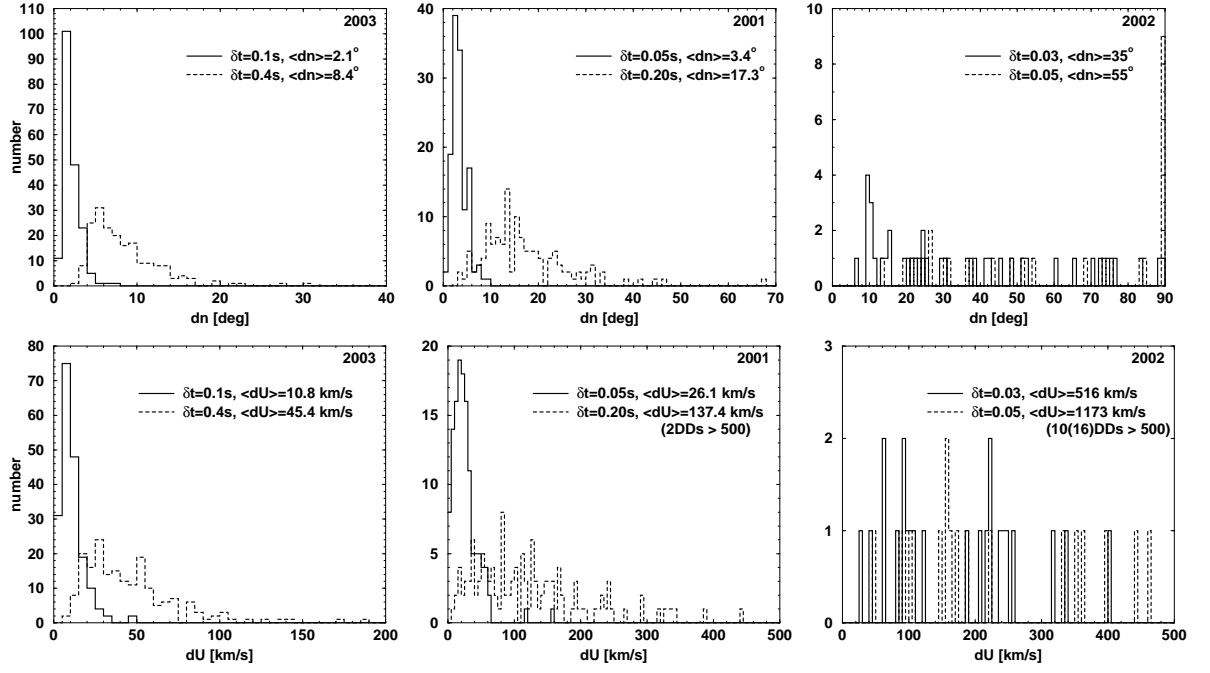


Figure 9.11: Histograms of dn (top) and dU (bottom) for δt^{\min} and δt^{\max} for each of the three years (2003, 2001, 2002 from left to right). Only DDs with $P < P_c$ are considered. Note the different ranges for the different data sets. For the illustration only, we limit the range of dU to 500 km/s. Larger errors for dU , i.e. $dU > 500$ km/s, are observed for 2 DDs in 2001 ($\delta t = 0.2$ s), for 10 DDs in 2002 ($\delta t = 0.03$ s) and for 16 DDs in 2002 ($\delta t = 0.05$ s).

Table 9.1: Average values of the error parameters and their standard deviations in brackets for various values of δt (in seconds) ranging from δt^{\min} to δt^{\max} (apart from 2002). $\langle \rangle$ denotes the average over all DDs with $P < P_c$. The units of dn and dU are degrees and km/s, respectively.

yr	δt	$\langle dn \rangle$	$\langle dn_{95} \rangle$	$\langle Dn \rangle$	$\langle dU \rangle$	$\langle dU_{95} \rangle$	$\langle DU \rangle$
2003	0.10	2.1(1.0)	1.6(0.8)	4.1(2.0)	10.8(7.0)	8.3(5.1)	21.2(13.6)
	0.20	4.2(2.1)	3.3(1.7)	8.1(4.0)	22.0(14.1)	16.8(10.3)	42.4(27.0)
	0.30	6.3(3.1)	4.9(2.5)	12.2(5.9)	33.6(21.5)	25.5(15.7)	63.6(39.7)
	0.40	8.4(4.2)	6.5(3.3)	16.2(7.8)	45.4(28.8)	34.3(21.2)	84.2(51.9)
2001	0.05	3.4(1.7)	2.5(1.2)	6.4(3.0)	26.1(20.3)	20.1(15.9)	48.3(35.4)
	0.10	7.4(3.7)	5.0(2.4)	13.0(6.1)	56.8(47.4)	43.0(36.5)	98.0(73.8)
	0.15	11.9(6.3)	7.8(3.8)	19.9(9.5)	93.2(84.2)	69.2(63.0)	151.0(119.0)
	0.20	17.3(9.4)	10.8(5.4)	27.3(13.1)	137.4(139.8)	99.0(96.8)	209.6(180.0)
2002	0.01	8.6(6.3)	5.8(4.2)	14.9(10.3)	118(124)	87(89)	201(199)
	0.03	35(25)	21(16)	47(29)	516(850)	343(523)	706(953)
	0.05	55(29)	39(25)	65(26)	1173(2502)	527(624)	1430(2599)
	0.07	71(22)	51(26)	80(17)	1996(2609)	691(626)	2298(2721)

The increase is far from linear in 2002 within the shown interval. The standard deviation is approximately half of the value of the parameters describing the directional error in 2003 and 2001. In contrast, it is large in 2002. Especially the standard deviation of the velocity error is

huge in 2002. $\langle dn_{95} \rangle$ and $\langle dU_{95} \rangle$ are considerably smaller than $\langle dn \rangle$ and $\langle dU \rangle$, respectively.

We have already pointed out that the error is expected to be largest for 2002. However, the large error estimates of Figure 9.11 and Table 9.1 are very conservative. A reason for overestimating the error may be that δt is most difficult to evaluate in 2002, because of the small relative timings. Whether $\delta t^{max} = 0.05$ s or 0.07 s or whether $\delta t^{min} = 0.01$ s instead of 0.03 s is hard to evaluate from the data, but makes a big difference to the error estimates. Therefore, we also show the values according to $\delta t = 0.01$ s and $\delta t = 0.07$ s in Table 9.1.

The choice of $I_{\delta t}$ is uncritical when the separations (and thus the relative timings) are larger. In these case (2003 and 2001), $I_{\delta t}$ is accurately determined and, even more important, variations of a few hundredth of a second do not strongly affect the error estimate. However, we are aware that the multi-spacecraft analysis we carry out is least reliable in 2002, and in addition the statistics are poor (only 33 events). So this particular set of DDs is certainly least relevant for the conclusions of this work related to true multi-spacecraft techniques. In contrast, excellent results are obtained for 2003. These are probably the best normal estimates ever determined for solar wind discontinuities. In addition, the good statistics (204 events) benefit the significance of our conclusions. The configurations present in 2001 yield an intermediate scenario.

Despite the excellent accuracy we achieve in 2003, the velocity error dU is on average still too large to distinguish RDs from TDs by means of propagation (see also section 8.8.6). This can be seen by comparing the observed Alfvén velocities ($|\mathbf{V}_A \cdot \mathbf{n}| < 10$ km/s in most cases in Figure 8.33) to $\langle dU \rangle$ ranging between 11 and 45 km/s in 2003. We point out, however, that here only average values are considered. For individual events the precision can be much better.

9.4 Error of B_n - consistency with the assumption of tangential discontinuities

Based on the measurement of very small normal components B_n of the magnetic field, we suggested in chapter 8 that all observed DDs may be tangential discontinuities. In this section we show that an analysis of the errors of B_n is consistent with that suggestion, albeit not a proof. We analyse the error of $|B_n|/B_{max}$ as a function of δt much in analogy to our previous analysis of \mathbf{n} , and verify consistency of $(\mathbf{V} \cdot \mathbf{n} - U)$ with the assumption of (non-propagating) TDs.

In the previous sections we have discussed the error of the DD normal \mathbf{n} . We have shown that in general the error is anisotropic. For that reason, comparing dn to the measured deviation of θ_{Bn} from 90° cannot answer whether $\theta_{Bn} = 90^\circ$ within error, as required for TDs. Only the component of the error parallel to the magnetic field is relevant. Therefore, we calculate the normalised magnetic field normal component $(\hat{b}_n)_i := (|B_n|/B_{max})_i$ and the angle $(\hat{\theta}_{Bn})_i$ between \mathbf{n} and \mathbf{B} for each of the 1330 $\hat{\mathbf{n}}_i$ for each event. We define $\hat{b}_n^{min} := \min((\hat{b}_n)_i)$ and $\hat{b}_n^{max} := \max((\hat{b}_n)_i)$, and $\hat{\theta}_{Bn}^{min}$ and $\hat{\theta}_{Bn}^{max}$, accordingly. Analogue to equations 9.1-9.4 we then

define:

$$DB_n := \hat{b}_n^{\max} - \hat{b}_n^{\min} \quad (9.5)$$

$$dB_n := \max(|B_n|/B_{\max} - \hat{b}_n^{\min}, \hat{b}_n^{\max} - |B_n|/B_{\max}), \quad (9.6)$$

$$D\theta_{Bn} := \hat{\theta}_{Bn}^{\max} - \hat{\theta}_{Bn}^{\min}, \quad (9.7)$$

$$d\theta_{Bn} := \max(\theta_{Bn} - \hat{\theta}_{Bn}^{\min}, \hat{\theta}_{Bn}^{\max} - \theta_{Bn}) \quad (9.8)$$

i.e., DB_n is the maximal difference found between the 1331 normalised normal components for each event, and dB_n is the maximal difference to the measured normal component $|B_n|/B_{\max}$ according to the normal \mathbf{n} .

A discontinuity is consistent with a TD, if at least one of the $(\hat{b}_n)_i$ is zero (or equivalently $(\hat{\theta}_{Bn})_i = 90^\circ$ for at least one solution $\hat{\mathbf{n}}_i$). The opposite conclusion is strictly speaking incorrect: Since we only calculate a limited number of normals $\hat{\mathbf{n}}_i$ for each DD, a direction in the continuum of normals according to $t_{ij} \pm \delta t$ can exist which is perpendicular to the magnetic field, even if $\hat{b}_n^{\min} \neq 0$. However, because of the high spatial density of the $\hat{\mathbf{n}}_i$ this is unlikely, unless δt is large.

Consistency with $B_n = 0$

Figure 9.12 shows the measured values of $|B_n|/B_{\max}$ (top) and θ_{Bn} (bottom) with error bars for all DDs in our set. The upper and lower boundaries of the error bars are \hat{b}_n^{\max} and \hat{b}_n^{\min} , and $\hat{\theta}_{Bn}^{\max}$ and $\hat{\theta}_{Bn}^{\min}$, respectively. The DDs are sorted in decreasing order of \hat{b}_n^{\min} and increasing order of $\hat{\theta}_{Bn}^{\max}$, respectively.

As already shown in chapter 8, the measured values of $|B_n|/B_{\max}$ are generally close to zero and the measured angles θ_{Bn} are close to 90° . This is particularly apparent for the DDs in 2003. With decreasing spacecraft separations (2001 and 2002) the clearness of this result fades. Figure 9.12 demonstrates that this increase of $|B_n|/B_{\max}$ correlates with the lengths of the error bars. The shown error bar lengths $\langle DB_n \rangle$ and $\langle D\theta_{Bn} \rangle$ are averaged over all DDs in each of the three sets. They clearly increase with decreasing spacecraft separations.³

To provide a point of reference, the value $|B_n|/B_{\max} = 0.4$ (often used as threshold to distinguish between RDs and TDs) is indicated by the horizontal line in Figure 9.12. Only for isolated events (with $P > P_c$ in 2003), \hat{b}_n^{\max} exceeds this value. Even in 2002, where the uncertainty is largest, only for 10 DDs, i.e., less than one third of all events, the maximum possible value within error exceeds 0.4. In general, \hat{b}_n^{\max} is clearly below this threshold.

The error bars of θ_{Bn} are also rather small. The average length is $\langle D\theta_{Bn} \rangle = 11.4^\circ$ in 2003 including DDs with $P > P_c$, and $\langle D\theta_{Bn} \rangle = 24.9^\circ$ in 2002. Most important, the upper boundary is $\hat{\theta}_{Bn}^{\max} = 90^\circ$ in most cases. Accordingly, $\hat{b}_n^{\min} = 0$, i.e., the constraint for consistency with TDs is satisfied. Only for 30 out of the 204 DDs in 2003 ($\approx 15\%$), 26 out of the 129 DDs in 2001 ($\approx 20\%$), and 8 out of 33 DDs in 2002 ($\approx 25\%$), $\hat{b}_n^{\min} \neq 0$ (or $\hat{\theta}_{Bn}^{\max} \neq 90^\circ$) for the δt s used in Figure 9.12.

³Note that these values differ from those in Table 9.2 where only DDs with $P < P_c$ are considered.

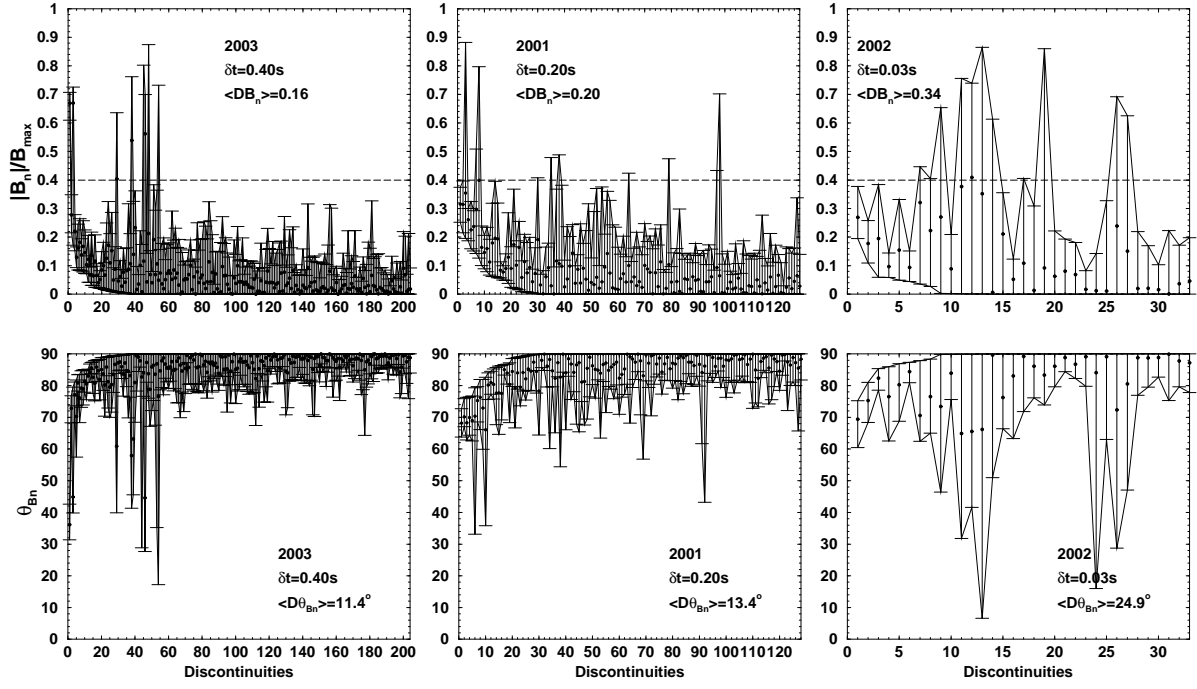


Figure 9.12: $|B_n|/B_{max}$ (top) and θ_{Bn} (bottom) with error bars for all DDs found in 2003 (left), 2001 (middle) and 2002 (right), including those with $P > P_c$. The DDs are sorted in decreasing order of \hat{b}_n^{min} (top) and increasing order of $\hat{\theta}_{Bn}^{max}$ (bottom), respectively. The upper and lower error boundaries are connected by solid lines to guide the eye. The measured values are indicated by circles. $\delta t = 0.4$ s, 0.2 s and 0.03 s for 2003, 2001 and 2002, respectively.

As pointed out in section 9.2, the intervals $I_{\delta t} = [\delta t^{min}, \delta t^{max}]$ do not include all individual uncertainties δt . In some cases, δt can exceed the values used in Figure 9.12. A careful examination of the events with $\hat{b}_n^{min} \neq 0$ for the given values of δt shows that this subset consists exactly of those DDs for which the relative timings are most difficult to determine, and thus δt is large. The reason for the poor correlation of the four time series is mostly a strongly fluctuating background magnetic field. This yields uncertainties δt of more than 1 s in individual cases in 2003.

Hence, considering that δt can be relatively large for individual events, we find that $|B_n|/B_{max} = 0$ and $\theta_{Bn} = 90^\circ$ within error for all DDs in our data set.

Consistency with zero propagation relative to the solar wind plasma

We now demonstrate that also $U = \mathbf{V} \cdot \mathbf{n}$ within error. Figure 9.13 shows the measured DD velocities U relative to Cluster in descending order (blue circles). The error bars are shown for δt^{max} of the particular year. The upper and lower boundaries (\hat{U}_{max} and \hat{U}_{min}) are connected by black lines to guide the eye. Also plotted are \hat{U}_{max} and \hat{U}_{min} for $\delta t = 0.2$ s in 2003, $\delta t = 0.1$ s in 2001 and $\delta t = 0.03$ s in 2002 (green line). Only those DDs are shown for which plasma data are available, in order to allow for comparison with the plasma velocity $\mathbf{V} \cdot \mathbf{n}$ (indicated by the red crosses). The DDs with $P > P_c$ are encircled. The average length of the error bars $\langle DU \rangle$ is shown for each year.⁴

⁴Note that these values differ from those in Table 9.1 where only DDs with $P < P_c$ are considered.

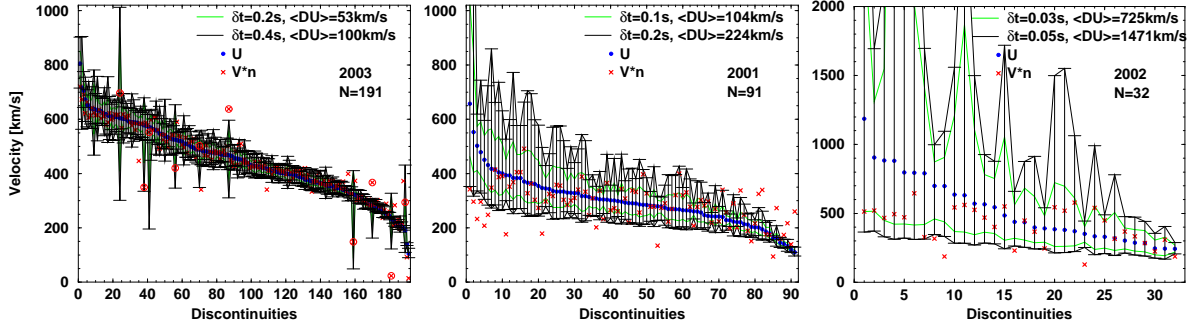


Figure 9.13: Velocity U (blue circles) in decreasing order with error bars for δt^{\max} . From left to right: 2003, 2001, 2002. Also shown are \hat{U}_{\min} and \hat{U}_{\max} for $\delta t = 0.2$ s in 2003, $\delta t = 0.1$ s in 2001 and $\delta t = 0.03$ s in 2002. Only DDs for which plasma data are available are shown. The red crosses indicate the values of $\mathbf{V} \cdot \mathbf{n}$. They are encircled when $P > P_c$.

The error bars show some interesting features: First, DU (see equation 9.3) increases with decreasing spacecraft separation. Second, the error bar length increases with increasing U . This trend is disrupted by some peaks caused by planar spacecraft configurations ($P > P_c$) in 2003. This is in agreement with the conclusions in section 9.2, i.e., that the error is mainly determined by the tetrahedral geometry and by U . Third, the error is asymmetric. As discussed in section 9.1, U is closer to \hat{U}_{\min} than to \hat{U}_{\max} , in general. The smaller the spacecraft separations, the more pronounced is the asymmetry. This is a consequence of increasing $\delta t/t_{ij}$ with decreasing tetrahedra size: The \hat{t}_{ij} in $\hat{U} = \mathbf{r}_{ij} \cdot \mathbf{n}/\hat{t}_{ij}$ can simultaneously get close to zero when $\delta t/t_{ij}$ is large.

For the majority of events, $\mathbf{V} \cdot \mathbf{n}$ is scattered around U within the error bars even for the smaller of the two shown uncertainty δt (green line). Especially in 2003, $\mathbf{V} \cdot \mathbf{n}$ is close to U . Only for 12 out of 191 events (6%), $\mathbf{V} \cdot \mathbf{n}$ is outside the error bars of U for $\delta t = 0.4$ s. Strong deviations between U and $\mathbf{V} \cdot \mathbf{n}$ are primarily observed when U is inaccurately determined.

Because θ_{Bn} is close to 90° , possible propagation velocities are likely to be less than 10 km/s (see previous section). Apparently, the error is larger than that. Note that besides U , also \mathbf{V} and \mathbf{n} are subject to error, not accounted for in Figure 9.13. Thus, all DDs are consistent with being non-propagating structures. In the few cases where $|\mathbf{V} \cdot \mathbf{n} - U|$ is greater than the error, the deviation cannot be explained by propagation, because the difference is too large (on the order of 100 km/s). Probably these large differences are due to a mixture of the named errors. Note, however, that $\mathbf{V} \cdot \mathbf{n}$ is still in the vicinity of \hat{U}_{\min} and \hat{U}_{\max} , respectively, for these DDs, indicating a reasonable choice of δt and thus reasonable error estimates in all three years.

Statistical analysis

Table 9.2 gives an overview of the average values of the used parameters characterising the error of $|B_n|/B_{\max}$ and θ_{Bn} for the same uncertainties δt as in Table 9.1. The average values confirm a small error, particularly in 2003. For instance, $\langle d\theta_{Bn} \rangle$ ranges between 1.7° for $\delta t = 0.1$ s and 6.8° for $\delta t = 0.4$ s, and $\langle dB_n \rangle$ ranges between 0.026 and 0.102 in 2003. Even in 2002 the error decisive for discerning RDs and TDs is moderate. The maximal observed deviation from the measured angle between \mathbf{n} and \mathbf{B} is on average 29° for $\delta t = 0.05$ s, and

Table 9.2: Same as Table 9.1 for $|B_n|/B_{max}$ and θ_{Bn} .

yr	δt	$\langle dB_n \rangle$	$\langle dB_{n95} \rangle$	$\langle DB_n \rangle$	$\langle d\theta_{Bn} \rangle$	$\langle d\theta_{Bn95} \rangle$	$\langle D\theta_{Bn} \rangle$
2003	0.10	0.026(0.014)	0.020(0.010)	0.046(0.025)	1.7(0.9)	1.3(0.7)	3.0(1.6)
	0.20	0.051(0.027)	0.040(0.021)	0.083(0.044)	3.4(1.7)	2.6(1.3)	5.5(2.9)
	0.30	0.077(0.040)	0.059(0.031)	0.114(0.059)	5.1(2.6)	3.9(2.0)	7.6(3.9)
	0.40	0.102(0.053)	0.079(0.041)	0.143(0.072)	6.8(3.5)	5.3(2.7)	9.6(4.8)
2001	0.05	0.032(0.017)	0.024(0.013)	0.056(0.032)	2.1(1.1)	1.6(0.8)	3.7(2.0)
	0.10	0.067(0.040)	0.050(0.029)	0.105(0.060)	4.4(2.6)	3.3(1.8)	7.0(3.8)
	0.15	0.104(0.067)	0.078(0.048)	0.152(0.090)	6.9(4.4)	5.2(3.1)	10(5.8)
	0.20	0.144(0.100)	0.107(0.069)	0.199(0.122)	9.8(6.9)	7.1(4.6)	13(8.3)
2002	0.01	0.074(0.058)	0.056(0.045)	0.123(0.109)	5.1(4.4)	3.8(3.4)	8.6(8.0)
	0.03	0.241(0.171)	0.180(0.131)	0.344(0.236)	18(15)	13(11)	25(20)
	0.05	0.366(0.189)	0.282(0.180)	0.483(0.235)	29(19)	21(16)	37(22)
	0.07	0.502(0.203)	0.373(0.177)	0.628(0.228)	42(20)	29(16)	50(23)

Table 9.3: Measured average values for the same data set as in Table 9.1 and 9.2. $\langle |90^\circ - \theta_{Bn}| \rangle$ is given in degrees and $|\mathbf{V} \cdot \mathbf{n} - U|$ in km/s.

	$\langle B_n /B_{max} \rangle$	$\langle 90^\circ - \theta_{Bn} \rangle$	$ \mathbf{V} \cdot \mathbf{n} - U $
2003	0.049	3.3	19
2001	0.078	5.3	61
2002	0.132	8.6	185

$\langle dB_n \rangle$ is less than 0.4. Note that the values of $\langle d\theta_{Bn} \rangle$ are smaller than the values of $\langle dn \rangle$ in Table 9.1, reflecting the anisotropy of the error. Also note the linear dependence on δt for all parameters in each year of observation.

It is instructive to compare the average error values to the actually measured average values (Table 9.3). Two observations are of interest: (1) The quantities in Table 9.3 increase with decreasing spacecraft separations, i.e., larger errors allow for larger measured values. (2) The measured average quantities are on the order of the associated error values in the low- δt region of the particular year: The values of $\langle |B_n|/B_{max} \rangle$, $\langle 90^\circ - \theta_{Bn} \rangle$ and $\langle \mathbf{V} \cdot \mathbf{n} - U \rangle$ are comparable to the values of $\langle dB_n \rangle$, $\langle d\theta_{Bn} \rangle$ and $\langle dU \rangle$, respectively, for $\delta t = 0.2$ s in 2003. For instance, the measured average deviation of θ_{Bn} from 90° is 3.3° and $\langle d\theta_{Bn} \rangle(\delta t = 0.2 \text{ s}) = 3.4^\circ$. The measured values in 2001 are on the order of their error values for $0.10 \text{ s} < \delta t < 0.15 \text{ s}$ on average, and the corresponding δt is between 0.01 s and 0.03 s in 2002.

Figure 9.14 compares the histograms of the measured values to the histograms of the associated errors. The histograms of the error parameters are shown for the same values of δt as in Figure 9.13. From top to bottom (i.e., with decreasing tetrahedra size) the histograms of the measured quantities widen in the same manner as the width of the histograms of the associated error parameters increases.

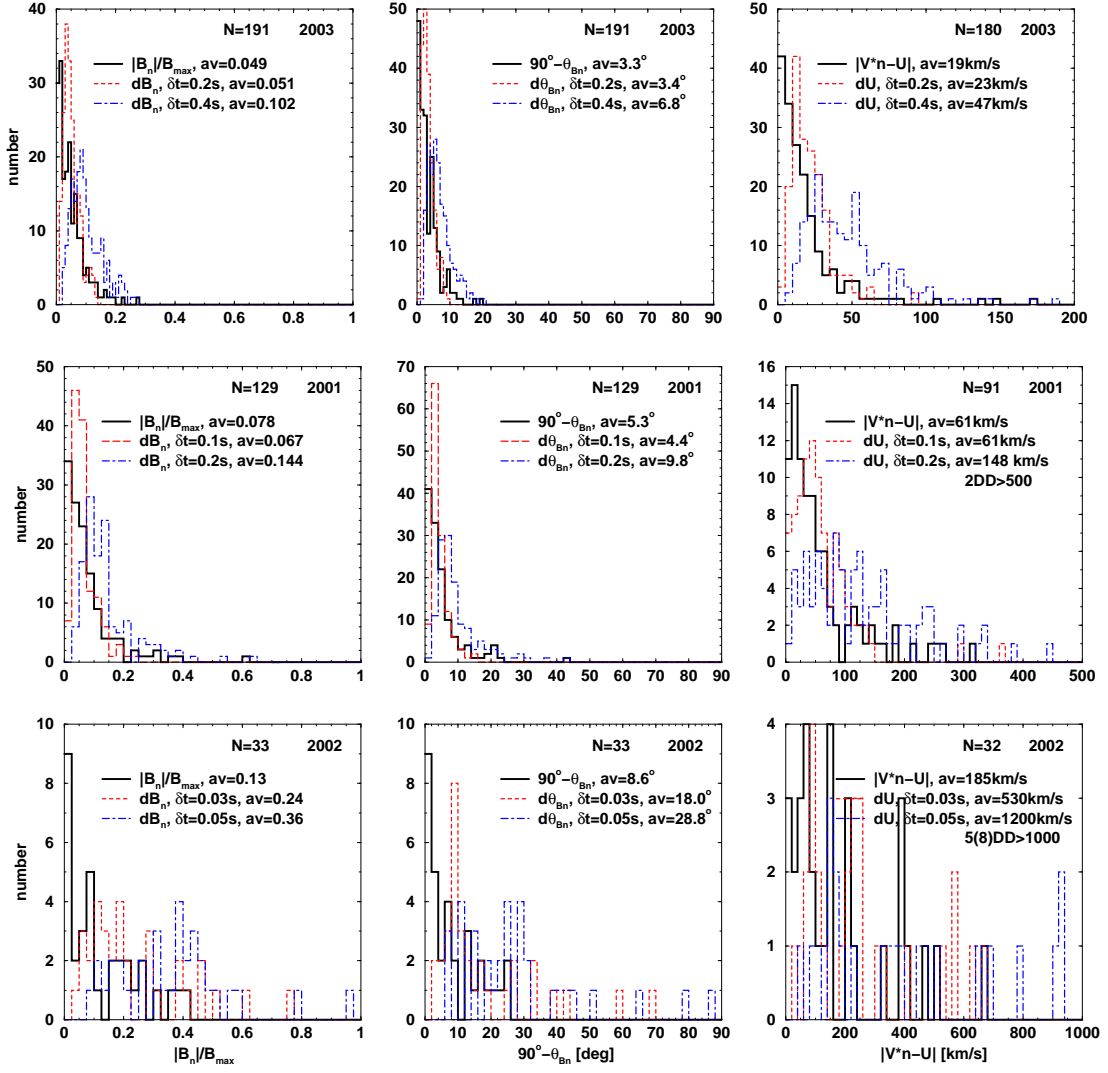


Figure 9.14: Histograms of the measured values of $|B_n|/B_{\max}$, $(90^\circ - \theta_{Bn})$ and $|\mathbf{V} \cdot \mathbf{n} - U|$ (from left to right) compared to the histograms of the associated error values for δt^{\max} and a smaller value of δt . From top to bottom: 2003, 2001, 2002. Only configurations with $P < P_c$ are considered. The histograms of $|\mathbf{V} \cdot \mathbf{n} - U|$ contain only those DDs for which plasma data are available. Note that for these histograms the ranges are different for each year. $dU > 500$ km/s for 2 DDs for $\delta t = 0.2$ s in 2001, and $dU > 1000$ km/s for 5 (8) DDs for $\delta t = 0.03$ s ($\delta t = 0.05$ s) in 2002.

Apparently, the measured values are as large as allowed for by the given error margin. Even the width associated to the lower δt error distribution equals or exceeds the width of the distribution of the measured values. This holds for all shown quantities in each year.

Figure 9.14 suggests that, if we were able to reduce the errors to infinitely small values, then the distributions of the measured values would approach a δ -distribution at zero. Recall that in Figure 8.9 we considered only those DDs for which the relative timings can be determined best, and found the expected tendency. This could be extended, e.g., by additionally requiring excellent tetrahedra qualities.⁵ We have not done this, but we are confident that the widths of the distributions of $|B_n|/B_{\max}$, $(90^\circ - \theta_{Bn})$ and $(\mathbf{V} \cdot \mathbf{n} - U)$ would decrease even more.

⁵Note that the separations between the Cluster spacecraft will be at 10000 km in the solar wind next year (see Figure 4.3). This provides an excellent opportunity to obtain even more accurate triangulation results than in 2003 with a nominal separation of 5000 km.

To conclude, the main result of this section is that the quantities $|B_n|/B_{max}$, $(90^\circ - \theta_{Bn})$ and $(\mathbf{V} \cdot \mathbf{n} - U)$ are all consistent with zero within the error for all DDs, i.e., all events in our set are consistent with being TDs. We have shown that the extent to which the quantities listed above differ from zero is related to the size of the error.⁶ According to these results, it is tempting to conclude that all DDs in our set (and maybe in general) *are* indeed TDs. Other authors (e.g. *Siscoe et al.* [1968]; *Burlaga* [1971b]; *Horbury et al.* [2001b]) conclude that the solar wind is dominated by TDs on grounds of observations less clear than our results. However, we deal with this issue with great care. At last we cannot strictly prove $|B_n|/B_{max} = 0$. Therefore, we have to allow for the possibility of small but finite magnetic field normal components, i.e., we are not able to prove that there are no RDs in our set of DDs in the last consequence (using magnetic field data only). However, we can conclude that if there were RDs, then they would all have extremely small values of $|B_n|/B_{max}$.

⁶Note that we find the same result for the MVA technique: Increasing the accuracy of that method yields smaller values of $|B_n|/B_{max}$ (see chapter 8).

DISCUSSION AND SUMMARY

In this work a statistical analysis of 366 interplanetary discontinuities at 1 AU is presented. It is the first study of this kind based on the simultaneous observation at four nearby spacecraft. Magnetic field and plasma data from the coordinated Cluster spacecraft flying in formation a few hundred to a few thousand kilometres apart are used. In nearly all related investigations the discontinuities have been analysed along the trajectory of only a single satellite. With four measuring platforms the ability to observe is considerably improved. This advantage is versatile. On the one hand, simple comparison of the time series acquired at different locations of the solar wind structures and application of well accepted single-spacecraft analysis techniques already yields surprising new results. On the other hand, by making use of a true multi-spacecraft technique, a completely new understanding of the solar wind micro-structure evolves.

Data set and experimental setup

The 366 DDs in our ensemble are selected by application of frequently used criteria, to provide consistency with previous work. Due to the near-Earth trajectory of the Cluster spacecraft, caution must be exercised to prevent the data from being contaminated by foreshock activity. By applying a rather conservative criterion, we ensure a clean set of discontinuities in the undisturbed solar wind. Unfortunately, this caution also leads to a considerable reduction in number of the original set of events.

The selected DDs are grouped in three sets according to the period of their observation, i.e., January - May of 2001, 2002 and 2003. The main distinction between these three sets is the different spacecraft separation from 100 km in 2002 to 5000 km in 2003, which enables us to investigate interplanetary discontinuities at different scales. For the triangulation method the small separations in 2002 are not of much use, because the small relative timings introduce

large uncertainties. However, to analyse the fluctuations that are superimposed on the pure discontinuities, for example, the variety of scale length is very useful. Triangulation performs best on the 2003 data set, where the separations are large. Probably the accuracy of the normal estimates for many DDs in this set is the highest ever achieved.

The continuous evolution of the tetrahedron built by the four spacecraft along the orbital trajectory can lead to extremely flattened configurations in 2003. To monitor the tetrahedral geometry, we introduce quality factors. Particularly helpful are the 2-D factors planarity and elongation. Based on an error analysis, we determine a cut-off value for the planarity below which satisfactory accuracy is guaranteed.

Another difference between the three sets are the different prevailing solar wind conditions. Whereas predominantly slow streams are observed in 2001, we are able to assign recurring fast streams in 2003 to coronal holes on the Sun. We define a subset of the largest set DD_{2003} (204 events) which contains only DDs in coronal hole streams.

Minimum Variance Analysis is much less reliable than previously assumed

Our analysis demonstrates that the Minimum Variance Analysis (MVA), a widely used analysis technique to compute normals of discontinuities, is much less reliable than previously assumed. Using the data of the four coordinated Cluster spacecraft we determine new criteria to decide whether or not MVA yields reliable normal estimates.

The surface normal of an ideal 1-D MHD discontinuity is well defined as the direction with zero variance of the magnetic field ($\lambda_3 = 0$). Generally, superposed fluctuations yield an increase of λ_3 , and the 1-D structure does not appear as such anymore. Consequently, the accuracy of MVA decreases. The ratio of intermediate to minimum variance (λ_2/λ_3) is an important parameter to assess the reliability of this method. Numerical simulations of an ideal discontinuity superposed by isotropic noise suggest a lower limit of $(\lambda_2/\lambda_3)^L = 1.8$ for MVA to determine sufficiently accurate normal estimates [Lepping and Behannon, 1980]. Accordingly, in most studies on discontinuities $(\lambda_2/\lambda_3)^L = 2$ has been used to ensure reasonable results.

Our analysis shows that this limitation is not strict enough. We conclude that 3-D wave fields also propagating perpendicular to the surface normal and involving non-isotropic fluctuations affect the MVA result, even if $\lambda_2/\lambda_3 > 2$. To prevent MVA normal estimates from being contaminated by wave fields, we suggest applying MVA only if $\lambda_2/\lambda_3 \gtrsim 10$. We point out that besides λ_2/λ_3 , the spreading angle ω is also an important parameter affecting the accuracy of MVA (see also Lepping and Behannon [1980]). In order to *a priori* ensure reasonable MVA results, a preselection of events with $\omega \gtrsim 60^\circ$ appears adequate. Further quality tests (much stricter than in common practice) should then be done by inspecting the eigenvalue ratio λ_2/λ_3 after MVA is performed. Unfortunately these strict requirements entail serious practical consequences as they dramatically reduce the number of DDs suitable for MVA.

Moreover, we show that a large eigenvalue ratio is only a necessary condition for reliable MVA normal estimates, not a sufficient one. Particularly when the intermediate eigenvalue λ_2 of the actual discontinuity is small, the minimum variance direction of the total structure

(discontinuity plus waves) can be determined mainly by superposed fluctuations. According to previous studies, the wave-vector of the superposed fluctuations is likely to be aligned to the mean magnetic field. We do not answer questions regarding the nature and particularly the origin of the superimposed waves. Whether the superposed fluctuations are MHD waves independently existing in the solar wind or the discontinuities generating wave modes of their own is left unanswered. However, a likely explanation is given by *Horbury et al.* [2001b] who suggest that surface waves [Hollweg, 1982] on discontinuity surfaces are responsible for the minimum variance direction not to coincide with the discontinuity normal.

We point out that MVA is a widely-used analysis tool. Therefore, awareness that this method performs poorly in many cases should be of considerable general interest for all communities involved in space plasma physics.

Not a single clear RD is found when timing-derived normals are used

We demonstrate that underestimating the MVA error has resulted in an incorrect understanding of the solar wind micro-structure. There has been a long going controversy about which type of discontinuity is more abundant in the interplanetary medium in the 1970s (and 1980s). Most authors claim a clear dominance of RDs, especially in fast solar wind streams. Others suggest that TDs are more abundant than RDs. However, all single-spacecraft studies have in common that two clearly distinct populations are found: TDs (identified by large magnitude changes of the magnetic field and small B_n) and a considerable number of RDs (large normal component of the magnetic field).

On the basis of the normal component of the magnetic field and the change in field magnitude across the DDs, we classify the selected events into RDs, TDs, EDs and NDs. Utilising MVA to determine the DD normals we end up with a large number of RDs when the same criteria as have been applied in previous studies are used. In fact, the classification into RDs, TDs, EDs and NDs is in good agreement with previous findings.

The timing-derived normals yield strikingly different results: Not a single clear RD is found.

We perform several consistency tests and a detailed error analysis to confirm that the normal components of the magnetic field determined by triangulation are reliable. Moreover, we show that $|B_n|/B_{max} = 0$ within error for all events. Thus, all DDs in our ensemble are consistent with being tangential. We point out that to our knowledge this is in apparent contradiction to all other studies. In addition, we find that the more precisely the normals are determined (both from triangulation and MVA) the more they tend to be perpendicular to the magnetic field. This observation may suggest that perhaps all DDs in our representative ensemble are tangential.

Our analysis reveals that the discrepancy between single and multi-spacecraft results occur when the MVA eigenvalue ratio λ_2/λ_3 (or the spreading angle ω) is small. Using only those DDs for which we assume MVA yields reliable normal estimates, the RD-category remains empty also in the single-spacecraft analysis. In other words, the population of the RD-category is simply a result of unreliable MVA normal estimates.

Being able to estimate the error in the determination of $|B_n|/B_{max}$ associated with MVA we can postulate new criteria to distinguish RDs from TDs in single-spacecraft studies. In previous studies the threshold $b_{nc} = 0.4$ has often been used in combination with $(\lambda_2/\lambda_3)^L = 2$. Our analysis shows that this is definitely overly optimistic; $b_{nc} = 0.6$ appears to be more realistic in that case. Conversely, we suggest that $b_{nc} = 0.4$ may yield meaningful classification results when only DDs with $\lambda_2/\lambda_3 \gtrsim 5$ or $\omega \gtrsim 60^\circ$ are considered.

Hence, by using data from the four spacecraft of the Cluster mission we shed some light on the long-going debate about which type of discontinuity dominates the solar wind. Evidently, the rate of occurrence of clear RDs in the solar wind is far less than was previously assumed. In our representative ensemble it is zero. However, since any method to determine DD normals is subject to error, it is impossible to claim that all events are TDs. The new perception is that all DDs are consistent with being TDs. Since in addition the majority of events have only small field magnitude changes across them, they could as well be RDs propagating almost perpendicular to the magnetic field. Hence, in order to determine the true type of these EDs ($\approx 90\%$ of the total number of DDs), the use of plasma data is necessary.

Using plasma data to identify possible RDs

We test several necessary conditions for RDs. These tests are complicated for instance by poorly determined thermal anisotropies. Because the DD normals are approximately perpendicular to the magnetic field, the normal components of the Alfvén velocity are generally rather small ($|\mathbf{V}_A \cdot \mathbf{n}|$ is less than 10 km/s for most events). Since this is on the order of the accuracy of $\mathbf{V} \cdot \mathbf{n}$ and U in the best cases, testing whether or not the DDs are propagating is difficult.

We find that the majority of events fail the polarisation relation: The magnitude of $[\mathbf{V}]$ is generally smaller than required for RDs from MHD theory. This has been observed in previous studies already (e.g. *Neugebauer et al.* [1984]) and has been a major problem, because according to B_n (derived from MVA) a considerable number of RDs were found. Therefore, the majority of these events were inconsistent with both RDs and TDs. Since all of the DDs in our sample are consistent with TDs, this problem does not occur anymore.

We find some DDs that satisfy the necessary RD conditions. This sample can be regarded as being consistent with RDs. Therefore, we cannot exclude the possibility that there are some RDs with small B_n in the solar wind at 1 AU. However, it may well be that the RD conditions are satisfied only incidentally and that the discontinuities we identify as possible RDs are, in fact, TDs. Furthermore, we point out that the argumentation in *Neugebauer et al.* [1984], who suggest that the majority of EDs are rotational, must be dealt with great care. This reasoning is based on a comparison of the properties found for their EDs with those found for their TDs and RDs. Since their RD population is apparently caused by inaccurate MVA normal estimates, these DDs are probably, in fact, EDs, and the comparison is thus invalid.

Another surprising observation is that possible RDs are predominantly found in stream-stream interaction regions and not in the fast solar wind originating from coronal holes, as previously assumed.

Discussion of the physical implications of our results

Since DDs are known to be a fundamental feature of the interplanetary medium, these new observational results are of considerable importance in many aspects which shall be discussed in the following.

Since all DDs in our sample are consistent with TDs, and the majority of DDs are inconsistent with RDs, it is reasonable to assume that the solar wind is dominated by TDs. This greatly enhances our understanding of the solar wind micro-structure. By definition, the magnetic signature of a TD reveals the crossing of two regions magnetically not connected. In other words, when a TD is observed, the local medium is split into two distinct plasma regions, contrary to an RD. A high occurrence rate of TDs implies that the solar wind is formed of many such regions, with no plasma flow between them. This might have consequences for the diffusion coefficients of energetic particles: *Sari and Ness* [1969] suggest that if DDs are basically tangential, low-energy cosmic rays (kinetic energy $T < 100$ MeV/nucleon) having gyro-radii less than the average discontinuity separation would tend not to be scattered by DDs but rather by the magnetic fluctuations between the DDs. Thus, the mean free path would be much greater than the distance between the DDs. On the other hand, if DDs are rotational, cosmic rays travelling along field lines are likely to encounter and be scattered by them.

Two of the long-standing goals of solar wind research have been to identify and to understand the mechanisms for heating the solar corona and accelerating the solar wind. Among the obstacles to realising these goals are the limitations of coronal observations to remote sensing at a variety of electromagnetic wavelengths and the limitation of direct, in situ measurements of the plasma, fields and waves to distances outside the regions where the heating and acceleration occur. If we accept the premise that most of the DDs observed near 1 AU originate close to the Sun, their properties may help to understand their role in the physics of the corona. An inherent problem is to distinguish those parameters that retain some signature of coronal processes, as opposed to those which are strongly modified by interplanetary processes, such as non-linear dynamics.

Parker [1987; 1990] has suggested that the convection driven, random shuffling of the foot points of closed field lines at the surface of the Sun necessarily leads to the creation of TDs. Bursts of magnetic reconnection across these TDs yield “nanoflares” which are responsible for the development of the hot X-ray corona. Recent observations [*Solanki et al.*, 2003] support this idea. Theorists will want to know on a quantitative level whether such current sheets are common, i.e., whether the heating associated with the dissipation of these currents can account for the observed coronal heating. Since observations of the lower corona are difficult, a quantitative evaluation of TDs in the solar wind might help. The abundance of TDs that we observe at 1 AU may be relevant in this regard. Also the observed distribution

$$\text{number of DDs}(\omega) \propto \exp(-\omega/75^\circ)^2 \quad (10.1)$$

may be looked at from a different perspective now. All previous studies find this distribution or a similar one. The new input from the present work is that the DDs might all be TDs. A reason for the observed decrease with increasing ω could then be that TDs with $\omega = 180^\circ$ are destroyed after reconnection according to *Parker* [1987; 1990] and are thus not observed in the solar wind.

However, we do not know anything about the connection between the TDs in the lower corona and those that we find in the solar wind. Also note that *Parker* [1987; 1990] further suggests that on solar field lines that are open to the solar wind (coronal holes) TDs are less likely to form, because the disturbances created by the shuffling foot points can be carried away by waves. According to our analysis, however, the abundance of TDs is not reduced in coronal hole streams, which one should expect according to *Parker* [1987; 1990].

The most important relevance of our work is perhaps the aspect of using the solar wind as a laboratory for plasma physics, particularly in the context of non-linear dynamic processes. This issue is closely connected to identifying possible mechanisms responsible for the generation and the stability of discontinuities. Ever since the first observations of DDs in 1966, scientists seek to understand why the solar wind is discontinuous. In order to make progress in this regard, naturally the first step must be to acquire reliable observational input on the type of MHD discontinuities present.

Two scenarios are consistent with our results: (1) All DDs are tangential discontinuities. (2) Some of the DDs are rotational discontinuities with vanishing B_n . Scenario (1) is supported by a number of observations. One indication is for instance that the exact result $B_n = 0$ for TDs is approached with increased reliability of the normal estimates. Another argument is that necessary RD conditions may well be satisfied coincidentally. Let us assume that this scenario is correct. In that case the non-linear processes suggested to support RD generation must be regarded as not applicable. Since in particular we do not find clear RDs in coronal hole streams, which are characterised by an abundance of non-linear Alfvén waves, the presently well accepted idea of RDs being an integral part of phase steepened Alfvén waves is at best questionable. Hence, the concept of phase steepening needs to be rethought.

Another possibility would be that RD generation takes place, but any kind of RD is short-lived in the solar wind and is therefore not observed at 1 AU. This, however, is in apparent disagreement with the results of hybrid simulations and is therefore unlikely.

Now let us assume scenario (2) is correct, and the EDs that satisfy the polarisation relation are indeed rotational. Then the question immediately arises, why do they all have such small values of B_n ? Is it because the generation mechanisms are such that RDs with large B_n are not supported? Are all kinds of RDs (with arbitrary B_n) generated, but only those with small B_n survive until they reach 1 AU? Is a dynamic process, that deforms or turns the RD surfaces such that they must have small B_n near the ecliptic, physically possible? These questions, arising from the results presented in this work, are of fundamental importance for the progress of understanding the generation and the dynamics of the solar wind. Certainly, it is beyond the scope of this thesis to answer these questions, but we may contribute some thoughts on them:

Let us assume for a moment that there is indeed a direct connection between Alfvén waves and the generation of RDs. Then, θ_{Bn} being close to 90° for all RDs implies that the wave vectors of the Alfvén waves must also be oriented almost perpendicular to \mathbf{B} . The general belief, however, is that the propagation direction of Alfvén waves in the interplanetary medium is strongly oriented along the ambient magnetic field. Note that this assumption is predominantly based on MVA (see e.g. *Denskat and Burlaga* [1977] and references therein). *Denskat and Burlaga* [1977] study general Alfvénic fluctuations with two spacecraft and find that the distribution of $\angle(\mathbf{n}, \mathbf{B})$ peaks near 90° when the relative timings between the spacecraft are utilised, in contrast to the MVA result. Thus, perhaps our result must be understood to be more general, in the sense that it is not only applicable to discontinuities, but also to other magnetic field fluctuations in the solar wind. According to *Denskat and Burlaga* [1977] the majority of Alfvénic fluctuations are also non-propagating. The question to be answered is, can these “quasi-static” structures phase steepen into RDs?

Since we assume that stream-stream interaction regions are favourable plasma regions to contain possible RDs, future investigations (both experimental and theoretical) should focus on the physical characteristics of these regions when seeking likely generation mechanisms.

The stability of RDs has been the subject of a considerable amount of theoretical work. The hypothesis that RDs with large B_n are generated but short-lived is supported by the hybrid simulations presented by *Richter and Scholer* [1989]. They find that in contrast to RDs with a large magnetic field normal component, RDs with small B_n are long-lived structures. However, more extended simulations show that also RDs with large B_n are stable [*Goodrich and Cargill*, 1991]. Hence, provided that RDs with a large magnetic field normal component are generated near the Sun, they should be observed near 1 AU. Since this is apparently not the case, we must conclude that they are not generated.

The final possibility we mentioned above to explain our observations under assumption (2) is a dynamic process that deforms or turns the RDs such that they have small B_n at the position where we observe them. A reason for such a deformation is suggested by *de Keyser* [2003] who claims that a configuration consisting of a more or less planar RD over large distance scales close to the heliospheric current sheet is not possible, because the RD surface then would cut the current sheet. Since the plasmas on both sides of the “structural TD” have completely different origins, it is unlikely that a common wave would propagate through both. *de Keyser* [2003] suggests that RDs propagating outward along \mathbf{B} could be common near the centre of coronal holes. Since such RDs do not cut the heliospheric current sheet, their shape must rapidly deform and necessarily be almost parallel to the sector boundary yielding \mathbf{n} to be nearly perpendicular to \mathbf{B} .

However, this type of argumentation may hold for the events observed in the slow solar wind in 2001, but not for the events found within coronal hole streams, where Cluster is far away from the heliospheric current sheet. Since we also invariably find small normal field components for the latter DDs, this explanation is insufficient to explain all the characteristics of our observations

According to the above discussion the most likely interpretation of our observational results is that RDs (with large B_n) are not generated at all.

As a matter of course, the question also arises, what causes the high occurrence rate of TDs? If indeed most (or all) DDs are tangential, then the TD occurrence rate is one to two per hour. The problem of finding suitable TD generation mechanisms appears to be particularly challenging for the fast streams emanating from coronal holes on the Sun.

Further results

Utilising the enhanced possibility of the four-spacecraft Cluster mission, we also tackle other problems:

- A more reliable determination of the discontinuity thickness is possible. However, our results are basically in good agreement with previous single-spacecraft studies. In particular, we can confirm that the width of the thinnest observed DDs is a few proton gyro-radii.
- The high accuracy of the DD normals principally allows for an enhanced description of the DD orientation in space. We find that the normals tend to be in the ecliptic plane and perpendicular to the local magnetic field. We point out, however, that our results may be biased due to the selection criteria regarding the foreshock region. Since application of the cross product method to determine the surface normals appears justified (because B_n is small), one may rely on previous studies using this technique. They find that the most likely orientation in the ecliptic plane is perpendicular to the Parker spiral.
- Another consequence of the inaccurate MVA normals is that attempts to assess large scale curvature of DD surfaces must be carefully interpreted. We claim that MVA may not be appropriate of determining a typical degree of surface curvature. It is not possible to differentiate between true large scale curvature, inaccurate MVA normals or ripples on otherwise planar structures. However, we are rather certain that the assumption of planar DDs on the Cluster separation scale is well justified.

Final remarks

The observations and conclusions presented in this work suggest that an appropriate model for discontinuities in the interplanetary medium is a 1-D structure that is planar on the Cluster separation scale on which non-ideal wave fields in the sense of non-isotropic fluctuations are superposed.

We believe that the results presented in this work justify the proposition for an interplanetary multi-spacecraft mission operating permanently in the solar wind. As Cluster, this mission should consist of at least four spacecraft with variable separations.¹ Then, many things that have been done with only a single spacecraft could be repeated with reliable surface normals. It would be interesting, for instance, whether or not the orientations of consecutive DDs are related to each other. Analysis of that kind is important to better understand the topology of

¹Ideally the mission should consist of two or more sets of “Clusters” with variable separations between the sets, to allow for large scale studies.

the interplanetary magnetic field and would also contribute to understanding the discontinuous nature of the solar wind. Another requirement would be to have excellent plasma data that for instance would also allow determining the chemical compositions on both sides of the DDs. This would considerably facilitate the classification into RDs and TDs.

The main focus of the present work is a thorough analysis of multi-point solar wind observations, incorporating many technical details. We considerably contribute to understanding the solar wind micro-structure. This work is of great interest in that it evidently abandons misconceptions that persisted for over three decades. However, it can only be understood as a first step. The next and decisive step is to build a theoretical framework which is consistent with the observations. For instance, a definite proposition on the stability of RDs (with large B_n) is mandatory. If the present status is correct, i.e., RDs are long-lived structures, then theory needs to establish generation processes that produce only RDs with small normal components of the magnetic field.

Also the question regarding particular solar wind structures that are likely to contain RDs is of interest. We assume stream-stream interaction regions to be important and propose an extended study (only one spacecraft is needed) to verify this assumption. In addition, the work of *Lyu* [2003] may provide a theoretical framework.

The other possibility that becomes increasingly tempting in the course of this work is that the solar wind contains no RDs at all. The possible impact of this conclusion on, for instance, the heating of the solar corona and the acceleration of the solar wind, or the propagation of cosmic rays on their way through the heliosphere is beyond the scope of this work. In any case, it appears worthwhile to investigate these questions in the light of our conclusions.

MATHEMATICS OF A TETRAHEDRON

To calculate the 1-D quality factors Q_{GM} , Q_{RR} and Q_{R8} (equations 5.1, 5.2 and 5.4), the geometrical properties of a tetrahedron need to be studied. The summary we present here is based on *Daly* [1994].

Consider the tetrahedron defined by four points in space numbered 1 to 4, with position vectors \mathbf{r}_1 , \mathbf{r}_2 , \mathbf{r}_3 , \mathbf{r}_4 . Without any loss of generality, we may consider only the differences $\mathbf{d}_\alpha = \mathbf{r}_\alpha - \mathbf{r}_4$ in describing the points.

A.1 Area of the sides

The area S of a parallelogram bounded by two vectors \mathbf{d}_1 and \mathbf{d}_2 is given by the magnitude of their cross product. Any triangle is half of a parallelogram, so its area is

$$S = \frac{1}{2} |\mathbf{d}_1 \times \mathbf{d}_2|$$

where \mathbf{d}_1 and \mathbf{d}_2 are the vectors for any two sides of the triangle.

We specify side α of the tetrahedron to be the one opposite vertex α , i.e. it does not contain the point α . The areas of the four sides of the tetrahedron are then given by

$$S_1 = \frac{1}{2} |\mathbf{d}_2 \times \mathbf{d}_3| \tag{A.1}$$

$$S_2 = \frac{1}{2} |\mathbf{d}_1 \times \mathbf{d}_3| \tag{A.2}$$

$$S_3 = \frac{1}{2} |\mathbf{d}_1 \times \mathbf{d}_2| \tag{A.3}$$

$$S_4 = \frac{1}{2} |(\mathbf{d}_2 - \mathbf{d}_1) \times (\mathbf{d}_3 - \mathbf{d}_1)| = \frac{1}{2} |\mathbf{d}_1 \times \mathbf{d}_2 + \mathbf{d}_2 \times \mathbf{d}_3 + \mathbf{d}_3 \times \mathbf{d}_1| \tag{A.4}$$

The total surface S is the sum $\sum_{\alpha=1}^4 S_{\alpha}$.

A.2 Volume of the tetrahedron

The volume V of a parallelepiped defined by three vectors in space is the triple product of those vectors. Any tetrahedron is $1/6$ of such a figure, hence

$$V = \frac{1}{6} |\mathbf{d}_1 \cdot \mathbf{d}_2 \times \mathbf{d}_3| \quad (\text{A.5})$$

A.3 Circumscribing sphere

To find the circumscribing sphere, we need the point that is equidistant from all four vertices, i.e. we want \mathbf{r} such that

$$(\mathbf{r} - \mathbf{r}_{\alpha}) \cdot (\mathbf{r} - \mathbf{r}_{\alpha}) = r^2 - 2\mathbf{r} \cdot \mathbf{r}_{\alpha} + r_{\alpha}^2 = \rho^2 \quad \text{for } \alpha = 1 \text{ to } 4$$

If we take point 4 as the origin, i.e. if we use the \mathbf{d}_{α} vectors in place of the \mathbf{r}_{α} , then $r^2 = \rho^2$ and this equation reduces to

$$2\mathbf{r} \cdot \mathbf{d}_{\alpha} = d_{\alpha}^2 \quad \text{for } \alpha = 1 \text{ to } 3 \quad (\text{A.6})$$

This matrix equation can be solved for the vector \mathbf{r} and the radius of the sphere $\rho^2 = r^2$. The volume V_0 of the circumscribing sphere is then

$$V_0 = \frac{4}{3} \pi \rho^3 \quad (\text{A.7})$$

A.4 The regular tetrahedron

The regular tetrahedron of unit side is the ideal against which the true figure of the four spacecraft is to be measured. All relevant quantities can easily be derived from the equations above. They are listed in Table A.1.

Table A.1: Values for the regular tetrahedron of unit side.

Quantity	Value
S_{α}	$\sqrt{3}/4$
S	$\sqrt{3}$
V	$\sqrt{2}/12$
ρ	$\sqrt{6}/4$
V_0	$\frac{4}{3} \pi \left(\frac{3}{8}\right)^{\frac{3}{2}}$

A.5 Calculating the quality factors Q_{GM} , Q_{RR} and Q_{R8}

The quality factors in equations 5.1, 5.2 and 5.4 can now easily be calculated from the above quantities.

For Q_{GM} the true volume and the true surface are needed. They are found from equations A.5 and A.1 - A.4, respectively. To get the side L of the “ideal” regular tetrahedron we average the 6 distances between the 4 points. The “Ideal Volume” and the “Ideal Surface” are then given by $V_{ideal} = L^3\sqrt{2}/12$ and $S_{ideal} = L^2\sqrt{3}$, respectively. Then we can express Q_{GM} as:

$$Q_{GM} = \frac{V}{V_{ideal}} + \frac{S}{S_{ideal}} + 1 \quad (\text{A.8})$$

The calculation of Q_{R8} (equation 5.4) is according to this.

For Q_{RR} the radius of the circumscribing sphere is calculated from equation A.6. The “Sphere Volume” is then obtained from equation A.7. For a regular tetrahedron $Q_{RR} \stackrel{!}{=} 1$. Thus, substituting $V = \sqrt{2}/12$ and $\rho = \sqrt{6}/4$ from Table A.1 into equation 5.2 and setting $Q_{RR} = 1$ we get

$$\mathcal{N} = \left(\frac{9\pi}{2\sqrt{3}} \right)^{\frac{1}{3}}. \quad (\text{A.9})$$

The actual volume of the sphere need not be calculated. The constant factors in equation A.7 can be included in the normalisation factor \mathcal{N} . Then we get

$$Q_{RR} = \left(\frac{9\sqrt{3}}{8} V \right)^{\frac{1}{3}} \cdot \rho^{-1} \quad (\text{A.10})$$

APPENDIX B

TABLES

Table B.1: *Minimum, Maximum and average separation between the six pairs of spacecraft in km.*

2001	D_{12}	D_{13}	D_{14}	D_{23}	D_{24}	D_{34}
Min	827	479	828	1066	1069	370
Max	1111	744	1028	1303	1309	701
Ave	1043	637	967	1232	1236	539
2002	D_{12}	D_{13}	D_{14}	D_{23}	D_{24}	D_{34}
Min	137	136	81	180	179	64
Max	186	173	121	225	224	120
Ave	177	165	108	213	212	92
2003	D_{12}	D_{13}	D_{14}	D_{23}	D_{24}	D_{34}
Min	3097	3328	3278	2704	3230	3263
Max	4845	5687	8640	4311	4799	4605
Ave	3592	3769	4734	3428	3661	3981

Table B.2: *RD:TD:ED:ND Percentages from this work. MVA results from the individual spacecraft are shown. Deviations from 100 are due to truncation errors.*

DD_{2001}	DDs	RD:TD:ED:ND	R/T	DD_{2002}	DDs	RD:TD:ED:ND	R/T
All	432	35:16:47:2	2.1	All	113	42: 6:48:4	6.7
CI1	109	35:17:47:1	2.0	CI1	28	43: 7:46:4	6.0
CI2	106	28:15:53:4	1.9	CI2	28	43: 4:50:4	12.0
CI3	106	37:16:44:3	2.3	CI3	27	37:11:44:7	3.3
CI4	111	38:16:44:2	2.3	CI4	30	43: 3:50:3	13.0
DD_{2003}	DDs	RD:TD:ED:ND	R/T	DD_{2003CH}	DDs	RD:TD:ED:ND	R/T
All	698	42: 9:48:1	4.5	All	282	37:11:49:3	3.3
CI1	180	42: 8:48:1	5.1	CI1	71	34:10:54:3	3.4
CI2	175	41:10:49:1	4.2	CI2	71	41:13:45:1	3.2
CI3	168	38:10:51:1	3.8	CI3	71	34:13:51:3	2.7
CI4	175	46: 9:43:2	5.3	CI4	69	39:10:45:6	3.9

MVA ERROR ANALYSIS

This appendix contains additional approaches, to those presented in section 7.2.2, to assess the uncertainty of MVA.

Standard differential approach

Sonnerup [1971] uses a standard differential approach. The angular error estimate for \mathbf{x}_3 is proposed to consist of the angular change produced by changing the minimum variance away from λ_3 by the amount $\Delta\lambda_3$ given by

$$|\Delta\lambda_3|^2 = \frac{1}{(N-1)N} \sum_{i=1}^N [(\mathbf{B}^i \cdot \mathbf{n} - \langle \mathbf{B} \rangle \cdot \mathbf{n})^2 - \lambda_3]^2 \quad (\text{C.1})$$

i.e. $(\Delta\lambda_3)^2$ is taken to be the variance of the N individual measurements $(\mathbf{B}^i \cdot \mathbf{n} - \langle \mathbf{B} \rangle \cdot \mathbf{n})^2$ of λ_3 divided by $(N-1)$ [*Sonnerup*, 1971]. From the two conditions

$$(\mathbf{x}_3 + \Delta\mathbf{x}_3) \mathbf{M}^B (\mathbf{x}_3 + \Delta\mathbf{x}_3) = \lambda_3 + \Delta\lambda_3 \quad (\text{C.2})$$

$$(\mathbf{x}_3 + \Delta\mathbf{x}_3)^2 = 1 \quad (\text{C.3})$$

one then finds in second order

$$|\Delta\lambda_3| = (\Delta x_{31})^2 (\lambda_1 - \lambda_3) + (\Delta x_{32})^2 (\lambda_2 - \lambda_3) \quad (\text{C.4})$$

where Δx_{3j} denotes the j -component of $\Delta\mathbf{x}_3$. Note that the covariant matrix \mathbf{M}^B remains undisturbed. Equation C.4 describes an error cone of elliptical cross section with the minor semi-axis of length

$$|\Delta x_{31}| = [|\Delta\lambda_3| / (\lambda_1 - \lambda_3)]^{\frac{1}{2}} \quad (\text{C.5})$$

along \mathbf{x}_1 and the major semi-axis of length

$$|\Delta x_{32}| = [|\Delta \lambda_3|/(\lambda_2 - \lambda_3)]^{\frac{1}{2}} \quad (\text{C.6})$$

along \mathbf{x}_2 . Note that the error explicitly depends on the eigenvalue separations $(\lambda_2 - \lambda_3)$ and $(\lambda_1 - \lambda_3)$ and that the error is asymmetric for $\lambda_1 \neq \lambda_2$. As expected from the discussion in the previous section, the error is larger along \mathbf{x}_2 than along \mathbf{x}_1 , indicating that the largest uncertainties in the normal vector are associated with rotations of that vector about \mathbf{x}_1 . The values $|\Delta x_{31}|$ and $|\Delta x_{32}|$ from equations C.5 and C.6, respectively can then be used to calculate $|\Delta \langle \mathbf{B} \cdot \mathbf{x}_3 \rangle|$ [Sonnerup, 1971].

Hoppe et al. [1981]

We only briefly mention *Hoppe et al. [1981]*. They present a qualitative discussion of the angular uncertainties in \mathbf{x}_3 and suggest

$$|\Delta x_{3j}| = \tan^{-1}[\lambda_3/(\lambda_j - \lambda_3)], \quad j = 1, 2 \quad (\text{C.7})$$

i.e. the error is solely determined by the eigenvalues.

Bootstrap method

Another interesting concept is the *bootstrap method* [Efron, 1979]. *Kawano and Higuchi [1995]* introduce the application of that method to the estimation of the error in MVA. A *bootstrap sample* is generated by drawing successively N vectors with replacement from the measured set of N vectors. Thereby each of the N vectors from which to be drawn has the same probability to be chosen. The resulting bootstrap sample may contain identical vectors so that a sample usually does not contain all the measured vectors. A large number ($K \geq 10^3$) of bootstrap samples is generated in this fashion and each of these randomised samples is subjected to MVA, producing a set of K minimum variance eigenvectors \mathbf{x}_3 and corresponding normal-field components $\langle \mathbf{B} \rangle \cdot \mathbf{x}_3$. The distribution of these quantities can then be statistically characterised, and the standard deviation may be used as an error estimate.

GENERALISED FORMALISM OF THE RELATIVE TIMING TECHNIQUE

Harvey [1998] presents a treatment of determining \mathbf{n} and U from the simultaneous observation of a discontinuity at $N \geq 4$ spacecraft which is formulated by means of the volumetric tensor (equation 5.5 chapter 5). It is a homogeneous least squares method.

Considering a cluster of $N \geq 4$ spacecraft the positions \mathbf{r}_α of the spacecraft can be expressed relative to their mean position, i.e. the mesocentre (equation 5.6 in chapter 5). Then,

$$\sum_{\alpha=1}^N \mathbf{r}_\alpha = \mathbf{0} \quad (\text{D.1})$$

The time of observation on spacecraft α is denoted by t_α . The “best” values of \mathbf{n} and U are determined by minimising the expression

$$S = \sum_{\alpha=1}^N [\mathbf{n} \cdot \mathbf{r}_\alpha - U(t_\alpha - t_0)]^2 \quad (\text{D.2})$$

where t_0 is some origin of time. Dividing the above equation by U^2 and using $\mathbf{m} = \mathbf{n}/U$, the only undetermined quantities are t_0 and the three components m_k of the vector \mathbf{m} . Minimising S by putting $\partial S / \partial t_0 = 0$ and $\partial S / \partial m_k = 0$ and using equation D.1 yields¹ (see *Harvey* [1998])

$$t_0 = \frac{1}{N} \sum_{\alpha=1}^N t_\alpha \quad (\text{D.3})$$

i.e. t_0 is simply the time at which the mesocentre of the polyhedron crosses the discontinuity; and

$$m_j R_{jk} = \frac{1}{N} \sum_{\alpha=1}^N t_\alpha r_{\alpha k} \quad (\text{D.4})$$

¹Note that we use the summation convention as described in chapter 5.

where R_{jk} is the volumetric tensor as defined in equation 5.8. Provided that $|R| \neq 0$ the inverse of the volumetric tensor exists and satisfies $R_{jk}R_{kl}^{-1} = \delta_{jl}$, where δ_{jl} is the Kronecker delta. Then equation D.4 may be solved to give

$$m_l = \frac{1}{N} \left(\sum_{\alpha=1}^N t_{\alpha} r_{\alpha k} \right) R_{kl}^{-1} \quad (\text{D.5})$$

Note that this solution for $\mathbf{m} = \mathbf{n}/U$ only contains absolute spacecraft positions and absolute crossing times, in contrast to equation 7.10 where only differences in position and time are used. In general, it is easier to determine time delays of the observations made on one spacecraft with respect to those made on each of the other spacecraft (as we do). With N spacecraft, this yields $N(N-1)/2$ time delays $t_{\alpha\beta} = t_{\alpha} - t_{\beta}$, with $1 \leq \alpha \leq N$ and $1 \leq \beta < \alpha$. Minimising

$$S = \sum_{\alpha=1}^N \sum_{\beta=1}^N [\mathbf{n} \cdot (\mathbf{r}_{\alpha} - \mathbf{r}_{\beta}) - U t_{\alpha\beta}]^2 \quad (\text{D.6})$$

\mathbf{n} and U can be determined using relative positions and timings. This ansatz yields (see *Harvey* [1998])

$$m_l = \frac{1}{N^2} \left[\sum_{\alpha \neq \beta} t_{\alpha\beta} (r_{\alpha k} - r_{\beta k}) \right] R_{kl}^{-1} \quad (\text{D.7})$$

provided that $|R| \neq 0$. The symbol $\sum_{\alpha \neq \beta}$ indicates summation over the $N(N-1)/2$ (and not $N(N-1)$) terms with $\alpha \neq \beta$.

Note that the condition

$$t_{\alpha\beta} + t_{\beta\gamma} + t_{\gamma\alpha} = 0 \quad (\text{D.8})$$

may or may not be satisfied exactly for $\alpha \neq \beta \neq \gamma \neq \alpha$, i.e. the time differences can be mutually inconsistent. If condition D.8 is satisfied for all values of α , β and γ the information from all $N(N-1)/2$ time differences are redundant. In that case there are only $N-1$ independent time offsets $t_{\alpha\beta}$, and for $N=4$ the least squares method is formally identical to the method we use (equation 7.10). A failure of this consistency check would mean that at least one of our assumptions, the planarity of the discontinuity or the uniformity of the motion, is not valid. Another possibility would be that the time delays are not determined accurately. In either case application of relative timing methods is not advisable. However, since the method presented by *Harvey* [1998] uses six instead of three time differences it may be less sensitive to errors made in determining the precise timings to the extent that these relative timings are determined with statistically independent errors.

Bibliography

- Andretta, V. and H. P. Jones**, On the role of the solar corona and transition region in the excitation of the spectrum of neutral helium, *Astrophys. J.*, 489, 375–394, 1997.
- Arge, C. N. and V. J. Pizzo**, Space weather forecasting at NOAA/SEC using the Wang-Sheeley model, in *Astronomical Society of the Pacific Conference Series*, 423–430, 1998.
- Balogh, A. et al.**, The cluster magnetic field investigation, *Space Sci. Rev.*, 79, (1/2), 65–91, 1997.
- Balogh, A. et al.**, The Cluster magnetic field investigation: overview of in-flight performance and initial results, *Ann. Geophysicae*, 19, (10-12), 1207–1217, 2001.
- Bame, S. J., J. R. Asbridge, W. C. Feldmann and J. T. Gosling**, Evidence for a structure-free state at high solar wind speeds, *J. Geophys. Res.*, 82, (10), 1487–1492, 1977.
- Barnstorff, H.**, *Stromschichten im interplanetaren Raum*, Dissertation, TU Braunschweig, Braunschweig, 1980.
- Belcher, J. W.**, Statistical properties of interplanetary microscale fluctuations, *J. Geophys. Res.*, 80, (34), 4713, 1975.
- Belcher, J. W. and L. Davis Jr.**, Large-amplitude Alfvén waves in the interplanetary medium, 2, *J. Geophys. Res.*, 76, (16), 3534, 1971.
- Belcher, J. W. and C. V. Solodyna**, Alfvén waves and directional discontinuities in the interplanetary medium, *J. Geophys. Res.*, 80, (1), 181, 1975.
- Biermann, L.**, Kometenschweife und solare Korpuskularstrahlung, *Z. f. Astrophysik*, 29, 274–286, 1951.
- Brajsa, R. et al.**, Helium 1083 Å measurements of the sun, *Solar Physics*, 163, 79–91, 1996.

- Burlaga, L. F.**, Micro-scale structures in the interplanetary medium, *Solar Physics*, 4, 67–92, 1968.
- Burlaga, L. F.**, Directional discontinuities in the interplanetary magnetic field, *Sol. Physics*, 7, 54, 1969a.
- Burlaga, L. F.**, Large velocity discontinuities in the solar wind, *Sol. Physics*, 7, 72–86, 1969b.
- Burlaga, L. F.**, Hydromagnetic waves and discontinuities in the solar wind, *Space Sci. Rev.*, 12, 600–657, 1971a.
- Burlaga, L. F.**, Nature and origin of directional discontinuities in the solar wind, *J. Geophys. Res.*, 76, (19), 4360–4365, 1971b.
- Burlaga, L. F. and N. F. Ness**, Tangential discontinuities in the solar wind, *Sol. Physics*, 9, 467–477, 1969.
- Burlaga, L. F., J. F. Lemaire and J. M. Turner**, Interplanetary current sheets at 1 AU, *J. Geophys. Res.*, 82, (22), 3191–3200, 1977.
- Buti, B.**, Stochastic and coherent processes in space plasmas, in *Cometary and Solar Plasma Physics*, edited by B. Buti, 221, World Scientific, Singapore, 1988.
- Cargill, P. J.**, Hybrid simulations of tangential discontinuities, *Geophys. Res. Lett.*, 17, (8), 1037–1040, 1990.
- Cargill, P. J. and T. E. Eastman**, The structure of tangential discontinuities 1. Results of hybrid simulations, *J. Geophys. Res.*, 96, (A8), 13763–13779, 1991.
- Carrington, R. C.**, Description of a singular appearance seen in the sun on September 1, 1859, *Monthly Notices of the Roy. Astron. Soc.*, 20, 13, 1859.
- Chanteur, G.**, Spatial interpolation for four spacecraft: Theory, in *Analysis Methods for Multi-Spacecraft Data*, edited by G. Patschmann and P. W. Daly, 349–369, ISSI, Bern, Switzerland, 1998.
- Chanteur, G.**, Four spacecraft determination of wave front normals and velocities, *Spatio-Temporal Analysis and Multipoint Measurements in Space*, Orléans, France, 2003.
- Chanteur, G. and C. C. Harvey**, Spatial interpolation for four spacecraft: Application to magnetic gradients, in *Analysis Methods for Multi-Spacecraft Data*, edited by G. Patschmann and P. W. Daly, 371–393, ISSI, Bern, Switzerland, 1998.
- Chanteur, G. and F. Mottez**, Geometrical tools for cluster data analysis, in *Proceedings of the Spatio-Temporal Analysis for Resolving plasma Turbulence (START) conference*, ESA WPP-047, 341–344, ESA, Paris, France, 1993.
- Colburn, D. S. and C. P. Sonett**, Discontinuities in the solar wind, *Space Sci. Rev.*, 5, 439–506, 1966.

- Credland, J., G. Mecke and J. Ellwood**, The cluster mission: ESA's spacefleet to the magnetosphere, in *The Cluster and the Phoenix Missions*, edited by C. P. Escoubet, C. T. Russell, and R. Schmidt, 33–64, Kluwer Academic Publishers, Dordrecht, 1997.
- Daly, P. W.**, The tetrahedron quality factors of CSDS, technical Report MPAe-W-100-94-27, Max-Planck-Institut für Aeronomie, Kaltenburg-Lindau, Germany, 1994.
- Daly, P. W.**, Users guide to the Cluster science data system, DS-MPA-TN-0015, Max-Planck-Institut für Aeronomie, Kaltenburg-Lindau, Germany, 2002.
- DDID**, Data Delivery Interface Document for the Cluster Data Disposition System, CL-ESC-ID2001, ESOC, Darmstadt, Germany, 2000.
- de Keyser, J.**, *Private Communications*, 2003.
- de Keyser, J., M. Roth and A. Söding**, Flow shear across solar wind discontinuities: WIND observations, *Geophys. Res. Lett.*, 25, (14), 2649–2652, 1998.
- Delaboudinière, J. P. et al.**, EIT: Extreme-ultraviolet imaging telescope for the SOHO mission, *Solar Physics*, 162, 291–312, 1995.
- Denskat, K. U. and L. F. Burlaga**, Multispacecraft observations of microscale fluctuations in the solar wind, *J. Geophys. Res.*, 82, (19), 2693–2704, 1977.
- Domingo, V., B. Fleck and A. I. POLAND**, The SOHO mission: An overview, *Solar Physics*, 162, 1–37, 1995.
- Dunlop, M. W. and T. I. Woodward**, Multi-spacecraft discontinuity analysis: Orientation and motion, in *Analysis Methods for Multi-Spacecraft Data*, edited by G. Patschmann and P. W. Daly, 271–305, ISSI, Bern, Switzerland, 1998.
- Dunlop, M. W., T. I. Woodward, D. J. Southwood, K. H. Glassmeier and R. Elphic**, Merging 4 spacecraft data: Concepts used for analysing discontinuities, *Adv. Space Res.*, 20, 1101–1106, 1997.
- Dunlop, M. W., A. Balogh, P. Cargill, R. C. Elphic, K. H. Fornacon, E. Georgescu, F. Sedgemore-Schulthess and the FGM team**, Cluster observes the Earth's magnetopause: coordinated four-point magnetic field measurements, *Ann. Geophysicae*, 19, 1449–1460, 2001.
- Dunlop, M. W., A. Balogh and K. H. Glassmeier**, Four-point Cluster application of magnetic field analysis tools: The discontinuity analyzer, *J. Geophys. Res.*, 107, (A11), 1385, doi:10.1029/2001JA005089, 2002.
- Efron, B.**, Bootstrap methods: Another look at the jackknife., *Annals of Statistics*, 7, 1–26, 1979.
- Escoubet, C. P., R. Schmidt and M. L. Goldstein**, Cluster - science and mission overview, in *The Cluster and the Phoenix Missions*, edited by C. P. Escoubet, C. T. Russell, and R. Schmidt, 11–32, Kluwer Academic Publishers, Dordrecht, 1997.

- Escoubet, C., M. Fehringer and M. Goldstein**, The Cluster mission, *Ann. Geophysicae*, 19, (10-12), 1197–1200, 2001.
- Fairfield, D. H.**, Average and unusual locations of the Earth's magnetopause and bow shock, *J. Geophys. Res.*, 76, (28), 6700, 1971.
- Feldman, W. C., J. R. Asbridge, S. J. Bame and M. D. Montgomery**, Double ion streams in the solar wind, *J. Geophys. Res.*, 78, 2017, 1973.
- Fränz, M.**, *Private Communications*, 2004.
- Gloeckler, G. et al.**, Investigation of the composition of solar and interstellar matter using solar wind and pickup ion measurements with SWICS and SWIMS on the ACE spacecraft, *Space Sci. Rev.*, 86, (1), 497–539, 1998.
- Goldstein, B. E., M. Neugebauer and E. J. Smith**, Alfvén waves, alpha particles, and pickup ions in the solar wind, *Geophys. Res. Lett.*, 22, (23), 3389–3392, 1995.
- Goodrich, C. C. and P. J. Cargill**, An investigation of the structure of rotational discontinuities, *Geophys. Res. Lett.*, 18, (1), 65–68, 1991.
- Haaland, S. E. et al.**, Four-spacecraft determination of magnetopause orientation, motion and thickness: comparison with results from single-spacecraft methods, *Ann. Geophysicae*, 22, 1347–1365, 2004.
- Hanstein, T., H. Eilenz and K.-M. Strack**, Einige Aspekte der Aufbereitung von LOTEM Daten, in *Protokoll über das 11. Kolloquium 'Elektromagnetische Tiefenforschung'*, edited by V. Haak and J. Homilius, 319–328, Lehrbach bei Köln, 1986.
- Hapgood, M. A.**, Space physics coordinate transformations: A user guide, *Planet. Space Sci.*, 40, (5), 711–717, 1992.
- Harvey, C. C.**, Spatial gradients and the volumetric tensor, in *Analysis Methods for Multi-Spacecraft Data*, edited by G. Patschmann and P. W. Daly, 307–322, ISSI, Bern, Switzerland, 1998.
- Hathaway, D. H., R. M. Wilson and E. J. Reichmann**, A synthesis of solar cycle prediction techniques, *J. Geophys. Res.*, 104, (A10), 22375–22388, 1999.
- Hodgson, R.**, On a curious appearance seen in the sun, *Monthly Notices of the Roy. Astron. Soc.*, 20, 15, 1859.
- Ho, C. M., B. T. Tsurutani, B. E. Goldstein, J. L. Phillips and A. Balogh**, Tangential discontinuities at high heliographic latitudes ($\sim -80^\circ$), *Geophys. Res. Lett.*, 22, 3409, 1995.
- Ho, C. M., B. T. Tsurutani, R. Sakurai, B. E. Goldstein, A. Balogh and J. L. Phillips**, Interplanetary discontinuities in corotating streams and their interaction regions, *Astron. Astrophys.*, 316, 346–349, 1996.

- Hollweg, J. V.**, Surface waves on solar wind tangential discontinuities, *J. Geophys. Res.*, **87**, (A10), 8065–8076, 1982.
- Hoppe, M. M., C. T. Russel, L. A. Frank, T. E. Eastman and E. W. Greenstadt**, Upstream hydromagnetic waves and their association with backstreaming ion pulsations: ISEE 1 and 2 observations, *J. Geophys. Res.*, **86**, (A6), 4471–4492, 1981.
- Horbury, T. S., D. Burgess, M. Fränz and C. J. Owen**, Prediction of earth arrival times of interplanetary southward magnetic field turnings, *J. Geophys. Res.*, **106**, (A12), 30001–30010, 2001a.
- Horbury, T. S., D. Burgess, M. Fränz and C. J. Owen**, Three spacecraft observations of solar wind discontinuities, *Geophys. Res. Lett.*, **28**, (4), 677–680, 2001b.
- Horbury, T. S., P. Cargill, E. A. Lucek, A. Balogh, M. W. Dunlop, T. Oddy, C. Carr, A. Szabo and K. H. Fornacon**, Cluster magnetic field observations of the bowshock: Orientation, motion and structure, *Ann. Geophysicae*, **19**, 1399–1409, 2001c.
- Horbury, T. S., P. J. Cargill, E. A. Lucek, J. Eastwood, A. Balogh and M. W. Dunlop**, Four spacecraft measurements of the quasiperpendicular terrestrial bow shock: Orientation and motion, *J. Geophys. Res.*, **107**, (A8), 1208, doi:10.1029/2001JA000273, 2002.
- Hudson, P. D.**, Discontinuities in an anisotropic plasma and their identification in the solar wind, *Planet. Space Sci.*, **18**, 1611–1622, 1970.
- Hundhausen, A. J., S. J. Bame, J. R. Asbridge and S. J. Sydoriak**, Solar wind proton properties: Vela 3 observations from July 1965 to June 1967, *J. Geophys. Res.*, **75**, (25), 4643, 1970.
- Karimabadi, H., D. Krauss-Varban and N. Omidi**, On the stability of rotational discontinuities: One- and two-dimensional hybrid simulations, *Geophys. Res. Lett.*, **22**, (21), 2989–2992, 1995.
- Kawano, H. and T. Higuchi**, The bootstrap method in space physics: Error estimation for the minimum variance analysis, *Geophys. Res. Lett.*, **22**, (3), 307–310, 1995.
- Kawano, H. and T. Higuchi**, A generalization of the minimum variance analysis method, *Ann. Geophysicae*, **14**, 1019–1024, 1996.
- Kennel, C. F., B. Buti, T. Hada and R. Pellat**, Nonlinear, dispersive, elliptically polarized Alfvén waves, *Phys. Fluids*, **31**, 1949, 1988.
- Khrabrov, A. V. and B. U. Ö. Sonnerup**, Error estimates for minimum variance analysis, *J. Geophys. Res.*, **103**, (A4), 6641–6651, 1998.
- Knetter, T., F. M. Neubauer, T. Horbury and A. Balogh**, Discontinuity observations with Cluster, *Adv. Space Res.*, **32**, (4), 543–548, 2003.
- Knetter, T., F. M. Neubauer, T. Horbury and A. Balogh**, Four-point discontinuity observations using Cluster magnetic field data: A statistical survey, *J. Geophys. Res.*, **109**, (A06102), doi:10.1029/2003JA010099, 2004.

- Krauss-Varban, D.**, Structure and length scales of rotational discontinuities, *J. Geophys. Res.*, 98, (A3), 3907–3917, 1993.
- Krauss-Varban, D., H. Karimabadi and N. Omid**, Kinetic structure of rotational discontinuities: implications for the magnetopause, *J. Geophys. Res.*, 100, 11981–12000, 1995.
- Landau, L. D. and E. M. Lifschitz**, *Elektrodynamik der Kontinua*, vol 8, Akademie Verl., Berlin, 3. Auflage, 1967.
- Lang, K. R.**, *The Cambridge Encyclopedia of the Sun*, Cambridge Univ. Press, Cambridge, UK, 2001.
- Lee, L. C., L. Huang and J. K. Chao**, On the stability of rotational discontinuities and intermediate shocks, *J. Geophys. Res.*, 94, 8813, 1989.
- Lemaire, J. and L. F. Burlaga**, Diamagnetic boundary layers: A kinetic theory, *Astrophys. Space Sci.*, 45, 303–325, 1976.
- Lepping, R. P. and K. W. Behannon**, Magnetic field directional discontinuities: 1. Minimum variance errors, *J. Geophys. Res.*, 85, 4695–4703, 1980.
- Lepping, R. P. and K. W. Behannon**, Magnetic field directional discontinuities: Characteristics between 0.46 and 1.0 AU, *J. Geophys. Res.*, 91, 8725, 1986.
- Lepping, R. P., C. C. Wu and K. McClernan**, Two-dimensional curvature of large angle interplanetary MHD discontinuity surfaces: IMP-8 and WIND observations, *J. Geophys. Res.*, 108, (A7), 1279, doi:10.1029/2002JA009640, 2003.
- Lyu, L. H.**, *Private Communications*, 2003.
- Maksimovic, M., S. D. Bale, T. S. Horbury and M. André**, Bow shock motions observed with Cluster, *Geophys. Res. Lett.*, 30, (7), 1393, doi:10.1029/2002GL016761, 2003.
- Mariani, F., B. Bavassano, U. Villante and N. F. Ness**, Variations of the occurrence rate of discontinuities in the interplanetary magnetic field, *J. Geophys. Res.*, 78, (34), 8011, 1973.
- Mariani, F., B. Bavassano and U. Villante**, A statistical study of MHD discontinuities in the inner solar system: Helios 1 and 2, *Solar Physics*, 83, 349–365, 1983.
- Marsch, E., W. G. Pilipp, R. Schwenn, K. H. Mühlhäuser and H. Rosenbauer**, Some characteristics of proton velocity distributions in the solar wind as observed by the Helios solar probes, in *Solar Wind Four*, MPAE-W-100-81-31, 273, MPAE, Lindau, Germany, 1981.
- Martin, R. N., J. W. Belcher and A. J. Lazarus**, Observation and analysis of abrupt changes in the interplanetary plasma velocity and magnetic field, *J. Geophys. Res.*, 78, (19), 3653, 1973.
- McComas, D. J., B. L. Barraclough, J. T. Gosling, C. M. Hammond, J. L. Phillips, M. Neugebauer, A. Balogh and R. J. Forsyth**, Structures in the polar solar wind: Plasma and field observation from Ulysses, *J. Geophys. Res.*, 100, (A10), 19893–19902, 1995.

- McComas, D. J. et al.**, Solar Wind Electron Proton Alpha Monitor (SWEPAM) for the Advanced Composition Explorer, *Space Sci. Rev.*, 86, (1), 563–612, 1998.
- McCracken, K. G. and N. F. Ness**, The collimation of cosmic rays by the interplanetary magnetic field, *J. Geophys. Res.*, 71, (13), 3315, 1966.
- Mottez, F. and G. Chanteur**, Surface crossing by a group of satellites: A theoretical study, *J. Geophys. Res.*, 99, (A7), 13499–13507, 1994.
- Ness, N. F., C. S. Scearce and S. Cantarano**, Preliminary results from the Pioneer 6 magnetic field experiment, *J. Geophys. Res.*, 71, (13), 3305–3313, 1966.
- Neubauer, F. M.**, Jump relations for shock waves in an anisotropic magnetized plasma, *Z. f. Physik*, 237, 205–223, 1970.
- Neubauer, F. M. and H. Barnstorf**, Recent observational and theoretical results on discontinuities in the solar wind, in *Solar Wind Four*, edited by H. R. Rosenbauer, MPAE-W-100-81-31, 168, MPAE, Lindau, Germany, 1981.
- Neugebauer, M.**, Alignment of velocity and field changes across tangential discontinuities in the solar wind, *J. Geophys. Res.*, 90, 6627–6630, 1985.
- Neugebauer, M.**, The structure of rotational discontinuities, *Geophys. Res. Lett.*, 16, (11), 1261–1264, 1989.
- Neugebauer, M. and C. J. Alexander**, Shuffling foot points and magnetohydrodynamic discontinuities in the solar wind, *J. Geophys. Res.*, 96, (A6), 9409–9418, 1991.
- Neugebauer, M. and B. Buti**, A search for evidence of the evolution of rotational discontinuities in the solar wind from nonlinear Alfvén waves, *J. Geophys. Res.*, 95, (A1), 13–20, 1990.
- Neugebauer, M. and C. W. Snyder**, Mariner 2 Observations of the Solar Wind, *J. Geophys. Res.*, 71, (19), 4469–4484, 1966.
- Neugebauer, M., D. R. Clay, B. E. Goldstein, B. T. Tsurutani and R. D. Zwickl**, A reexamination of rotational and tangential discontinuities in the solar wind, *J. Geophys. Res.*, 89, (A7), 5393–5408, 1984.
- Neugebauer, M., C. J. Alexander, R. Schwenn and A. K. Richter**, Tangential discontinuities in the solar wind: Correlated field and velocity changes and the Kelvin-Helmholtz instability, *J. Geophys. Res.*, 91, (A12), 13694–13698, 1986.
- Neugebauer, M., B. E. Goldstein, D. J. McComas, S. T. Suess and A. Balogh**, Ulysses observations of microstreams in the solar wind from coronal holes, *J. Geophys. Res.*, 100, (A12), 23389–23395, 1995.
- Neugebauer, M., P. C. Liewer, E. J. Smith, R. M. Skoug and T. H. Zurbruchen**, Sources of the solar wind at solar activity maximum, *J. Geophys. Res.*, 107, (A12), 1488, doi:10.1029/2001JA000306, 2002.

- Omidi, N.**, Rotational discontinuities in anisotropic plasmas, *Geophys. Res. Lett.*, *19*, (13), 1335–1338, 1992.
- Parker, E. N.**, Dynamics of the interplanetary gas and magnetic fields, *Astrophys. J.*, *128*, (3), 664–676, 1958.
- Parker, E. N.**, Magnetic reorientation and the spontaneous formation of tangential discontinuities in deformed magnetic fields, *Astrophys. J.*, *318*, 876, 1987.
- Parker, E. N.**, Intrinsic magnetic discontinuities and solar x-ray emission, *Geophys. Res. Lett.*, *17*, 2055, 1990.
- Parker, E. N.**, Convection, spontaneous discontinuities, and stellar winds and x-ray emission, *Rev. Modern Astr.*, *4*, 1–17, 1991a.
- Parker, E. N.**, Space plasma and its origin at the sun, *Phys. Fluids B*, *3*, (8), 2367–2373, 1991b.
- G. Paschmann and P. W. Daly (Ed.), *Analysis Methods for Multi-Spacecraft Data*, ISSI, Bern, Switzerland, 1998.
- Peredo, M., J. A. Slavin, E. Mazur and S. A. Curtis**, Three-dimensional position and shape of the bow shock and their variation with Alfvénic, sonic and magnetosonic Mach numbers and interplanetary magnetic field orientation, *J. Geophys. Res.*, *100*, (A5), 7907–7916, 1995.
- Rème, H. et al.**, First multispacecraft ion measurements in and near the Earth's magnetosphere with the identical Cluster ion spectrometry (CIS) experiment, *Ann. Geophysicae*, *19*, (10-12), 1303–1354, 2001.
- Richter, P. and M. Scholer**, On the stability of rotational discontinuities, *Geophys. Res. Lett.*, *16*, (11), 1257–1260, 1989.
- Robert, P. and A. Roux**, Influence of the shape of the tetrahedron on the accuracy of the estimation of the current density, in *Proceedings of the Spatio-Temporal Analysis for Resolving plasma Turbulence (START) conference*, ESA WPP-047, 289–293, ESA, Paris, France, 1993.
- Robert, P., A. Roux and G. Chanteur**, Accuracy of the determination of the current density via four satellites, International Union of Geodesy and Geophysics, XXI General Assembly, Boulder, Colorado, presentation GAB51H-06, 1995a.
- Robert, P., A. Roux and O. Coeur-Joly**, Validity of the estimate of the current density along cluster orbit with simulated magnetic data, in *Proceedings of Cluster Workshops*, ESA SP-371, 229–233, ESA, Paris, France, 1995b.
- Robert, P., A. Roux, C. C. Harvey, M. W. Dunlop, P. W. Daly and K. H. Glassmeier**, Tetrahedron geometric factors, in *Analysis Methods for Multi-Spacecraft Data*, edited by G. Paschmann and P. W. Daly, 323–348, ISSI, Bern, Switzerland, 1998.

- Roelof, E. C. and D. G. Sibeck**, Magnetopause shape as a bivariate function of interplanetary magnetic field B_z and solar wind dynamic pressure, *J. Geophys. Res.*, 98, 21421–21450, 1993.
- Russell, C. T., M. M. Mellott, E. J. Smith and J. H. King**, Multiple spacecraft observations of interplanetary shocks: Four spacecraft determination of shock normals, *J. Geophys. Res.*, 88, (A6), 4739–4748, 1983.
- Sakai, J.-I. and B. U. O. Sonnerup**, Modulational instability of finite amplitude dispersive Alfvén waves, *J. Geophys. Res.*, 88, 9069, 1983.
- Sari, J. W. and N. F. Ness**, Power spectra of the interplanetary magnetic field, *Solar Physics*, 8, 155–165, 1969.
- Schatten, K. H., J. M. Wilcox and N. F. Ness**, A model of interplanetary and coronal magnetic fields, *Sol. Physics*, 6, 442–455, 1969.
- Scholer, M.**, Die Magnetopause der Erdmagnetosphäre, in *Plasmaphysik im Sonnensystem*, edited by K.-H. Glaßmeier and M. Scholer, BI Wiss. Verl., 1991.
- Schröder, M.**, Automatisierte Identifizierung und Dickenbestimmung von Richtungsdiskontinuitäten im Sonnenwind, Diplomarbeit, Institut für Geophysik und Meteorologie der Universität zu Köln, 2002.
- Schwarz, S. J.**, Shock and discontinuity normals, mach numbers, and related parameters, in *Analysis Methods for Multi-Spacecraft Data*, edited by G. Patschmann and P. W. Daly, 249–270, ISSI, Bern, Switzerland, 1998.
- Schwenn, R.**, Large - scale structure of the interplanetary medium, in *Physics of the Inner Heliosphere I*, edited by R. Schwenn and E. Marsch, Springer, 1990.
- Sen, A. K.**, Stability of hydromagnetic Kelvin-Helmholtz discontinuity, *Phys. Fluids*, 6, (8), 1154–1163, 1963.
- Sestero, A.**, Structure of plasma sheaths, *Phys. Fluids*, 7, (1), 44–51, 1964.
- Siscoe, G. L., L. Davis, P. J. Coleman, E. J. Smith and D. E. Jones**, Power spectra and discontinuities of the interplanetary magnetic field: Mariner 4, *J. Geophys. Res.*, 73, (1), 61–82, 1968.
- Smith, E. J.**, Identification of interplanetary tangential and rotational discontinuities, *J. Geophys. Res.*, 78, 2054, 1973a.
- Smith, E. J.**, Observed properties of interplanetary rotational discontinuities, *J. Geophys. Res.*, 78, 2088, 1973b.
- Smith, E. J., A. Balogh, M. Neugebauer and D. McComas**, Ulysses observations of Alfvén waves in the southern and northern solar hemispheres, *Geophys. Res. Lett.*, 22, (23), 3381–3384, 1995.

- Smith, C. W. et al.**, The ACE Magnetic Field Experiment, *Space Sci. Rev.*, 86, (1), 613–632, 1998.
- Söding, A.**, *Magnetfeldstrukturen im Sonnenwind: Beobachtungen von Diskontinuitäten in der 3-D-Heliosphäre und Methoden zur Untersuchung von 1-D- und 2-D-Strukturen*, Dissertation, Institut für Geophysik und Meteorologie der Universität zu Köln, 1999.
- Söding, A. and F. M. Neubauer**, Minimum variance analysis for 2D structures using two satellites, in *Solar Wind Nine: Proc. of the Ninth Int. Solar Wind Conference*, edited by S. R. Habbal, R. Esser, J. V. Hollweg, and P. A. Isenberg, AIP Conference Proceedings 471, New York, 1999.
- Solanki, S. K., A. Lagg, J. Woch, N. Krupp and M. Collados**, Three-dimensional magnetic field topology in a region of solar coronal heating, *Nature*, 425, 692–695, 2003.
- Solodyna, C. V., J. W. Sari and J. W. Belcher**, Plasma field characteristics of directional discontinuities in the interplanetary medium, *J. Geophys. Res.*, 82, (1), 10, 1977.
- Sonnerup, B. U. Ö.**, Magnetopause structure during the magnetic storm of September 24, 1961, *J. Geophys. Res.*, 76, 6717–6735, 1971.
- Sonnerup, B. U. Ö. and L. J. Cahill**, Magnetopause structure and attitude from Explorer 12 observations, *J. Geophys. Res.*, 72, (A1), 171–183, 1967.
- Sonnerup, B. U. Ö. and L. J. Cahill**, Explorer 12 observations of the magnetopause current layer, *J. Geophys. Res.*, 73, 1757, 1968.
- Sonnerup, B. U. Ö. and M. Scheible**, Minimum and maximum variance analysis, in *Analysis Methods for Multi-Spacecraft Data*, edited by G. Patschmann and P. W. Daly, 185–220, ISSI, Bern, Switzerland, 1998.
- Sonnerup, B. U. Ö., I. Papamastorakis, G. Paschmann and H. Lühr**, Magnetopause properties from AMPTE/IRM observations of the convection electric field: Method development, *J. Geophys. Res.*, 92, (A11), 12137–12159, 1987.
- Sperveslage, K.**, *Dynamische Strukturen im Sonnenwind: Vorschöckwellen und magnetische Löcher*, Dissertation, Institut für Geophysik und Meteorologie der Universität zu Köln, 1999.
- Stone, E. C. et al.**, The Advanced Composition Explorer, *Space Sci. Rev.*, 86, (1), 1–22, 1998.
- Swift, D. W. and L. C. Lee**, Rotational discontinuities and the structure of the magnetopause, *J. Geophys. Res.*, 88, 111, 1983.
- Treumann, R. A. and W. Baumjohann**, *Advanced Space Plasma Physics*, Imperial College Press, London, 1997.
- Tsurutani, B. T. and P. Rodriguez**, Upstream waves and particles: An overview of ISEE results, *J. Geophys. Res.*, 86, (A6), 4319, 1981.

- Tsurutani, B. T. and E. J. Smith**, Interplanetary discontinuities: Temporal variations and the radial gradient from 1 to 8 AU, *J. Geophys. Res.*, **84**, 2773, 1979.
- Tsurutani, B. T., C. M. Ho, E. J. Smith, M. Neugebauer, B. E. Goldstein, J. S. Mok, J. K. Arballo, A. Balogh, D. J. Southwood and W. C. Feldmann**, The relationship between interplanetary discontinuities and Alfvén waves: Ulysses observations, *Geophys. Res. Lett.*, **21**, 2267–2270, 1994.
- Tsurutani, B. T., J. Smith, C. M. Ho, M. Neugebauer, B. E. Goldstein, J. S. Mok, A. Balogh, D. Southwood and W. C. Feldman**, Interplanetary discontinuities and Alfvén waves, *Space Sci. Rev.*, **72**, 205, 1995.
- Tsurutani, B. T., C. M. Ho, J. K. Arballo, E. J. Smith and B. E. Goldstein**, Interplanetary discontinuities and Alfvén waves at high heliographic latitudes: Ulysses, *J. Geophys. Res.*, **101**, (A5), 11027–11038, 1996a.
- Tsurutani, B. T., C. M. Ho, R. Sakurai, B. E. Goldstein, A. Balogh and J. L. Phillips**, Symmetry in discontinuity properties at the north and south heliographic poles: Ulysses, *Astron. Astrophys.*, **316**, 342–345, 1996b.
- Turner, J. M.**, On the relation between solar wind structure and solar wind rotational and tangential discontinuities, *J. Geophys. Res.*, **78**, (1), 59, 1973.
- Turner, J. M. and G. L. Siscoe**, Orientations of rotational and tangential discontinuities in the solar wind, *J. Geophys. Res.*, **76**, (7), 1816, 1971.
- Turner, J. M., L. F. Burlaga, N. F. Ness and J. F. Lemaire**, Magnetic holes in the solar wind, *J. Geophys. Res.*, **82**, (13), 1921–1924, 1977.
- vom Stein, R., K. H. Glassmeier and M. Dunlop**, A configuration parameter for the Cluster satellites, technical Report 2/1992, Institut für Geophysik und Meteorologie der Technischen Universität Braunschweig, 1992.
- von Steiger, R. et al.**, Composition of quasi-stationary solar wind flows from Ulysses/Solar Wind Ion Composition Spectrometers, *J. Geophys. Res.*, **105**, (A12), 27217–27238, 2000.
- Wang, Y.-M. and N. R. Sheeley Jr.**, Solar wind speed and coronal flux-tube expansion, *Astrophys. J.*, **355**, 726–732, 1990.
- Wang, Y. M. and N. R. Sheeley Jr.**, On potential field models of the solar corona, *Astrophys. J.*, **392**, 310–319, 1992.

Acknowledgements

First of all I want to thank my supervisor Prof. F. M. Neubauer for the profound scientific education and for giving me the chance to become an active member of the exciting Cluster mission. He was able to arouse my interest for this field of research and to keep it on a constantly high level. I also want to thank him for encouraging me to present and discuss my results on numerous workshops and conferences.

My thanks go to Prof. M. Kerschgens for being my co-supervisor.

I thank all colleagues of our institute, particularly my room mates Nico Schilling, Sven Jacobsen, Heiko Backes, Annika Steuer and Gudela von Gronefeld for providing a good working atmosphere. The system administration group under the leadership of Dr. A. Wennmacher has always done an excellent job.

During the whole period of my research I could always rely on the loyal and faithful support from Stefan Höfs. Many thanks for numerous graphics and programs.

For spending their time on proof-reading the draft of this work I thank Gerd Schröder, Nico Schilling, Gudela von Gronefeld, Tetsuya Tokano, Heiko Backes, Johan de Keyser, Ron Lepping and Marcia Neugebauer.

My special thanks go to Ron Lepping, Lennard Burlaga, Aaron Roberts, Marcia Neugebauer, Joe Giacalone, Randy Jokipii, Ed Smith and Bruce Tsurutani for their hospitality and intense and inspiring discussions. In particular, I thank Marcia Neugebauer for helping me out with the Kitt Peak data.

Marcus Fränz contributed a great deal in providing and explaining the plasma data and software from the CIS instruments. Thanks also to Axel Korth, Iannis Dandouras and the PI Henry Rème.

Many thanks also to the FGM team for a smooth collaboration. In particular, I thank the PI André Balogh, Tim Horbury for numerous scientific discussions and Karl-Heinz Fornaçon for providing special calibration files.

My parents Reinhild and Manfred have contributed to this work more than they may believe. Thank you for your support. Particularly I thank Reinhild for her constant patience and Manfred for sharing his passion for sailing with my brother Christian and me. Perhaps this combination was the first and enduring cornerstone in our scientific education. Thanks to my brother for being a companion in living, sailing and physics.

My deepest gratitude is reserved for my dearest one, my beloved Petra, for her presence in my life.

I acknowledge the financial support by DLR under the Cluster program.

Erklärung

Ich versichere, dass ich die von mir vorgelegte Dissertation selbständig angefertigt, die benutzten Quellen und Hilfsmittel vollständig angegeben und die Stellen der Arbeit - einschließlich Tabellen, Karten und Abbildungen -, die anderen Werken im Wortlaut oder dem Sinn nach entnommen sind, in jedem Einzelfall als Entlehnung kenntlich gemacht habe; dass diese Dissertation noch keiner anderen Fakultät oder Universität zur Prüfung vorgelegen hat; dass sie - abgesehen von unten angegebenen Teilpublikationen - noch nicht veröffentlicht worden ist sowie, dass ich eine solche Veröffentlichung vor Abschluss des Promotionsverfahrens nicht vornehmen werde. Die Bestimmungen dieser Promotionsordnung sind mir bekannt. Die von mir vorgelegte Dissertation ist von Prof. F.M. Neubauer betreut worden.

Köln, den 20. Juli 2005

Teilpublikationen

- **Knetter, T., F. M. Neubauer, T. Horbury und A. Balogh**, Discontinuity observations with Cluster, *Adv. Space Res.*, 32, (4), 543-548, 2003
- **Knetter, T., F. M. Neubauer, T. Horbury und A. Balogh**, Four-point discontinuity observations using Cluster magnetic field data: A statistical survey, *J. Geophys. Res.*, 109, (A06102), doi:10.1029/2003JA010099, 2004

Lebenslauf

Persönliche Daten

Name: Thorsten Knetter
Geburtsdatum: 02.06.1974
Geburtsort: Troisdorf
Familienstand: ledig
Staatsangehörigkeit: deutsch
Anschrift: Clarenbachstr. 200
50931 Köln

Schulbildung

1980 - 1984 Grundschohle Neuenrade
1984 - 1993 Albert-Schweitzer-Gymnasium Plettenberg
Juni 1993 Abitur

Hochschulstudium

Okt. 1994 Immatrikulation an der Universität zu Köln,
Studiengang: Physik, Diplom
Okt. 1996 Vordiplom
Juni 2000 Abschluss der Diplomarbeit
bei Priv. Doz. Dr. H. Rieger
seit Okt. 2000 Promotion in Geophysik an der Universität zu Köln
unter Anleitung von Prof. Dr. F. M. Neubauer

Tätigkeit

seit Okt. 2000 Wissenschaftlicher Mitarbeiter am Institut für
Geophysik und Meteorologie der Universität zu Köln